



**Università  
degli Studi  
di Palermo**

AREA QUALITÀ, PROGRAMMAZIONE E SUPPORTO STRATEGICO  
SETTORE STRATEGIA PER LA RICERCA  
U. O. DOTTORATI

Dottorato in Scienze Fisiche e Chimiche  
Dipartimento di Fisica e Chimica “Emilio Segré”  
SSD - FIS/05F

## Data-driven MHD simulations of the Parker spiral and interplanetary propagation of solar transients

IL DOTTORE  
**Ruggero Biondo**

IL COORDINATORE  
**Marco Cannas**

IL TUTOR  
**Fabio Reale**

I CO TUTOR  
**Alessandro Bemporad**  
**Paolo Pagano**

CICLO XXXV  
ANNO CONSEGUIMENTO TITOLO 2023

## Abstract

The accurate reconstruction of the plasma and magnetic field parameters in the ambient interplanetary medium is fundamental to reproduce the interplanetary propagation of solar disturbances such as solar energetic particles (SEPs), stream and corotating interaction regions (SIRs and CIRs), and coronal mass ejections (CMEs), both for understanding the physics of these phenomena and for applications in space weather forecasting. The small-scale features of the ambient solar wind, in fact, affect the evolution, arrival times, and geo-effectiveness of solar transients.

The Reverse In situ and MHD Approach (RIMAP) is a hybrid analytical-numerical method to reconstruct the heliosphere on the ecliptic plane from in situ measurements acquired by spacecraft with heliocentric orbits. RIMAP uses the in situ measurements as boundary conditions for a MHD simulation based on the PLUTO code, combining ballistic and MHD approaches in order to preserve the small-scale variability of the solar wind flow lines and thus offering a structured, realistic background medium for modelling the propagation of solar eruptions.

In this dissertation, after an introduction about the main topics and models of heliospheric physics and the magnetohydrodynamics equations, we present the detailed description of the novelties of the RIMAP model, and its application to the measurements acquired by spacecraft at 1 AU in correspondence of solar minima configurations.

Then, one of these reconstructions is used as a background medium to propagate an interplanetary CME. The perturbation is modelled as a spheroidal, homogeneous plasma cloud without internal magnetic flux rope. We use an artificial, passive tracer to quantify the mixing at 1 AU between ambient solar wind material and the one with coronal eruption origins, in order to evaluate the fraction of plasma measured in situ that can be traced back to its sources on the Sun.

The RIMAP reconstruction is also carried out using measurements acquired by NASA's Parker Solar Probe (PSP) during its seventh solar encounter, in January 2021, between 20 and 40 solar radii. This was the time of the first quadrature between PSP and ESA-NASA's Solar Orbiter (Solo), which at the time was orbiting the Sun around 0.5 AU and providing remote sensing observations of the solar corona via the Metis coronagraph. The RIMAP reconstruction connects density and wind speed estimates inferred from the coronal features observed by Metis/Solo between 3 and 6 solar radii to the measurements acquired by PSP at 21.5 solar radii along the corresponding plasma streamline. Thus, the magnetic connection between the inner corona and the super Alfvénic wind is reconstructed with a high degree of accuracy with a detailed data-driven MHD simulation.

Finally, we describe the possible future developments of the RIMAP technique such as the extension to a two-fluids treatment, the testing of different models of magnetized coronal mass ejections, the simulation of solar wind switchbacks, and the extension to full three-dimensional boundaries, using coronagraphic observations to infer the input parameters.

# Contents

<b>1</b>	<b>Introduction</b>	<b>3</b>
1.1	Units and Constants . . . . .	3
1.2	The Solar Atmosphere . . . . .	3
1.2.1	The Corona . . . . .	5
1.2.2	The Solar Wind . . . . .	8
1.2.3	Solar transients and Coronal Mass Ejections . . . . .	12
1.2.4	Space weather . . . . .	16
1.3	Magnetohydrodynamics equations . . . . .	18
1.3.1	Ideal MHD and Alfvén's theorem . . . . .	24
1.4	The Parker model for Solar Wind . . . . .	26
1.4.1	Magnetized Solar Wind . . . . .	30
1.4.2	Global structure of the Parker Spiral . . . . .	34
1.5	Modelling interplanetary coronal mass ejections . . . . .	36
1.6	Heliospheric spacecraft relevant to this work . . . . .	39
1.6.1	GSS Wind . . . . .	39
1.6.2	STEREO-A . . . . .	40
1.6.3	Parker Solar Probe . . . . .	41
1.6.4	Solar Orbiter . . . . .	42
<b>2</b>	<b>Models and methods: the RIMAP model</b>	<b>45</b>
2.1	Analytical and Numerical Models . . . . .	45
2.1.1	Ballistic models . . . . .	45
2.1.2	Forward numerical models . . . . .	46
2.2	The Reverse in situ and MHD Approach . . . . .	51
2.2.1	Inverse mapping of the inner boundary . . . . .	52
2.2.2	PLUTO code . . . . .	56
2.3	Using RIMAP with measurements acquired at 1 AU . . . . .	62
2.3.1	Preparing Wind data . . . . .	63
2.3.2	Grid Layout and Boundary Conditions . . . . .	63
2.3.3	Results . . . . .	64
2.4	Conclusion . . . . .	75
<b>3</b>	<b>Tracing ICME plasma with the RIMAP model</b>	<b>77</b>
3.1	Context . . . . .	77
3.2	Tracing plasma in the interplanetary medium . . . . .	79
3.2.1	Ice-cream Cone Modelled ICME . . . . .	80
3.2.2	Results . . . . .	82
3.3	Conclusions . . . . .	86

<b>4</b>	<b>Connecting PSP in situ measurements and Metis remote sensing observations with the RIMAP model</b>	<b>88</b>
4.1	Context . . . . .	88
4.2	Spacecraft data . . . . .	90
4.3	Magnetic connection between super and sub-Alfvénic Corona . . . . .	92
4.3.1	Refinements of the RIMAP technique . . . . .	93
4.3.2	Results . . . . .	94
4.4	Conclusions . . . . .	98
<b>5</b>	<b>Future prospects and conclusions</b>	<b>100</b>
5.1	Switchback simulations . . . . .	100
5.2	Magnetized ICMEs . . . . .	104
5.3	Two-fluid treatment . . . . .	106
5.4	3D internal boundary from coronagraphic observations . . . . .	108
5.5	Summary and conclusions . . . . .	109
<b>6</b>	<b>Bibliography</b>	<b>112</b>
	<b>List of Figures</b>	<b>143</b>
	<b>List of Tables</b>	<b>151</b>

# Chapter 1

## Introduction

### 1.1 Units and Constants

In this work, most physical quantities are written in the Centimetre-Gram-Second (CGS) system of units. The exceptions are thermal pressure and magnetic field, which for in situ data are more conveniently described in their Metre-Kilogram-Second (MKS) units: respectively, in Tesla, Pascal, and their submultiples.

The following constants are also used:

$R_{\odot} = 6.96 \cdot 10^{10}$ cm	solar radius
$M_{\odot} = 1.99 \cdot 10^{33}$ g	solar mass
$L_{\odot} = 3.83 \cdot 10^{33}$ g cm <sup>2</sup> s <sup>-3</sup>	solar luminosity
$m_p = 1.67 \cdot 10^{-24}$ g	proton mass
$m_e = 9.11 \cdot 10^{-28}$ g	electron mass
$c = 3.00 \cdot 10^{10}$ cm s <sup>-2</sup>	speed of light
$e = 4.80 \cdot 10^{-10}$ cm <sup>3/2</sup> g <sup>1/2</sup> s <sup>-1</sup>	electron charge
$G = 6.67 \cdot 10^{-8}$ g <sup>-1</sup> cm <sup>3</sup> s <sup>-2</sup>	constant of gravitation
$k_B = 1.38 \cdot 10^{-16}$ g cm <sup>2</sup> s <sup>-2</sup> K <sup>-1</sup>	Boltzmann constant

When discussing distances on interplanetary scale, astronomical units are often used in the following sections and chapters, with

$$1 \text{ AU} = 1.496 \cdot 10^{13} \text{ cm} \approx 215 R_{\odot}.$$

Except where explicitly mentioned otherwise, the geometry used is spherical and the frame of reference is heliocentric, with  $(r, \theta, \varphi)$  denoting the radial, colatitudinal and longitudinal coordinates, respectively.

### 1.2 The Solar Atmosphere

The solar atmosphere is defined as the part of the Sun from which photons can escape directly into space. It consists of three regions, often conveniently but incorrectly pictured as a series of spherical shells (Priest, 2014), with different physical properties.

The lowest of these shells is called the photosphere, which is a thin layer only several hundred kilometers thick, relatively dense and opaque. Most of the solar

radiation come from this layer. It has an optical thickness  $\tau_\lambda \lesssim 1$  in the near-ultraviolet (UV), visible (V), and near-infrared (IR) continua, but it is optically thick in all spectral lines except the weakest ones. The optical thickness  $\tau_\lambda$  is a measure of the transparency of a medium at a determined wavelength  $\lambda$ , and it is defined by

$$I = I_0 e^{-\tau_\lambda}$$

where  $I_0$  is the intensity of radiation at the source and  $I$  the observed intensity after a given path.

Above the photosphere lies the chromosphere, rare and more transparent, which can be seen for a few seconds at the beginning and at the end of a solar eclipse, as a red glow. The chromosphere is optically thin in the near-UV, V, and near-IR continua, but is optically thick in strong spectral lines.

The outer layer is called the corona. It extends from the top of a narrow transition region (less than 100 km thick) and out into the solar wind, which fills the heliosphere. This wind of electric charged particles tends to constantly expand, until the pressure of the interstellar medium pushes it back, delimiting at the heliopause the borders of the solar system, around 120 AU (as measured ten years ago by the Voyager I probe; Cowen, 2013). The corona is optically thin over the whole electromagnetic spectrum, except for radio waves and a few spectral lines.

Figure 1.1 shows a simplified schematics of the mean variations of density and temperature as one moves away from the solar surface, as described by the semi-empirical one-dimensional model of Vernazza et al. (1981). The density of the solar atmosphere decreases rapidly with height: going from the  $10^{29}$  particles per cubic centimeter ( $\text{cm}^{-3}$ ) in the photosphere,  $10^{18} \text{ cm}^{-3}$  at the height of 1 solar radius,  $10^{13} \text{ cm}^{-3}$  at 1 AU, and  $10^{12} \text{ cm}^{-3}$  in the interstellar medium (Priest, 2014). Before 1940, it was thought that the temperature decreased in a similar manner above the solar surface. Instead, it has been realized that, after falling from 6600 K at the bottom of the photosphere to a value of about 4400 K at  $\sim 500$  km, the temperature rises slowly through the lower chromosphere and then abruptly through the transition region, up to a few million degrees in the corona. Thereafter, it falls slowly in the outer corona, to a value of approximately  $10^5$  K at 1 AU.

However, this behaviour is not simple like the representation depicted in figure 1.1, since models like those of Vernazza et al. (1981) only indicates the mean properties. In reality, the solar atmosphere is constantly seething, its temperature and density continually changing as the material heats and cools dynamically over short length scales (Priest, 2014).

When the Sun is observed through filters at different wavelengths, it is possible to obtain images of the solar structure at different layers. For instance, the chromosphere is revealed using an  $\text{H}\alpha$  filter (with  $\text{H}\alpha$  being the Balmer line corresponding to the atomic transition from the second to the third energetic level), which is important for following the evolution of active regions, prominence, and for observing the low-temperature parts of solar flares. Figure 1.2 shows four images taken from the Solar Dynamic Observatory (SDO; Pesnell et al., 2012) at different spectral lines. From left to right, and from top to bottom these are (as described in Lemen et al., 2012):  $6173 \text{ \AA}$ , corresponding to the Fe I absorption line, used to visualize the line-of-sight photospheric magnetic fields;  $1700 \text{ \AA}$ , used to visualize the photosphere and a layer of the chromosphere at the temperature minimum around  $\sim 10^{3.7}$  K;  $304 \text{ \AA}$ , corresponding to the He II line, used to image the chromosphere and the transition region at the typical temperature of  $10^{4.7}$  K; and  $193 \text{ \AA}$ , corresponding to

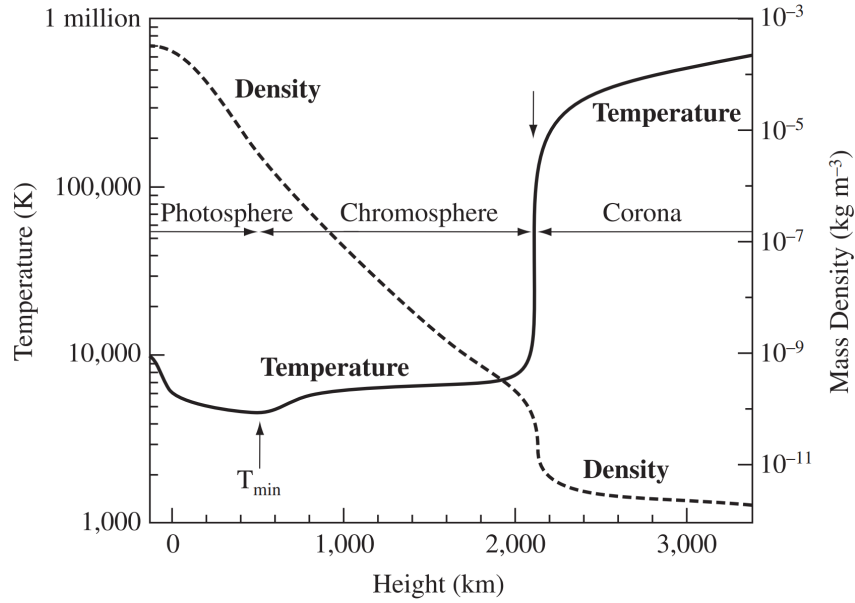


Figure 1.1: Schematics of the average variation with height of temperature and density in the solar atmosphere, according to the theoretical 1D model of Vernazza et al. (1981). In practice, the solar atmosphere is an highly inhomogeneous, dynamic, and time-varying environment, hence this schematics is an oversimplification of the actual conditions.

Source: Priest (2014), © Cambridge University Press.

the lines of Fe XII and Fe XXIV, showing the corona at the temperatures of  $10^{6.1}$  and  $10^{7.3}$  K.

### 1.2.1 The Corona

The corona is observed at solar eclipses as a faint halo, as bright as the full Moon. The coronal features seen in visible light during an eclipse (such as in figure 1.3) are due by the scattering of photospheric light coming up from below, both off electrons (the K-corona) and dust (the F-corona) (Priest, 2014). Within 2.3 solar radii, the K-corona is dominant. The right panel of figure 1.3 shows an eclipse image taken near the maximum of sunspot solar cycle 21, with a filter more sensitive near its edge. Close to the Sun, most of the coronal structure is due to closed magnetic field lines, while moving outwards most of it is due to open field line, stretched-out by the flowing solar wind.

Between the 1870s and the 1930s, it was supposed that the corona was populated by an exotic element, aptly called coronium. This happened because none of the lines in the visible coronal spectrum (of which the most intense is the green line at  $5303 \text{ \AA}$ ) had ever been reproduced in laboratory, nor indeed had they ever been observed in any other celestial source, except for a brief appearance during a nova-like outburst in 1933 (Hunter, 1942). Finally, Grotrian (1939) and Edlén (1943) realised that coronal emission lines arise from normal elements, such as iron, ionized by extremely high temperatures on the order of millions of Kelvin. This is so hot that hydrogen becomes fully ionized, and heavier nuclei may lose up to fifteen of their electrons. The corona is therefore emitting in X-rays, and can be imaged in soft X rays or in extreme ultra-violet light (EUV) only from space-based observations (as in the bottom right panel of figure 1.2), since Earth's atmosphere is not transparent to EUV

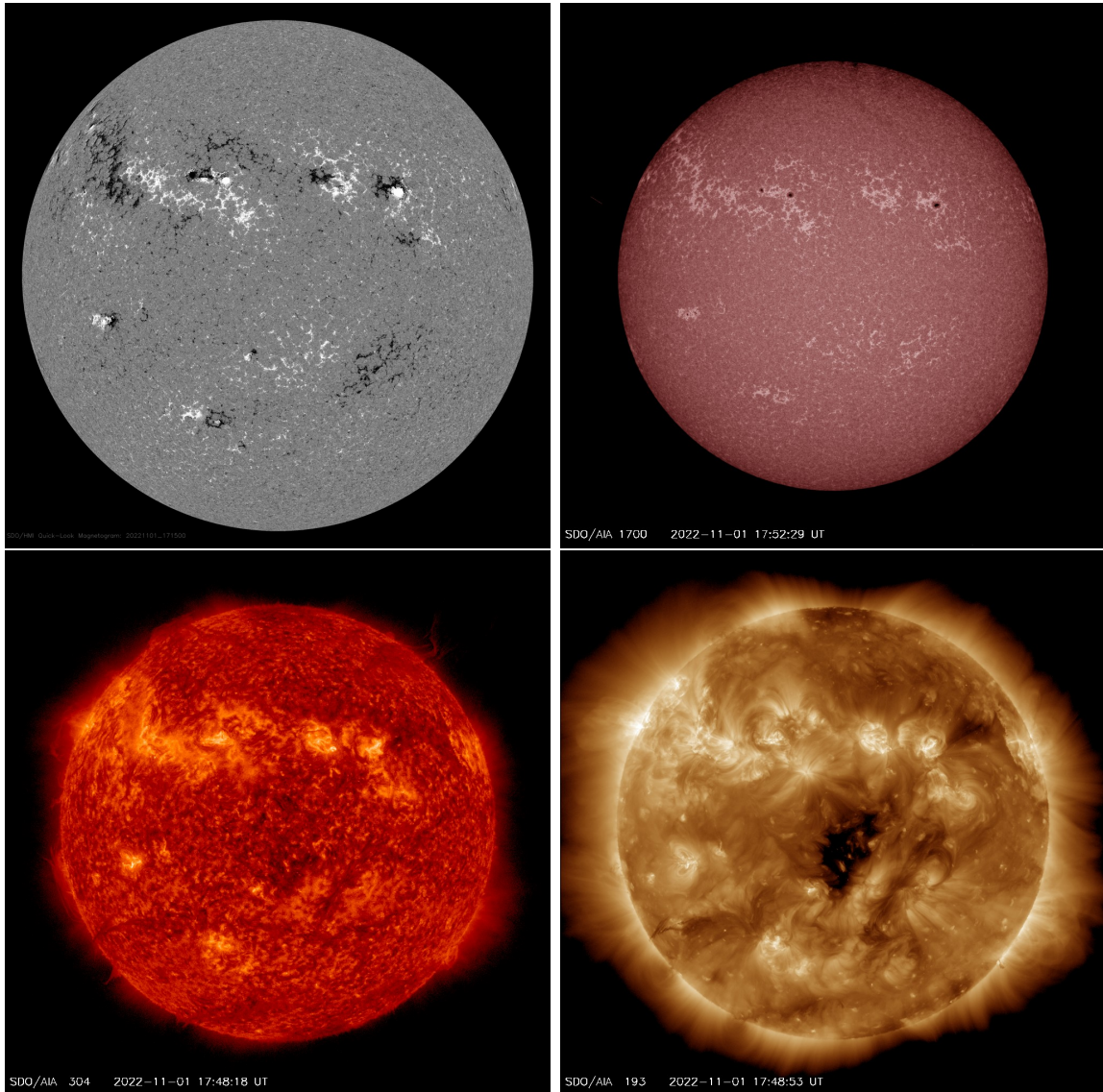


Figure 1.2: Images of different layers of the Sun obtained by the Solar Dynamics Observatory on November 1, 2022 with the instruments HMI and AIA at different wavelengths. The left top panel shows the photospheric magnetic field on the line of sight, with positive polarity in white and negative in black ( $6173 \text{ \AA}$ ); in the right top panel, the photosphere and a layer of the chromosphere at its temperature minimum are depicted ( $1700 \text{ \AA}$ ); the left bottom panel shows the chromosphere and the transition region ( $304 \text{ \AA}$ ); in the right bottom panel we find the solar corona ( $193 \text{ \AA}$ ).

radiation. Understanding the mechanisms responsible for the heating of the corona still remains a major problem in solar physics, with different theories proposed to explain it.

Coronal magnetic fields vary typically between few Gauss (G) and many hundreds of G. They have been measured directly from radio emission or from the Zeeman splitting of infra-red coronal emission lines (Priest, 2014).

As we said above, the corona was originally observed only during solar eclipses, since it cannot be seen otherwise in white light against the million times brighter photosphere. The inconvenience of having to rely on the natural occurrence of solar eclipses (on average one every three years) led to the development of coronagraphs,

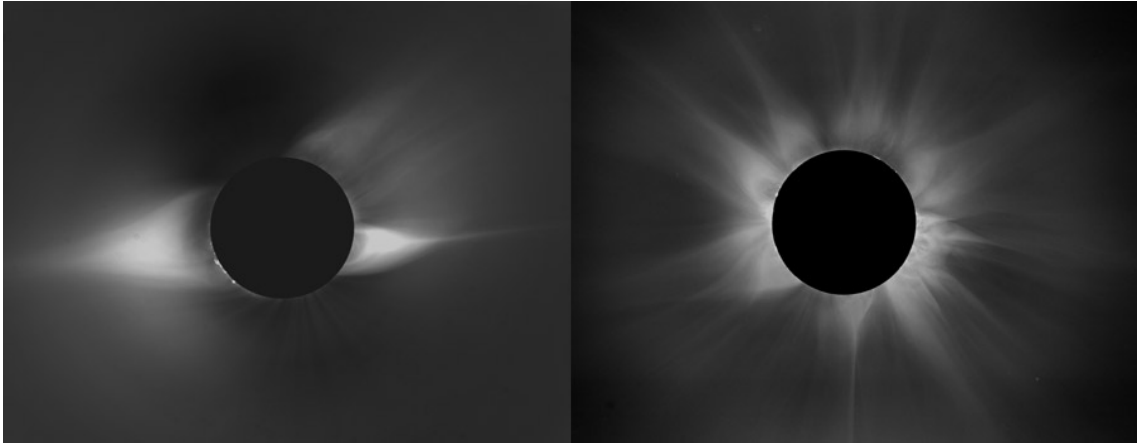


Figure 1.3: The corona in white light during a total solar eclipse, as seen during a solar minimum (on the left, November 1994), and during a solar maximum (on the right, February 1980).

Credits: [National Center for Atmospheric Research's High Altitude Observatory and Rhodes College](#).

which are telescopes containing an occulting disk in order to eliminate the photospheric glare, thus mimicking the natural phenomenon. The first one was designed by Lyot (1939). Much progress has been made from coronagraphs on board satellites in outer space, where unwanted light is much reduced. In 2027, the recently launched spacecraft Solar Orbiter (described in section 1.6.4) will bring its Metis coronagraph to 0.28 AU, the closest heliocentric distance ever achieved by such instruments.

In soft X-rays and EUV the corona may be viewed directly, since in these bands the contribution from the lower layers of the Sun is negligible. The disadvantage is that light in soft X-rays and EUV is absorbed by the Earth's atmosphere, thus much has been learned from space-based observations, revealing a much greater complexity in the coronal structure than the one seen from solar eclipses.

The corona (showed in EUV in the bottom right panel of figure 1.2 and in figure 1.4) has a three-part structure (Priest, 2014): relatively dark coronal holes, where material is escaping outwards along open magnetic fields; brighter coronal loops, which are magnetically closed and connect photospheric regions of opposite polarity; and small intense features called X-ray bright points, scattered over the whole solar disk, consisting of little loops.

In the outer corona, as seen in white light from ground-based observation as in fig. 1.3 and space-based ones such as those from the Large Angle and Spectrometric Coronagraph (LASCO; Brueckner et al., 1995) instrument on board the Solar and Heliospheric Observatory (SOHO; Domingo et al., 1995), depicted in figure 1.5, one can observe several large bright structures extending outwards, called coronal streamers or helmet streamers. They lie above prominences and active regions, and consist of arches of closed magnetic field lines surmounted by a blade of open lines. They form when the upper part of a coronal arch reaches a sufficient altitude and it get stretched open and out by the solar wind.

As clearly depicted in figure 1.3, the overall shape of the solar corona changes with the 11-year Solar cycle: near solar minima, the streamers are only found around the solar equator, with coronal holes occupying the poles; near solar maxima, instead, both coronal streamers and coronal holes extend outwards in every direction at any latitude.

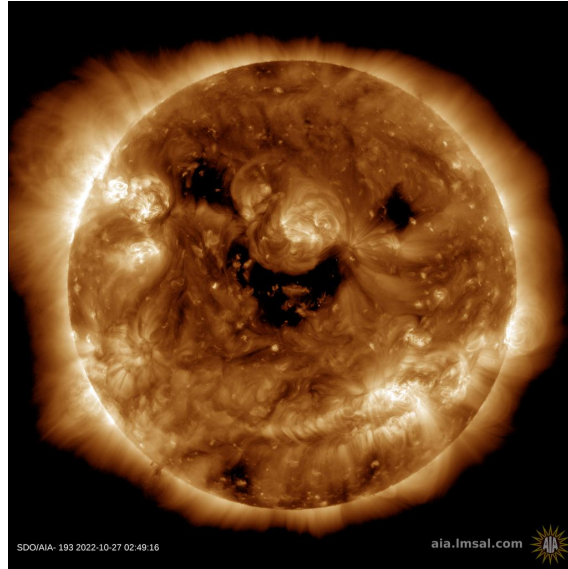


Figure 1.4: The solar corona observed on October 27, 2022 in the 193 Å spectral line by SDO. The dark regions that draw the "smiley face" are coronal holes. Coronal loops and bright points are also visible.

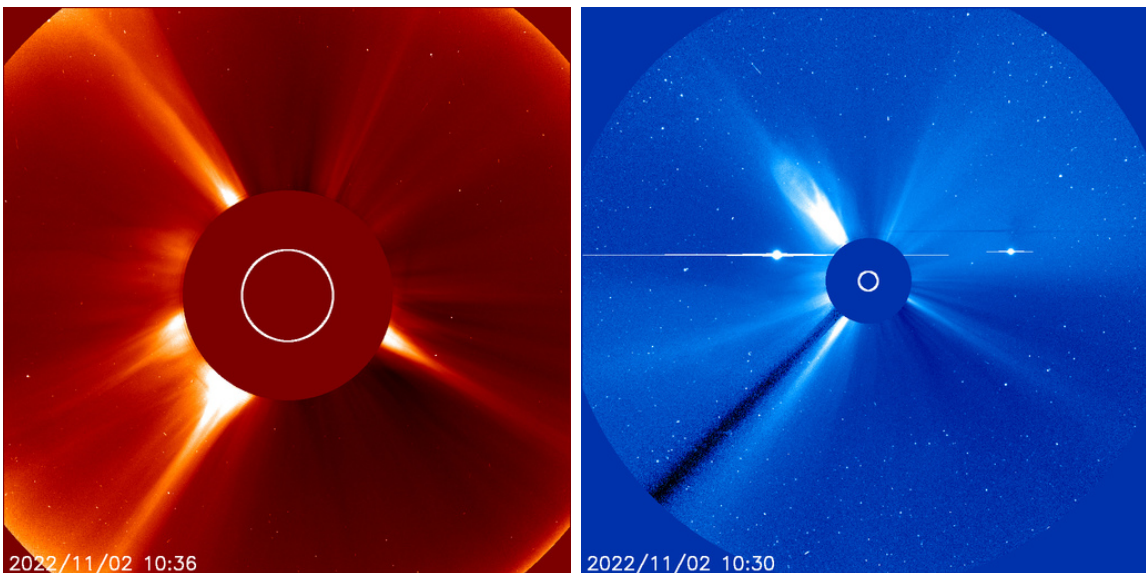


Figure 1.5: The outer solar corona observed on November 2, 2022 in white light with two of the coronagraphs that compose LASCO, called C2 (on the left, imaging from 2.5 to 6  $R_{\odot}$ ) and C3 (on the right, 3.7-30  $R_{\odot}$ ). Multiple coronal streamers are visible, which begin to be distributed on higher latitudes as the Sun approaches the maximum of the current activity cycle (estimated to be in 2025).

## 1.2.2 The Solar Wind

The outer solar corona is not in a condition of hydrostatic equilibrium. Instead, it is continuously expanding into the interplanetary space as a flow of particles, called solar wind. The first spacecraft to measure its properties in situ were the Luna II in 1958 and Mariner II in 1962 (Ness and Wilcox, 1964; Neugebauer and Snyder, 1962). Later on, the Helios probes (launched in 1974 and 1976) did it, approaching the distance of 0.3 AU from the Sun (Porsche, 1977, 1981), while Pioneer 10 and 11, and Voyager 1 and 2 measured solar wind properties at the edges of the solar system.

The recently launched Parker Solar Probe (discussed in section 1.6.3) has already broken the record of closest spacecraft to the Sun, approaching 0.17 AU on October 29, 2018. Its closest approach to our star will be at 0.040 AU ( $\lesssim 10 R_{\odot}$ ). Due to the Earth’s orbital velocity of 30 km/s, most of the in situ information are acquired on the ecliptic plane, that is the plane in which the heliocentric orbital motion of Earth happens. After the Voyager probes, another exception was the Ulysses mission (Wenzel et al., 1992), which used a Jupiter fly-by to swing in an orbit inclined at  $80^{\circ}$  to the ecliptic, and passed over the solar poles in 1994, 2000, and 2007. Another one will be the recently launched Solar Orbiter, which will reach a  $17^{\circ}$  inclination after a fly-by with Venus in 2025, that will gradually increase to  $33^{\circ}$  during the later phases of its mission.

At 1 AU, the solar wind presents the main characteristics summarized in table 1.1. It consists of two regimes: the slow solar wind, with typical speeds of 400 km/s, and the fast solar wind, usually around 750 km/s, less dense and hotter. The two regimes have different composition, pointing to different coronal sources.

	Min	Average	Max
Velocity	200 km/s	400 km/s	900 km/s
Density	$0.04 \text{ cm}^{-3}$	$5 \text{ cm}^{-3}$	$8 \text{ cm}^{-3}$
Electron temperature	$5 \cdot 10^3 \text{ K}$	$2 \cdot 10^5 \text{ K}$	$10^6 \text{ K}$
Proton temperature	$3 \cdot 10^3 \text{ K}$	$5 \cdot 10^4 \text{ K}$	$10^6 \text{ K}$
Magnetic field	0.25 nT	6 nT	40 nT

Table 1.1: Properties of the ambient solar wind at 1 AU, from Zhou et al. (2020) and Priest (2014).

Slow solar wind is highly variable, and its precise origin is still uncertain (Abbo et al., 2016). Theories and observations suggest that slow solar wind streams may originate at the tips of helmet streamers (Einaudi et al., 1999; Lapenta and Knoll, 2005) from rearrangements in the magnetic topology near coronal hole boundaries (Antiochos et al., 2011; Fisk and Schwadron, 2001), or within coronal holes with highly diverging magnetic fields (Cranmer, 2009; Wang and Sheeley, 1992). Recently, Parker Solar Probe at 36-54  $R_{\odot}$  measured slow solar wind emerging from a small equatorial coronal hole (Bale et al., 2019). This is more common during solar maxima, while during solar minima the slow solar wind is more frequently associated with high-latitude coronal holes and streamers. The temperature of its ionized oxygen, a parameter which is conserved (as will be discussed in sections 1.3 and 1.5) outside a few solar radii and thus reflects the inner coronal temperature, is around  $1.1 \cdot 10^6 \text{ K}$  (Priest, 2014).

Fast solar wind is relatively steady and originates in coronal holes, as it has been established since the work of Wilcox (1968) (Abbo et al., 2016; Bale et al., 2016; Cranmer, 2002). For this reason fast solar wind streams tend to recur every 27 days at the solar equatorial rotation rate and are correlated with the recurrence of geomagnetic storms (Kamide and Maltsev, 2007; Priest, 2014). The fast wind has an oxygen temperature of  $1.6 \cdot 10^6 \text{ K}$  (Priest, 2014), although UVCS measurements reveal that in coronal holes heavy ions are heated 100 times more than protons, reaching temperatures of  $10^8 \text{ K}$  (e.g. Antonucci et al., 2000). At solar minimum, it is not found in the equatorial regions, while at solar maximum it occurs as narrow streams at all latitude, as depicted in figure 1.6.

In coronal holes, the dominant energy loss is advective transport by the solar

wind rather than downward convective flux (Priest, 2014). In polar coronal holes, the solar wind accelerates rapidly, reaching half of its terminal speed between 2 and 4 solar radii (Kohl, 2006). From the cusps of equatorial helmet streamers, a continual release of faint blobs can be seen with coronagraphs, accelerated to 300-400 km/s within 30 solar radii (Chen et al., 2009; Sheeley et al., 1997).

Proton temperature is higher in the fast solar wind, while the electron one is the same. The mass flux is the same,  $10^8 \text{ cm}^{-2} \text{ s}$ , to within a factor of two for all solar wind conditions.

	Speed	Electron density	Ram pressure
Fast	750 km/s	$2.5 \text{ cm}^{-3}$	$2.6 \cdot 10^{-9} \text{ Pa}$
Slow	400 km/s	$7.0 \text{ cm}^{-3}$	$2.1 \cdot 10^{-9} \text{ Pa}$

Table 1.2: The fast and slow solar wind show different typical properties at 1 AU.

The solar wind is mostly composed of electrons and protons, with its 3-4% being  $\alpha$  particles (Hydrogen nuclei). In the fast solar wind, there is a preferential heating of heavy ions in respect to the other particles, and of ions perpendicular to the magnetic field than parallel to it.

The solar wind is time-dependent, and varies with a frequency modulated by the 11-year solar cycle. Tangential and rotational discontinuities are common, and fast magneto-acoustic shocks are often found, generated by disturbances of solar origin or by complex interactions between streams of different speeds.

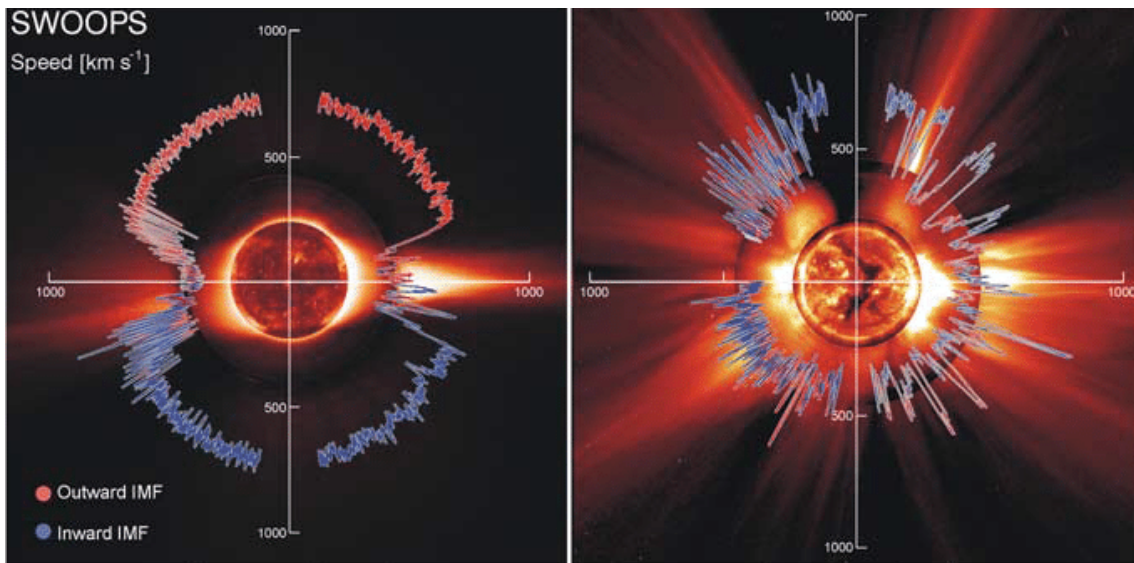


Figure 1.6: Polar plots of solar wind speed as a function of solar latitude for the first two orbits of the Ulysses mission. Both are plotted over composite solar images characteristic of solar minimum (1996, on the left) and maximum (2000, on the right). Outward-directed magnetic field is colored in red, the inward-directed one in blue. Notice how the solar wind speed distribution is much more isotropic in the right panel.

Reproduced from McComas et al. (2003), © American Geophysical Union.

At solar minima, the opposite polarities of the solar magnetic field exiting from the two polar coronal holes are separated at the equator by one or two helmet streamers, as visible in the left panel of figure 1.3. They lie below a neutral heliospheric current

sheet that stretches outwards from the height of one or two solar radii to the edges of the heliosphere. In an ideal, dipolar symmetric atmosphere, the current sheet would lie on the equatorial plane. However, this symmetry lacks (due to different reasons discussed in more detail in section 1.4.2) and this causes the warping of the current sheet in a characteristic shape that resembles the brim of an old hat, or a ballerina skirt, as shown on the sketch in figure 1.7. At solar minima, the sheet is typically inclined by about 7 degrees with respect to the ecliptic plane. Thus, as the Sun spins, an observer at 1 AU is alternatively exposed to fast solar winds coming from one solar hemisphere or from the other, with disturbed periods of slow solar winds in between (Priest, 2014). The current sheet itself is called a sector boundary as it moves past the observer, and the whole pattern is known as a sector structure. The most common configuration is a set of four streams, two of high speed and two of low speed, with a unipolar magnetic field in each sector (ibid.), as depicted in the second panel of figure 1.7.

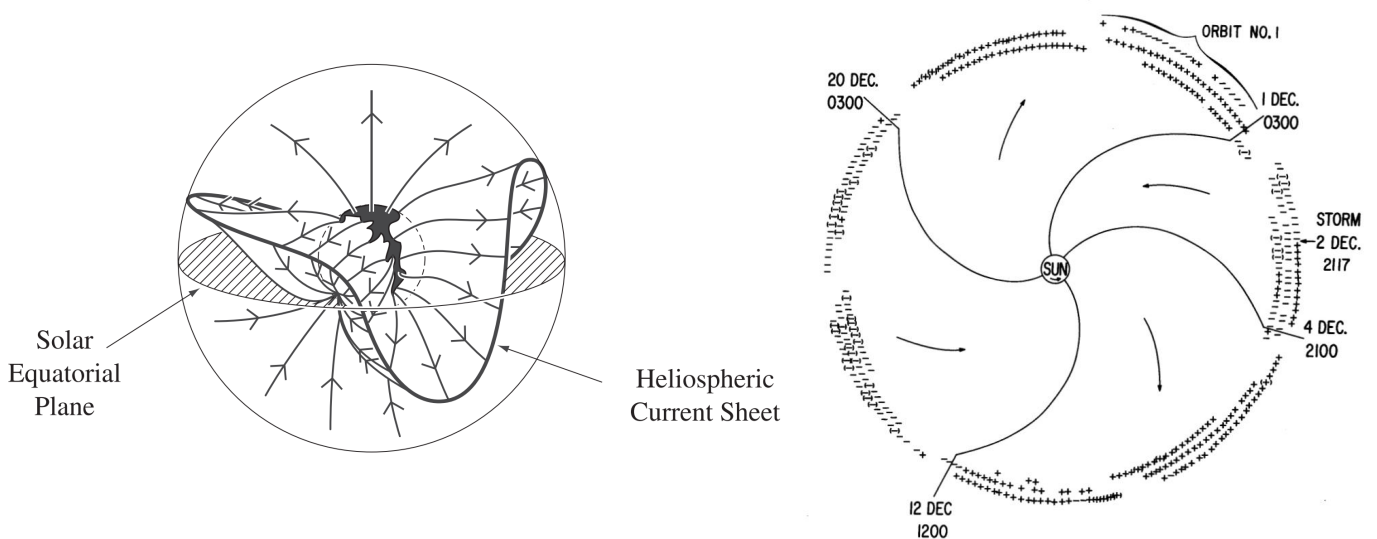


Figure 1.7: On the left panel, a sketch taken from Hundhausen (1977) of the warped heliospheric current sheet (bounded by the black solid line), with the magnetic field lines represented as arrowed lines. On the right, taken from Wilcox and Ness (1965), a sketch of the sector boundaries encountered at 1 AU as the Sun rotates. The plus symbols indicate outward magnetic field, while the minus symbols stand for inward magnetic field. © American Geophysical Union.

Figure 1.8 shows an example of in situ measurements of solar wind acquired at 1 AU near a solar minimum (in this case, 2007). The profiles exhibit small fluctuations over small timescales, but also a regular alternation of high-speed and low-speed streams, in which the density varies by a factor of ten and the speed by a factor of two. The speed arises abruptly and then slowly decreases, with density peaking in correspondence of the increases. On the other hand, radial magnetic field changes sign when a new fast stream of wind is crossed, and it remains constant inside the sector. This shows the two regimes of solar wind: the fast one, tenuous and uniform, and the slow one, much denser and structured.

Figure 1.6 shows an important result from the Ulysses mission: how the solar wind speed varies with latitude and with the solar cycle (McComas et al., 2003). Speed is represented as a polar plot, such that the distance from the centre is proportional to the speed at each latitude. Time starts on the left, and progresses in an anti-clockwise

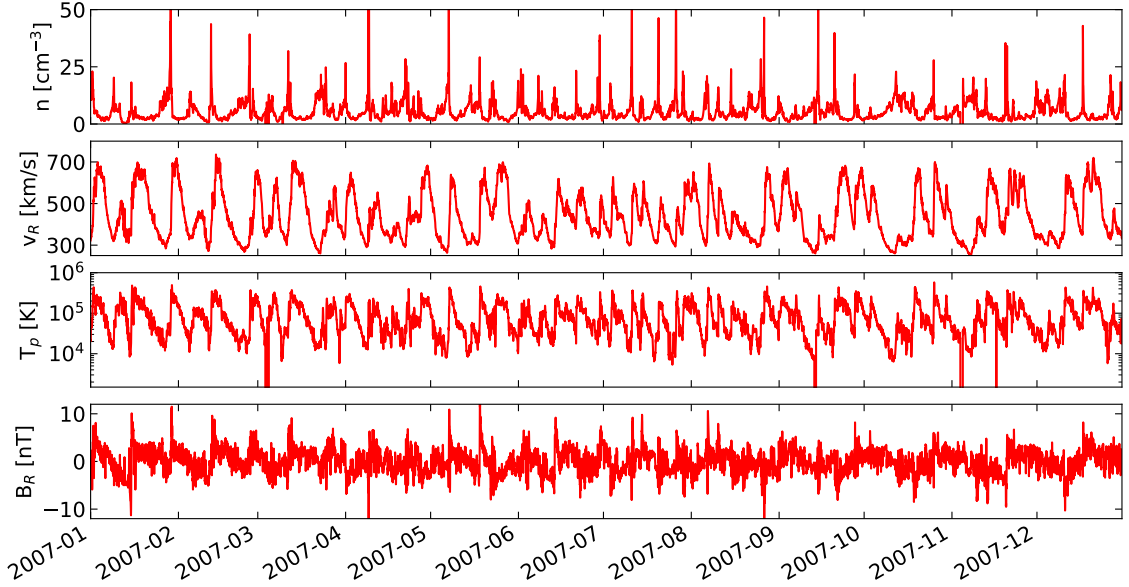


Figure 1.8: In situ measurements of the solar wind and interplanetary magnetic field acquired at 0.99 AU over the year 2007 by the spacecraft Wind, taken from the [OMNI database](#). From top to bottom: the profiles of particle density, bulk speed, proton temperature, and radial magnetic field.

direction. Near solar minimum (left panel), the coronal structure is simple: two large coronal hole in correspondence of the solar poles and an equatorial helmet streamer; wind speed is almost constant and high at all latitudes, except for a  $\pm 20^\circ$  band of variable solar wind at the solar equator; the magnetic field is outward in most of the northern hemisphere and inward in the southern one. Near solar maximum (on the right) instead, the heliospheric current sheet is highly irregular and distorted: the coronal structure is much more complex, with bright streamers extending out from any latitudes; the solar wind measured by Ulysses is aptly complex, with alternating fast and slow solar wind streams, both slower and smaller than at the solar minimum.

The flow speed of solar wind increases monotonically from low values in the inner corona, eventually becoming super-sonic a few solar radii above the solar surface. Whereas sunlight takes eight minutes to reach Earth, usually fast solar wind travels the same distance in about four or five days. Beyond Earth, the solar wind extends out to the heliospheric boundary with the interstellar medium at 50-100 AU, where the pressure of the other stellar winds slow the flow, making it subsonic again. More quantitative details about the behaviour of the solar wind, and the description and derivation of the classical solar wind theoretical models are presented in section 1.4.

### 1.2.3 Solar transients and Coronal Mass Ejections

We have seen how, on large time scales, the two solar wind regimes exhibit a certain regularity dictated by the solar rotation and the star’s cycles. In addition to this, however, the interplanetary medium is crowded with a bubbling of events characterized by shorter time scales, that on the Sun occur in minutes to hours, while their effects on interplanetary space can take place in minutes to days (Zhang et al., 2021). Such transients events can be categorized into four types, depending on the signatures they exhibit both in remote sensing observations and/or in situ measurements (Intriligator, 1980): solar flares (Fletcher et al., 2011; Hudson, 2011;

Shibata and Magara, 2011), solar energetic particles (SEPs; Reames, 1999, 2013, 2020), stream and corotating interaction regions (SIRs and CIRs; Cranmer et al., 2017; Cranmer and Winebarger, 2019; Richardson, 2018; Wilcox and Ness, 1965), and coronal mass ejections (CMEs; Kilpua et al., 2017; Luhmann et al., 2020).

Solar flares are probably the oldest transient phenomenon ever observed on the Sun (Carrington, 1859; Hodgson, 1859). They are observed as sudden enhancements in luminosity over a broad range of wavelengths that includes radio waves, visible light, EUV, X-, and gamma rays (Zhang et al., 2021). They release about  $10^{28}$ - $10^{32}$  ergs during time scales of minutes to hours. Flares are classified on a logarithmic scale depending on their peak of 1 to 8 Å in the X-ray flux measured by the GOES spacecraft, as either A, B, C, M, or X. An X-class flare have peak flux on the order of the 0.01% of the solar luminosity. Within each class there is a scale from 1 to 9, such that an X3 flare is 50% more powerful than an X2 flare. There are typically 1 to 10 X-class events per year, and 20 to 300 M-class ones. The larger flare of modern times was detected on November 4, 2003: it saturated the GOES spacecraft (e.g. Darnel et al., 2022), so its actual classification was extrapolated, initially as X28 and then between X34 and X48 (Brodrick et al., 2005). It is believed that the flare of Carrington (1859) was probably larger than that (Cliver, 2006; Cliver and Dietrich, 2013). It is well known that the process of flares is strongly coupled with that of CMEs (Hudson, 2020; Zhang et al., 2021). Very often, the term solar eruptions is used to refer to transient and large-scale energy release on the Sun, and a solar eruption contains both flare and CME, along with other associated phenomena (Zhang et al., 2021).

Solar energetic particles (SEPs) were first observed as sudden increases in intensity in ground-based ion chambers and neutron monitors during large solar flares (Forbush, 1946). It was once assumed that SEPs originated exclusively from solar flares, thus in point-like sources. It is now known that there are two types of SEPs: impulsive and gradual events. The sources of the first ones are impulsive flares on the Sun, while the latter are originated in large-scale long-lasting shocks driven by coronal mass ejection in interplanetary space (Reames, 1999). Impulsive events only last for a few hours, while gradual SEPs can typically last even several days.

We said how solar wind is composed by two regimes, fast and slow solar wind. The interaction between fast and slow stream creates stream interaction regions. SIRs are related to coronal holes: due to the quasi-stationary location of low-latitude coronal holes, the interaction of fast and slow speed streams results in a compression of plasma and magnetic field, occurring at certain distances from the Sun (Cranmer et al., 2017). As the Sun rotates, SIRs are referred to as corotating interaction regions.

Coronal Mass Ejections (CMEs) are the most recently discovered transient phenomena (Kilpua et al., 2017; Webb and Howard, 2012; Zhang et al., 2021). While related phenomena such as prominence eruptions and flares have been known since the 19th century, and energetic particles (Forbush, 1946) and interplanetary shocks (Sonett et al., 1964) were observed since the 1940s, 50s, and 60s, CMEs were first observed only in the early 1970s with space-based optical coronagraphs (Hansen et al., 1971; Tousey, 1973). The original definition of a CME (found in Hundhausen et al., 1984) describes it as "an observable change in coronal structure that occurs on a time scale of a few minutes and several hours, and involves the appearance and the outward motion of a new, discrete, bright, white light feature in the coronagraph field of view" (Schwenn, 2006). The central and the right panel of figure 1.9 reflect

this definition, showing the coronagraphic observation made by LASCO of a CME erupting in May 1, 2013.

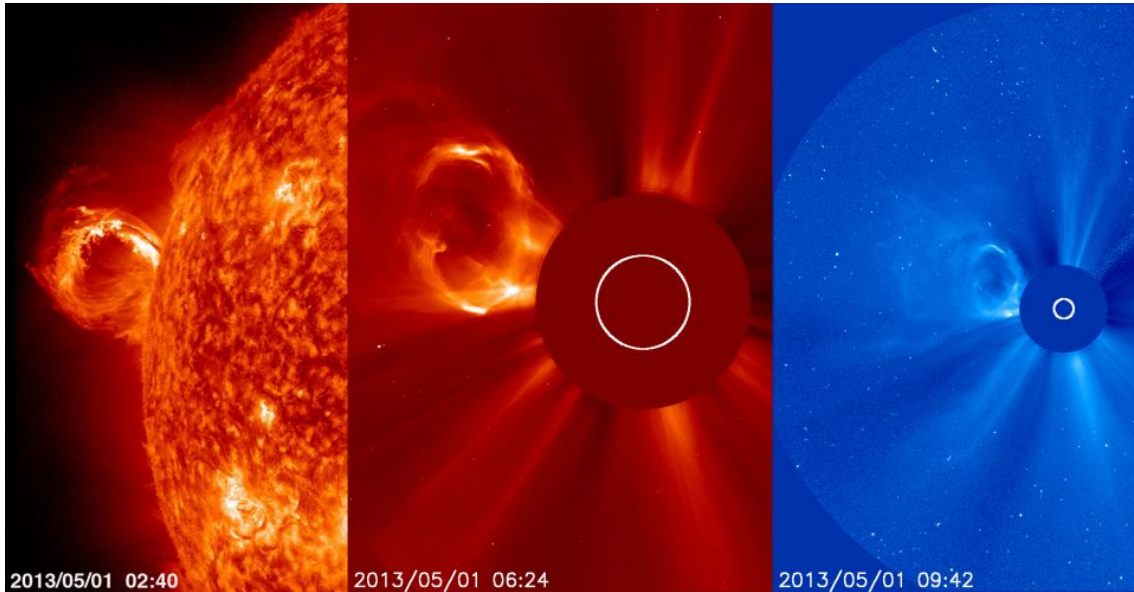


Figure 1.9: Observation of the same transient emerging in the eastern limb of the Sun, as seen in May 1, 2013 by SDO in the chromosphere (left panel), by LASCO-C2 in the inner corona (center panel), and by LASCO-C3 in the outer corona (right panel). An erupting solar prominence emerges from the chromosphere into the upper layers of the solar atmosphere, until it is explosively ejected into outer space by yet not fully understood mechanisms of magnetic nature.

About one third of all CME events (Chen, 2011) exhibits a three-part structure which consists of a bright outer loop (called shell or front), a dark cavity, and a bright core, as shown in the right panel of figure 1.10. It is still unclear whether the remaining two thirds do not exhibit this structure as result of projection effects due to the optically thin nature of the emission or not (Vourlidas et al., 2013). Some CMEs appear as narrow jets, some arise from pre-existing coronal streamers (streamer blowout CMEs; Vourlidas and Webb, 2018; Webb and Howard, 2012). Sometimes the streamer reforms after the eruption and sometimes it disappear. Often CMEs go on one side of the Sun, but occasionally they move directly towards or away from Earth, and they are observed as halo CME (as in the left panel of figure 1.10). Halo CME are usually associated with flares within  $30^\circ$  of the disk centre (Priest, 2014).

The term stealth-CME is commonly used to refer to an event with no apparent associated signature on the solar surface, and therefore no easy way to determine its source on the Sun (Howard and Harrison, 2013; Kilpua et al., 2014; Pal et al., 2022). While their status as a separate category is not unanimous (Howard and Harrison, 2013), other studies suggest that stealth-CMEs may originate at relatively high heights in the corona ( $\approx 1.3 R_\odot$ ; O’Kane et al., 2021; Robbrecht et al., 2009), owing their faint appearance and lower propagation speed (500 km/s; D’Huys et al., 2014) to the relative low magnetic field strength and low plasma density of their sources. Despite their weak disk signatures making them difficult to early identify with Space Weather patrol programs, these events when directed towards the Earth can also be drivers of minor and medium geomagnetic storms, making them of interest for Space Weather.

A CME directed to Earth usually takes two to five days to reach 1 AU, while

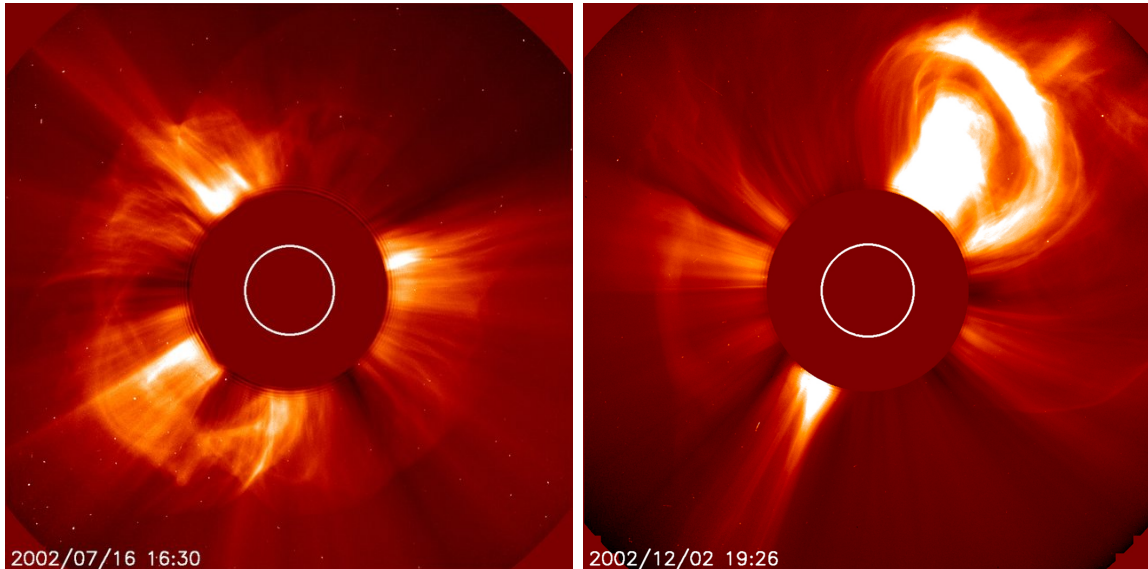


Figure 1.10: Coronal mass ejections observed in white light with LASCO C2, on July 16 (left) and December 12, 2002 (right). In the first case, the CME was directed towards Earth, so it appeared to expand in all direction from the Sun: this kind of event is called Halo CME. In the second case, the CME moved from one limb of the Sun, and its 3-part, lightbulb-like structure is visible: a bright core, a dark cavity, and an arcade feature.

SEP accelerated by the flares associated with the ejection can reach Earth even in only 80 minutes (Reames, 2020): these particles produce a snow-like effect as they hit the CCD detectors. Most of the CME acceleration occurs below 2 solar radii (Kilpua et al., 2017; Priest, 2014; Zhang et al., 2021), and between 2 and 6  $R_{\odot}$  its speed is either decreasing (fast CMEs) or constant or even slightly increasing (slow CMEs). They reach their terminal speed in time ranges from minutes to hour, with median value at 54 min (Zhang and Dere, 2006). These speeds have a wide range, going from even less than 100 km/s to up to 2000 km/s and in some cases even to 3000 km/s (Moussas et al., 2002; Priest, 2014), with an average speed of 300 km/s at solar minima and 500 km/s at solar maxima (Moussas et al., 2002). The average speed of halo CMEs is 960 km/s, twice as fast than that of other CMEs, which is 420 km/s. CMEs associated with powerful flares usually escape more rapidly (775 km/s) than those associated with less active solar prominences (330 km/s) (Priest, 2014).

Their masses range between  $10^{13}$  and  $4 \cdot 10^{16}$  g, so that CMEs account for nearly 5 to 10% of the total solar wind mass loss, depending on the phase of the solar cycle. Thus, they cause major modifications in the large-scale structure of the solar corona, such as depletions of coronal material (which are called coronal dimmings) and the creation of transient coronal holes. Their angular width usually ranges from  $20^{\circ}$  to  $360^{\circ}$ , though some are even narrower (Moussas et al., 2002; Priest, 2014), and it show a dependency on the solar cycle, being on the average  $47^{\circ}$  at solar minimum and  $61^{\circ}$  at maximum.

Their rate of occurrence also follows the solar cycle, with a peak delayed of 6 to 12 months (Gopalswamy et al., 2003). At solar minimum between 0.5 and 2 events per day happen, while at solar maximum they go to 6-8  $\text{day}^{-1}$  (Robbrecht et al., 2009). They are clustered around the equatorial regions at minima, and broadly distributed in latitude at maxima.

Magnetic field plays a pivotal role in their formation and acceleration. One third

of the CMEs observed with LASCO show disconnected concave-upward structures (St. Cyr et al., 2000), and in half of these a bright ray (suggestive of a current sheet) appears in the wake of the CME, lasting for hours or days (Webb et al., 2003). With time, theories progressed towards a more physical basis for the mechanisms of CME initiation, focusing on three-dimensional magnetic topologies that could account for the three-part structure and the association between prominences and CMEs. This led to pictures of rising coronal loops, overlying prominences, which undergo a rearrangement of their magnetic topology forming magnetic flux ropes (Anzer and Pnevman, 1982; Forbes, 1990). While the question of whether the flux rope is formed before or during the coronal eruption remains open, the majority of models agree on the fact that the erupting structure is always a flux rope (Chen, 2011), since no physical mechanism can produce a large-scale fast eruption from the solar corona without ejecting a flux rope (Vourlidas et al., 2013). Thus, Vourlidas et al. (*ibid.*) proposes the definition of a flux rope CME as the eruption of a coherent magnetic, twist-carrying magnetic cloud with angular width of at least  $40^\circ$  and able to reach beyond  $10 R_\odot$ , which occurs on a time scale of a few minutes to several hours.

Besides the ejected materials and the magnetic flux rope, a fast CME can generate a driving wider shock ahead of itself in the interplanetary medium, forming a turbulent sheath region between the eject front and the shock front. The shock is the main source of gradual SEPs, while the sheath can cause geomagnetic storms in planetary magnetosphere (Kilpua et al., 2017). Figure 1.11 shows on the left a schematic picture of an interplanetary CME (ICME), where the flux rope magnetic field lines are depicted as closed, that is, still connected to the corona at both ends. This is due to a feature often detected in ICME in situ measurements: the presence of counterstreaming suprathermal electrons. Single electron streams would instead suggest that magnetic field has reconnected and become open.

At the orbit of Earth, the passage of an ICME takes usually a day, corresponding to a spatial structure of almost 0.3 AU (*ibid.*). The right panel of figure 1.11 shows in situ measurements from the Advanced Composition Explorer (ACE; Stone et al., 1998), a spacecraft located in the Earth-Sun Lagrangian point L1. The sudden simultaneous increase of magnetic field magnitude and solar wind speed marks the beginning of the ICME event, in which the measured magnetic field is often enhanced and rotating in direction. Field variability is also reduced. In this kind of in situ profiles, an ICME can be distinguished (not always without ambiguity (Gosling, 1997; Kilpua et al., 2013)) by a set of signatures, that will be discussed in more detail in chapter 3. Measurements show that, by the time ICME reach 5 AU, 50% of them become magnetically disconnected from the Sun (Owens et al., 2009). ICMEs and their shock and sheaths are the most important drivers of space weather disturbances in the near Earth environment (Gopalswamy et al., 2014; Kilpua et al., 2017; Richardson et al., 2001; Zhang et al., 2021), such as geomagnetic storms and the polar aurorae.

## 1.2.4 Space weather

The term space weather refers to the conditions on the Sun and in the solar wind, planetary magnetospheres, ionospheres and thermospheres that can influence the performance and the reliability of space- and ground-based technological systems (Green and Baker, 2015; Hapgood, 2011; Schrijver et al., 2015; Schwenn, 2006).

The final goal in space-weather-related studies would be to be able to predict the

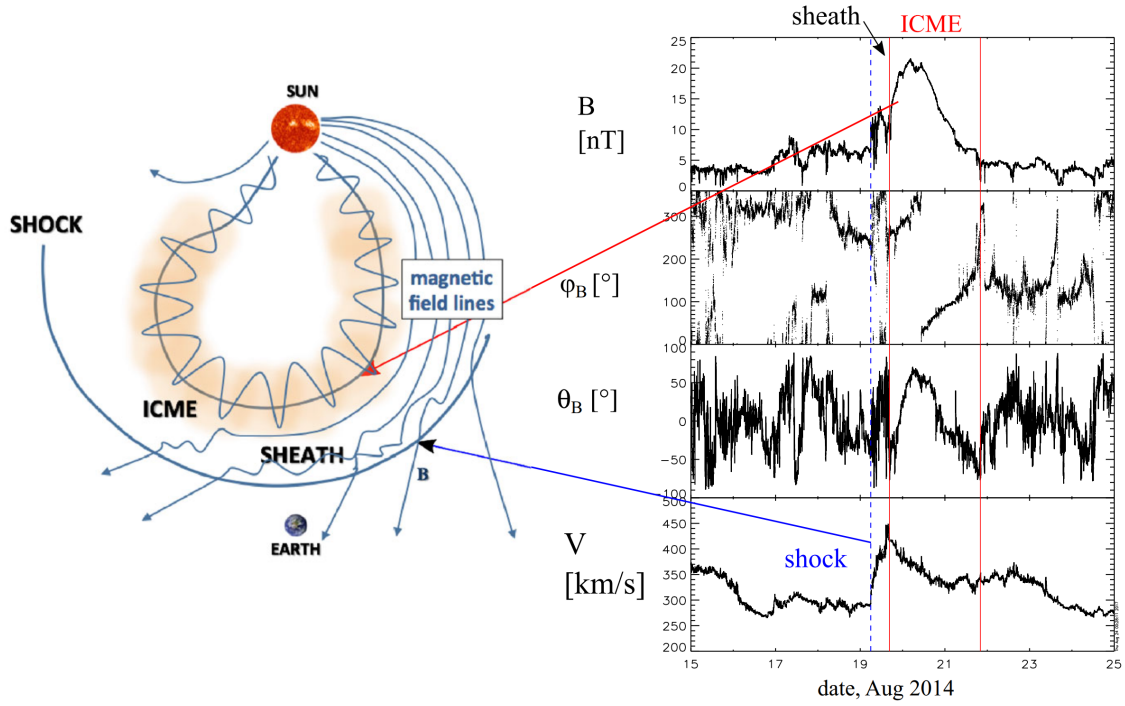


Figure 1.11: On the left, a cartoon depiction of the structure of an ICME. The ICME has a magnetic flux rope, still connected at both end to the corona, a feature not always detected in situ. The ICME drives an interplanetary shock, behind which the ambient solar wind is compressed in the turbulent sheath. On the right, in situ measurements of magnetic field magnitude, longitudinal and latitudinal inclination of the magnetic field, and solar wind speed acquired by the ACE spacecraft. The blue dashed line marks the shock, while the actual ICME is bounded by red lines. Reproduced from Kilpua et al. (2017), © Springer Nature.

chain of processes that occur in the entire solar-terrestrial environment (Gopalswamy et al., 2006; Kamide and Maltsev, 2007), that is, the network of influences and relationships that link solar phenomena and Earth magnetosphere. As a discipline, space weather has its roots in the inspection of geomagnetic storms in the 19th century (Kamide and Maltsev, 2007). A geomagnetic storm is temporary disturbance of Earth magnetosphere, caused by interaction with shock wave of solar wind and clouds of magnetic field interacting with Earth's magnetic field. Different indices are used to monitor geomagnetic activity (Kamide and Maltsev, 2007; Matzka et al., 2021; Nitti et al., 2023). Among these, the Disturbance storm time index ( $d$ )efines a geomagnetic storm as a depression in the horizontal component of the terrestrial magnetic field, lasting usually over one to several days. Geomagnetic storms are monitored by the Dst index,

$$Dst = \frac{1}{N} \sum_{n=1}^N \frac{(H - H_{\text{quiet}})_n}{\cos \theta_n} \text{ [nT]},$$

where  $H$  is the horizontal component measured at a given station,  $H_{\text{quiet}}$  is the average value for the quietest days,  $\theta_n$  is the station latitude and  $N$  is the total number of stations. Geomagnetic storms happens when  $Dst < -50$  nT. According to this criterion, about 20-50 storm events occur annually, depending on the solar cycle. The minimum Dst value reached in an event represent the magnitude of the storm: according to Gonzalez et al. (1994), for a moderate Dst storm,  $B_z$  must be below -5

nT for at least 2 hours, and for an intense storm ( $Dst < -100$  nT), the requirement is that  $B_z < 10$  nT for at least 3 hours.

Another of the most extensively used (Matzka et al., 2021) indices of geomagnetic activity is the planetary  $K_p$  index (Bartels, 1949), which purpose is to monitor geomagnetic disturbances from 13 observatories located in sub-auroral latitudes.  $K_p$  quantifies disturbances in the horizontal component of Earth’s magnetic field, observed on a magnetometer during a three-hour interval (Bartels et al., 1939). It assigns to the maximum fluctuations of  $H$  an integer on a quasi-logarithmic scale in the range 0-9, with 1 indicating calm conditions, and 5 or more indicating a geomagnetic storm. The  $K_p$  index is available since 1932 and thus is valuable to space climate studies, however it shows some limitations when compared to younger geomagnetic indices. For instance, time resolution of  $K_p$  is lower than that of the  $Dst$  index, which is one-hour (Matzka et al., 2021). Nevertheless, it is still widely used. It is currently the basis for the NOAA Geomagnetic Storms scale, ranging from minor (G1) for  $K_p = 5$  to extreme (G5) for  $K_p = 9$ , and it is also one of the indices distributed by ESA’s Space Situational Awareness Program (ibid.).

Among solar transients, ICMEs are the only disturbances capable to produce extreme geomagnetic storms (Luhmann et al., 2020), being the most massive transient heliospheric structures (Mishra et al., 2021). The majority of ICMEs do not drive intense shocks (Cane and Richardson, 2003; Richardson and Cane, 2010), but the small number of shock-driving ICME has the most intense consequences in the heliosphere (Kilpua et al., 2017; Zhang et al., 2021). Gradual SEP events are closely related to ICMEs, being generated in their shocks, and once released, their further propagation and evolution depends on the condition of the background solar wind medium (see e.g. Chané et al., 2005; He et al., 2011; Temmer and Nitta, 2015). The magnetic structure of the shock sheath and the driving flux rope determine the onset of a geomagnetic storm, with the main requirement being the presence of intense and prolonged magnetic field pointing southward (Kamide and Chian, 2007; Zhang et al., 2021).

Severe space weather conditions can damage satellite operations, as well as infrastructures on Earth such as power grid and navigation systems (Schwenn, 2006). This has deep economic consequences (Baker, 2005; Kamide and Chian, 2007; Lanzerotti, 2001): it has been estimated that an event similar to the Carrington (1859) one, in which an  $\sim X40$ -class solar flare was followed a few days after by a massive ICME that hit our magnetosphere, would cost today damages on the order of one trillion US dollars, and would take up to ten years in repairs to recover (Eastwood et al., 2017; National Research Council, 2008; Pomoell and Poedts, 2018). It is then not surprising that a great number of resources have been dedicated to the understanding and the forecasting of the intense phenomena of solar origin that we discussed above, by the scientific community, space agencies, and the private sector.

### 1.3 Magnetohydrodynamics equations

The solar wind is a collection of charged particles, mostly protons, electrons, and  $\alpha$ -particles, that are governed by Maxwell’s equations for the electric field  $\mathbf{E}$  and

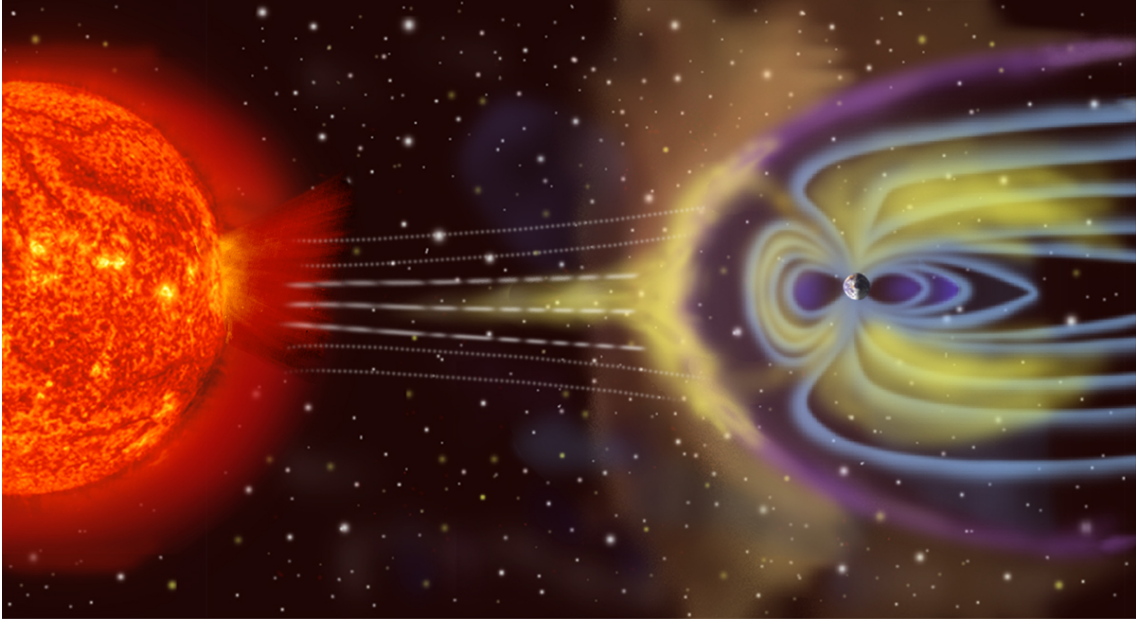


Figure 1.12: Artist's depiction of the interaction between solar wind and Earth's magnetosphere. When the former impacts on the magnetopause most of the solar materials are deflected away, while some of them are directly channeled into the polar cusps towards Earth's atmosphere.

Source: NASA, [from wikimedia](#).

magnetic field  $\mathbf{B}$ . These are:

$$\nabla \times \mathbf{B} = \frac{4\pi}{c} \mathbf{J} + \frac{1}{c} \frac{\partial \mathbf{E}}{\partial t} \quad (1.1a)$$

$$\nabla \cdot \mathbf{B} = 0 \quad (1.1b)$$

$$\nabla \times \mathbf{E} = -\frac{1}{c} \frac{\partial \mathbf{B}}{\partial t} \quad (1.1c)$$

$$\nabla \cdot \mathbf{E} = 4\pi q \quad (1.1d)$$

where  $q$  and  $\mathbf{J}$  are the total charge and current densities of the system. Equation (1.1a) is the Ampère's circuital law, which shows that currents and time-varying electric fields produce magnetic fields. Equation (1.1b) assumes that there are no magnetic monopoles and implies that a magnetic flux tube has a constant strength along its length. Equation (1.1c) is the Faraday's law of induction, which states that time-varying magnetic fields produce electric fields. Equation (1.1d) is the Gauss' law, and states that electric fields are also produced by electric charges.

This collection of particles can be described as a plasma, that is, an ionized gas for which the number of particles in a sphere of Debye radius

$$\lambda_D = \left( \frac{k_B T}{4\pi n e^2} \right)^{\frac{1}{2}} \quad (1.2)$$

is very large. In equation (1.2),  $T$  is the temperature, and  $n$  the particle density, which for a full ionized hydrogen plasma is equal to the sum of proton and electron density,  $n_p + n_e = 2n_e$ . The Debye length  $\lambda_D$  determine the distance over which the plasma is approximately charge-neutral, that is,  $n_p - n_e \ll n$ . For a plasma such as the solar wind, a temperature of  $10^5$  K and a density of  $10 \text{ cm}^{-3}$  give  $\lambda_D \approx 740 \text{ cm}$ .

Plasma moving at non-relativistic velocity  $\mathbf{v}$  in presence of a magnetic field is subject to two electrical fields:  $\mathbf{E}$ , which would act on the material at rest, and  $\mathbf{v} \times \mathbf{B}/c$ . Ohm's law states that the current density in the frame of reference moving with the plasma is then proportional to the total electric field,

$$\mathbf{J} = \sigma \mathbf{E} + \frac{\sigma}{c} \mathbf{v} \cdot \mathbf{B} = 0 \quad (1.3)$$

where  $\sigma$  is the electrical conductivity of the plasma.

Coupling the non-relativistic limit of equation (1.1a), which for  $v \ll c$  is

$$\nabla \times \mathbf{B} = \frac{4\pi}{c} \mathbf{J}$$

with equations (1.1c) and (1.3), it is possible to write

$$\begin{aligned} \frac{\partial \mathbf{B}}{\partial t} &= -c \nabla \times \left( -\frac{1}{c} \mathbf{v} \times \mathbf{B} + \frac{1}{\sigma} \mathbf{J} \right) \\ &= \nabla \times (\mathbf{v} \times \mathbf{B}) - \nabla \times \left( \frac{c^2}{4\pi\sigma} \nabla \times \mathbf{B} \right) \end{aligned}$$

and using the vector identity

$$\nabla \times (\nabla \times \mathbf{B}) = \nabla(\nabla \cdot \mathbf{B}) - \nabla^2 \mathbf{B}$$

one finds, for a uniform and constant  $\sigma$ , the induction equation

$$\frac{\partial \mathbf{B}}{\partial t} = \nabla \times (\mathbf{v} \times \mathbf{B}) + \eta \nabla^2 \mathbf{B} \quad (1.4)$$

where we defined a new parameter,

$$\eta = \frac{c^2}{4\pi\sigma} \quad (1.5)$$

which is called magnetic diffusivity. Equation (1.4) states that the rate of change of magnetic field in a plasma is provided by it being carried with the fluid motion, and by its diffusion in the plasma. It is the conservative form of equation (1.1c).

The plasma parameters of solar wind change over time, distance from the Sun and solar latitude and longitude ( $r$ ,  $\theta$ , and  $\varphi$  respectively). The large number of particles involved, combined with the non-linear nature of their interactions, makes it impossible to describe them individually. Instead, what is done is to think of the plasma as a conductive fluid that can be described by macroscopic, collective quantities such as density, speed, pressure and so on. The plasma is thus treated as a continuum, which is valid provided that the length-scales for variations greatly exceeds internal plasma lengths.

Assuming also that the plasma is in thermodynamic equilibrium, the collective quantities are derived by the moments of the Boltzmann equation for the system distribution function that define all the information of a given statistical ensemble. This holds true if the timescales are much larger than the collision times between the individual particles, and if the length-scales are much longer than the mean free paths.

For the purposes of this treatment, we also: assume that most of the plasma properties are isotropic; neglect relativistic effect considering velocities much smaller

than the speed of light; and treat the plasma as a single fluid instead of separating electrons and ions.

Within these assumptions, one can obtain the conservation equations for mass, momentum and energy. Equation

$$\frac{d\rho}{dt} = -\rho\nabla \cdot \mathbf{v} \quad (1.6)$$

is the continuity equation, which regulates the transport of plasma mass, stating that the density at a point changes when mass flows into or out the surrounding region.  $\rho$  is the mass density, equal to  $n_p m_p + n_e m_e \approx n_e m_p$  in a fully ionized hydrogen plasma, and  $t$  is time. In equation (1.6), the derivative used is

$$\frac{d}{dt} = \frac{\partial}{\partial t} + \mathbf{v} \cdot \nabla \quad (1.7)$$

which is the total (or material) derivative.

Under the condition of electrical neutrality of the plasma, the equation of motion is

$$\rho \frac{d\mathbf{v}}{dt} = -\nabla p + \frac{1}{c} \mathbf{J} \times \mathbf{B} + \mathbf{F}_{\text{ext}} \quad (1.8)$$

and it states that the momentum of the system must be conserved. The motion of the plasma is determined by the sum of the pressure gradient, the Lorentz force, and other external forces acting on the system. In equation (1.8),  $p$  is the thermal pressure,  $\mathbf{J}$  is the electric current density,  $B$  is the magnetic field, and  $\mathbf{F}_{\text{ext}}$  represent other forces, such as gravity, viscosity, and the fictitious forces that arise in non-inertial frames of reference.

The thermal pressure obeys the law

$$p = nk_B T \quad (1.9)$$

which is the ideal gas law. For the fully ionized hydrogen plasma  $n = 2n_e$ , while in the solar atmosphere the presence of heavier ions results in  $n \approx 1.9n_e$ . Within our assumptions, the thermal pressure also enters in the energy equation

$$\rho\varepsilon = \frac{p}{\gamma - 1} \quad (1.10)$$

with  $\varepsilon$  being the internal energy per unit mass, and where  $\gamma$  is the ratio between the specific heat at constant pressure and the specific heat at constant volume. For a fully ionized plasma with three degrees of freedom  $\gamma = 5/3$  and thus  $\rho\varepsilon = 3p/2$ . In the actual solar atmosphere the value of  $\gamma$  ranges from a minimum of 1.1 to a maximum of 5/3.

The third conservation equation, the energy one, is built considering all the energetic contributions to the system. If these are only the ones considered above, the equation is

$$\frac{\partial}{\partial t} \left( \frac{1}{2} \rho v^2 + \rho\varepsilon + \frac{B^2}{8\pi} \right) + \nabla \cdot \left[ \left( \frac{1}{2} \rho v^2 + \rho\varepsilon + p \right) \mathbf{v} + \frac{c}{4\pi} \mathbf{E} \times \mathbf{B} \right] = \mathbf{v} \cdot \mathbf{F}_{\text{ext}} \quad (1.11)$$

and it states that variations in internal, kinetic, and electromagnetic energies balance each other and are due to the work done by the thermal pressure and external forces. In equation (1.11), the quantity

$$S = \frac{c}{4\pi} \mathbf{E} \times \mathbf{B} \quad (1.12)$$

is called the Poynting vector, and represents the directional energy transfer per unit area and unit time of an electromagnetic field.

Using Ampère's law (1.1a), the Lorentz force term in equation (1.8) can also be expressed as

$$\begin{aligned} \frac{1}{c} \mathbf{J} \times \mathbf{B} &= \frac{1}{4\pi} (\nabla \times \mathbf{B}) \times \mathbf{B} \\ &= \frac{1}{4\pi} [-(\mathbf{B} \cdot \nabla)\mathbf{B} + (\nabla \cdot \mathbf{B})\mathbf{B} + \nabla(\mathbf{B} \cdot \mathbf{B})] \\ &= \frac{1}{4\pi} (\mathbf{B} \cdot \nabla)\mathbf{B} - \nabla \left( \frac{B^2}{8\pi} \right) \end{aligned} \quad (1.13)$$

that is, the sum of a vector called magnetic tension, which is a restoring force with units of force density that acts to straighten bent magnetic field lines, and the gradient of a scalar called magnetic pressure  $p_B$ . The magnetic pressure is used to define an important non-dimensional parameter in magnetohydrodynamics,

$$\beta = \frac{p}{p_B} = \frac{8\pi p}{B^2}. \quad (1.14)$$

In plasma with  $\beta > 1$ , the dynamics is dominated by the fluid quantities, otherwise with  $\beta < 1$ , magnetic field leads the dynamics of the system. The plasma Beta rapidly decreases with altitude above the solar surface, reaching a minimum in solar corona, and then arising again in the solar wind and interplanetary space, as solar magnetic field starts to fade with distance. The altitude trend of  $\beta$  from the model of Gary (2001) is depicted in figure 1.13. The quantity

$$p + \frac{B^2}{8\pi} = p \left( 1 + \frac{1}{\beta} \right) \quad (1.15)$$

is called the total pressure of the system.

Equation (1.13) shows how the Lorentz force can be interpreted as the sum of magnetic tension and magnetic pressure. One of the effects of a tension  $\mathcal{T}$  in a material of density  $\rho$  is to permit transverse waves to propagate along the material with a certain speed  $(\mathcal{T}/\rho)^{1/2}$ . By analogy, it is reasonable to expect magnetic tension to produce transverse waves that propagate along the magnetic field with the so-called Alfvén speed

$$v_A = \frac{B}{\sqrt{4\pi\rho}}. \quad (1.16)$$

For values such as those characteristic of the corona above an active region,  $B \approx 100$  G and  $n \approx 10^{10} \text{ cm}^{-3}$ ,  $v_A \approx 3000$  km/s. It is known that the pressure of a gas obeying the adiabatic law

$$p/\rho^\gamma = \text{constant} \quad (1.17)$$

produce longitudinal sound waves with phase speed  $\sqrt{\gamma p/\rho}$ . By analogy, we expect the magnetic pressure  $p_B$  to generate longitudinal magnetic waves propagating across the magnetic field. If the electrical conductivity of the plasma is high, the magnetic diffusivity in the induction equation (1.4) can be neglected, and the field strength and plasma density vary such that  $B/\rho = \text{constant}$ , which in terms of magnetic pressure means that  $p_B/\rho^2 = \text{constant}$ . By comparing with the adiabatic law (1.17), this suggests that the value of  $\gamma$  for these magnetic waves is 2, and thus their wave speed must be  $\sqrt{2p_B/\rho}$ , which is again the Alfvén speed defined in equation (1.16).

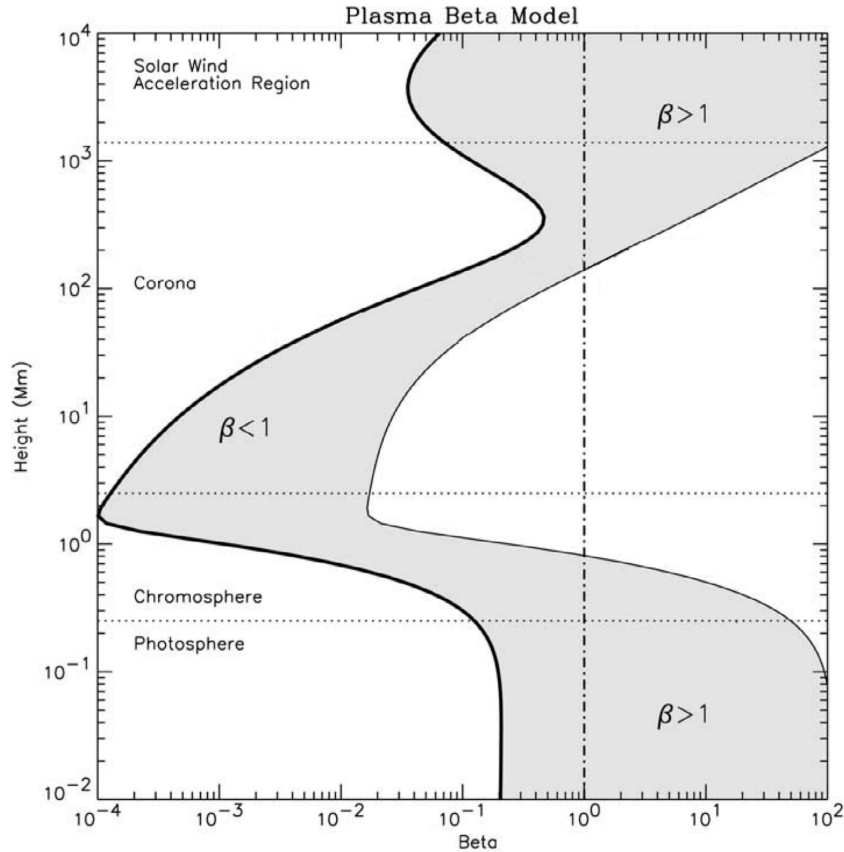


Figure 1.13: Plasma beta above an active region, depending on the height. The convective motion of plasma still dominates the dynamic of the innermost layers of the solar atmosphere, so that  $\beta \gtrsim 1$  in all the photosphere. It rapidly decreases in the chromosphere and in the transition region, reaching a minimum in the corona, where the magnetic field leads plasma motion.

Adapted from Gary (2001), © Springer Nature.

The two types of magnetic waves, called Alfvén waves (or torsional Alfvén waves) and compressional Alfvén waves, are depicted in figure 1.14. When both the magnetic force and the thermal pressure gradient are important in a plasma, one can find magnetoacoustic waves, which also depend on the angle between the direction of propagation  $\mathbf{k}$  and the magnetic field  $\mathbf{B}$ . Magnetoacoustic waves come in two modes, the fast mode and the slow mode, with speeds respectively higher and slower than the Alfvén speed.

Expanding the material derivative (1.7) and using the expression of the Lorentz force in terms of magnetic pressure and tension in the equation of motion (1.8),

$$\begin{aligned} \rho \frac{d\mathbf{v}}{dt} &= \rho \left[ \frac{\partial \mathbf{v}}{\partial t} + (\mathbf{v} \cdot \nabla) \mathbf{v} \right] \\ &= \frac{\partial}{\partial t} (\rho \mathbf{v}) + \nabla \cdot (\rho \mathbf{v} \mathbf{v}) \end{aligned}$$

with  $\mathbf{v} \mathbf{v}$  being the stress tensor, and considering the identity

$$(\mathbf{B} \cdot \nabla) \mathbf{B} = \nabla \cdot (\mathbf{B} \mathbf{B})$$

with  $\mathbf{B} \mathbf{B}$  being the Maxwell stress tensor, the equation of motion can be also written in conservative form. The same can be done for the equation of continuity. Thus, the

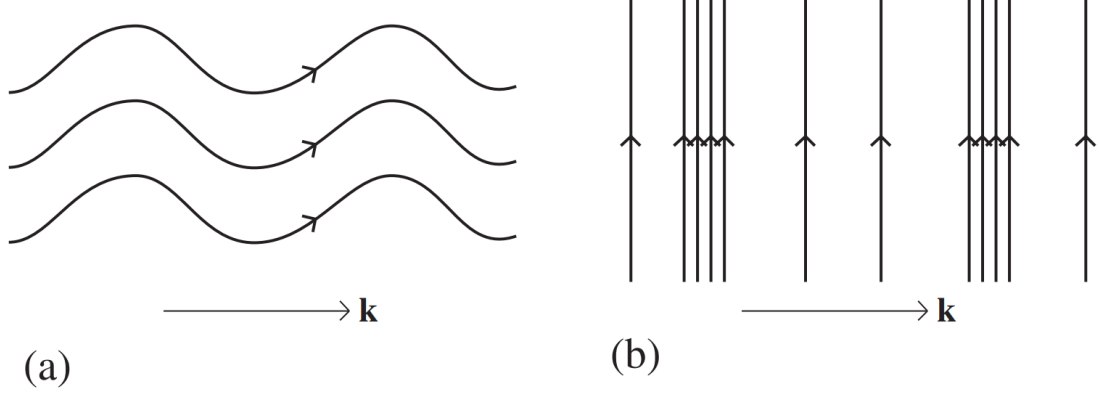


Figure 1.14: On the left (panel a), ripples of magnetic field caused by a transverse wave propagating along the magnetic field lines in direction  $\mathbf{k}$ . On the right (panel b), the compression and rarefaction of magnetic field lines due to a compressional wave propagating across the field in direction  $\mathbf{k}$ .

Source: Priest (2014), © Cambridge University Press.

complete set of magnetohydrodynamics (MHD) equations is formed (Chiuderi and Velli, 2012; Priest, 2014). In conservative form and assuming there are no external forces, they are:

$$\frac{\partial \rho}{\partial t} + \nabla \cdot (\rho \mathbf{v}) = 0 \quad (1.18a)$$

$$\frac{\partial}{\partial t}(\rho \mathbf{v}) + \nabla \cdot \left[ \rho \mathbf{v} \mathbf{v} - \frac{\mathbf{B} \mathbf{B}}{4\pi} + \left( p + \frac{B^2}{8\pi} \right) \mathbb{1} \right] = 0 \quad (1.18b)$$

$$\frac{\partial}{\partial t} \left( \frac{1}{2} \rho v^2 + \frac{p}{\gamma - 1} + \frac{B^2}{8\pi} \right) + \nabla \cdot \left[ \left( \frac{1}{2} \rho v^2 + \frac{\gamma}{\gamma - 1} p \right) \mathbf{v} + \frac{c}{4\pi} \mathbf{E} \times \mathbf{B} \right] = 0 \quad (1.18c)$$

$$\frac{\partial \mathbf{B}}{\partial t} = \nabla \times (\mathbf{v} \times \mathbf{B}) + \eta \nabla^2 \mathbf{B}. \quad (1.18d)$$

where  $\mathbb{1}$  is the unit tensor. The MHD equations (1.18) for the conservation of mass, momentum, energy, and the induction equation completely describe the behaviour of a magnetized fluid under the assumption listed at the beginning of this section.

### 1.3.1 Ideal MHD and Alfvén's theorem

The equations (1.18) can be further simplified by neglecting the effects of the magnetic diffusivity  $\eta$ , which means assuming infinite electrical conductivity  $\sigma$ . Neglecting also the viscosity and heat conduction in the plasma, one defines the ideal magnetohydrodynamics regime. To define the transition between ideal (or convective) and resistive (or diffusive) regime, a dimensionless ratio called Lundquist Number is introduced:

$$S = \frac{v_A r_0}{\eta} \quad (1.19)$$

where  $r_0$  is the scale length of significant variations of electro-magnetic fields, density, and electric conductivity in the considered plasma. For a plasma with very high electric conductivity,  $\sigma \rightarrow \infty$ , magnetic diffusivity  $\eta$  can be neglected and  $S \gg 1$ . If this condition holds true, the assumption of ideal MHD is valid, and the MHD equations for energy (1.18c) and induction (1.18d) are modified accordingly.

Rewriting for completeness the equations of continuity and motion, the ideal MHD equations are:

$$\frac{\partial \rho}{\partial t} + \nabla \cdot (\rho \mathbf{v}) = 0 \quad (1.20a)$$

$$\frac{\partial}{\partial t}(\rho \mathbf{v}) + \nabla \cdot \left[ \rho \mathbf{v} \mathbf{v} - \frac{\mathbf{B} \mathbf{B}}{4\pi} + \left( p + \frac{B^2}{8\pi} \right) \mathbb{1} \right] = 0 \quad (1.20b)$$

$$\frac{\partial}{\partial t} \left( \frac{1}{2} \rho v^2 + \frac{p}{\gamma - 1} + \frac{B^2}{8\pi} \right) + \nabla \cdot \left[ \left( \frac{1}{2} \rho v^2 + \frac{\gamma}{\gamma - 1} p \right) \mathbf{v} - \frac{1}{4\pi} (\mathbf{v} \times \mathbf{B}) \times \mathbf{B} \right] = 0 \quad (1.20c)$$

$$\frac{\partial \mathbf{B}}{\partial t} = \nabla \times (\mathbf{v} \times \mathbf{B}). \quad (1.20d)$$

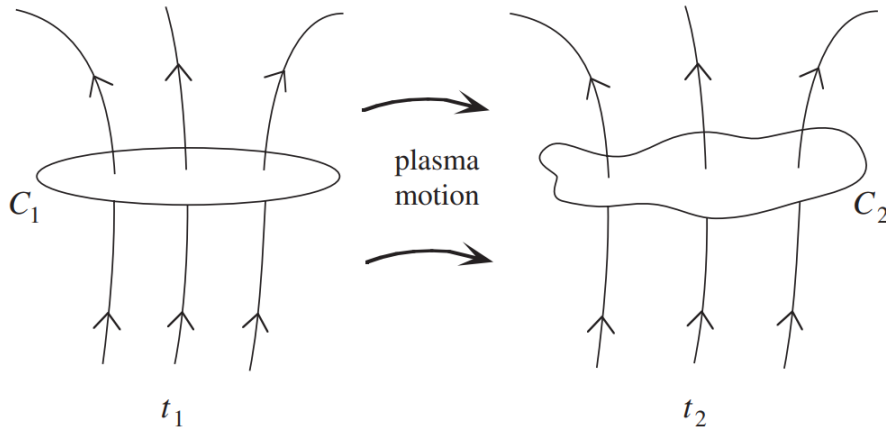


Figure 1.15: The conservation of total magnetic flux through a surface. If the curve  $C_1$  is distorted into  $C_2$  by plasma motion, the flux through  $C_1$  at  $t_1$  equals the flux through  $C_2$  at  $t_2$ .

Source: Priest (2014), © Cambridge University Press.

If ideal MHD can be assumed, the Alfvén's frozen-in theorem is valid. It states that when  $\eta = 0$  the magnetic flux is conserved, so that the magnetic field moves with the plasma. Consider a curve  $C$ , bounding a surface  $S$ , moving with the plasma such that, in a time interval  $dt$ , an element  $d\mathbf{l}$  of  $C$  sweeps out an element of area  $\mathbf{v} \times d\mathbf{l}dt$ . Then, the rate of change of magnetic flux through  $C$  is

$$\frac{d}{dt} \iint_S \mathbf{B} \cdot d\mathbf{S} = \iint_S \frac{\partial \mathbf{B}}{\partial t} \cdot d\mathbf{S} + \oint_C \mathbf{B} \cdot \mathbf{v} \times d\mathbf{l}. \quad (1.21)$$

As  $C$  moves, the flux changes because the magnetic field changes with time, and because  $C$  itself moves. Using the identity

$$\mathbf{B} \cdot \mathbf{v} \times d\mathbf{l} = -\mathbf{v} \times \mathbf{B} \cdot d\mathbf{l}$$

and applying Stoke's theorem to the second term on the right of equation (1.21)

$$\oint_C \mathbf{B} \cdot \mathbf{v} \times d\mathbf{l} = -\oint_C \mathbf{v} \times \mathbf{B} \cdot d\mathbf{l} = -\iint_S \nabla \times (\mathbf{v} \times \mathbf{B}) \cdot d\mathbf{S},$$

we obtain

$$\frac{d}{dt} \iint_S \mathbf{B} \cdot d\mathbf{S} = \iint_S \left( \frac{\partial \mathbf{B}}{\partial t} - \nabla \times (\mathbf{v} \times \mathbf{B}) \right) \cdot d\mathbf{S} \quad (1.22)$$

and using ideal limit (1.20d) of the induction equation, we obtain

$$\frac{d}{dt} \iint_S \mathbf{B} \cdot d\mathbf{S} = 0. \quad (1.23)$$

Thus, the total magnetic flux remains constant as it moves with the plasma: the plasma elements that initially form a flux tube, continue to do so at later times (figure 1.15). This implies that the magnetic field is frozen into the fluid and has to move along with it, so the field topology cannot change.

For the main purpose of this dissertation, which mainly focuses around the description of the ambient conditions of the solar wind assuming a certain stationarity, it is allowed to treat the plasma with the equations (1.20). In the areas of the heliosphere where this assumption is no longer valid, and magnetic diffusivity is no longer negligible, a rearrangement in the topology of  $\mathbf{B}$  accompanied by strong energy release can occur, which is called magnetic reconnection.

## 1.4 The Parker model for Solar Wind

The first clues of the solar wind's existence came in the nineteenth century, from the observation of strong variations in the Earth's magnetic field. First a sharp increase (by  $\sim 10^{-3}$  G), then a slow decrease: these phenomena were called geomagnetic storms. Soon it became clear that a link between these variations and large solar flares existed, because the latter were often followed by the former, a day or two later. Furthermore, both phenomena exhibited an 11-year periodicity in occurrence and intensity.

Chapman (1929) suggested that geomagnetic storms were caused by streams of particles, travelling at  $10^3$  km/s, ejected during solar flares. Years later, in order to explain the deflection angle between the ion comet tails and the radial direction, Biermann (1951) proposed that the Sun is emitting solar corpuscular radiation in a continuous rather than a sporadic way. Chapman and Zirin (1957) formulated the first theory for an extended corona: they considered a static, spherically symmetric atmosphere, but their model predicted at large distance a pressure far greater than the reasonable value, and a density that became indefinitely large.

Finally, Parker (1958) solved this inconsistency by considering the corona in a steady, constant outward expansion: with nothing strong enough to hold it in, the solar corona must stream away from the Sun as a breeze. With a simple yet very reasonable model, Parker was capable of finding solutions where the pressure is zero at large distance. These results were highly controversial until, in 1958, the Luna II satellite observed a flux of ions, in 1962 the NASA probe Mariner II confirmed the existence of a continuous flow of charged particles in interplanetary space (Ness and Wilcox, 1964; Neugebauer and Snyder, 1962), and subsequent measurements found values of velocity consistent with the Parker model.

Neglecting the influence of the magnetic field  $\mathbf{B}$  and of the solar rotation, the governing forces leading the coronal expansion are the pressure gradient and the gravity. Assuming spherical symmetry the equations of mass continuity (1.18a) and

momentum conservation (1.18b) become:

$$r^2 \rho v_r = \text{const} \quad (1.24a)$$

$$\rho v_r \frac{dv_r}{dr} = -\frac{dp}{dr} - \frac{GM_\odot}{r^2} \rho \quad (1.24b)$$

where  $v_r$  is the radial speed of the plasma. Using the ideal gas law (1.9) in the form

$$\frac{dp}{d\rho} = \gamma \frac{p}{\rho} = c_s^2 \quad (1.25)$$

where  $c_s$  is the sound speed, and assuming isothermality ( $\gamma = 1$ ), the pressure gradient in equation (1.24b) can be eliminated by writing

$$\frac{dp}{d\rho} = \frac{dp}{d\rho} \frac{d\rho}{dr} = c_s^2 \frac{d\rho}{dr}$$

so that equation (1.24b) becomes

$$\rho v_r \frac{dv_r}{dr} = -c_s^2 \frac{d\rho}{dr} - \frac{GM_\odot}{r^2} \rho.$$

Deriving equation (1.24a) the density gradient can also be eliminated

$$\begin{aligned} 2r\rho v_r + \frac{d\rho}{dr} r^2 v_r + \frac{dv_r}{dr} r^2 \rho &= 0 \\ \frac{1}{\rho} \frac{d\rho}{dr} &= -\frac{1}{v_r} \frac{dv_r}{dr} - \frac{2}{r} \end{aligned}$$

thus obtaining the equation for the solar wind radial speed

$$\left( v_r - \frac{c_s^2}{v_r} \right) \frac{dv_r}{dr} = \frac{2c_s^2}{r} - \frac{GM_\odot}{r^2}. \quad (1.26)$$

In equation (1.26) it is only possible to have  $v = c_s$  at a critical point  $r_c$  defined as

$$r_c = \frac{GM_\odot}{2c_s^2} \quad (1.27)$$

which is  $\sim 11.5R_\odot$  for a typical  $T_{corona} \sim 10^6$  K. The advantage of the isothermal case is that the integral of equation (1.26) exists and it can be written as

$$\left( \frac{v_r}{c_s} \right)^2 - \ln \left( \frac{v_r}{c_s} \right)^2 = 4 \ln \left( \frac{r}{r_c} \right) + \frac{4r_c}{r} + C \quad (1.28)$$

where  $C$  is a constant of integration. Different values of  $C$  draw four different classes of solutions, as depicted in figure 1.16. For the Sun, a small speed at  $r = R_\odot$  is required, as in solutions of class I and II. Small pressure at large  $r$  is also needed: for an isothermal wind  $p \propto \rho \propto v_r^{-1}$ , so the pressure will be small provided that  $v_r$  is large. This point to class II and IV. Therefore, the only solution that satisfies both requirements is class II, obtained when  $C = -3$  in equation (1.28) as may be verified by imposing the solution to pass through the critical point  $r_c$ .

In Parker (1958) one can find the first prediction for the general shape of the interplanetary magnetic field (IMF). The inclusion of solar rotation and/or a magnetic field break the assumption of spherical symmetry because, unlike gravity, the

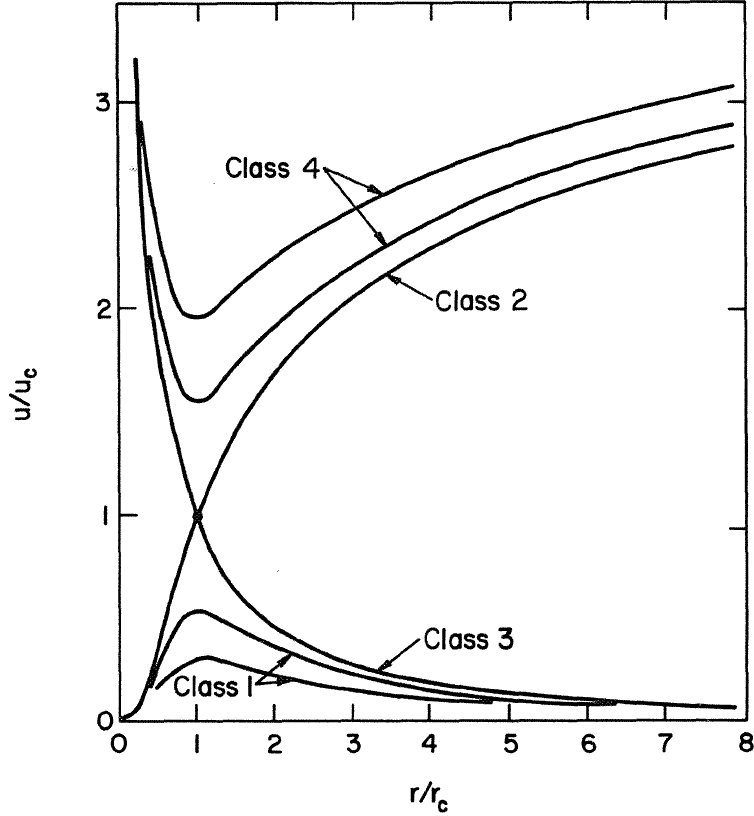


Figure 1.16: The four classes of solutions of equation (1.28) for an isothermal and spherical coronal expansion. Only class 2 satisfies the requirements of supersonic flow ( $u_c \equiv c_s$ ) at  $r/r_c \gg 1$  and small speed very close to the Sun. Source: Hundhausen (1972), © Springer-Verlag.

centrifugal and the Lorentz force are not depending on central distance  $r$  alone. Assuming for the solar wind a purely radial flow  $\mathbf{v} = v_r \mathbf{e}_r$  beyond some distance  $r = r_b$ , in a spherical coordinate system corotating with the Sun, the solar wind velocity has components

$$V_r = v_r, \quad V_\varphi = -\Omega_\odot r \sin \theta, \quad V_\theta = 0 \quad (1.29)$$

where

$$\Omega_\odot = 2.8 \cdot 10^{-6} \text{ rad s}^{-1} \quad (1.30)$$

is the angular rotational velocity of the Sun's equator. The Sun is subject to differential rotation, that is, solar rotation varies with latitude. Polar regions of the Sun rotate 30% more slowly than its equator, taking almost 38 days to cover one period. Nevertheless, the inclusion of differential rotation is not necessary for the purposes of the following discussion, since the attention will be limited to the plane of the ecliptic.

As discussed in section 1.3, the high electrical conductivity  $\sigma$  of the solar wind plasma means that the frozen-in Alfvén theorem can be applied, so the magnetic field must be transported out into interplanetary space by the wind velocity. Parker considered a small magnetic pressure compared with the thermal one ( $\beta \gg 1$ ) so that  $\mathbf{B}$  just acts like a tracer and does not affect the wind speed. Hence, the magnetic

field follow a path which is a velocity streamline in this corotating frame, defined by

$$\frac{1}{r} \frac{dr}{d\varphi} = -\frac{v_r}{\Omega_{\odot} r \sin \theta} \quad (1.31)$$

The physical solution of equation (1.28) predicts that for distances  $r \gg r_c$  the wind speed is almost constant, because the gravitational attraction and the acceleration due to the thermal pressure gradient can be neglected. Considering  $v_r = v_0$ , equation (1.31) can be integrated from  $r = r_b$  (corresponding to a surface close to  $R_{\odot}$ ) to  $r$  to give

$$r - r_b = -\frac{v_0}{\Omega_{\odot} r \sin \theta} (\varphi(r) - \varphi_0) \quad (1.32)$$

where  $\varphi_0$  is the initial angle at the surface of radius  $r_b$ . Thus, the overall effect of the solar rotation is the bending of the plasma trajectories in the arms of an Archimedean spiral, commonly called the interplanetary Parker Spiral, defined by equation (1.32). While the geometrical figure of the spiral lines corotates, the plasma accelerated by the wind does not corotates but only moves radially. Material on closed field lines in the corona must instead corotate with the Sun, since the coronal magnetic field is much stronger than the solar wind one and thus  $\beta \ll 1$ , as depicted in figure 1.13.

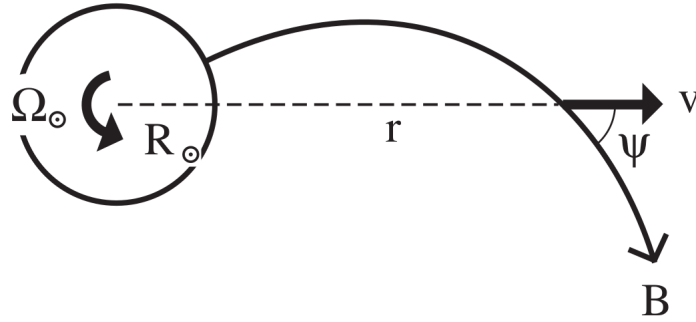


Figure 1.17: A spiral field line attached to the Sun in the equatorial plane. The wind moves radially with speed  $v$  inclined to the field at angle  $\psi$ . Source: Priest (2014), © Cambridge University Press.

Suppose that at distance  $r$ , the magnetic field  $\mathbf{B}$  is inclined to the radial speed  $\mathbf{v}$  at angle  $\psi$ . Then the  $\mathbf{v}$  component normal to  $\mathbf{B}$  must be equal to the speed of the field line in that direction, because of the frozen-in condition. The field line corotate with the Sun, so in the equatorial plane ( $\theta = \pi/2$ )

$$v_r \sin \psi = \Omega_{\odot} (r - r_b) \cos \psi \quad \text{or}$$

$$\psi = \arctan \frac{\Omega_{\odot} (r - r_b)}{v_r} \quad (1.33)$$

which gives at the Earth's orbit ( $r = 215 R_{\odot} \sim 1.5 \cdot 10^{13}$  cm) with a speed of  $400 \text{ km s}^{-1}$  a value of  $\psi \approx \frac{\pi}{4}$ . From equation (1.33) it can be inferred that at distance  $r = r_b$   $\psi = 0$ , so the magnetic field has been assumed normal to that surface. An

arm of the spiral in the equatorial plane has wrapped once around the Sun at the winding distance

$$\Delta R = \frac{2\pi v_0}{\Omega_\odot} \quad (1.34)$$

which, for a speed of 400 km/s is nearly 6 AU.

In this theoretical discussion it has been assumed that the wind velocity has a uniform value around the Sun at a distance  $r$ . However that is not true, because it actually varies substantially as consequence of the variation of coronal conditions. For instance, consider in the Sun equatorial plane a stream of slow wind with velocity  $v_1$  issuing from  $(r_1, \varphi_1)$  accompanied by a stream of fast wind with  $v_2 > v_1$  from  $(r_2, \varphi_2)$ . From equation (1.32) the two streams spiral paths are

$$r - r_1 = \frac{v_1}{\Omega_\odot}(\varphi - \varphi_1)$$

and  $r - r_2 = \frac{v_2}{\Omega_\odot}(\varphi - \varphi_2)$ .

The two paths collide in a certain  $(r, \varphi)$  where

$$\varphi = \frac{\varphi_1 v_1 - \varphi_2 v_2}{v_1 - v_2} + \frac{\Omega_\odot (r_2 - r_1)}{v_1 - v_2} \quad (1.35a)$$

$$r = \frac{r_1 + r_2}{2} - \frac{v_1 v_2}{\Omega_\odot} \left( \frac{\varphi_2 - \varphi_1}{v_2 - v_1} \right) - \frac{r_1 - r_2}{2} \left( \frac{v_1 + v_2}{v_1 - v_2} \right). \quad (1.35b)$$

When  $r_1 = r_2$  (and equal, for instance, to  $r_b$ ) the expressions (1.35) reduce to

$$\varphi = \frac{\varphi_1 v_1 - \varphi_2 v_2}{v_1 - v_2} \quad (1.36a)$$

$$r = r_b + \frac{v_1 v_2}{\Omega_\odot} \left( \frac{\varphi_2 - \varphi_1}{v_2 - v_1} \right). \quad (1.36b)$$

This is the basis of the corotating interaction regions phenomenon, the principal source of disturbances to the ambient conditions of the interplanetary plasma in the distant solar wind. If  $v_1=400$  km/s and  $v_2=600$  km/s, with  $\varphi_2 - \varphi_1 = \pi/2$ , the two streams intersect at  $r - r_b \approx 6 \cdot 10^{13}$  cm=4 AU, where the spiral is more longitudinal than radial. The fast stream runs into the sunward side of the slow stream with a relative velocity of  $v_2 - v_1 = 200$  km s<sup>-1</sup>. The magnetic field in both streams is compressed and there is shock propagation, both forward and backward, away from the contact surface. Figure 1.18 shows a cartoon depiction of the phenomena.

### 1.4.1 Magnetized Solar Wind

The magnetic field has several effects on the properties of the solar wind. It causes differences in parameters parallel and perpendicular to the field, such as the temperature. It supports waves (as mentioned in section 1.3) and produces instabilities (Hellinger et al., 2006; Kasper et al., 2006; Kellogg, 2022) such as turbulence (e.g. Schwartz and Roxburgh, 1980; Telloni et al., 2021b).

In the radial equation of motion, the magnetic terms are small compared to the gravitational and pressure ones; however they are the dominant ones in the rotational equation of motion and must be included even in the radial one to give a complete

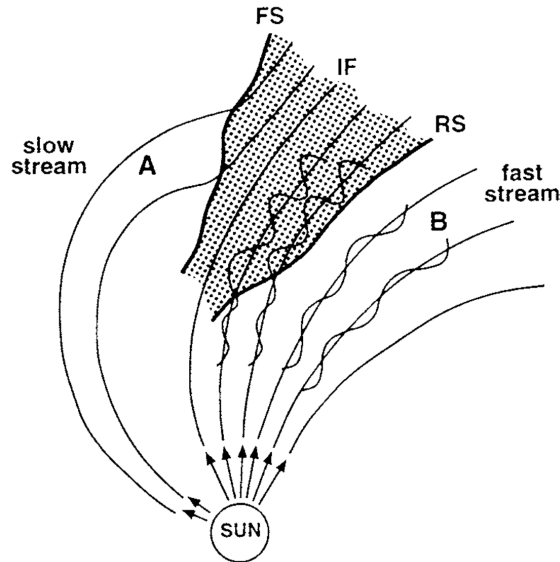


Figure 1.18: Schematic of the formation of corotating interaction regions (CIRs), from Kamide et al. (1998). The interaction between a high-speed stream (B) and a slow-speed stream (A) are shown together with the CIR (shaded). The forward shock (FS), interface surface (IF), and reverse shock (RS) are also indicated.

solution. Weber and Davis (1967) developed a steady-state model of the solar wind, showing how the solar magnetic field plays a substantial role in the loss of angular momentum of the Sun. They modelled the interaction between the solar wind and a magnetic field which is uniform and radial at the solar surface. They also restricted their discussion to equatorial winds, assumed  $B_\theta = 0 = v_\theta$ , and that variations along  $\varphi$  may be negligible, either for all  $\varphi$  or in small regions where  $\partial_\varphi B_\varphi$  and  $\partial_\varphi v_\varphi$  can be neglected. Hence, the divergence of the magnetic field (1.1b) implies that

$$B_r = \frac{B_0 r_b^2}{r^2} \quad (1.37)$$

where  $B_0$  is the field strength at the surface in which the field is purely radial.

In the original Weber and Davis (*ibid.*),  $r_b = 1 R_\odot$  and  $B_0$  is the photospheric field. However, as discussed in section 1.2, the magnetic field in the inner solar atmosphere is far from being that ordered, as was already known in the 1960s (e.g. Davis, 1965; Schatten et al., 1969, and references therein). It is also known that the source of most of the solar wind is not that low in the solar atmosphere, and instead most of its acceleration happens in the transition region between chromosphere and corona. Thus, most models assume purely radial field at a certain source surface  $r_b = R_{ss}$ , usually placed between  $1.1 R_\odot$  and  $5 R_\odot$  (Hoeksema et al., 1983; Levine et al., 1977; Mackay and Yeates, 2012; Schatten, 1971). Figure 1.19 shows the IMF spiraling from the source surface, while below the magnetic field can assume a closed-field configuration, typical of helmet streamers.

The next equation is provided by the fourth of the ideal MHD equations (1.20) for a stationary magnetic field ( $\partial_t \equiv 0$ ):

$$\nabla \times (\mathbf{v} \times \mathbf{B}) = 0. \quad (1.38)$$

The equation above is a vector equation, which splits into 3 equations, one for each component. The  $\theta$  one is useless because the only non-zero component of  $\mathbf{v} \times \mathbf{B}$

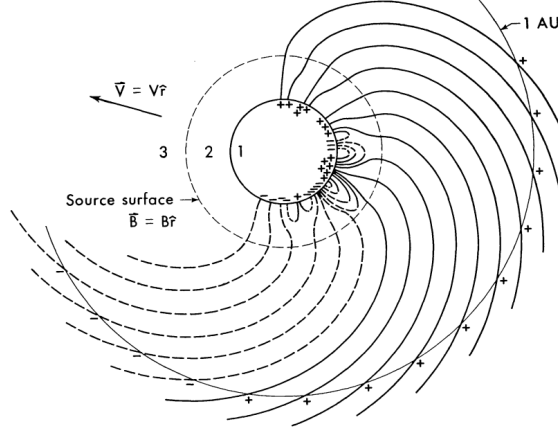


Figure 1.19: Schematic representation of the purely radial IMF spiraling out due to solar rotation from the source surface (dashed circle), which is placed above the solar surface (solid circle, enclosing 1). In the region (2) between those two surfaces, closed magnetic field exist.  
 Reproduced from Schatten et al. (1969), © Springer Nature.

is the latitudinal one, and thus the latitudinal component of equation (1.38) is the subtraction of two null quantities. The equations for the radial and the longitudinal component are:

$$\frac{\partial}{\partial r} r (v_\varphi B_r - v_r B_\varphi) = 0 \quad (1.39a)$$

$$\frac{\partial}{\partial \varphi} r (v_\varphi B_r - v_r B_\varphi) = 0 \quad (1.39b)$$

Equation (1.39b) can be integrated to give

$$v_\varphi B_r - v_r B_\varphi = \frac{C}{r}.$$

The constant of integration is found by considering a purely radial field at the corotating surface  $r = r_b$ :  $B_\varphi(r_b) = 0$  and  $v_\varphi(r_b) = \Omega_\odot r_b$ . Then,

$$C = -\Omega_\odot r_b^2 B_0 = -\Omega_\odot r^2 B_r \quad (1.40)$$

so that the longitudinal component of the magnetic field is

$$B_\varphi = \frac{v_\varphi - \Omega_\odot r}{v_r} B_r. \quad (1.41)$$

To see how the wind speed trends change in the Weber and Davis (1967) model compared to the simple Parker (1958) treatment, consider the components of the motion equation

$$\rho(\mathbf{v} \cdot \nabla) \mathbf{v} = -\nabla \left( p + \frac{B^2}{8\pi} \right) + (\mathbf{B} \cdot \nabla) \frac{\mathbf{B}}{4\pi} - \frac{GM_\odot \rho}{r^2} \mathbf{e}_r \quad (1.42)$$

which is the extension of (1.24b) when  $\mathbf{B} \neq 0$ . The longitudinal component is

$$\rho v_r \frac{d}{dr} (r v_\varphi) = \frac{B_r}{4\pi} \frac{d}{dr} (r B_\varphi)$$

where, because of (1.37) and the continuity equation (1.24a),  $\rho v_r/B_r$  is a constant. Thus an integration gives

$$rv_\varphi - \frac{Br}{4\pi\rho v_r}rB_r = L. \quad (1.43)$$

The constant  $L$  can be interpreted as the total angular momentum per unit mass carried by kinetic plasma motion and by magnetic stresses: during its lifetime, the Sun was slowed down by the torque transmitted to its surface by the Lorentz force as the magnetized wind was blown out.

Using (1.41) to eliminate  $B_\varphi$  and defining the radial Alfvén Mach number as

$$M_A = \frac{v_r}{v_{Ar}} \equiv \frac{\sqrt{4\pi\rho}}{B_r}v_r, \quad (1.44)$$

equation (1.43) can be manipulated to give

$$v_\varphi = \frac{\Omega_\odot r}{M_A^2 - 1} \left( \frac{M_A^2 L}{\Omega_\odot r^2} - 1 \right). \quad (1.45)$$

The total angular momentum per unit mass  $L$  can be determined by imposing the longitudinal speed to be finite for any  $r$ . In the low corona the plasma longitudinal flow is sub-Alfvénic ( $M_A^2 \ll 1$ ) because the values for the flow speed are typically below 10 km/s while those for  $v_A$  lie between  $10^2$  and  $10^3$  km/s (Priest, 2014; Reginald et al., 2011). At Earth's orbit and beyond, instead,  $v_r \approx 200 - 800$  km/s and  $v_A \approx 50 - 60$  km/s, so the flow is super-Alfvénic ( $M_A^2 \gg 1$ ).

The Alfvén critical point  $r_A$  is defined as the distance  $r$  where the Alfvén speed equals the flow one, so that  $M_A^2 = 1$ . Within this radius, magnetic field is so strong that it tends to keep the solar wind corotating with the Sun, increasing the angular momentum of the plasma as it moves out. Beyond the Alfvén radius, the magnetic field has less effect on the plasma motion, which therefore conserve its angular momentum. Thus,  $r_A$  may be defined as the outer boundary of the solar corona, since in the super-Alfvénic solar wind communication with the Sun via Alfvén-waves is no longer possible.

Thus, to avoid equation (1.45) being an undetermined form, it must be

$$L = \Omega_\odot r_A^2 \quad (1.46)$$

so the density of angular momentum carried by the rotating and magnetized solar wind is equivalent to that of a rigid rotation out to the alfvénic point  $r_A$ . The longitudinal speed can then be expressed as

$$v_\varphi = \frac{\Omega_\odot r}{M_A^2 - 1} \left( \frac{M_A^2}{\left(\frac{r}{r_A}\right)^2} - 1 \right) \quad (1.47)$$

to show that, while close to the Sun rotation is almost rigid ( $v_\varphi \rightarrow \Omega_\odot r$ ) due to the stronger magnetic pressure ( $M_A^2 \ll 1$ ), far from it the angular momentum is conserved with longitudinal speed going as  $\Omega_\odot r_A^2/r$ .

The radial wind solution for the Weber and Davis model is found considering the corresponding component of equation (1.42),

$$\rho v_r \frac{dv_r}{dr} - \frac{\rho v_\varphi^2}{r} = -\frac{dp}{dr} - \frac{B_\varphi}{4\pi r} \frac{d}{dr} (rB_\varphi) - \frac{GM_\odot \rho}{r^2}, \quad (1.48)$$

eliminating  $v_\varphi$ ,  $B_\varphi$ ,  $\rho$  from it (using the above expressions for these quantities) and using the adiabatic law (1.17) to eliminate the pressure. The equation is then integrated to obtain a Bernoulli equation whose families of solutions are shown in figure 1.20. As in the isothermal, radially symmetric and unmagnetized Parker

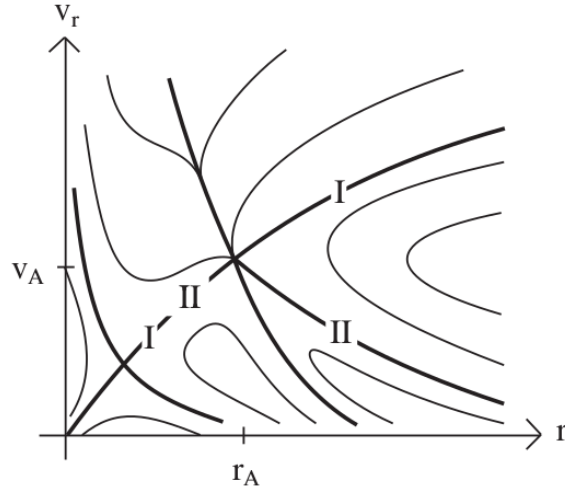


Figure 1.20: Schematic showing of solutions to equation (1.48). Consistently with the Parker treatment, the only physical solution is the one with low speed for  $r \rightarrow 0$  and low pressure for  $r \rightarrow \infty$ , in this case class I. The solution passes through the three critical points where the flow attains the speed of slow, alfvénic and fast-mode waves. The latter two are very close.

Source: Priest (2014), © Cambridge University Press.

model, there is only one solution that has zero speed at the Sun surface and that is supersonic at large distances. Unlike the Parker treatment, there are three critical points that must be crossed by the solution to consider it physical. These three points are found where the plasma radial flow speed reaches the values of slow-mode, Alfvén-mode and fast-mode waves mentioned in section 1.3. Since at  $r_A$  the thermal pressure is very low compared to the magnetic one, the critical points for alfvénic and fast-mode speeds are very close together and nearly indistinguishable.

## 1.4.2 Global structure of the Parker Spiral

To obtain expressions that can be integrated, the classical models of Parker (1958) and Weber and Davis (1967) must necessarily reduce the complexity of the solar wind, leaving out parts of its variability. The Sun, however, is far from being a uniform and stationary object, and this has repercussions on the complete structure of its atmosphere, of the interplanetary magnetic field, and of the solar wind streamlines.

The hypothesis of longitudinal invariance assumed in section 1.4 does not hold on closer inspection, even when it is restricted to the solar equatorial plane: this plane is rather divided into a variable number of sector boundaries, regions in which the magnetic field has different polarity and strength. Plasma streams in the sector boundaries have different densities and velocities that can collide (as seen with equations (1.36)) and interact, leading to the formation of corotating interaction regions.

The stationarity hypothesis should also be released, both on long and short time scales. As it is known since pre-telescopic times through sunspot counting

(Stephenson, 1990; Xu Zhen-tao, 1980), the Sun exhibits a cycle of activity with a period of (approximately) eleven years. Since many solar features owe their existence to the magnetic field, it is not just the sunspots number that varies with the solar cycle, but also the whole solar atmosphere and the features of solar activity. At the minimum, the shapes of the solar corona and the interplanetary magnetic field are closer to the dipolar one, with prominent open plumes at the poles and streamers at the equator, while as the cycle approaches its maximum it become much more isotropic, with streamers stretching out form all latitudes, until pole reversal occurs and the cycle restarts. Thus, following the rhythm of the solar cycle, the heliosphere expands at the solar minima and contracts at the solar maxima.

Also varying with the solar cycle, and more frequent in solar maxima, solar disturbances emerge from the inner solar atmosphere and then propagate and expand along the solar wind streamlines, distorting the surrounding magnetic field due to their magnetic properties. The shocks associated with corotating interaction regions and coronal mass ejections also constitute distortions in the local structure of the interplanetary field.

Furthermore, the Parker spiral and the interplanetary magnetic field are three-dimensional objects. The magnetic field component perpendicular to the equatorial plane ( $B_z$  or  $B_\theta$  in cylindrical or spherical coordinates) is the one that most affect space-weather conditions on planetary magnetospheres. Its orientation, parallel or anti-parallel to that of the planetary magnetic dipole, determines where the magnetic reconnection between the field lines of the magnetospheric field takes place, and therefore how much solar wind material enters the magnetosphere. Unfortunately, it is also the one component with the greatest lack of information. Before the launch of the Ulysses probe in the 90s, the solar poles and related magnetic field had never been directly observed, and still the vast majority of spacecraft focus on the ecliptic plane. As discussed in section 1.6.4, Solar Orbiter is expected to explore progressively higher latitudes in the later stages of its mission.

Although in a very first approximation the interplanetary magnetic field can be roughly described by a dipole field, its shape is indeed much more complex. Its lines ultimately lie on the photosphere, where their footpoints are subject to the turbulent motion of the surface. In addition to this, the differential rotation of the Sun, the asymmetry in the expansion of the various solar wind streams, and the stochastic component linked to the propagation of MHD waves contribute to tangle the field lines.

All of these features give a complicated, time-variant form to the global three-dimensional structure of the interplanetary Parker spiral, which models still struggle to completely grasp.

Figure 1.21 depicts an artist's view of the inner heliosphere as it may appear during a typical solar minimum. The pictured Sun is covered by large coronal holes, sources of fast solar wind (in yellow). The solar equatorial region is governed by bright active centers and their loop-like and mainly closed magnetic structures above (the red/blue colored coronal streamer). In green, what looks like the skirt of a spinning ballerina is the heliospheric current sheet, the warped separatrix between positive and negative solar magnetic field lines carried out into interplanetary space by the solar wind.

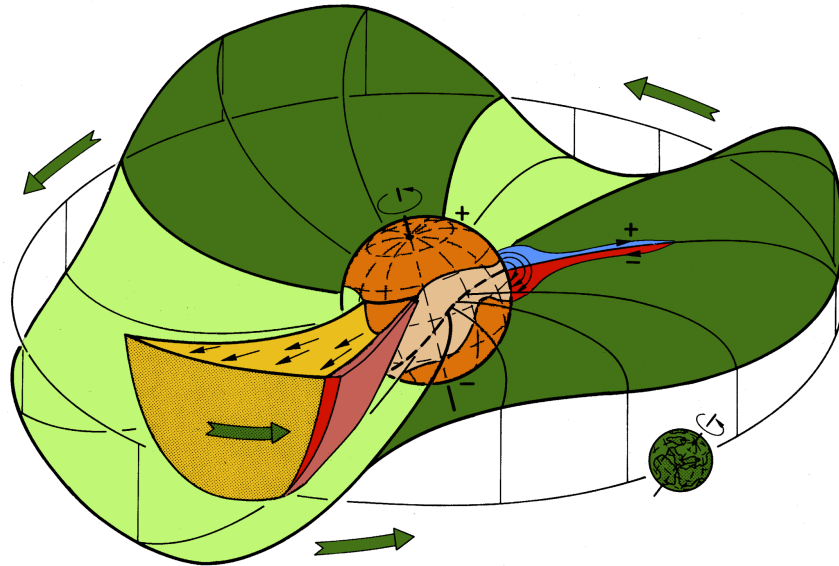


Figure 1.21: The "ballerina skirt" model of the three-dimensional heliosphere, according to Alfvén (1977).

Reproduced from Schwenn (2006), © Springer Nature.

## 1.5 Modelling interplanetary coronal mass ejections

Models for CMEs have evolved from very simple and qualitative cartoon models, to simple analytic and semi-analytic models, to 2D, 2.5D, and 3D numerical models in growing levels of complexity (Mikić and Lee, 2006). A brief overview of these models is presented in this section.

Currently, no existing model is applicable to all cases (Kilpua et al., 2017). As discussed in section 1.2.3, ICMEs generally fall in one of two categories depending on whether or not their in situ measurements show the signatures of a magnetic cloud, and only a fraction (about one third) of all encounters show these signatures at 1 AU (Cane and Richardson, 2003; Gosling, 1990; Wu and Lepping, 2011). However, it is believed that this fraction is significantly larger, and that the capability to detect a magnetic cloud depends on the distance between its center and the spacecraft crossing the ICME. This was confirmed with multi-spacecraft observations such as the Helios probes by Cane et al. (1997), or later with STEREO and L1 probes (Kilpua et al., 2011). Jian et al. (2006) demonstrated this by looking at profiles of total pressure perpendicular to the magnetic field, showing that ICME encounters at 1 AU can be categorized into three groups, depending on where the spacecraft hits the perturbation: in the first group the cloud is crossed centrally, in the second one the spacecraft hits the ICME closer to its edges, in the third group the magnetic cloud is barely touched. An ICME can also be distorted by and can dissipate into the interplanetary medium, eroding its magnetic structure as it propagates across the heliosphere. The possibility that ICMEs with or without magnetic clouds could have different origins at the Sun (thus being different phenomena) seems unlikely, since magnetic flux ropes play a fundamental role in the eruption of a CME (see e.g. Vourlidis et al., 2013).

In a first approximation, a magnetic cloud can be described as a cylindrically symmetric flux rope with a force-free magnetic field, a condition in which the magnetic pressure is balanced by the tension of the curved magnetic field lines. According to

equation (1.13), this means that the Lorentz force is null. Under this condition, the electric current density  $\mathbf{J}$  and the magnetic field  $\mathbf{B}$  must be parallel to each other, so that:

$$\mathbf{J} \times \mathbf{B} = 0 \Rightarrow \nabla \times \mathbf{B} = \alpha(\mathbf{r})\mathbf{B} \quad (1.49)$$

where  $\alpha(\mathbf{r})$  is an unknown function of the position. The study of physical equilibria satisfying the non linear equation (1.49) has been the focus of much theoretical research over the years (Kilpua et al., 2017; Mikić and Lee, 2006). One of the earliest (but still widely used) models was developed by Burlaga (1988) using the assumption of constant  $\alpha$ . This is a special configuration in space plasmas, since it is a state of lowest magnetic energy in ideal MHD where a plasma with finite resistivity bounded by perfectly conducting walls evolves (Burlaga, 1988; Taylor, 1986; Woltjer, 1958). In this form, a solution to equation (1.49) was given by Lundquist (1950) in terms of the 0th and 1st order Bessel functions as:

$$\begin{aligned} B_R &= 0 \\ B_z &= B_0 j_0 \left( \frac{\alpha_0 R}{R_0} \right) \\ B_\varphi &= \pm B_0 j_1 \left( \frac{\alpha_0 R}{R_0} \right) \end{aligned} \quad (1.50)$$

where  $R$ ,  $z$ ,  $\varphi$  are the cylindrical coordinates,  $R_0$  the radius of the magnetic cloud and  $B_0$  the field strength at the center of the flux rope. Later, a number of works generalized the finding of Burlaga (1988), e.g. Vandas and Romashets (2003), which generalized the Lundquist solution to the case of oblate cylinders, in order to account for ICMEs expansion and distortion. Even relaxing the assumption of constant  $\alpha$ , it is still possible to obtain a solution for the force-free equilibrium that resembles the Lundquist one. The Gold and Hoyle (1960) solution of (1.49) is:

$$\begin{aligned} B_R &= 0 \\ B_z &= \frac{B_0}{1 + (kR)^2} \\ B_\varphi &= kRB_z, \end{aligned} \quad (1.51)$$

found in (1.49) when  $\alpha(r) = 2k/[1 + (kr)^2]$ , with  $k \in \mathbb{R}$ . The field lines of this solution, uniform in  $\varphi$  and  $z$ , lie on surface of constant  $R$  along which the quantity  $\varphi - kz$  takes a constant value. In this case all field lines have uniform twist, and the length along the  $z$ -axis for one rotation is  $2\pi/k$ . This solution was used by Low (1977) and later generalized by Low and Berger (2003).

A force free approach is appropriate when non-magnetic forces can be neglected. This is generally true for low  $\beta$  plasma such as the corona (Golub and Pasachoff, 1997) and parts of the solar wind (Hundhausen, 1995). However, sometimes plasma effects are important for the dynamics of magnetic clouds and a non-force-free approach must be considered. This is usually the case in the front and rear regions of ICMEs, where the interaction with the background solar wind can lead to an increased current perpendicular to the field (see e.g. Möstl et al., 2009a). For instance, Hidalgo (2016) proposed a non-force free model used to fit magnetic field and plasma parameters of observed magnetic clouds.

While ICMEs are usually described as flux ropes loops, alternative morphologies have been taken into account, such as writhed fields, toroidal-like structures and spheromaks. The latter are helical toroid magnetic flux ropes confined within a sphere, and have been studied for two decades, starting from the first works of Vandas et al. (1998, 1997) and Gibson and Low (1998) and continuing in the following years (see e.g. Kataoka et al., 2009; Manchester et al., 2004, 2014). Shiota and Kataoka (2016) proposed an improved spheromak model for SUSANOO, that was also recently implemented inside the EUHFORIA model (Scolini et al., 2019; Verbeke, C. et al., 2019, see section 2.1.2 for a description of heliospheric MHD models such as SUSANOO and EUHFORIA). Spheroidal models can fit the magnetic field data as well as the flux ropes models and capture many complexities of magnetic profiles. However, observations give stronger support for flux ropes curving back and being attached to the Sun (Kilpua et al., 2017).

Despite the sophistication achieved by flux rope models, simpler approaches are still relevant in modelling ICMEs. Cone models (Howard et al., 1982; Odstrčil and Pizzo, 1999a; Zhao et al., 2002) describe them as homogeneous plasma clouds, isotropic in expansion, and with radial bulk velocity. The small number of input parameters needed by this class of methods make them particularly convenient for routine applications in space weather forecasting (Pomoell and Poedts, 2018; Scolini et al., 2018) despite the drawback of absence of internal magnetic field in the ejecta. The first cone model was originally developed for halo CMEs by Zhao et al. (2002), on the basis that CMEs observed near the solar limb maintain their angular widths constant as a function of radial height and propagate radially beyond the first solar radii (Odstrčil et al., 2004; Plunkett et al., 1997; Webb et al., 1997). The free parameters of the model are the angular width of the cone and the orientation of its central axis. For a halo CME, both can be determined by matching the cone cross section at a certain radial distance (projected on the sky plane) with the observed bright ring at a certain time. Xie et al. (2004) extended the cone model of Zhao et al. (2002), improving the method to determine the free parameters and deriving a relation between observed projection speed and the actual speed of the perturbation. Xue et al. (2005) developed the ice-cream cone model, called in this way because of the combination of a circular cone with a sphere on top of it. Later, Gopalswamy et al. (2009) derived a ratio of radial speed to expansion speed of the ICME as a function of angular width for three types of cone model: a cone with flat front (like the original model of Zhao et al. (2002), a spherical front (shallow ice-cream cone), and a hemispherical front (full ice-cream cone). The full ice-cream cone model is found to be the one that most closely resembles coronal observations (Gopalswamy et al., 2009; Na et al., 2017), and it also has the advantage of being similar to a flux-rope structure (Na et al., 2017). Recently, Zhang (2021) further generalized cone models, applying them to non-radial prominence eruptions, using cones with apexes located at the source region of the ejecta instead of the Sun center.

Cone models are easy to use and provide a stable running environment, due to a long period of use and fine-tuning of the numerical algorithms involved (Verbeke, C. et al., 2019). While the magnetic structure of the ejected material (in particular its  $B_z$ ) is the main responsible for driving strong geomagnetic storms, speed and density of an ICME nevertheless play a role in impacting the compression of the magnetosphere (Kilpua et al., 2017). This is one of the reason why ENLIL and EUHFORIA still use cone models for routine application of space-weather.

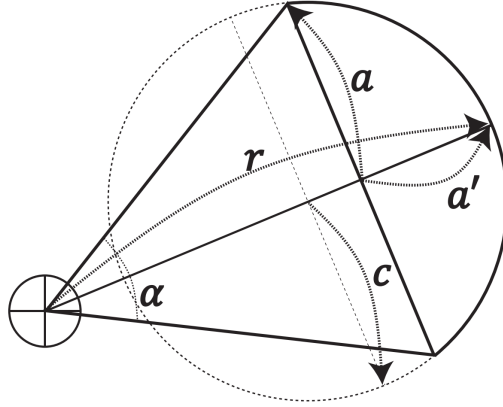


Figure 1.22: Geometry for determining cone shape parameters. Here,  $\alpha$  is the angular width of a CME,  $a$  its half linear width,  $a'$  the distance from the center of the linear width to the CME front,  $c$  the curvature radius of the CME front and  $r$  a distance from the center of the Sun to the CME front. If  $c/r \rightarrow \infty$ ,  $a'/a \rightarrow 0$  and the CME is described by a flat cone. A shallow ice-cream is obtained when  $c/r = 1$ , so that  $a'/a = \text{constant}$  under the assumption of self-similar expansion. If  $a'/a = 1$ , the CME is a full ice-cream, and in this case  $c/r$  is constant under the assumption of self-similar expansion.

Source: Na et al. (2017), © The American Astronomical Society.

## 1.6 Heliospheric spacecraft relevant to this work

Since the launch of the Helios mission in the 70s, a great number of robotic probes has been dedicated to the exploration of the heliosphere and the investigation of heliophysics and solar wind.

Currently, the Sun and the heliospheric plasma is constantly monitored via a combination of remote-sensing observations and in situ measurements by an expanding fleet of deep-space vessels that includes STEREO-A, Parker Solar Probe, Solar Orbiter, and BepiColombo (Benkhoff et al., 2021), in conjunction with probes orbiting the lagrangian point L1 such as Wind, ACE, SOHO, and Earth-orbiting satellites such as SDO, Hinode (Kosugi et al., 2007), the GOES fleet, and IRIS (De Pontieu et al., 2014).

In the next chapters, measurements from the following spacecraft were used, both as input for reconstructions of the Parker spiral or as comparisons for the accuracy of these.

### 1.6.1 GSS Wind

Launched in 1994, the Global Geospace Science Wind (Wind; Harten and Clark, 1995) NASA mission orbits the Sun at L1 continuously since May 2004. Its primary science objectives are to provide complete plasma and magnetic field parameters for magnetospheric and ionospheric studies, to investigate basic plasma processes occurring in the near-Earth solar wind environment, and to provide baseline ecliptic plane observations for inner and outer heliospheric missions. Among its instruments, those relevant to this work are:

- the Solar Wind Experiment (SWE; Ogilvie et al., 1995), a set of sensors

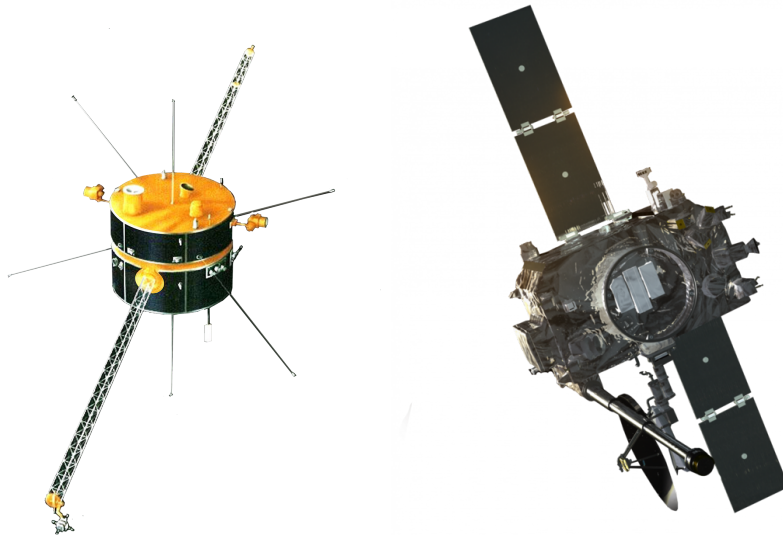


Figure 1.23: Renderings of the Wind spacecraft (left) and STEREO (right).

dedicated to determine solar wind parameters. It consists of two Faraday Cup sensors with an energy/charge range of 150 to 8000 V, a vector ion spectrometer with a range of 7-24800 V, a strahl sensor, and an on-board calibration system. SWE's time resolution can be of the order a few seconds for three-dimensional measurements;

- the Magnetic Field Instrument (MFI; Lepping et al., 1995), composed of dual triaxial fluxgate magnetometers with a dynamic range of  $\pm 4 \cdot 10^{-5}$  G to  $\pm 6.5 \cdot 10^{-4}$  G. Data sample rates vary from 44 samples per second (sps) to 10.87 sps in snapshot memory.

### 1.6.2 STEREO-A

The NASA operated Solar Terrestrial Relations Observatory (STEREO; Wuelser et al., 2004) was originally designed as a mission composed of two twin probes, STEREO-A and STEREO-B, which departed Earth in 2006, and are now in heliocentric orbit around the Sun close to 1 AU. STEREO-A's orbit is inside that of our planet taking  $\approx 347$  days for a revolution, while the orbit of STEREO-B is outside the Earth's one, taking  $\approx 387$  days for a complete revolution. The primary goal of STEREO was to provide stereoscopic images of the Sun, being able to see its disk from different points of view in the ecliptic plane, with emphasis on space-weather phenomena research and forecasting (see e.g. Jian et al., 2018). Contact with STEREO-B was lost on October 1, 2014, due to a failure in a planned automation test. NASA terminated all STEREO-B recovery operations on October 17, 2018. STEREO-A continues to operate normally. All STEREO scientific instrumentation has been specifically designed for space-weather purposes. Among its equipment, plasma and magnetic field measurements used come from two instrument suites:

- Plasma and Supra-Thermal Ion Composition investigation (PLASTIC; Galvin et al., 2008), which samples the plasma parameters of protons, alpha particles, and heavier ions composing the solar wind. It has nearly complete angular coverage in the ecliptic plane and an energy range from  $\approx 0.3$  to 80 keV/e, from which the distribution functions of suprathermal ions are provided;

- In situ Measurements of Particles and CME Transients (IMPACT; Luhmann et al., 2005), which samples the three-dimensional distribution and provide plasma characteristics of solar energetic particles and the local vector magnetic field. Magnetic field measurements were taken from its triaxial fluxgate Magnetometer, which has two ranges: up to 65.536 nT and up to 500 nT, both with 0.1 nT accuracy.

### 1.6.3 Parker Solar Probe

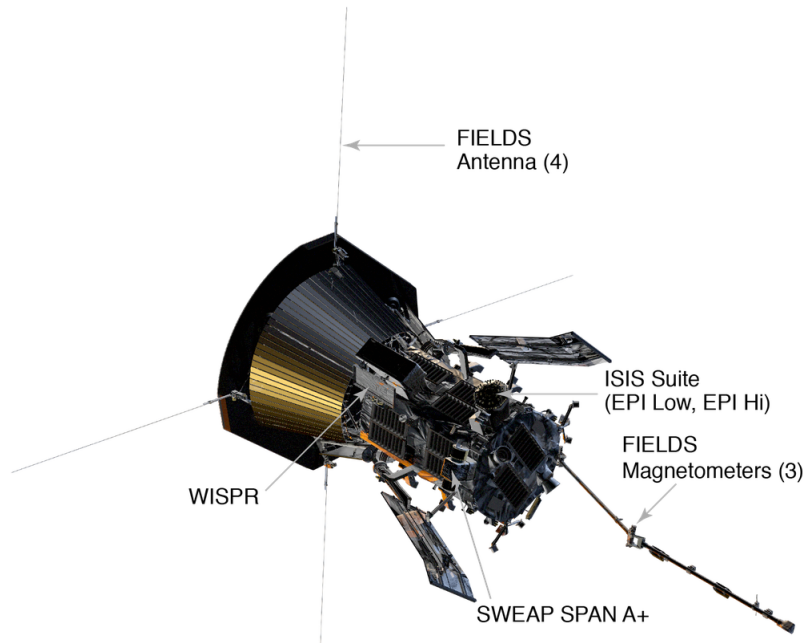


Figure 1.24: Rendering of the Parker Solar Probe ram-facing view. The positions of the four instrument suites ISIS, WISPR, SWEAP and FIELDS are labelled.

Source: NASA/JPL.

Launched on 12 August, 2018, Parker Solar Probe (PSP; Fox et al., 2016) is a NASA spacecraft with the main mission of determine the structure and dynamics of the of the coronal magnetic field, understanding the coronal heating mechanism and the acceleration of the solar wind, and determine the process of acceleration of SEPs. It was launched in August 2018, and will perform a total of 24 orbits over a 7-year nominal mission duration (see figure 1.25). At 09:33 UT on 28 April 2021, PSP became the first spacecraft to enter the corona, crossing the Alfvén surface for 5 hours (Kasper et al., 2021). At its closest approach in 2025, it will reach  $9.86 R_{\odot}$  (0.0459 AU) from the center of the Sun, and will travel as fast as 191.67 km/s (Fox et al., 2016). It is already the fastest object ever built.

Among its four instruments suites, which also include the Integrated Science Investigation of the Sun (IS $\odot$ S; McComas et al., 2016) and the Wide-field Imager for Solar Probe (WISPR; Vourlidas et al., 2016), in chapter 4 were used measurements from:

- Solar Wind Electrons Alphas and Protons (SWEAP; Kasper et al., 2016), which consists of the Solar Probe Cup (SPC), designed to operate under extreme temperatures) and the Solar Probe Analyzers (SPAN), a combination of three electrostatic analyzers that make detailed measurements of ion and electron

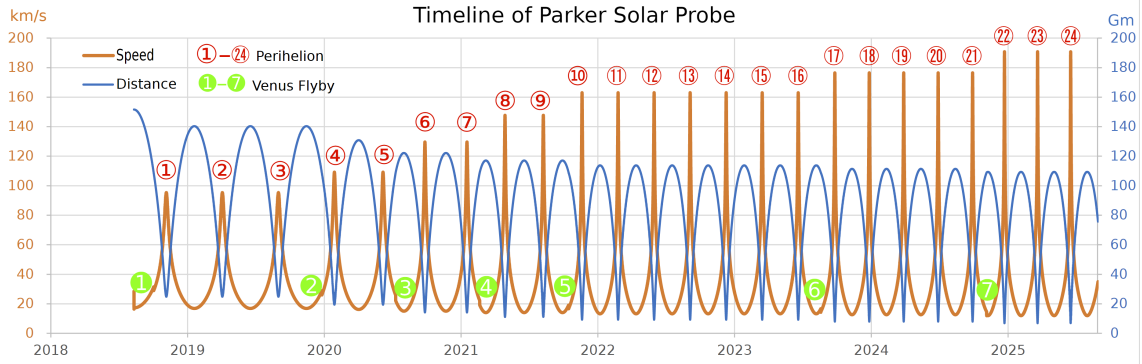


Figure 1.25: The speed (orange line) and distance from the Sun (blue line, in  $10^{11}$  cm) of PSP, from launch until 2026. The red circles mark the perihelii at each solar encounter, the green ones mark the flyby with Venus. Source: NASA / JPL, [from wikimedia](#).

velocity distributions from the shadowed region behind the spacecraft heat shield. SPC is a Faraday Cup that looks directly at the Sun and measures ion and electron fluxes and flow angles as a function of energy from 50 eV/q to 8 keV/q for ions and 50 eV to 2 keV for electrons. SPAN consists of an ion and electron electrostatic analyzer (ESA) on the ram side of SPP (SPAN-A) and an electron ESA on the anti-ram side (SPAN-B). The SPAN-A ion ESA measures ions as a function of direction and energy/charge from several eV/q to 20 keV/q and has a time of flight section that enables it to sort particles by their mass/charge ratio, permitting differentiation of ion species. The SPAN-A and SPAN-B electron ESAs also run from several eV to 20 keV;

- Electromagnetic Fields Investigation (FIELDS; Bale et al., 2016), which measures electric  $\mathbf{E}$  and magnetic  $\mathbf{B}$  fields, the properties of in situ plasma waves, electron density and temperature profiles, and interplanetary radio emissions. FIELDS measures electric field with five antennas, four of which stick out beyond the heat shield of PSP (visible in fig. 1.24) and experience temperatures higher than 1600 K. The fifth antenna is perpendicular to the others and helps making a three-dimensional picture of  $\mathbf{E}$  at higher frequencies. Magnetic fields are measured using both two fluxgate and a search-coil (induction) magnetometers mounted on a deployable boom shaded by the heat shield.

### 1.6.4 Solar Orbiter

Solar Orbiter (SolO; Müller et al., 2013) is a ESA/NASA mission launched on February 10, 2020. It aims to address key questions of solar physics, pertaining how the Sun creates and regulates the heliosphere, and why solar activity changes with time. It will combine in-situ measurements of solar wind and remote-sensing observations of the Sun to explore the sources of solar wind, the causes, evolution, and interaction with ambient solar wind of CMEs, and the origins, acceleration mechanisms, and transport of SEPs (Müller et al., 2020). The nominal mission is planned to last 7 years, plus 3 years of extension. SolO's orbit will be as close to the Sun as  $60 R_{\odot}$  (0.284 AU, see figure 1.27), placing it inside the perihelion of Mercury (0.3075 AU).

During the mission its orbital inclination will be raised, reaching  $18^{\circ}$  of heliographic

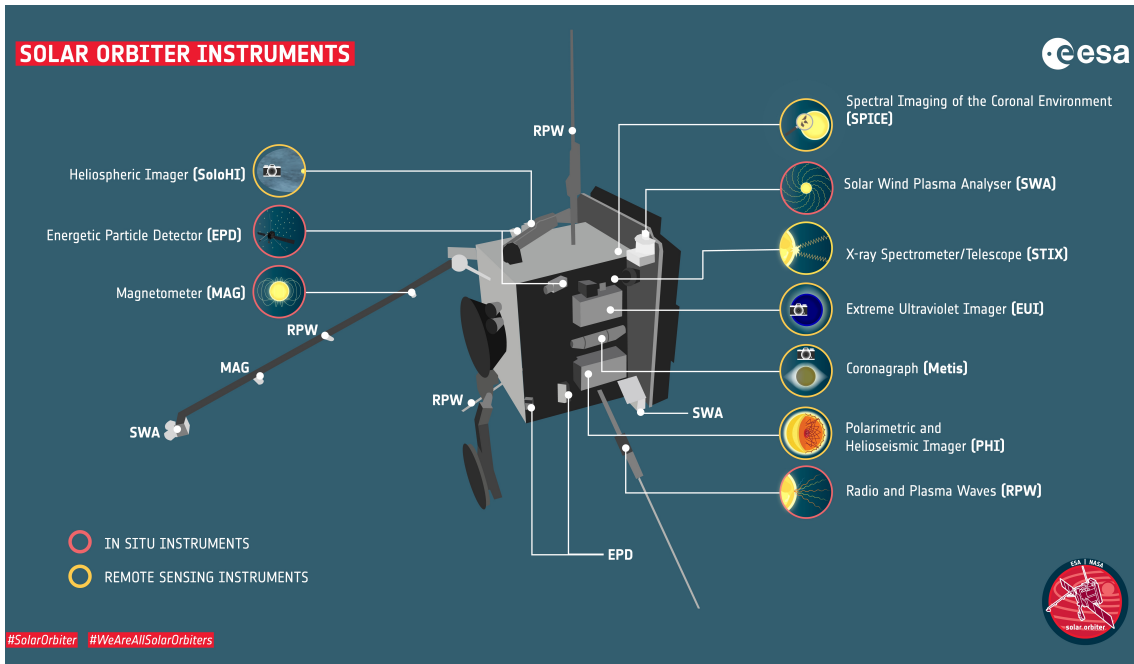


Figure 1.26: ESA poster depicting the rear view of the Solar Orbiter spacecraft. Labeled in red the positions of the four in situ instrument suites, in yellow those of the six remote sensing ones.

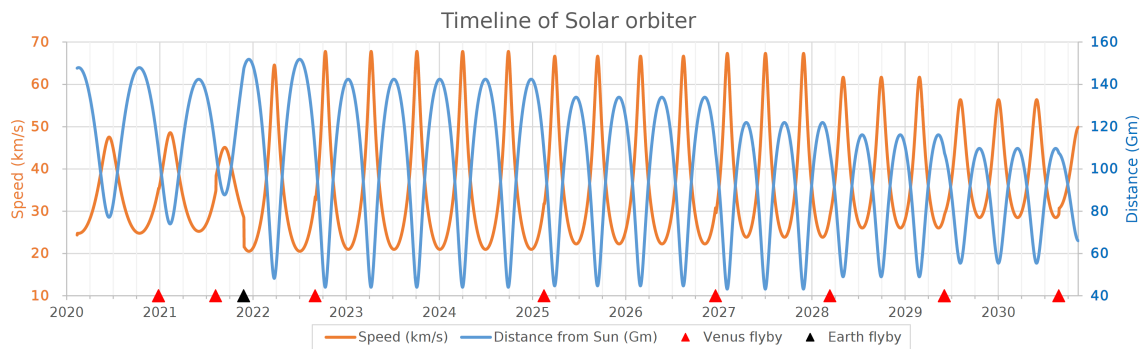


Figure 1.27: The speed (orange line) and distance from the Sun (blue line, in  $10^{11}$  cm) of Solar Orbiter, from launch until 2031. The red and black triangles mark the Venus and Earth flybys.

Data source: NASA/JPL, [from wikipedia](#).

latitude during the nominal mission phase and above  $30^\circ$  during the extended phase (see figure 1.28), allowing the observation of the solar poles. SolO data are expected to improve on those of the Helios probes and the Ulysses spacecraft (Müller et al., 2020), being acquired much closer to the Sun than the previous ones. At those high latitudes, SolO will provide the first-ever images and magnetic maps of the solar poles, drastically improving our knowledge about the mechanism underlying the solar cycle.

Solo's payload consists of ten experiments, some of which have several sensors for in situ measurements, other have multiple telescope channels for remote imaging of the Sun and its atmosphere. Four of these are in situ instruments: the Energetic Particle Detector (EPD; Rodríguez-Pacheco et al., 2020), the Magnetometer (MAG; Horbury et al., 2020), the Radio and Plasma Waves instrument (RPW; Maksimovic et al., 2020), and the Solar Wind Analyser (SWA; Owen et al., 2020). The other six

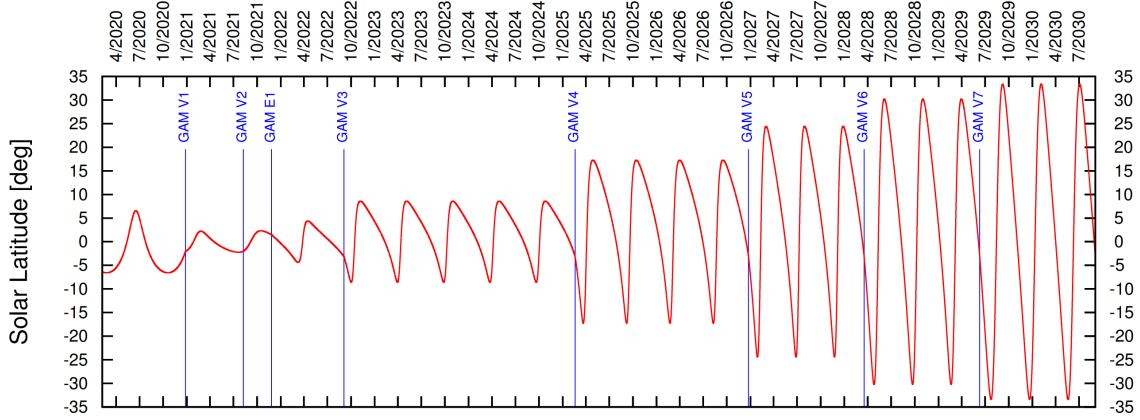


Figure 1.28: Solar Orbiter heliocentric latitude plotted as a function of time. The blue vertical lines mark the Venus and Earth flybys. Reproduced from Müller et al. (2020), © European Southern Observatory.

are remote-sensing instruments: the Extreme Ultraviolet Imager (EUI; Rochus et al., 2020), the Polarimetric and Helioseismic Imager (PHI; Solanki et al., 2020), the SoHO Heliospheric Imager (SoloHI; Howard et al., 2020), the Spectral Imaging of the Coronal Environment (SPICE; SPICE Consortium et al., 2020), the Spectrometer/Telescope for Imaging X-rays (STIX; Krucker et al., 2020) and the Metis coronagraph (Antonucci et al., 2020). In chapter 4, observations from the latter were used.

Metis is an externally occulted coronagraph that performs broad-band and linearly polarised imaging of the corona in visible light (with a bandpass of 580-640 nm), simultaneously with imaging of the UV corona in a narrow spectral range centred on the Lyman- $\alpha$  line of hydrogen (121.6 nm). Metis observe the inner corona in a square field of view of  $\pm 2.9^\circ$  width, with the inner edge of the field of view starting at  $1.6^\circ$ , and thus spanning the solar atmosphere from  $1.7 R_\odot$  up to  $9 R_\odot$ , depending on solar distance. Metis observe the proton and electron components of the solar wind the goal to obtain plane-of-the-sky maps of bulk speed and density in the coronal regions of wind acceleration (see 4.2 for further details). During the later out-of-ecliptic phase of the mission, Metis will trace CMEs out to  $9 R_\odot$  and, for the first time, will measure their longitudinal distribution.

# Chapter 2

## Models and methods: the RIMAP model

### 2.1 Analytical and Numerical Models

The amount of information about plasma parameters available to correctly model the outer corona, the solar wind and the rest of the heliosphere, and the propagation of solar disturbances is limited, and it is mostly provided by in situ spacecraft located around 1 AU near to the ecliptic plane, and by remote-sensing observations. Furthermore, the dynamic processes that underlie the acceleration of solar wind, coronal mass ejections, and solar energetic particles are not fully understood. It is known that the configuration of the magnetic field in their regions of origin, and their internal structures, must play a key role (see e.g. Forbes, 2000); however, the determination of magnetic field configurations is not a trivial task, since direct measurements of magnetic fields are routinely available only for the solar photosphere (Howard and Tappin, 2009).

Different methods and approaches have been developed to reconstruct the Parker spiral, that can be classified in two main categories: backward analytic reconstruction starting from in situ measurements usually acquired at 1 AU (such those of the ballistic models), and forward numerical reconstructions starting from remote sensing observation of the solar disk.

#### 2.1.1 Ballistic models

Often employed to investigate the solar wind sources at the Sun (Neugebauer et al., 1998, 2002), these methods usually assume a stationary flow from the Sun, allowing the tracing of the solar wind quantities from the heliocentric distance at which the spacecraft acquired its data to a source surface close to the solar one, using the Parker equation (1.32). The wind flow is treated as purely kinematic, with dynamics being totally ignored, as in the classical applications, or ad hoc introduced as a heuristic correction at the end of the calculation, as in the more recent examples of this approach (Pizzo, 1981).

The first works to use these techniques were those of Schatten et al. (1968), which mapped the interplanetary magnetic field in the ecliptic plane from 1.0 to 0.4 AU, and Wilcox (1968), who traced the solar source of sector pattern observed at 1 AU; later on, multiple spacecraft data were taken into account to improve the quality of these reconstructions (e.g. Behannon, 1978; Nolte and Roelof, 1973).

The limits of this approach were discussed already decades ago: Pizzo (1981) and Riley et al. (1999) used inward MHD mappings to show that the ballistic model is inadequate for the description of temporal and spatial profiles of plasma parameters. Since these methods neglect dynamical interaction, they perform best in reproducing details of parameters variations along the trailing edges streams (Nolte et al., 1977), but offer poorer results in the neighborhood of stream fronts, where the interaction is dominant (Burlaga, 1974). The reconstructions are also complicated by magnetic clouds (Klein and Burlaga, 1982), interplanetary shocks (Dryer, 1974), and any other transient phenomena.

More recently, due to the advancements in computational capabilities and the progressive developments of a fleet of spacecraft dedicated to heliospheric observations, the ballistic methods were reconsidered (e.g. Florens et al., 2007). Further developments include taking into account non-zero longitudinal components of the magnetic field at the source surface (Schulte in den Bäumen et al., 2011, 2012), the conservation of angular momentum (Tasnim and Cairns, 2016), and lack of corotation at the source surface (Tasnim et al., 2018).

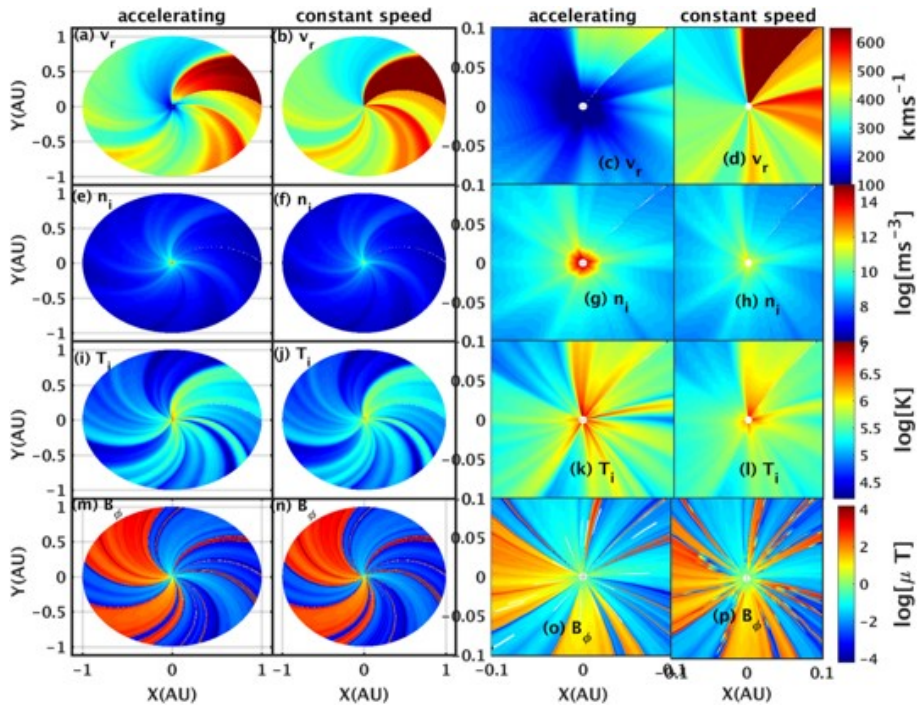


Figure 2.1: An example of ballistic reconstructions provided with the accelerating-wind model of Tasnim et al. (2018) (on the columns a, e, i, m, and c, g, k, o) compared with the constant-speed model of Schulte in den Bäumen et al. (2012) (on the remaining columns) from data acquired by the Wind spacecraft for the period 1-27 August 2010. From top to bottom, ecliptic maps of solar wind bulk speed, ion number density, ion temperature, and longitudinal magnetic field. Reproduced from Tasnim et al. (2018), © American Geophysical Union.

## 2.1.2 Forward numerical models

Works based on this approach usually start from observations of the visible solar disk (such as photospheric magnetograms) to reconstruct the plasma and magnetic

field parameters in the inner and intermediate solar corona, and then they expand the derived parameters at a given altitude in the interplanetary medium.

The reconstruction of plasma parameters in the whole three-dimensional corona follow two different methods. The first one consists in running a full self-consistent MHD numerical simulation, using photospheric observations as initial conditions (see e.g. Mikić et al., 1999; van der Holst et al., 2014; Yang et al., 2012). The other one extrapolate the photospheric magnetic fields, filling them with plasma up to a distance varying between 2.5 and 5  $R_{\odot}$  via semi-empirical relationships (e.g. Riley et al., 2006) or evolving them using time-relaxation methods (Feng et al., 2015), and then modeling with MHD simulation plasma and magnetic field up to 1 AU and beyond. These models rely on a variety of free parameters and assumptions which affect the final results. Lee et al. (2009) compared the two approaches discussed above with measurements from the ACE spacecraft, founding an overall agreement for the general large-scale solar wind between observation and results, with no particular preference. Gressl et al. (2014) also compared different models with each other and with in situ measurements from spacecraft at 1 AU, founding that the choice of synoptic map significantly affects the model performance. Réville and Brun (2017) compared constraints from three-dimensional coronal models expanded up to 1 AU with in situ observations. Pinto and Rouillard (2017) proposed the MULTI-VP model, an hybrid method to fill the gap between full 3D MHD models and purely semi-empirical methods. Asvestari et al. (2019) varied the heights of the boundaries for the inner and the outer solar corona, founding that lower values of these parameters improved model results.

Among different extrapolation methods, the Potential Field Source Surface (PFSS) is the most straightforward and therefore most commonly used technique for modeling the global coronal magnetic field (Mackay and Yeates, 2012). First developed by Schatten et al. (1969) and Altschuler and Newkirk (1969), and then refined by Hoeksema (1984) and Wang and Sheeley (1992), the PFSS model assumes that the electric currents in the solar corona are zero, neglecting their influence on the global field structure. This is reasonable because most of the coronal field is approximately free of Maxwell-stress most of the time ( $\mathbf{BB} \approx 0$ ): while twisting and shearing are present in active regions, and despite inertial forces being imposed on streamers by the solar wind, neglecting these effects does not severely undermine the PFSS model, which compares well with MHD models (Neugebauer et al., 1998; Riley et al., 2006). The magnetic field is computed between  $R_{\odot}$ , the photosphere, where the radial magnetic field distribution is specified, and  $R_{ss}$ , the outer source surface where the field is assumed to be entirely radial. The idea of the source surface is to model the effect of the solar wind outflow, which distorts the magnetic field away from a current-free configuration above approximately 2  $R_{\odot}$ , once the magnetic field strength has fallen off sufficiently (Mackay and Yeates, 2012). Following Hoeksema et al. (1983)  $R_{ss} = 2.5 R_{\odot}$  is commonly used, but values as low as 1.3 solar radii have been suggested (Levine et al., 1977), and it appears that the optimal  $R_{ss}$  could vary over time (Bělák et al., 2007; Lee et al., 2011). The absence of currents in the inner corona is a strong assumption: the actual coronal magnetic field does not become purely radial within the radius where electric currents may be neglected, as can be seen in eclipse observations (see figure 2.2a). Real coronal streamers bend more equatorward at solar minima and more poleward at solar maxima, and polar plumes bend more equatorward than those in the PFSS models. Furthermore, solar eruptions occur in coronal regions where the magnetic field configuration are non-potential,

that is, currents play a key role. Measurements from Parker Solar Probe allowed to infer the non-sphericity of the source surface (Panasenco et al., 2020), a feature that recently Kruse et al. (2021) incorporated into a generalization of the PFSS model. Despite its simplicity, the PFSS model is a well established technique providing a quite good description of the overall coronal field configuration and the location of open and closed field regions (Mandrini et al., 2014; Nitta et al., 2006). Other extrapolation methods exist, but they requires high-resolution vector magnetic fields measurements (Aschwanden, 2016; De Rosa et al., 2009) that, alike line-of-sight magnetograms, are not currently available for the whole photosphere.

Schatten (1971) showed that the PFSS models could be improved by replacing the source surface with an intermediate boundary at  $R_{cp} = 1.6 R_{\odot}$ , and introducing electric currents for  $r > R_{cp}$ . To avoid a Lorentz force too strong, these currents are limited to regions of weak field, namely to sheets between regions of  $B_r > 0$  and  $B_r < 0$ . These current sheets support a more realistic non-potential magnetic field in  $r > R_{cp}$ . This Schatten-Current-Sheet (SCS) model generates better field structures, particularly at larger solar radii, leading to its widespread use in models for the forecasting of solar wind and space weather conditions.

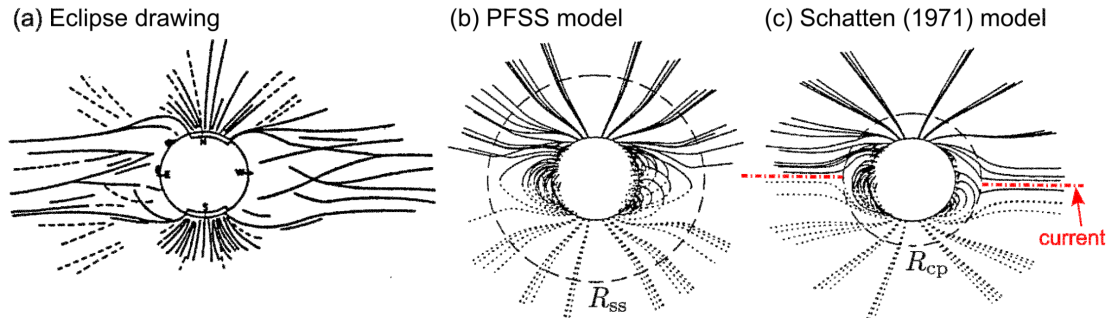


Figure 2.2: (a) A drawing of the real solar corona as seen in an eclipse, (b) the standard Potential Field Source Surface model of Schatten et al. (1969), and (c) the standard Current-Sheet model of Schatten (1971).

Once the coronal fields have been reconstructed up to a spherical surface concentric to the Sun in quasi real-time with similar methods, modelling the interplanetary expansion of the solar wind requires a method to convert these fields into plasma parameters. The Wang-Sheeley-Arge (WSA) technique (Arge and Pizzo, 2000; Sheeley and Wang, 1991; Wang and Sheeley, 1990, 1992) infer the solar wind speed from an empirical relationship (Arge et al., 2004; Arge et al., 2003) between the divergence of the magnetic field and the proximity of a selected open field line foot-point to the nearest coronal hole. The general idea is that, far from the Sun, the speed of the solar wind depends on the path that the wind took as it passed through the lower corona: if the flux tube that guided the flow had a large expansion, then the wind speed will be slow; else, if the flux tube remained focused, the wind speed would be fast. The amount of expansion is obtained from a current-free extension of the photospheric field (Sheeley Jr., 2017). This is based on results found by Levine et al. (1977): the fastest streams are correlated with flux tubes that expand least during their passage through the lower corona, and thus the divergence of the magnetic field must play a crucial role in the acceleration of the solar wind. Figure 2.3 show an example from Arge et al. (2004) of solar wind speed extrapolation at  $5 R_{\odot}$  from synoptic maps of photospheric fields

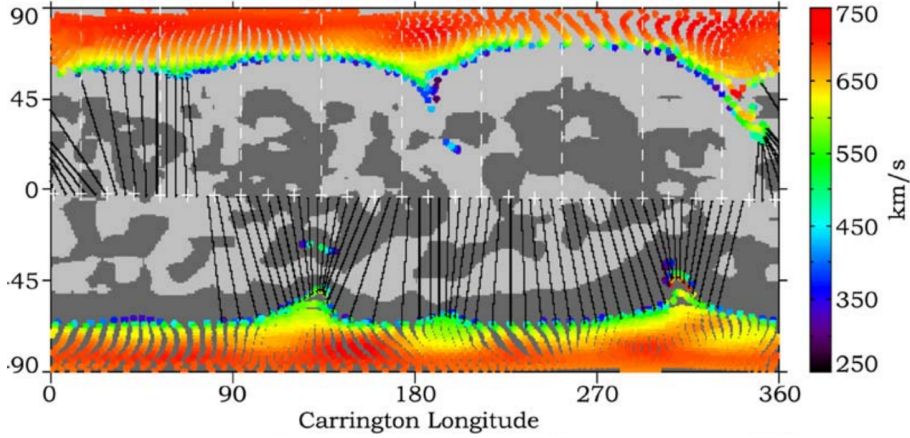


Figure 2.3: A synoptic map is used to build the photospheric field polarity map (dark and light grey as negative and positive polarity), used in turn as input by a PFSS+SCS combination to infer the coronal hole distribution (colored dots) at  $5 R_{\odot}$ . Then, an empirical function give the speed (color) of the solar wind outflowing from these coronal holes. Reproduced from Arge et al. (2004), © Elsevier.

Alternatively, the coronal magnetic fields and plasma conditions can be reconstructed by running a numerical simulation of the coronal plasma, starting again from photospheric field measurements. Among different models that have been developed by different research groups, one of the most established models is the Magnetohydrodynamic Algorithm outside a Sphere (MAS; Mikić et al., 1999) model, that has been optimized over the last decades to provide the best agreement between observed and simulated full disk images of the Sun acquired in extreme ultra-violet bands by different instruments (Riley et al., 2011) as well as to predict the appearance of the solar corona during total solar eclipses (e.g. Mikić et al., 2018). Full MHD code coronal solution reproduce the same large-scale structure (i.e. patterns of open and closed flux) as the PFSS models, and produce more realistic cusp-like topologies at the tip of the heliospheric current sheet streamer, where the PFSS models produce more rounded structures and appear to underestimated the amount of open flux in the heliosphere (MacNeice et al., 2018; Wiegmann et al., 2017). Nevertheless, the full-MHD models still must employ empirical and semi-empirical functions to model the coronal heating (Lionello et al., 2003; Riley et al., 2011), and these functions must be tuned and optimized in order to obtain the best agreement with EUV observation of the corona (MacNeice et al., 2018).

These methods show a significant level of agreement between observations and simulations in the distribution of coronal features, and between the extrapolated magnetic field lines and the observed orientation of coronal structures. However, the large spatial scales involved in the propagation of solar disturbances require that the model reconstruct the whole corona, a task that demands the knowledge of the magnetic fields over the entire photospheric surface at a given times. Nevertheless, current real-time measurements of the photospheric fields over the solar disk are limited to the visible hemisphere. The only available components measured directly are those along the line-of-sight, and the knowledge about polar fields is scarce (the investigation of the solar magnetic poles is in fact one of the main scientific objective of the Solar Orbiter mission). Recently, the launch of the Solar Orbiter mission made it possible to obtain magnetographic and helioseismology information outside of the Sun-Earth line thanks to the Polarimetric and Helioseismic Imager (PHI; Solanki

et al., 2020), although these magnetograms are not provided in real-time due to the complex orbit of the spacecraft.

Usually, photospheric fields in the hemisphere not visible from Earth are evaluated with complex flux-transport and flux-balance models (Worden and Harvey, 2000). The Air-Force Data Assimilative Photospheric flux Transport (ADAPT; Arge et al., 2013, 2010) is one of the most used models for evolving an ensemble of magnetographic observations during periods for which there are no observations, updating the ensemble using a data assimilation method that account for model and observational uncertainties. These models, however, cannot fully capture the complexity of the photospheric evolution that, in the end, is dictated by the solar dynamo, a phenomenon far from being understood. Hence, models such as ADAPT cannot forecast the emergence of sunspots, although this problem can partially be mitigated by the availability of far-side active region observations derived with helioseismology (González Hernández et al., 2007).

The above discussed coronal models, at the higher levels, are in general coupled with each other, simulating the interplanetary propagation of solar plasma from the photosphere to the heliosphere. The first (MacNeice et al., 2018) three-dimensional MHD model of the ambient global corona and inner heliosphere was that of Usmanov (1993). It used a PFSS model to initialize the inner coronal field and set surface boundary conditions. It divided the full simulation into two domains, an outer region of supersonic/super-Alfvénic flow from  $r_0 \approx 10 R_\odot$ , and an inner region from the solar surface to  $r_0$ , with different algorithms applied to the two regions. Almost all MHD solar wind model since then have followed the approach of coupling different codes beyond the sonic and Alfvénic points (MacNeice et al., 2018). In most cases, the inner region is modeled using a combination of the PFSS, Schatten CS and WSA techniques, and the outer region using an MHD algorithms. This approach is followed by ENLIL (Odstrčil, 2003; Odstrčil et al., 2004; Odstrčil and Pizzo, 1999a,b; Odstrčil et al., 1996), the most used (MacNeice et al., 2018) global heliospheric model routinely used for forecasting applications, and (to cite a few) by the Hybrid Heliospheric Modeling System (HHMS; Detman et al., 2006), the Multi-Scale Flux Kinetic Simulation Suite (MS-FLUKSS; Pogorelov et al., 2009), GAMERA (Merkin et al., 2011), CRONOS (Wiengarten et al., 2013), SUSANOO (Shiota et al., 2014), and the European Heliospheric Forecasting Information Asset (EUHFORIA; Pomoell and Poedts, 2018).

The coupled WSA/ENLIL model has become one of the workhorse models of both research and forecast communities (MacNeice et al., 2018; Sheeley Jr., 2017), and in 2011 it was made operational at the National Oceanic and Atmospheric Administration’s Space Weather Prediction Center (Pizzo et al., 2011). This model solves the three-dimensional equations of magnetohydrodynamics starting from inner boundary condition information derived by a WSA model, which in turn starts from the results of a PFSS/SCS model based on synoptic maps evolved on the entire solar surface via the ADAPT model. The model can be coupled with a cone model (e.g. Zhao et al., 2002, more details in chapter 3) to simulate the propagation of coronal mass ejections as unmagnetized clouds of plasma.

EUHFORIA is entirely developed by European research centers, mainly based in Belgium and Finland. It still starts from a PFSS model, using synoptic magnetograms provided by the Global Oscillation Network Group (GONG; Harvey et al., 1996) to extrapolate coronal fields on a source surface located at 2.3 solar radii. Then, a SCS model propagates these field up to 0.1 AU, where a WSA model provides plasma

speed and density, and a MHD code performs simulations of the inner heliosphere based on these data. Like ENLIL, EUHFORIA can be coupled with different coronal models in order to get its input at 0.1 AU. For instance, recently Samara et al. (2021) coupled it with the MULTI-VP model. It can also be coupled with a variety of coronal mass ejection models (e.g. Scolini et al., 2019, 2018; Verbeke, C. et al., 2019, more details in chapter 3).

While powerful, the WSA-like methods discussed above require considerable computational capabilities, mostly consumed by said extrapolations or reconstructions of the inner heliospheric conditions, even if with a significant reduction of with respect to the much more complex full MHD 3D models such as MAS. To make matter worse, their forecasting ability is still far from being optimal: these models are able, in an average sense, to predict the arrival time of major solar disturbances within  $\pm 10$  hours, but their associated standard deviations often exceed 20 hours (Riley et al., 2018). Furthermore, their ability to reconstruct the stationary conditions of the interplanetary plasma is still limited, as shown by the comparisons between model predictions and in situ measurements acquired by various spacecraft (Jian et al., 2016).

## 2.2 The Reverse in situ and MHD Approach

The techniques for reconstructing the interplanetary Parker spiral belong to one of this two categories: ballistic inverse mapping, starting from in situ measurements usually acquired at 1 AU, and then proceeding back to the Sun or the source surface with analytical methods; forward simulations, starting from photospheric field measurements on the Sun, and propagating the solar wind plasma up to 1 AU (or beyond) with MHD numerical methods. Nevertheless, on one hand empirical and analytical methods are computationally simple and have good accuracy for the reconstruction of large scale features in the solar wind plasma, but the models are not time dependent, they need to assume stationarity, and they usually assume the same average speed at all longitude in the mapping, to avoid the problem of streamlines crossing each other. On the other hand, the MHD models offer a deeper insight into the underlying physics, while cheaper models only provide partial information about the solar wind (MacNeice et al., 2018). MHD simulations are able to provide real-time evolution of the whole spiral at the same time, which is missing in analytical methods, but these models have limited knowledge of real plasma conditions at the inner boundaries.

The idea behind the Reverse in situ and MHD Approach (RIMAP; Biondo et al., 2021a) is to combine together the two methods, combining for the first time the ballistic back-mapping with time-dependent MHD numerical simulations. In particular, in RIMAP the complexity related with the reconstructions of the inner corona is completely avoided, and the numerical simulations of the ambient interplanetary plasma are bound to in situ measurements collected by spacecraft at 1 AU (Biondo et al., 2021a,b) or closer to the Sun (Biondo et al., 2022). To do this, the ambient plasma parameters of the inner heliosphere are reconstructed using in situ data provided by different spacecraft such as Wind, ACE, or the Parker Solar Probe, and then going backwards to an inner heliocentric distance following the spiraling arms of the interplanetary Parker spiral. This is possible by assuming stationarity for the conditions of the ambient solar wind in the time intervals selected for data acquisition. The back-reconstructed plasma parameters at this distance are

thus employed as inner boundary conditions for a MHD simulation of the solar wind expansion up to 1 AU.

As discussed in section 2.1.1, in situ measurements at 1 AU allow to reconstruct the inner heliospheric distribution of solar wind density and speed to a good degree of accuracy. However, the same cannot be said for temperature and magnetic field, whose interplanetary trends are not fully understood the more one gets closer to the corona. This is critical, because capturing the correct behaviour of temperature has important repercussions on the entire solar wind dynamic (see e.g. MacNeice et al., 2018). Furthermore, the reconstructed solar wind streams evolve during the MHD propagation interacting with each other and leading to the formation of CIRs. This concurs to make obtaining a good data-driven reconstruction of the plasma conditions a non-trivial task.

RIMAP provides a new method to reconstruct the real-time conditions of interplanetary plasma from the Sun to the Earth and beyond. Moreover, RIMAP is aimed at preserving the smaller-scale plasma and magnetic field inhomogeneities dragged by the solar wind, as these features ultimately influence the propagation of solar transients and disturbances (see e.g. He et al., 2011; Temmer and Nitta, 2015; Vršnak et al., 2013).

The following subsections describe how the mapping of in situ measurements takes place to build the internal boundary, how this is then propagated by solving the MHD equations through the MHD PLUTO code (Mignone et al., 2007, 2012), and how the RIMAP technique has been applied to measurements taken at 1 AU by Wind during two solar minima, March 2009 and January 2018.

### 2.2.1 Inverse mapping of the inner boundary

As discussed in section 1.4, Parker (1958) predicted the existence of the solar wind, by assuming that the governing forces involved in the coronal expansion are only the pressure gradient and gravitation. Including solar rotation and magnetic forces, considering the applicability of the frozen-in Alfvén theorem, and assuming that the thermal pressure dominates the magnetic one, the magnetic field follows a path which is a velocity streamline in a frame corotating with the Sun defined by equation (1.31). The Parker model predicts that, for distances greater than a certain critical radius, the wind speed is almost constant. Equation (1.31) can thus be integrated to give equation (1.32), which defines the interplanetary Parker spiral. The Weber and Davis (1967) model expands these findings, dealing with the magnetic field. These classical models of solar wind theory are the backbone of RIMAP ballistic mapping of in situ measurements.

The solar wind plasma measured at some distance  $r_{sp}$  by a spacecraft arrived there by propagating almost radially and forming the field lines of the spiral. Assuming a certain stationarity for the overall plasma flow, thus neglecting impulsive solar disturbances, turbulence, resistive effects, and interactions between adjacent flow tubes, it is possible to trace back the spiraling paths followed by the plasma flow lines. Currently, in RIMAP is not possible to automatically separate signatures of transients phenomena from the steady background wind on the measured time-series, hence the model also back-project transients as steady features and then propagate them forward with MHD simulation. To limit the possible consequence of this effect, the simulation presented in the first two implementations of RIMAP have been restricted to periods of solar activity minima. Within these assumptions, it is

possible to reconstruct in the inner heliosphere a map of the solar wind and magnetic field parameters distribution that led to the profiles acquired by the spacecraft.

To this end, the paths traced by Parker (1958) and Weber and Davis (1967) are followed, assuming that longitudinal invariance hold for each  $i$ -th flow tube, and considering the section of these centred around the longitudinal positions  $\varphi_i$  recorded by the spacecraft in the Heliocentric Inertial (HCI) frame of reference. Since for  $r \gg r_c, r_A$  (the critical radius and the Alfvén radius defined in (1.27) and (1.46)), both the solar gravity and the magnetic field are too tenuous to influence plasma motion, and its speed remains constant. Typical values for the Parker and Alfvén critical radii may vary depending on solar temperatures and coronal fields strength, but they are always estimated way below 20 solar radii. Therefore, the reconstruction can be safely extended backwards to some distance  $r_{ib}$ , considering within this domain (at least in the ecliptic plane) constant radial speed in each streamline:

$$v_i(r) \equiv v_i(r_{sp}) = v_i \quad \forall r \in [r_e; \infty[ \quad (2.1)$$

and since the latitudinal and longitudinal components are negligible compared to the radial one in the steady regime, it is possible to consider  $v_r$  the only non-zero speed.

The in situ measurements acquired by a spacecraft along its orbit can be thought as a ring of  $N$  cells, each marked with a label  $\varphi_i$ , that contain the corresponding values for the plasma parameters and the magnetic field. Since the longitudinal profiles of this ring of radius  $r_{sp}$  are known, those of the inner rings remain to be determined back to the radius  $r_{ib}$ . This is easily achieved by inverting the Parker spiral equation (1.32) for each cell  $(r_{sp}; \varphi_i)$ , so as to obtain their respective cells of origin  $(r_{ib}; \varphi'_i)$ , where

$$\varphi'_i = \varphi + \frac{\Omega_\odot}{v_i} (r_{sp} - r_{ib}) \quad (2.2)$$

as depicted in figure 2.4. Since the back-traced footpoints given by equation (2.2) will not be evenly spaced, a linear interpolation is carried out in order to match the corresponding values to the longitudinal computational grid. Notice that equation (2.2) is strictly valid only in the ecliptic plane, and for spacecraft that orbit the Sun with negligible eccentricity such as ACE, Wind and STEREO-A. A relaxation of these constrains is discussed in chapter 4, where measurements from Parker Solar Probe are used as input data.

The radial speed is assumed to be constant, therefore the values for plasma densities are directly obtained from the continuity equation

$$n'_i = n_i \left( \frac{r_{sp}}{r_{ib}} \right)^2 \quad (2.3)$$

and pressure  $p'_i$  is prescribed from the inner density using an adiabatic equation of state (1.17). In RIMAP, the temperature is a free parameter, so different scaling can be chosen. Further details would be given in the following sections and in chapter 4.

The radial and the longitudinal components are scaled according to equations (1.37) and (1.41) for the equatorial magnetized wind, as

$$B'_{r,i} = B_{r,i} \left( \frac{r_{sp}}{r_{ib}} \right)^2 \quad (2.4a)$$

$$B'_{\varphi,i} = B_{r,i} \left( \frac{v'_{\varphi,i} - \Omega_\odot r_{ib}}{v_i} \right) \quad (2.4b)$$

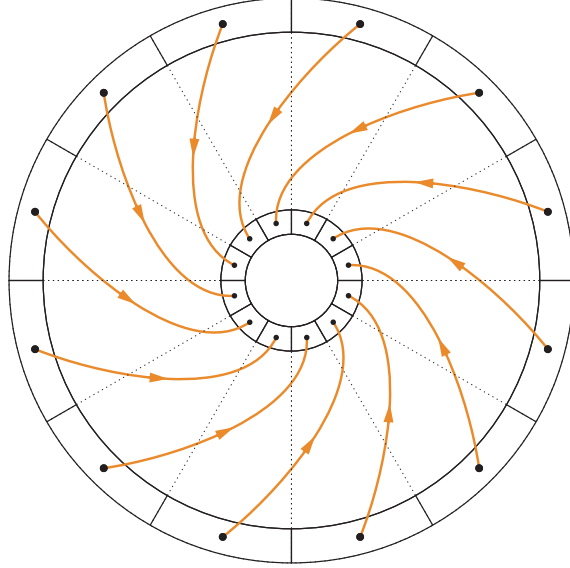


Figure 2.4: Cells of the outer ring are mapped into cells of the inner ring according to equation (2.2). It may be necessary to interpolate between the mapped  $\varphi'_i$  and the equidistant  $\varphi_j^{\text{ib}}$  of the computational grid to have cell-centred values. Then, the quantities  $q'_i$  at the inner cells are scaled according to the theoretical models.

However, according the Weber and Davis (1967) model, for  $r$  much greater than the Alfvén critical radius the longitudinal speed  $v_\varphi$  decreases as  $1/r$ , since the magnetic field is not intense enough to make the solar wind co-rotate. Therefore, at 1 AU the longitudinal component of the magnetic field should already be

$$B'_{\varphi,i} \approx -B'_{r,i} \frac{\Omega_\odot r_{sp}}{v_i} \quad (2.5)$$

while at the Alfvénic radius there must be co-rotation ( $v'_{\varphi,i}(r_A) = \Omega_\odot r_A$ ) and a purely radial field  $B'_{\varphi,i} = 0$ . In the theoretical model there is no longitudinal variability, so the Alfvén radius is the same for each streamline. Here, instead, there are different values of radial field and density at each  $\varphi_i$ , and therefore different Alfvén velocities  $v_{A,i}$  and Alfvén radii  $r_{A,i}$  should be defined. To avoid this, and to use the in situ measured longitudinal component, the following formulation of  $B_{\varphi,i}(r_{ib})$  was chosen,

$$B'_{\varphi,i} = B_{\varphi,i} \left( \frac{r_{sp}}{r_{ib}} \right) + B_{r,i} \frac{\Omega_\odot}{v_i} \left[ (r_{sp} - r_b) - (r_{ib} - r_b) \left( \frac{r_{ib}}{r_{sp}} \right)^2 \right] \quad (2.6)$$

where  $r_b = 2.5 R_\odot$  is the radius of the source surface at which  $B_\varphi = 0$ . Although in the real Sun this transition between corotation and non-corotation does occur, it is way more smooth and progressive than the that of the above description, and so is the generation of a rotation-induced latitudinal magnetic field. Nevertheless, the Weber and Davis (ibid.) approach capture the large-scale main features of the magnetized Parker spiral. For simplicity reasons and consistency with the Weber and Davis (ibid.) model, the latitudinal component  $B_\theta$  is set to zero in the internal boundary, in order to not having to deal with the complete and still mostly unknown three-dimensional behaviour of the heliospheric magnetic field. This choice clearly has consequence on the output magnetic fields, as discussed in section 2.3.3.

This is the general roadmap followed by RIMAP in the building of the internal boundary of the MHD model, using a ballistic mapping. However, before proceeding

to the description of the numerical methods used in the solution of the MHD equations, the problem of crossings between solar wind streams must be addressed. As described by equation (1.32), the curvature of an arm of the spiral constituting a streamline is inversely proportional to the speed of its flow. Because of this, two flows departed from  $(r; \varphi_i)$  and  $(r; \varphi_j)$  with speed  $v_i$  and  $v_j \neq v_i$  will necessarily cross at  $(R_X; \varphi_X)$ , where the radius  $R_X$  is

$$R_X = r + \frac{v_i v_j}{\Omega_\odot} \left( \frac{\varphi_j - \varphi_i}{v_j - v_i} \right) \quad (2.7)$$

as already described by equation (1.36b). Figure 2.5 shows a typical case of two streamlines crossing each other.

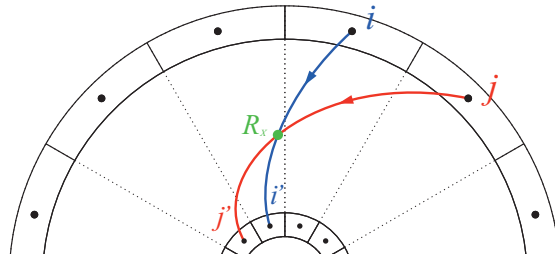


Figure 2.5: Having two different values of speed that do not satisfy condition given by eq. (2.8), the streamlines of cells  $i$  and  $j$  cross at  $(R_X; \varphi_X)$  before being mapped in  $i'$  and  $j'$ . One of them must be discarded, then the azimuthal profiles are refilled by interpolating the adjacent non-crossing streams.

In the actual forward propagation, this is the basis for the formation of corotating interaction regions, solar wind compression and decompression regions in the Parker spiral caused by the fast streams impacting on the slower ones. It is clear that, after having interacted, the two streams will have different properties than those of departure. However, it would be unrealistic to trace back the arms of the spiral if they intersect within the computational domain. In RIMAP, what is done is to calculate the crossing radius  $R_X^{(i,j)}$  for each pair of plasma measurements  $(i, j)$ . Then, if the condition

$$r_{ib} \leq R_X^{(i,j)} < r_{sp} \quad (2.8)$$

holds true, the data relative to the wind streamline with the lowest speed is discarded, being the one that most likely would cross other streamlines. The resulting "emptied" cells of the inner boundary are then filled by interpolating between adjacent non-crossing data point, until no pair satisfies condition (2.8). In principle, the opposite selection criterion (i.e. to remove among the crossing streamlines the one with the highest speed) would also be acceptable. Nevertheless, we decided to keep the information about the high-speed streams because these are more of interest for the possible space weather effects when impacting on planetary magnetospheres. Moreover, this criterion allows to keep the information about any possible transient phenomenon propagating faster than the background solar wind speed. The number of removed streamlines clearly varies depending on the specific configuration analyzed. Periods associated with solar activity minima generally have more uniform radial velocity profiles and will be subject to fewer removals (about 5 to 10% of total streamlines). On the other hand, solar maxima and periods containing eruptive events present more complex configurations, with a much greater number of possible crossings

(and consequently even 40% of the cells may have to be removed). Finally the inner boundary under the stationary condition of the ambient solar wind parameters is ready to be used for forward MHD simulations.

### 2.2.2 PLUTO code

First presented in 2007 and updated with the addition of adaptive grids in 2012, PLUTO (Mignone et al., 2007, 2012) is a finite-difference, finite-volume, shock-capturing numerical code designed to simulate astrophysical plasma. It is written almost entirely in C language, with the exception of the CHOMBO library used for adaptive mesh refinement, written in C++ and Fortran. PLUTO is based on an implementation of high resolution shock-capturing (HRSC) algorithms, consisting of a conservative formulation of the fluid equations, whose proper discretization requires an approximate solution to the associated Riemann problem. They date back to the works of Sergei Godunov (Godunov and Bohachevsky, 1959). HRSC schemes are based on the reconstruct-solve-average approach: first, volume averages are reconstructed using monotonic interpolants inside each cell of the computational grid; then a Riemann problem is solved at each interface with discontinuous left and right states; finally the solution is let evolve in time (LeVeque et al., 1998; Roe, 1986; Toro, 2009).

PLUTO solves a general system of conservation laws written as:

$$\frac{\partial \mathbf{U}}{\partial t} + \nabla \cdot \mathbf{T}_h = \nabla \cdot \mathbf{T}_p + \mathbf{S}(\mathbf{U}) \quad (2.9)$$

where  $\mathbf{U}$  is a set of conservative quantities (such as energy, density, momentum...),  $\mathbf{T}_h(\mathbf{U})$  and  $\mathbf{T}_p(\mathbf{U})$  are the hyperbolic and parabolic flux tensors while  $\mathbf{S}(\mathbf{U})$  represents the source terms. Flow quantities are discretized on a logically rectangular grid enclosed by boundaries and expanded with ghost cells in order to assign boundary condition. The explicit form of the (2.9) terms depends on the particular physics module, chosen from

- *HD*, classical hydrodynamics;
- *MHD*, magnetohydrodynamics (ideal and resistive);
- *RHD*, special relativistic hydrodynamics;
- *RMHD*, special relativistic ideal MHD;

and also on the geometry selected for the problem, which can be

- *cartesian*,  $\{x_1, x_2, x_3\} = \{x, y, z\}$ ;
- *cylindrical*,  $\{x_1, x_2\} = \{R, z\}$  (only for a 1 or 2 dimensions);
- *polar*,  $\{x_1, x_2, x_3\} = \{r, \varphi, z\}$ ;
- *spherical*,  $\{x_1, x_2, x_3\} = \{r, \theta, \varphi\}$ .

For reasons of computational convenience, intermediate computations are done using primitive variables  $\mathbf{V}(\mathbf{U})$  (e.g. velocity and pressure) instead of conservative variables  $\mathbf{U}$ . This simplifies the process of maintaining some physical constraints, such as positive pressure and subluminal speed, especially useful in the RHD and RMHD

modules. After the  $\mathbf{U} \rightarrow \mathbf{V}(\mathbf{U})$  conversion, the next step is reconstruction: from the primitive quantities defined at the cells center, the respective left  $\mathbf{V}_{i+\frac{1}{2}L}$  and right  $\mathbf{V}_{i-\frac{1}{2}R}$  states inside each cell are computed adopting suitable interpolation and/or extrapolation. This reconstruction must obey some constraints (such as monotonicity) to avoid oscillations approaching discontinuities. Then a Riemann problem is solved between left and right states to compute, at the cell interfaces, the numerical flux function  $\mathbf{F}_{i\pm\frac{1}{2}} = \mathcal{R}(\mathbf{V}_{i+\frac{1}{2}L}, \mathbf{V}_{i-\frac{1}{2}R})$ .  $\mathcal{R}$  denotes the chosen approximate Riemann solver, i.e. the specific numerical method employed to calculate the solution of the initial value problem defined in each cell. Different physical modules allow different sets of Riemann solvers, each with different levels of accuracy inversely proportional to their numerical diffusivity and, under some circumstances such as low density plasmas and high Mach numbers, to their code robustness. For magnetohydrodynamics, the Roe's linearized solver is one of the most popular methods (Musa et al., 2020), given its high numerical accuracy (Toro, 2009) and despite its computational cost (in comparison, for instance, to the less accurate but lighter solvers based on the work of Harten et al. (1983)). The last step is the temporal evolution, which goes back to the conservative quantities  $\mathbf{U}$ . Among the different time solvers provided by PLUTO, the 2<sup>nd</sup> order Runge-Kutta scheme was used:

$$\mathbf{U}^* = \mathbf{U}^n + \Delta t \mathcal{L}^n \quad (2.10a)$$

$$\mathbf{U}^{n+1} = \frac{1}{2} [\mathbf{U}^n + \mathbf{U}^* + \Delta t \mathcal{L}^*] \quad (2.10b)$$

where  $\Delta t$  is the time step, whose size is limited by the Courant-Friedrichs-Lewy condition (Courant et al., 1928)

$$\Delta t = \text{CFL} \left( \max_{ijk} \frac{1}{N_d} \sum_d \frac{|\lambda_d|_{i,j,k}}{\Delta x_{d,i,j,k}} \right)^{-1} \quad (2.11)$$

with  $\lambda_d$  is the largest characteristic velocity of the system in direction  $d$ ,  $\Delta x_d$  the spacing of grid  $d$ ,  $N_D$  the number of spatial dimensions and where CFL ( $\lesssim 1/N_D$ ) depends on the selected time stepping method.  $\mathcal{L}$  is the discretized spatial operator on the right-hand side of equation (2.9), defined (when  $N_d = 1$ , but its extension in 2D or 3D is straightforward) by

$$\mathcal{L}_i = -\frac{1}{\Delta x} \left( \mathbf{F}_{i+\frac{1}{2}} - \mathbf{F}_{i-\frac{1}{2}} \right) + \mathbf{S}_i \quad (2.12)$$

where  $\Delta x$  denotes the mesh spacing. This sequence of steps provides the general framework under which the code was developed.

The physical solution of the MHD equations must always satisfy the solenoidal constraint (1.1b). However, numerical methods do not automatically preserve this condition: non-solenoidal components may be generated during the computed evolution causing unphysical plasma behaviours, the most noticeable of which is plasma acceleration along the field lines. This can be avoided by specific discretization techniques. PLUTO implements three of these strategies: the eight waves (Powell, 1997; Powell et al., 1999) formulation, where the magnetic field retain a cell-centered representation (see figure 2.6) and an additional source term is added to the (1.18) equations; the constrained transport (Balsara and Spicer, 1999; Gardiner and Stone, 2005) method, where the two sets of field are used, one with a staggered collocation and the other cell-centered, and where (1.1b) is directly integrated with Stokes

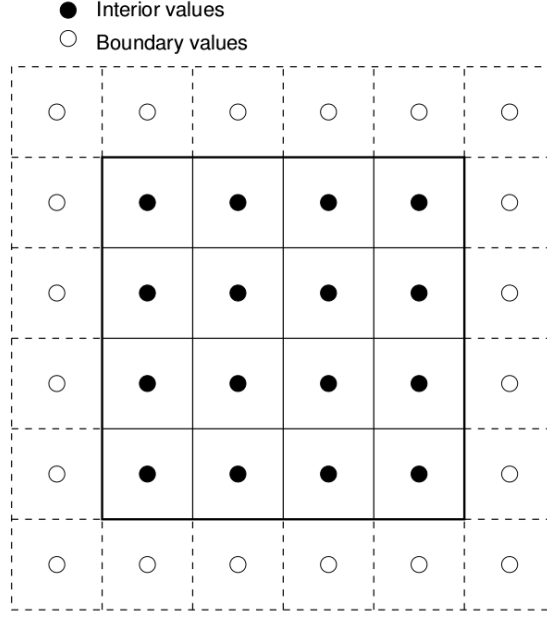


Figure 2.6: Representation of cell-centered collocation of physical variables inside a 2D grid. Filled symbols represents domain values part of the solution, empty symbols stands for the boundary values.

Source: Mignone et al. (2018), PLUTO User’s Guide, <http://plutocode.ph.unito.it>.

theorem; the hyperbolic/parabolic divergence cleaning (Dedner et al., 2002; Mignone et al., 2010) method, used for the simulations of this thesis and explained below, in which the field retains a cell-centered representation as in the eight waves formulation, but the constraint is enforced by solving a new set of conservation equations,

$$\frac{\partial \mathbf{B}}{\partial t} + \nabla \times (c\mathbf{E}) + \nabla \psi = 0 \quad (2.13a)$$

$$\frac{\partial \psi}{\partial t} + c_h^2 \nabla \cdot \mathbf{B} = - \left( \frac{c_h}{c_p} \right)^2 \psi \quad (2.13b)$$

where a generalized lagrangian multiplier  $\psi$  is introduced. In equations (2.13),

$$c_h = \text{CFL} \cdot \frac{\Delta l_{\min}}{\Delta t^n} \quad (2.14)$$

is the maximum speed compatible within the step size,  $\Delta l_{\min}$  is the minimum cell length,

$$c_p = \sqrt{\frac{\Delta l_{\min} c_h}{\alpha}} \quad (2.15)$$

and  $\alpha$  is a free parameter that controls the dampening rate of the monopole. Its value is user-defined, while the optimal range lies between 0.05 and 0.3. In this formulation, divergence errors are propagated towards the boundaries with  $c_h$  speed and they decay with time and distance, avoiding accumulation. The  $\psi$  scalar field is by default initialized and set to zero in the boundaries, but even this can be changed by the user. Main advantages of divergence cleaning are the absence of additional source terms in the MHD equations (so that they retain a conservative form), the cell-centered representation for all variables (including  $\mathbf{B}$ ), and the possibility of

using standard Riemann solvers. The divergence cleaning is the method used for the simulation performed with RIMAP in this and the following chapters.

Among the conservative and primitive variables that must obey equation (2.9), vectors  $\mathbf{U}$  and  $\mathbf{V}$  respectively include total energy density and pressure. PLUTO allows to chose among different equations of state (EOS) that provide the closure of MHD equations. Some of them are more conveniently written in the thermal form (1.9)

$$p = \frac{\rho}{m_u \mu} k_B T \quad (2.16)$$

of an ideal gas, where  $m_u$  is the atomic mass unit and  $\mu$  is the mean molecular weight, which can be defined by the user. Equations (1.9) and (2.16) are written in cgs units, but can be conveniently expressed as

$$p_{code} = \frac{\rho_{code} T}{\mathcal{K} \mu} \Leftrightarrow T = \frac{p_{code}}{\rho_{code}} \mathcal{K} \mu \quad (2.17)$$

where  $p_{code}$  and  $\rho_{code}$  are in code units,  $T$  is in Kelvin and

$$\mathcal{K} = \frac{m_u v_0^2}{k_B} \quad (2.18)$$

is a conversion factor, depending on the value  $v_0$  of the unit velocity chosen.

The other fundamental quantity for determining the state of a plasma is the specific internal energy  $\varepsilon$ , which obeys the 1<sup>st</sup> principle of thermodynamics

$$d\varepsilon = dQ - p d\left(\frac{1}{\rho}\right) \quad (2.19)$$

where  $Q$  is the exchanged heat. The internal energy is a state function and can be expressed with temperature and pressure, obtaining the caloric form of the equation (2.16):

$$\varepsilon = \varepsilon(T, \rho). \quad (2.20)$$

The isothermal EOS, already met as equation (1.25), is implemented by PLUTO in the thermal form

$$p = c_s^2 \rho$$

while the EOS used for simulations of the next chapter, the ideal equation of state, is written in the caloric form (1.10). The default value of specific heats ratio is  $\gamma = \frac{5}{3}$  but it can be modified by the user. The ideal EOS is compatible with all physical modules, geometries, algorithms and Riemann solvers in the PLUTO code.

The physical domain of the simulation and its computational mesh are user-definable in dimensions, extensions and numbers of points. One can also choose to generate uniform grid patches, where

$$\Delta x = \frac{x_R - x_L}{N} \quad (2.21)$$

with  $N$  as the number of point in the stretched grid, and  $x_L$  and  $x_R$  the leftmost and rightmost point of the patch, or non uniform ones, such as a stretched grid or a logarithmic one. In these two, the mesh size can increase or decrease with the coordinates. The first can be used if at least one uniform grid is present, and its stretching ratio  $r$  is computed as

$$\Delta x = \frac{x_R - x_L}{\sum_{i=1}^N r^i} \Rightarrow r \frac{1 - r^N}{1 - r} = \frac{x_R - x_L}{\Delta x} \quad (2.22)$$

where  $\Delta x$  is taken from the closest uniform grid. The second one can have increasing or decreasing mesh size:

$$\begin{aligned} \Delta x_i &= \left( x_{i-\frac{1}{2}} + |x_L| - x_L \right) (10^{\Delta\xi} - 1), \quad \Delta\xi = \frac{1}{N} \log_{10} \left( \frac{x_R + |x_L| - x_L}{|x_L|} \right) \\ \Delta x_i &= \left( x_{i-\frac{1}{2}} - |x_L| - x_R \right) (10^{\Delta\xi} - 1), \quad \Delta\xi = -\frac{1}{N} \log_{10} \left( \frac{x_R + |x_L| - x_L}{|x_L|} \right) \end{aligned} \quad (2.23)$$

This is particularly useful in polar or spherical geometry, where a radial logarithmic grid preserves the cell aspect ratio at any distance from  $r = 0$ . To obtain approximately squared cells (i.e. with an aspect ratio of  $\sim 1$ ) the condition is

$$\Delta r = r \Delta\varphi, \quad \text{where } \Delta r = r_L \left( \left( \frac{r_R}{r_L} \right)^{\frac{1}{N_r}} - 1 \right). \quad (2.24)$$

This condition can be used to determine the radial number of points from the longitudinal spacing or viceversa:

$$\log \left( \frac{r_R}{r_L} \right) = N_r \log \left( \frac{2 + \Delta\varphi}{2 - \Delta\varphi} \right). \quad (2.25)$$

Once the values of number of points (NX1, NX2 and NX3) in the  $x_1$ ,  $x_2$ ,  $x_3$  coordinates have been chosen and the grid has been generated, the calculations are performed on a domain ranging from  $\text{IBEG} \leq i \leq \text{IEND}$ , with  $\text{IEND} - \text{IBEG} + 1 = \text{NX1}$  and similarly for the other dimensions. In fact, as it can be seen in figures 2.6 and 2.7, ghost cells are added outside the computational domain to implement boundary conditions.

PLUTO provides several default conditions for the scalar quantities  $q$ , the  $\mathbf{v}$  and the  $\mathbf{B}$  fields at each boundary. Denoting with  $n$  and  $t$  the normal and tangent to the boundary plane directions:

- *outflow*

Zero gradient across the boundary

$$\frac{\partial q}{\partial n} = 0, \quad \frac{\partial \mathbf{v}}{\partial n} = 0, \quad \frac{\partial \mathbf{B}}{\partial n} = 0; \quad (2.26)$$

- *reflective*

Boundaries behave like rigid walls: variables are symmetrized across the boundary while vectors' normal components flip signs

$$q \rightarrow q, \quad \begin{cases} v_n \rightarrow -v_n \\ B_n \rightarrow -B_n \end{cases}, \quad \begin{cases} \mathbf{v}_t \rightarrow \mathbf{v}_t \\ \mathbf{B}_t \rightarrow \mathbf{B}_t \end{cases}; \quad (2.27)$$

- *axis symmetric*

Same as reflective conditions, except for sign change even in the longitudinal component  $\varphi$  of vectors

$$q \rightarrow q, \quad \begin{cases} v_n \rightarrow -v_n \\ B_n \rightarrow -B_n \end{cases}, \quad \begin{cases} v_\varphi \rightarrow -v_\varphi \\ B_\varphi \rightarrow -B_\varphi \end{cases}, \quad \begin{cases} v_{axis} \rightarrow v_{axis} \\ B_{axis} \rightarrow B_{axis} \end{cases}; \quad (2.28)$$

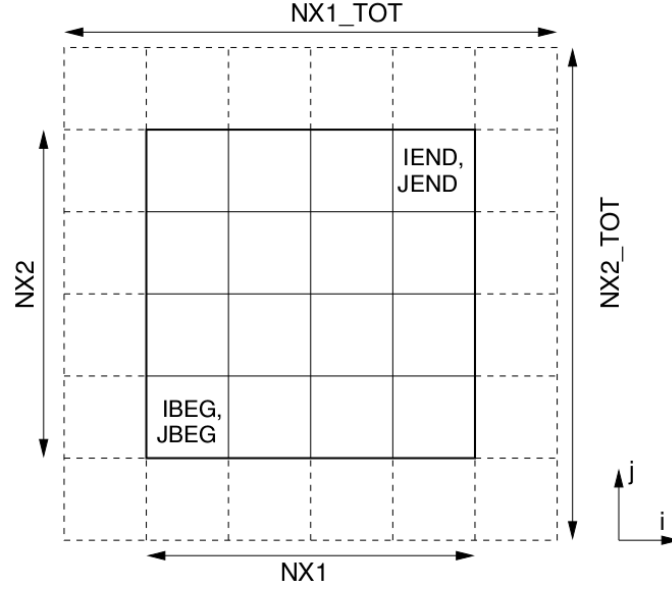


Figure 2.7: Two-dimensional grid with  $NX1=NX2=4$  and 1 ghost zone. The  $i$  and  $j$  indices span internal zones (solid boxes) from  $I,JBEG$  to  $I,JEND$ , while the ghost cells are filled with the boundary conditions.

Source: Mignone et al. (2018), PLUTO User's Guide, <http://plutocode.ph.unito.it>.

- *equatorial symmetric*

Equatorial symmetry with respect to a plane. Similar to reflective

$$q \rightarrow q, \quad \left\{ \begin{array}{l} v_n \rightarrow -v_n \\ B_n \rightarrow B_n \end{array} \right\}, \quad \left\{ \begin{array}{l} \mathbf{v}_t \rightarrow \mathbf{v}_t \\ \mathbf{B}_t \rightarrow -\mathbf{B}_t \end{array} \right\}; \quad (2.29)$$

- *periodic*

All variables are periodic on both sides of the computational domain.

Furthermore, PLUTO has a specific function used to prescribe user-defined boundary conditions at a selected physical boundary. This feature allows the user to directly access the individual ghost cells of the arrays  $(i, j, k)$  constituting the boundaries, assigning them the desired values. The *userdef* option has been used extensively in the internal radial boundary of data-driven simulations in Chapter 2, Chapter 3, and Chapter 4.

Selecting the MHD module with no resistivity ( $\eta=0$ ), the presence of a gravitational potential, and a rotating frame of reference, the system of conservation laws (2.9) become

$$\begin{aligned} \frac{\partial \rho}{\partial t} + \nabla \cdot (\rho \mathbf{v}) &= 0 \\ \frac{\partial (\rho \mathbf{v})}{\partial t} + \nabla \cdot \left[ \rho \mathbf{v} \mathbf{v} - \mathbf{B} \mathbf{B} + \mathbb{1} \left( p + \frac{B^2}{2} \right) \right] &= \mathbf{F}_{\text{cor}} - \rho \nabla \Phi \\ \frac{\partial \mathcal{E}_{\text{tot}}}{\partial t} + \nabla \cdot \left[ (\mathcal{E}_{\text{tot}} + p + \frac{B^2}{2} + \rho \Phi) \mathbf{v} - \mathbf{B} (\mathbf{v} \cdot \mathbf{B}) \right] &= \mathbf{v} \cdot \mathbf{F}_{\text{cor}} \\ \frac{\partial \mathbf{B}}{\partial t} - \nabla \times (\mathbf{v} \times \mathbf{B}) &= 0 \end{aligned} \quad (2.30)$$

which is the set of ideal MHD equations (1.20) with additional source terms. Note that a factor of  $\sqrt{4\pi}$  has been reabsorbed in the definition of the magnetic field vector  $\mathbf{B}$ . In equation (2.30),

$$\mathcal{E}_{\text{tot}} = \frac{p}{\gamma - 1} + \frac{1}{2}\rho\mathbf{v}^2 + \frac{B^2}{2} \quad (2.31)$$

is the total energy density for a plasma obeying the ideal gas law, with  $\gamma = 5/3$  being the specific heat ratio chosen.

The solar gravitational potential  $\Phi$  is expressed as

$$\Phi = -\frac{GM_{\odot}}{|\mathbf{r}|} \quad (2.32)$$

with  $\mathbf{r}$  being the position vector with origin on the center of the Sun.

The force  $\mathbf{F}_{\text{cor}}$  can be identified with the Coriolis force due to the solar rotation in the corotating frame of reference:

$$\mathbf{F}_{\text{cor}} = -\rho[2\boldsymbol{\Omega} \times \mathbf{v} + \boldsymbol{\Omega} \times (\boldsymbol{\Omega} \times \mathbf{r})] \quad (2.33)$$

where  $\boldsymbol{\Omega} = \Omega_{\odot} \cos(\theta)\hat{\mathbf{r}} - \sin(\theta)\hat{\boldsymbol{\theta}}$ .

Considering a typical population of solar wind particles, a value of  $\mu = 0.67$  is assumed for the mean molecular weight.

For the purposes of the work here presented, the most convenient geometry is the spherical one, identifying  $(r, \theta, \varphi)$  with the corresponding coordinates in heliocentric systems of reference.

The RIMAP setup usually employs 2<sup>nd</sup>-order Runge-Kutta time stepping, linear reconstruction in primitive variables and the Roe's approximate Riemann solver. A value of 0.3 is chosen for the CFL number to use in the condition (2.11). In some configurations, due to the noisy characterization of the in situ measurements used, the relaxation to a steady state can require more diffusive numerical treatments. In those cases, the approximate Riemann solver method can be changed, for instance from Roe to a Harten-Lax-van Leer (HLL; Harten et al., 1983) scheme. Moreover, a set of flux limiters to be applied to the linear reconstruction is available, of which the most diffusive is the Minmod limiter (Roe, 1986).

The RIMAP approach solves the full time-dependent MHD equations in three dimensions and, as such, it is not limited to the restrictions imposed by the one-dimensional upwind method of Riley et al. (2011), which instead seeks for stationary solutions neglecting pressure gradient, gravity terms, and magnetic fields.

## 2.3 Using RIMAP with measurements acquired at 1 AU

We discuss here the reconstruction of the ambient Parker spiral condition in correspondence of two solar minima configurations: March 2009 and January 2018. These reconstructions are carried-out starting from in situ measurements collected at the Lagrangian point L1, at 0.99 AU, using them to build via the ballistic technique discussed in the previous section.

Due to its proximity, L1 is a privileged site of observation for the solar wind that impact Earth's magnetosphere. Currently, L1 host four operational spacecraft

dedicated to the investigation of the solar plasma: the Deep Space Climate Observatory (DSCOVR; Burt and Smith, 2012), ACE, SOHO, and the Wind probe. In the following, the application of RIMAP to in situ measurements collected by the latter is described.

### 2.3.1 Preparing Wind data

During its heliocentric orbit at L1, the Wind spacecraft acquires measurements of plasma density and speed, and magnetic field at regular intervals. The solar wind plasma is sampled through the Faraday cups of SWE, while the magnetic field components are registered by the magnetometers of MFI suite (see section 1.6.1 for a description of the Wind spacecraft and its relevant instruments).

For the purposes of the application here described, a simple conversion is carried out on the time intervals  $t$  of data acquisition, transforming them into longitudinal positions  $\varphi$  in a chosen heliocentric coordinate system. The conversion uses the solar equatorial synodic period of

$$\mathbb{T}_{\odot} = 26.5 \text{ days}, \quad (2.34)$$

obtained by averaging the estimates of equatorial sidereal speed provided by Snodgrass and Ulrich (1990, 14.71°/day) and Wöhl et al. (2010, 14.499°/day), using thus a value of 14.6°/day. In this way, the temporal profiles of the plasma and magnetic field quantities  $q(t)$  are transformed into longitudinal profiles  $q(\varphi)$ .

The selected reference system in this application is the Heliocentric Earth Ecliptic (HEE) system, in which the  $x$ -axis coincides with the Sun-Earth line, the  $z$ -axis is perpendicular to the ecliptic plane, and the  $y$ -axis completes the triad. Another possible choice could be the Heliocentric Earth Equatorial (HEEQ) system, in which the  $x$ -axis is perpendicular to the intersection of the solar equator and the solar central meridian as seen from Earth, while the  $z$ -axis is the solar rotational axis. Another valid frame of reference is the Heliocentric Inertial (HCI), in which the origin is centred on the Sun, the  $z$ -axis is aligned with the Sun's north pole, and the  $x$ -axis (0° longitude and 90° colatitude) is aligned with the solar ascending node on the ecliptic. The choice fell on the first because of its greater immediacy in converting the measurements taken by Wind into data usable in the reconstruction of the spiral.

The 0.99 AU data for the different selected periods were normalized as arrays  $\{q_i\}$  of 361 elements, converted to the *cgs* units system, and tabulated as

$\varphi_i$ [rad]	$n_i$ [cm <sup>-3</sup> ]	$v_{xi}$ [cm/s]	$v_{yi}$ [cm/s]	$v_{zi}$ [cm/s]	$B_{xi}$ [G]	$B_{yi}$ [G]	$B_{zi}$ [G]
-------------------	---------------------------	-----------------	-----------------	-----------------	--------------	--------------	--------------

After normalization to code units, these longitudinal profiles are ready to be mapped to the inner radial boundary of the simulation, as discussed in section 2.2.1, following the assumptions on the conservation laws, and eliminating the pair of intersecting streamlines. The new reconstructed profiles are made periodic to facilitate the subsequent interpolation between them and the grid of the internal radial boundary of RIMAP, thus making each data point to fall at the center of the corresponding ghost cell.

### 2.3.2 Grid Layout and Boundary Conditions

The radial computational grid chosen extends from  $r_{ib} = 21.5R_{\odot}$  ( $\approx 0.1$  AU) to  $236.5 R_{\odot}$  ( $\approx 1.1$  AU), with 384 uniformly spaced cells.

Due to the previously mentioned lack of information outside of the ecliptic plane, the latitudinal aperture is restricted to  $2^\circ$  centred around the the colatitude of  $90^\circ$ . The number of cells in this direction is 9: an odd number was chosen in order to have a set of cells centred on the ecliptic plane. The spacing is also uniform.

The longitudinal grid covers the entire interval. The number of cells is chosen to be four times that of the radial direction, 1536, with uniform spacing. This is done to obtain approximately squared cells in the central region of the domain, around  $r = 108 R_\odot$ .

The boundary conditions are prescribed as follows. At the inner radial boundary the `userdef` option is set, and the plasma and magnetic field parameters of the Parker spiral are imposed interpolating between the computational longitudinal domain and the  $\{\varphi_i\}$  array. The zero-gradient outflow condition is set at the outer radial boundary, in order to mimic the physical behaviour of the solar wind, in which no back flow is allowed. At the latitudinal extremes reflecting boundary conditions are applied, mirroring the latitudinal components of  $\mathbf{v}$  and  $\mathbf{B}$ , and copying the other quantities into the ghost cells. This reflection guarantees flux conservation of momentum, and the solenoidality of  $\mathbf{B}$ . In the longitudinal direction, instead, the condition of periodicity holds.

The grid and boundaries layout is summarized in table 2.1.

Direction	Interval	Number of cells	Style	Boundary conditions
$r$	$21.5 R_\odot - 236.5 R_\odot$	384	u	userdef-outflow
$\theta$	$89^\circ - 91^\circ$	9	u	reflective-reflective
$\varphi$	$-90^\circ - 90^\circ$	1536	u	outflow-outflow

Table 2.1: Computational grid used for the numerical simulations in this section.

### 2.3.3 Results

A simulation run proceeds as follows. After setting up the PLUTO code as described at the end of section 2.2.2, RIMAP accesses the in situ data files, reading them and storing them in a  $361 \times 8$  elements matrix, where each row represents a point of the 0.99 longitudinal profiles, and each column is a solar wind parameter. Then, the Parker spiral ballistic inverse reconstruction is performed, mapping each  $i - th$  data point back to the internal boundary  $r_{ib} = 0.1$  AU at the corresponding  $\varphi'_i$  defined in (2.2), and applying the conservation laws (2.3), (2.4), and (2.6).

Having built the inner radial boundary, RIMAP sets in motion the apparatus of numerical techniques described in section 2.2.2 to make the input data evolve through the MHD equations. Different configurations have been tested for the initial condition of the computational domain, without finding particular variations either in the final results of the simulations or in the time in which they reach a steady state. In the runs here presented, the initial profiles for density, pressure, and magnetic field were taken from Perrone et al. (2019), while the radial speed is assumed to be 400 km/s in each cell of the computational domain.

At the beginning of the time evolution, each simulation crosses a sequence of transient states, characterized by the natural expansion of the solar wind plasma filling the available volume and ejected at the inner boundary with the parameters provided by the in situ data. In this implementation, ideal MHD conditions are assumed, neglecting turbulence and resistive effects. Albeit the computation rely on

the numerical solution of the ideal MHD equations in the form (2.30), some level of numerical resistivity is inherited from the discretization process. The amount of numerical resistivity, however, does not seem to affect RIMAP results, which are consistently reproduced also for smaller grid sizes.

A stationary state is reached after an initial transient period. In particular, the simulations stop at  $t = 500 t_0 \approx 10$  days (of simulation time), when the system has already reached a steady state (visually determinable when the ecliptic maps, as well as the individual quantity profiles, have stopped time evolution). A scheme summarizing the main steps in the RIMAP pipeline is shown in Figure 2.8. The scheme also includes the final verification (described later on) based on a comparison between the input in situ data at 1 AU and the output plasma parameters from RIMAP. The results from RIMAP simulations using the measurements acquired by Wind are presented in the following sections.

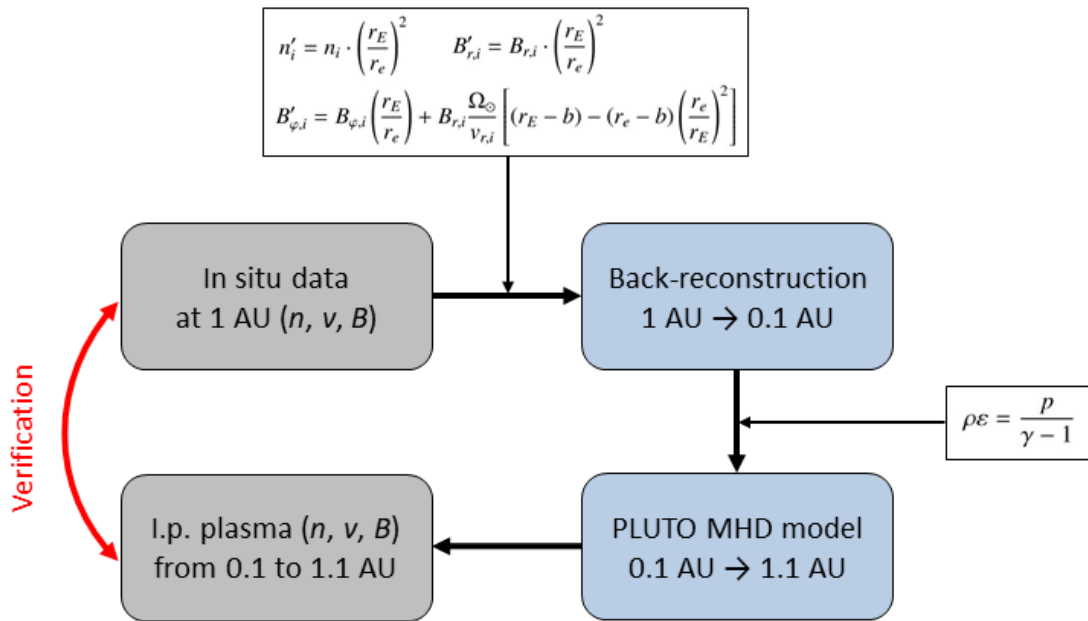


Figure 2.8: A schematic of the steps involved in RIMAP for the reconstruction of heliospheric plasma conditions starting from in situ measurements.

### Solar minimum of March 2009

The input data used in this subsection were collected in 2009 by GGS Wind from the L1 point (at heliocentric distance of  $0.99 \text{ AU} = 212.85 R_{\odot}$ ) between 08:02:09.05 UT of March 3<sup>rd</sup>, and 20:02:09.11 UT of March 29<sup>th</sup>, 2009. This interval corresponds to a total time of about 26.5 days. Due to the conversion described in section 2.3.1, time-direction in the longitudinal comparisons of the following subsections goes from right to left.

Figure 2.9 shows the resulting 2D distributions on the ecliptic plane of plasma density, radial velocity, and radial component of magnetic field. Each of the streamlines is individually discernible, resulting in a high structured ambient Parker spiral. The solar wind conditions are quite calm, with velocities way lower than 600 km/s for all the longitudinal positions and densities at 1 AU around 10 particles per cubic centimeter. The values of magnetic field oscillate around zero with an amplitude

approximately 5 nT. Most of the interplanetary magnetic field shows a positive polarity, with a minor polarity reversal before  $\varphi=90^\circ$  covering almost a quarter of the spiral.

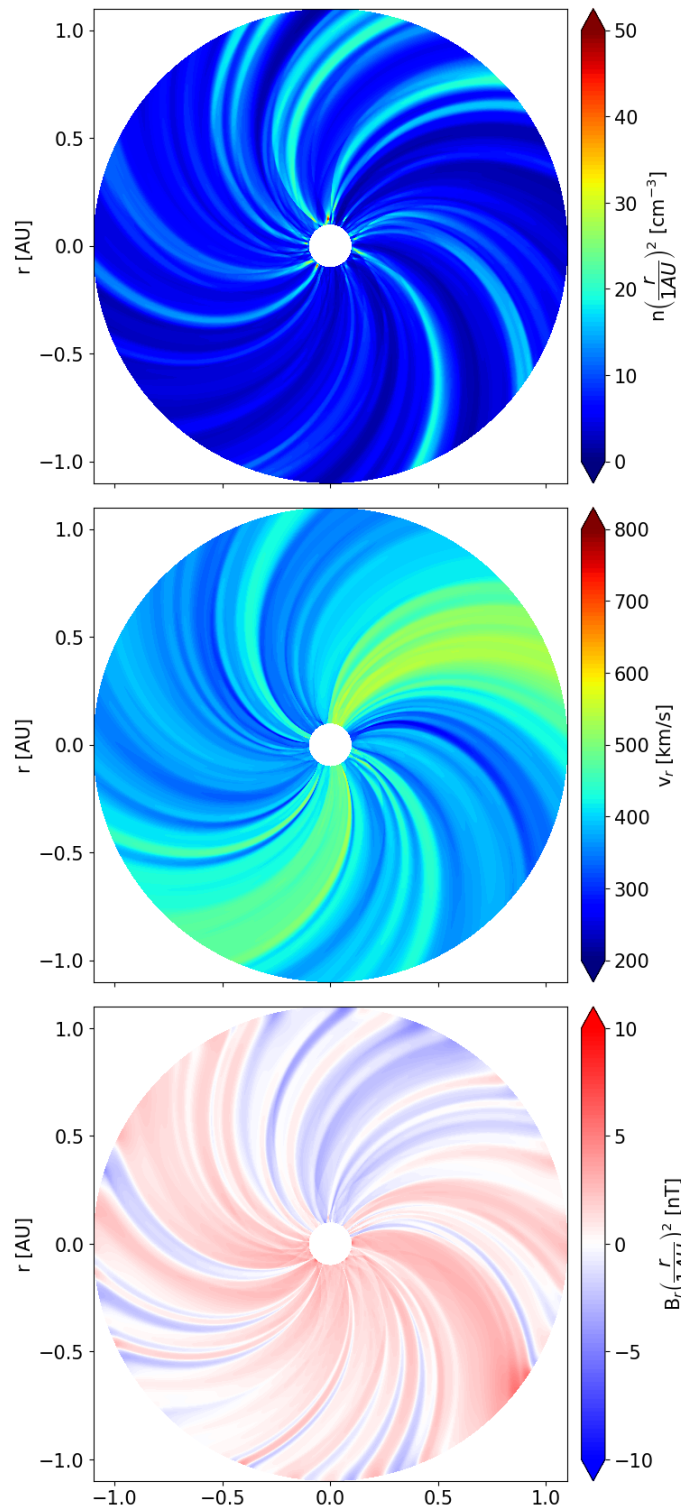


Figure 2.9: Ecliptic maps of the plasma number density (top panel), radial speed (middle panel), and radial magnetic field (bottom panel) obtained with RIMAP from the in situ observations acquired by the Wind spacecraft at 0.99 AU during March 2009.

The first important verification for the model results is the reproduction of the expected physical trends of the quantities as a function of heliocentric distance. By averaging over all longitudes  $\varphi$  we found that the resulting plasma density drops like  $1/r^2$ , as one would expect from simple mass flux conservation. The corresponding averaged radial trend for the flow speed  $v_r$  is shown in figure 2.10. Since a radial gradient of density, and therefore of pressure, is present, following from the continuity equation one should observe a progressive acceleration as the solar wind is blown away, as observed. In any case, at these distances the wind almost reached its final speed, and the variations shown in Figure 7 are small with respect to the average wind speed, in general around  $\sim 10\%$ .

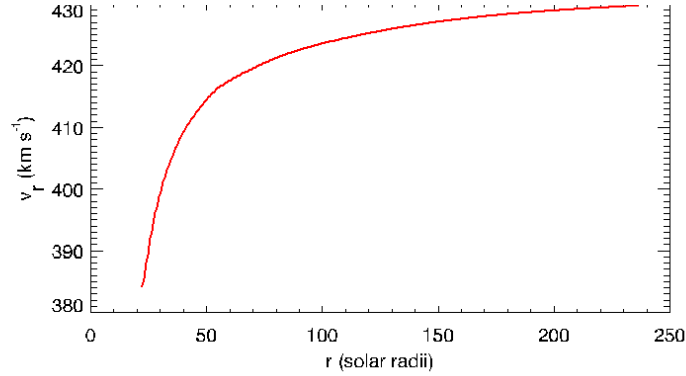


Figure 2.10: The mean trend for the radial speed, as derived by averaging at each altitude over all longitudes; a slight acceleration is still present, mainly due to the thermal pressure gradient.

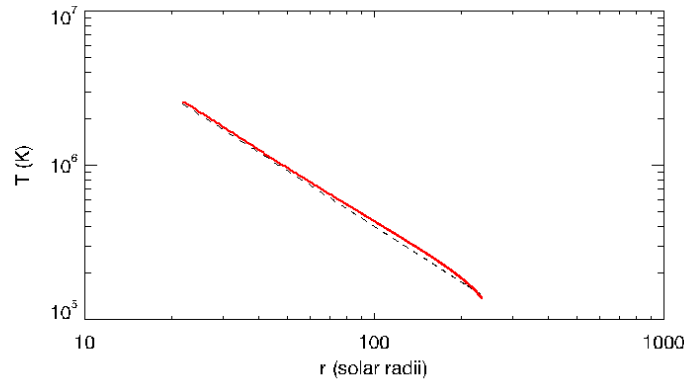


Figure 2.11: In solid red, the mean radial behaviour for the plasma temperature, as derived by averaging at each altitude over all longitudes. Overplotted in dashed black is the reference trend (2.35) of Perrone et al. (2019).

A very interesting parameter is the radial trend of the average plasma (proton) temperature  $T_p$ . Different trends of temperature can be used for the inner boundary: the one that seems to give the best overall agreement with the longitudinal profiles described below is taken from Perrone et al. (2019). In that work, the total proton temperature is estimated to decrease more slowly than the simple adiabatic trend,

$$T_p = (1.9 \pm 0.1) \cdot 10^5 \left( \frac{r}{1 \text{ AU}} \right)^{-(0.9 \pm 0.1)} \text{ K}, \quad (2.35)$$

giving thus at the inner boundary of  $21.5 R_{\odot}$  a value of  $T_p \approx 1.5$  MK. However, the radial trend of temperature resulting in this RIMAP setup drops faster, approximately as  $r^{-1.2}$  as can be seen from figure 2.11. Lowering the polytropic index of the PLUTO EOS could result in a slower trend, but this in turn would increase the wind acceleration, worsening the match with the plasma parameters measured at 1 AU. Since the focus of the RIMAP model lies in the accurate reconstruction of the Parker spiral in which the measurements were made, this has been avoided. Nevertheless, considering the simplified description of plasma assumed in the first implementation of our model, we consider our results in satisfactory agreement with the observations.

One way to verify the implementation of the scheme illustrated in figure 2.8, is to perform a final comparison between the input in situ measurements acquired at 1 AU, and the output plasma parameters at the same distance obtained from the simulation with RIMAP. A good agreement between input and output parameters would indicate that this reconstruction as a viable approach in determining the ambient conditions of the heliospheric plasma. Moreover, because the reconstruction is performed here by using data acquired by a single spacecraft, this corresponds to assuming stationarity over the time interval required for one full solar rotation. The reliability of this assumption can be tested by making a comparison between in situ data acquired by spacecraft located at different longitudes along the Earth orbit, as it is done here in this section. Figure 2.12 shows the longitudinal comparisons between input and output plasma densities, speeds, and magnetic fields. Although the structures carried by the solar wind show discrepancies with the input measurements at high frequencies (small scales), at low frequencies (larger scales) a greater agreement can be noted, particularly for the radial velocity. The large amount of short fluctuations clearly shows how strong the longitudinal variability along the ecliptic plane is. Nevertheless, the general azimuthal behaviour of these quantities is well reproduced, even with a relatively small number of points on  $\varphi$ . In particular, the root mean square error (RMSE) between input in situ measurements and output parameters is about  $\Delta n = 4 \text{ cm}^{-3}$  for the number density and  $\Delta v = 50 \text{ km/s}$  for the wind speed. The larger disagreements between the input and output curves are most likely related to the crossing-streamlines removal procedure discussed in section 2.2.1. In fact, as it is shown by the speed profile in figure 2.12, the slower wind streams (removed for the sake of consistency in the inner boundary reconstruction) are not well reproduced. In correspondence with the longitudes where this happens, such as between  $-60^\circ$  and  $-30^\circ$  or  $50^\circ$  and  $70^\circ$ , the density and magnetic field profiles of RIMAP also show the worse agreement with the Wind measurements.

As also expected, the main disagreements are observed in correspondence with the transit of SIRs/CIRs: the plots of figure 2.12 show the longitudinal locations of these features, identified based on the automated analysis of STEREO data for the considering period, with the numbering provided by [an online catalogue](#) (Jian et al., 2019). The comparison shows that the larger discrepancies are located at longitudinal positions where the slow wind streams are preceding (in the sense of Parker spiral rotation) the arrival of SIRs/CIRs. It is worth noting that the passage of a SIR/CIR can correspond to a sudden increase in speed: therefore, there is a connection between the passage of these structures and the need to eliminate intersecting streams.

The last two panels of figure 2.12 show the comparisons between input and output radial and longitudinal magnetic field components. The latitudinal component is null on the entire computational domain, coherently with the value set in the in

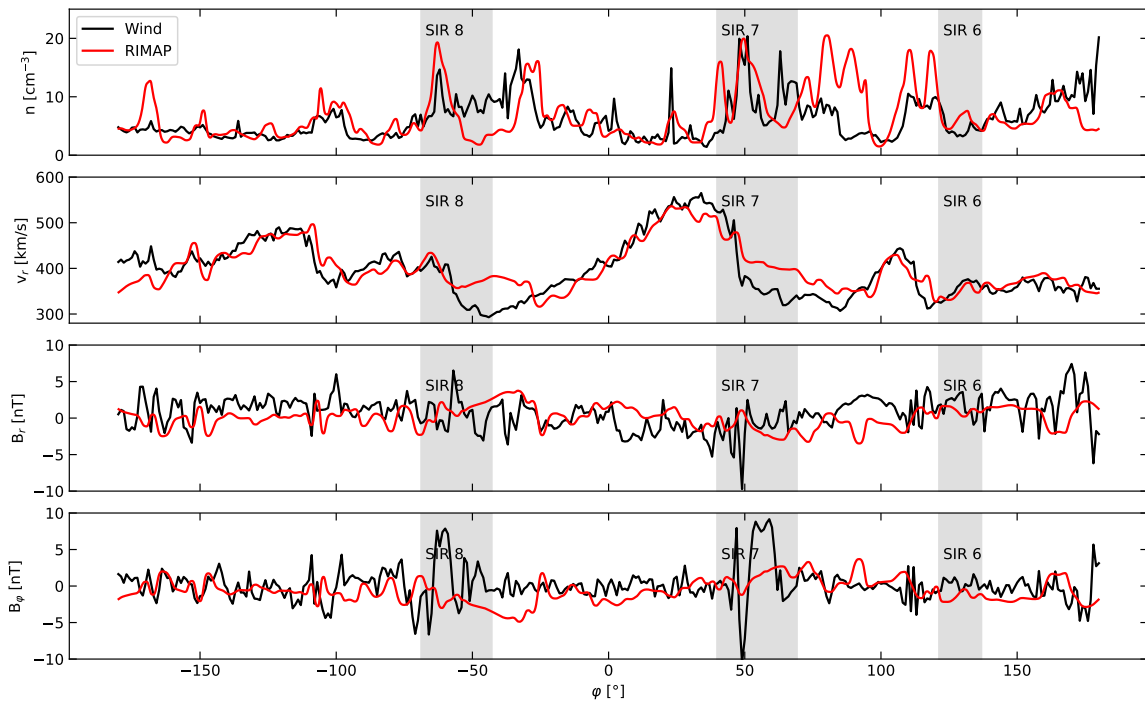


Figure 2.12: For the March 2009 Wind data set: 1 AU longitudinal comparisons between the input (black line) and the output (red line) profiles of (from top to bottom) plasma density, radial speed, radial and longitudinal components of the magnetic field. Superimposed as vertical grey bars, longitude intervals corresponding to SIRs/CIRs identified with STEREO (Jian et al., 2019). In this plots, the time direction runs from right to left.

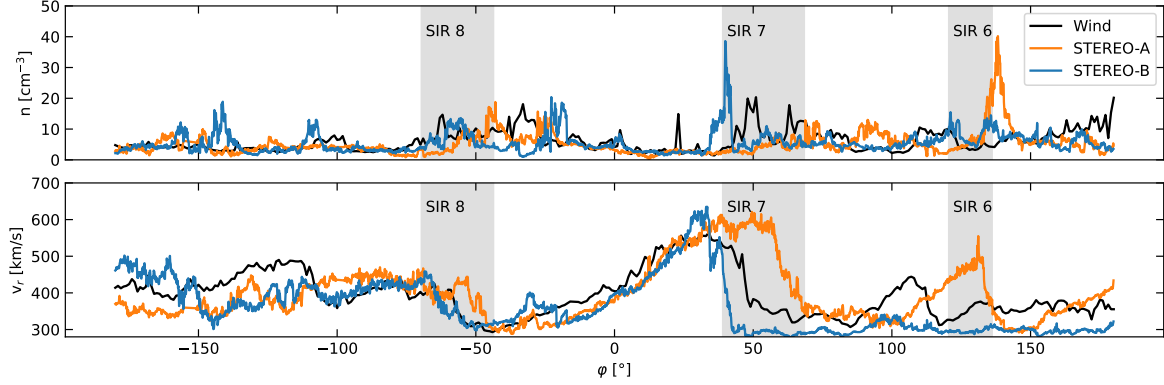


Figure 2.13: Longitudinal comparisons between the profiles of plasma density and radial speed measured by STEREO-A (orange line), STEREO-B (blue), and Wind (black line) on March 3-29, 2009. Superimposed as vertical grey bars, longitude intervals corresponding to SIRs/CIRs identified with STEREO (Jian et al., 2019). Time runs from right to left.

the internal boundary. The field perpendicular to the ecliptic plane is an important source of space weather activity for the planetary magnetosphere: nevertheless, a more complete treatment of  $B_\theta$  is currently beyond the scope of RIMAP, since it would require the determination of a different internal boundary for each  $\theta$  value, a task that will be discussed in chapter 5. In light of this consideration, it is therefore positive remarkable that RIMAP can capture the average longitudinal behaviour of the radial and the longitudinal fields with such good agreement, having used only the simple two-dimensional model of Weber and Davis (1967) in the reconstruction of the internal boundary. The resulting RMSE for the radial and longitudinal component are  $\Delta B_r = 2.6$  nT and  $\Delta B_\varphi = 2.9$  nT, respectively. As mentioned above for density and radial speed, the profiles of the magnetic field exhibit a strong variability at small scales (high frequencies). Although it is possible that part of these structures can be reproduced by increasing the spatial resolution of the simulation, many of them are instead attributable to intense transient phenomena (see for example the sudden peak of  $\mathbf{B}$  near 50 degrees, accompanied by simultaneous increases in solar wind density and speed), whose reproduction would at least require an extension of the model to the not-ideal MHD regime to realistically treat MHD shocks.

It is interesting to compare the Wind measurements acquired in L1 with those collected by the twin STEREO probes at the same time intervals, but from different positions along their heliocentric orbits. As explained in section 1.6.2, the two probes STEREO-A and STEREO-B are always located, respectively, ahead of and behind the Earth along its orbit around the Sun. During their orbits, there can be at times large latitudinal deviations between these three spacecraft. However, during March 2009 the latitudinal separation between the STEREO probes and Wind was modest, starting from around 0.2 degrees on March 3<sup>rd</sup> and progressively decreasing, being less than 0.08° on March 29<sup>th</sup>. Therefore, a direct comparison between the quantities measured by these two probes and by Wind, can be also a test for the stationarity hypothesis of the solar wind plasma conditions. As a reference for the approximate position of STEREO spacecrafts during the March 2009 time interval considered in this analysis, one can assume the position measured 13.25 days after the beginning of observations. In particular, considering the reference date of March 16,

14:02:09.05 UT, the corresponding longitudinal angles between different spacecraft were at that time  $\Delta\varphi_{\text{STA-Wind}} = 44.639^\circ$  and  $\Delta\varphi_{\text{STB-Wind}} = 47.512^\circ$ , respectively between STEREO-A and Wind, and between STEREO-B and Wind. These angles can be converted into time shifts  $\Delta t$ , by assuming again the same rotational period of the Sun (2.34). The resulting time shifts are  $\Delta t_{\text{STA-Wind}} = 3.286$  days and  $\Delta\varphi_{\text{STB-Wind}} = 3.498$  days, respectively between STEREO-A and Wind, and between STEREO-B and Wind. In particular, the data acquired by Wind in L1 have been compared with data acquired by STEREO-A 3.286 days later (i.e. between March 6, 14:53:59.05 UT and April 2, 02:53:59.11 UT), and by STEREO-B 3.498 days before (i.e. between February 27, 20:55:34.05 UT and March 26, 08:55:34.11 UT).

The comparison is shown in figure 2.13 for the evolution of total density (top panel) and outflow speed (bottom). In particular, the comparison between the longitudinal distributions of solar wind speeds  $v_r$ , measured by ST-A and ST-B and by the Wind spacecraft shows a quite good agreement, with large scale fast and slow wind regions observed approximately at the same longitudinal location (as dragged by the solar rotation) by the three spacecraft at three different times. Again, while at small scales there are significant discrepancies due to transient phenomena (like the two density peaks of  $\sim 40 \text{ cm}^{-3}$  associated with the transit of SIRs/CIRs), at large scales there is overall a good agreement between the measured profiles. This means that the fast and slow wind streams at solar minimum conditions are surviving for many days, making the assumption of stationarity performed to run the RIMAP simulation quite realistic.

The comparison between the longitudinal distributions of densities measured by the three spacecraft shows in general a quite good agreement as well, considering the large scale (low frequency) structures dragged by the solar wind expansion. On the other hand, at higher frequencies the three curves show significant disagreements, in particular with the formation of a narrow density peak observed by STEREO-B and not observed 3.498 days later (dragged by solar rotation) by Wind. A similar peak is observed also by STEREO-A, but located in a totally different longitude, and not observed by Wind 3.286 days before. This suggests that these two major density peaks (as well many as many other peaks) are short-duration transient phenomena with lifetime smaller than three days: similar transient phenomena cannot be reproduced by our model.

### Solar minimum of January 2018

January 2018 offers another quiet configuration of the Parker Spiral to test the reconstruction procedures of RIMAP. The measurements relative to 2018 analyzed here were collected by Wind in L1 between January 3, 06:10:45.63 UT and January 29, 18:10:45.69 UT, to cover again an entire solar rotation.

Figure 2.14 shows the ecliptic maps of plasma density and solar wind speed obtained with RIMAP from the in situ measurements of Wind. The plasma density values, normalized at 1 AU, are below 30 particles per cubic centimeter across all the latitudinal domain, with few outliers that will be discussed below. Unlike the more uniform configuration of March 2009, here more high-speed solar wind streams are visible, with the highest being around 600 km/s, and found in correspondence of the streamline passing through  $r = 100R_\odot$ ,  $\varphi = 30^\circ$ . The rest of the Parker spiral has instead speeds between 300 and 500 km/s.

The radial trends do not show significant differences with the behaviours obtained for the March 2009 dataset.

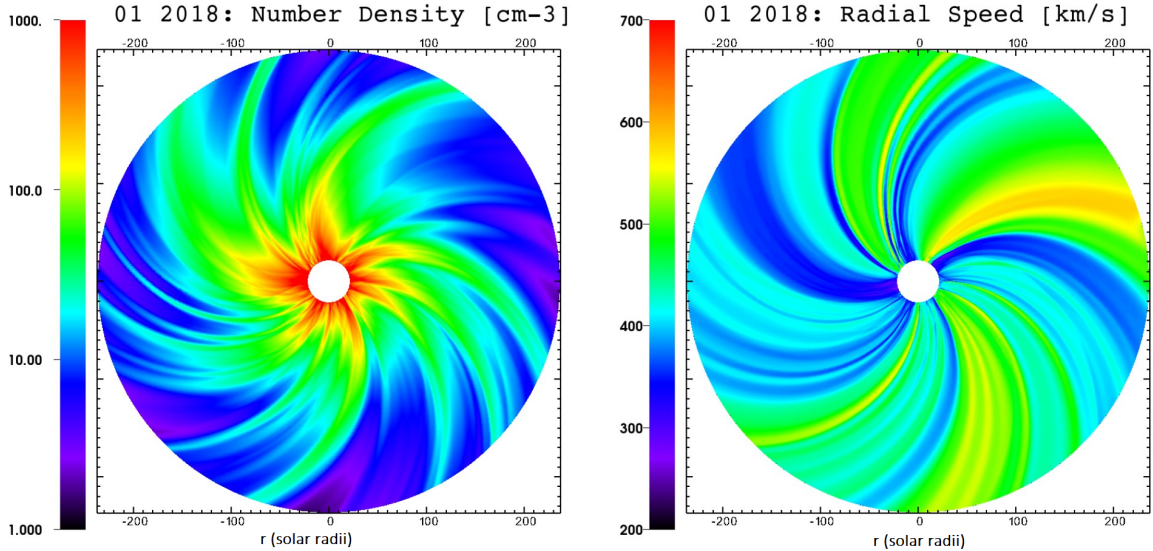


Figure 2.14: Ecliptic maps of the plasma number density (left panel) and radial speed (on the right) obtained with RIMAP from the in situ observations acquired by the Wind spacecraft at 0.99 AU during January 2018.

Figure 2.15 shows a comparison between the longitudinal profiles of the plasma and magnetic field parameters at 1 AU of RIMAP (red line) and Wind (black line).

The density profile measured by Wind exhibits two relatively high peaks near  $40^\circ$  and  $115^\circ$ , respectively at  $30$  and  $50 \text{ cm}^{-3}$ . From the profiles of the other quantities, it appears that the highest of such peaks could be associated with an intense transient event similar to those recorded by STEREO in March 2009. Despite the disturbance caused by these transients, the low-frequencies behaviour of the plasma density is reproduced by RIMAP. The comparison with the SIRs/CIRs provided by the STEREO catalog show that larger discrepancies between input and output profiles are located at longitudinal angles where the slow wind streams are following the arrival of the transients. The RMSE between the two curves is around  $\Delta n = 7 \text{ cm}^{-3}$ .

The comparison between measured and simulated radial speed shows how RIMAP is capable of reproducing the four high-speed wind streams recorded in situ. However, due to the crossing streamlines removal, lowest speed values are not well reproduced by the model, as already noticed for previous run. This is particularly noticeable between 2 and 2.5 radians, just before the 53<sup>rd</sup> SIR of 2017: streamlines in this region have much lower speeds than those in the surrounding areas, so they intersect them in the back-projection and must therefore be removed. The result of the subsequent interpolation is a bump above  $400 \text{ km/s}$ . Although this can and should be improved, we remind that, for the purposes of Space Weather forecasting it is more important to correctly reproduce the high-speed solar wind streams, more than the low speed ones that are associated with calmer space-weather conditions (Badruddin and Singh, 2009; Gerontidou et al., 2018; Kamide and Maltsev, 2007). However, we point out that the complete reconstruction of an high speed stream involves not only the reproduction of the absolute value of the speed increment, but also the amplitude of the associated variation with respect to the its baseline level. The computed RMSE for solar wind speed is  $\Delta v_r = 70 \text{ km/s}$ .

The agreement between input and output components of the magnetic field is slightly worse than the 2009 case, with their RMSE being  $\Delta B_r = 3.5 \text{ nT}$  and  $\Delta B_\varphi = 3.64 \text{ nT}$ . This is probably due to the greater gradients in longitude for this

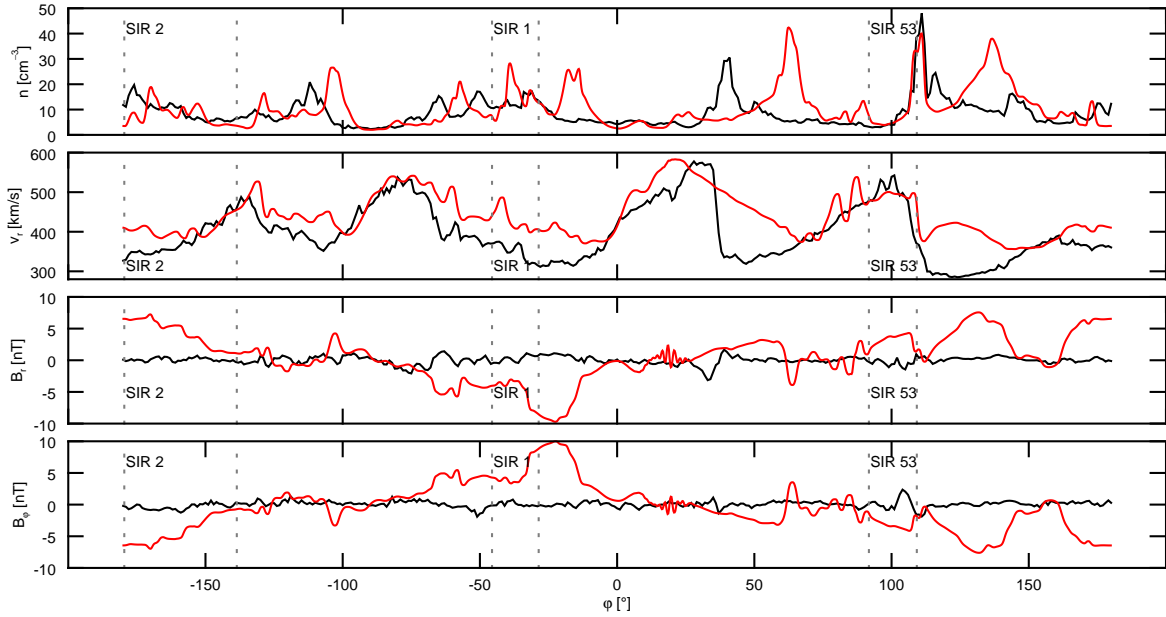


Figure 2.15: For the January 2018 Wind data set: 1 AU longitudinal comparisons between the input (black line) and the output (red line) profiles of (from top to bottom) plasma density, radial speed, radial and longitudinal components of the magnetic field. Delimited by vertical dashed lines, longitude intervals corresponding to SIRs/CIRs identified with STEREO (Jian et al., 2019). In this plots, the time direction runs from right to left.

dataset, with deviation of even 14 nT in the space of a few degrees. Given the irregularities of the longitudinal profiles and the fact that PLUTO tries to preserve the solenoidality of a field of which the latitudinal component has been suppressed, the general reproduction of the trend at large scales is to be considered a good result.

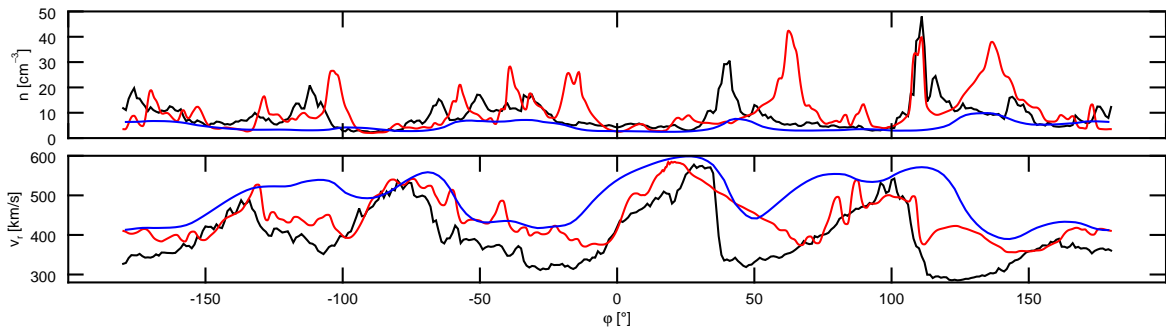


Figure 2.16: Comparison between the longitudinal profiles of number density (top) and radial speed (bottom) as measured at 1 AU by GGS Wind (black line) and simulated by WSA-ENLIL (blue) and RIMAP (red). The RMSE between ENLIL forecasts and Wind measurements are  $\Delta n \simeq 6 \text{ cm}^{-3}$  and  $\Delta v \simeq 110 \text{ km s}^{-1}$ .

For January 2018, it is possible to compare the RIMAP reconstruction of the inner interplanetary Parker spiral with the forecasts provided by the WSA/ENLIL code (since their earliest available simulation date back to November 2013). Figure 2.17 shows a the density and velocity maps obtained with RIMAP with the ENLIL forecast for January 16, 2018, while figure 2.16 show the longitudinal profiles of both models at 1 AU. As one could expect, the general configuration of the plasma

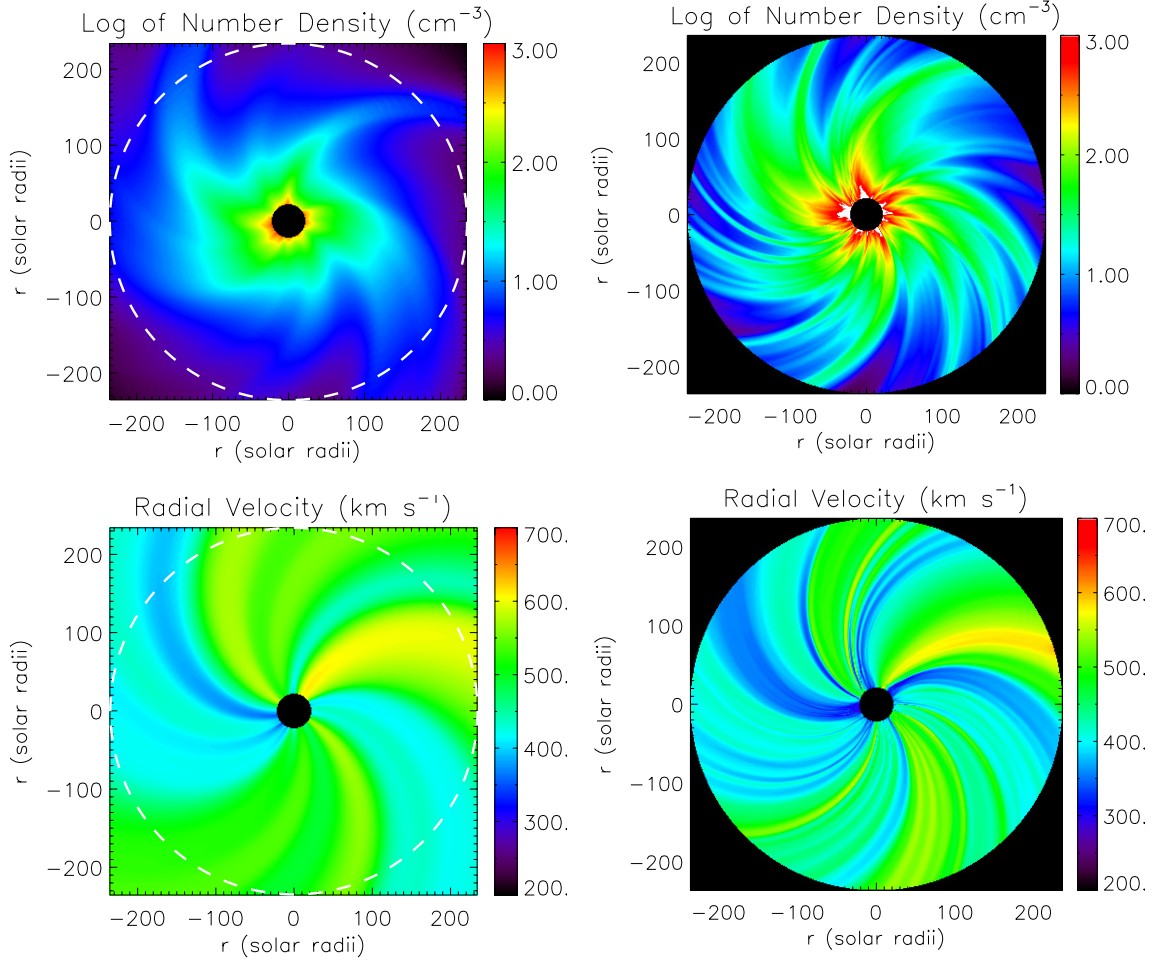


Figure 2.17: Visual comparison between the ENLIL forecast of the plasma conditions on the ecliptic plane of January 16, 2018 (on the left) and the simulation made with RIMAP starting from data acquired at 1 AU (on the right). Notice that the ENLIL domain extends nearly up to 2.0 AU, while the RIMAP one extends to 1.1 AU ( $\simeq 236.5 R_{\odot}$ ).

streamlines is similar at large scales, but not entirely identical. As discussed in section 2.1.2, WSA/MHD simulations ultimately start from ground-based observation of the photospheric fields, relying to complex extrapolations and semi-empirical assumptions to build the 0.1 AU solar wind plasma, then propagated by the MHD codes. This makes predictions at 1 AU challenging. In contrast, the reconstructions carried out by RIMAP are entirely based on direct observations of the plasma parameters (in this application at 1 AU). This means that errors are due only to transients that could temporarily weaken the validity of the stationary hypothesis (which we have seen to be generally valid within 1 week, at least in solar minima) and to the necessary suppression of some crossing streamlines.

The second striking feature is the greater number of individual solar wind streamlines discernible in the reconstruction performed with RIMAP: this is due to the fact that, with the exception of the above-mentioned removals, each point of the in situ data profile is mapped into the internal boundary and from there propagated outward. RIMAP naturally maintains the longitudinal variability present in the parameters of the interplanetary plasma, which allows to explain the higher number of high-density streams found in our reconstruction, a variability that the WSA models struggle

more to reproduce. On the other hand, WSA-based models such as ENLIL and EUHFORIA possess an internal boundary with a much greater latitudinal interval, and therefore are able to provide forecast on the latitudinal components of solar wind speed and magnetic field, while RIMAP can only provide reconstructions on the orbital plane of the spacecraft used to acquire the in situ measurements.

## 2.4 Conclusion

The accurate reconstruction of the ambient interplanetary Parker spiral is a fundamental step in the heliospheric and space weather research, since the physical conditions of the solar wind plasma and magnetic field dictate the propagation of solar disturbances possibly affecting Earth and the other planets. Section 2.1 provided a short review of the usual approaches to face this problem: ballistic inverse mappings, accurate but incapable of physical insights, and empirical-numerical modellings, very powerful but complex and founded on a great number of approximations and assumptions.

The Reverse In situ and MHD Approach acts as a bridge between these two methods, combining the accuracy of the former with the possibility offered by the latter to investigate the physics of phenomena of solar origin. The goal is to reconstruct the ambient plasma conditions on the ecliptic plane from the Sun to 1 AU and beyond, trying to maintain as faithfully as possible the solar wind smaller-scale fluctuations observed in situ, which photospheric-fields-based models struggle to predict.

RIMAP starts from in situ data, mapping them with the analytical models of Parker (1958) and Weber and Davis (1967) to a certain distance closer to the Sun. Then, the mapped solar wind parameters became the internal boundary of a MHD simulation, which propagates them forward providing the distribution of the interplanetary plasma and magnetic field across the spacecraft orbital plane. Adopting a two-dimensional description is indeed a non-trivial simplification, albeit a necessary one, since in situ measurements outside the ecliptic plane are very scarce and will remain so in the near future. Nevertheless, the Parker spiral reconstruction performed with RIMAP is conceptually much more simple than the computational expensive methods discussed in section 2.1.2. This means that this method can be more easily implemented on local machines, without the need for complex and expensive computer clusters, making it a viable method that can be potentially applied and tested by any research group, without the need of significant resources. Also, the simpler conceptual approach of RIMAP allows to have a much more direct control on the results, and to test more easily the possible causes of disagreements between plasma parameters of the model and the actual measurements and observations.

The comparisons between the input in situ measurements and the output plasma parameters derived at 1 AU have a relative agreement (based on the measured RMSE) comparable to what obtained with current analytical methods, and better than what is currently provided by MHD numerical simulations. Current empirical models have RMSEs for the wind velocities at 1 AU on the order of  $\Delta v = 50\text{-}100$  km/s (MacNeice et al., 2018), while MHD models on average reveal RMSEs around  $\Delta v = 100\text{-}150$  km/s, and time shifts in the arrival of the peak solar wind speed of about 1-3 days (Hinterreiter et al., 2019). On average, the modelled solar wind speed underestimate the in situ measured values, while the modelled plasma density is considerably higher than the observed one (ibid.). On the other hand, the RMSEs calculated for the

RIMAP reconstruction are lower: on the order of  $\Delta v = 50\text{-}70$  km/s and  $\Delta n = 4\text{-}7$   $\text{cm}^{-3}$ . While widely used, point-by-point analysis metrics such as computed RMSEs have their drawbacks, above all their weakness in quantifying time uncertainties (e.g. Owens et al., 2008; Samara et al., 2022). Time-window approaches (Owens, 2018) and hybrid metrics will be used in the future assessments of RIMAP performances.

The radial profiles of plasma parameters from 0.1 to 1 AU are also in good agreement with the current knowledge of interplanetary plasma conditions (Cranmer, 2002; Hellinger et al., 2011; Perrone et al., 2019). Modification of the polytropic index and/or addition of an energy and momentum source terms could also provide more realistic temperature radial trends (see discussion in chapter 5).

Moreover, RIMAP is aimed at preserving as much as possible the smaller-scale features of the solar wind, as they are sampled in situ by different spacecraft. This implies that, globally, the two-dimensional reconstruction performed by this method is much more representative of the real physical conditions of the interplanetary plasma, at least over the period of one solar equatorial rotation. Current analytical and numerical reconstruction of the interplanetary medium usually neglect the role of the small-scale features of the solar wind, providing only information on the larger scale features, as showed in figure 2.17 and 2.16. However, the finer details of the Parker spiral structuring play a key role in the propagation of solar disturbances, such as the solar energetic particle streams affected by stochastic magnetic field components (e.g. Pei et al., 2006; Ruffolo et al., 2003), and the interplanetary evolution of coronal mass ejections (e.g. Hostenaux et al., 2018, more in the following chapter 3). For these reasons RIMAP can be considered as a test-bench to better understand the propagation of solar transients across an interplanetary Parker spiral which is more representative of real conditions that these disturbances encounter, in particular for what concern the short-duration anisotropies of density, speed, and magnetic field.

In the implementation of RIMAP described in this chapter, only in situ data acquired at 1 AU by a single spacecraft have been employed. Nevertheless, RIMAP can ingest as input in situ measurements acquired by any spacecraft sampling the solar wind and the interplanetary magnetic field at different location in the heliosphere. For instance, going closer to the Sun, it is possible to significantly relax the stationarity hypothesis for the inverse mapping of the solar wind conditions. The different configurations assumed by very inner-heliospheric spacecraft such as Parker Solar Probe, Solar Orbiter, and BepiColombo (Benkhoff et al., 2021) can offer the opportunity to strengthen the accuracy of RIMAP reconstructions, and to investigate the sub-Alfvénic corona via multi-point-of-view observations (see e.g. Velli et al., 2020, more in chapter 4). Furthermore, the inclusion of plasma parameters measured with remote sensing data, for instance coronagraphic observations, could be considered to fully extend the model to the third dimension, as discussed in chapter 5.

# Chapter 3

## Tracing ICME plasma with the RIMAP model

### 3.1 Context

The heliosphere is a highly dynamic environment in which the ambient solar wind varies smoothly with the solar cycle and a plethora of localized, shorter-lived (minutes to hours) and intense phenomena superimposed on the quiet solar wind, continuously disrupting the regularity of the background interplanetary Parker spiral (Priest, 2014, sections 1.2, 1.7–1.9).

The behaviours and properties of these transients are sufficiently diversified to catalog them depending on their signatures both in remote observations and in situ measurements (Intriligator, 1980; Zhang et al., 2021). In section 1.2 we classified these solar transients into four main categories: solar flares, solar energetic particles, stream and corotating interaction regions, coronal mass ejections and their interplanetary counterpart.

All these phenomena can determine magnetospheric and ionospheric disturbances in the near-Earth space (Kamide and Maltsev, 2007) which can have significant effects on life and technological systems (e.g. Green and Baker, 2015; Hapgood, 2011; Pomoell and Poedts, 2018; Schrijver et al., 2015).

Among solar transients, ICMEs are the only structures capable to produce extreme geomagnetic storms (Kilpua et al., 2017; Luhmann et al., 2020), and they are by far the most prominent transient structures in the heliosphere, starting from few solar radii when in the outer solar corona and reaching up to hundreds of solar radii in the interplanetary medium as they expand during their propagation (Mishra et al., 2021). At 1 AU, is it possible to identify ICME plasma from in situ measurements by looking at certain signatures in the parameters, distinguishable from typical values of the background solar wind. These include enhancement in plasma densities and speeds, suprathermal electron beams, stronger magnetic fields, lower proton temperatures, anomalies in the chemical composition and higher charge states (Gosling et al., 1987; Kilpua et al., 2017; Richardson and Cane, 2010; Rodriguez et al., 2016; Zwickl et al., 1983). It is worth noticing that these in situ signatures are never found all together during a single event, different signatures come and go, and there is no specific signature always found in ICMEs (Kilpua et al., 2017). This often makes ICME identification ambiguous (Gosling, 1997; Kilpua et al., 2013; Richardson and Cane, 2010). In spite of this, plasma and magnetic field signatures offer a key opportunity: one can directly observe material coming from the deeper layers of

the solar atmosphere, and can infer the pre-eruption conditions from the in situ measurements (Rodriguez et al., 2016).

One interesting question about ICMEs is how the plasma properties measured in situ - usually far from the Sun - can be traced back to the ones observed remotely in the lower solar corona, and how the original perturbation material propagates and interacts with the interplanetary medium.

Another connected topic is the charge distribution and the chemical composition of ICME plasma: these two signatures are of great importance, being the parameters least affected by propagation effects. This happens because they freeze-in beyond a few solar radii (see e.g. Zhao et al., 2009), in contrast to density and temperature which may significantly change by compression and expansion. In the Sun, and in the heliosphere by extension, plasma from different sources is continuously mixed so that its chemical composition varies temporally (e.g. in solar flares and coronal eruptions; Brooks and Yardley, 2021; Lepri and Rivera, 2021) and spatially (e.g. between active and quiet regions, between different streams of solar wind, and between different layers of the solar atmosphere; Feldman, 1992; Landi and Testa, 2015). For instance, Livingston et al. (2007) showed that some strong lines with photospheric contributions display variations in phase with the solar cycle. Rodriguez Hidalgo et al. (1994) studied the latitudinal variations of Si I, Mn I, and Fe I, founding that the lines strength varies of a few percentils. Doschek and Warren (2019) found that elements with low FIP ( $<eV$ ) are enriched in coronal active regions by a factor 3-4, while abundances in the quiet Sun and the transition regions are photospheric. Sylwester et al. (1998) showed variations in Calcium abundances between solar flares coming from different active regions, and that these variations do not depend on the flare size. This topic is usually dealt with numerical models, alone or in combination with multi-spacecraft observations as constraints (see e.g. Gruesbeck et al., 2011; Lynch et al., 2011; Reinard et al., 2012).

Another important tool in the determination of elemental abundances is offered by spectroscopy (see e.g. Lee and Raymond, 2012): in turn these have been used, for instance, to detect the presence of SEPs in ICMEs tracking them back to their sources on the Sun (Brooks and Yardley, 2021). However, the best way to study the chemical composition of the mass transported from the innermost layers of the solar atmosphere to the near-Earth environment, is still provided by in situ measurements (e.g. taking advantage of the first ionization potential effect; Song and Yao, 2020).

The interplanetary Parker spiral in which solar transients propagate is far from being a homogeneous medium, as described in section 1.2. Thus, in order to accurately describe their evolution, propagation, and possible mixing with the background solar wind plasma, it is crucial to reconstruct the ambient condition of the heliosphere, since these conditions influence the propagation of SEP streams (e.g. He et al., 2011) and the interplanetary evolution of CMEs (see, for instance, Chané et al., 2005; Maloney and Gallagher, 2010; Temmer and Nitta, 2015; van der Holst et al., 2007; Vršnak et al., 2013).

Providing accurate reconstruction would not only have repercussions in the field of pure solar physics, it would also have practical applications. As we discussed in section 1.2.4, ICMEs and related gradual SEP events are a major source of damage for space-based technological and human operations. Improving the forecasting capabilities concerning those transient phenomena is crucial to the safety of solar system exploration, both robotic and human (National Research Council, 2003, 2008).

Heliospheric MHD models such as ENLIL, EUHFORIA and SUSANOO today are able to provide forecasting of the space weather conditions from the Sun to 1 AU and beyond in real time. However, as discussed in sections 2.1 and 2.2, these models still have a limited capability and resolution in the reconstruction of the interplanetary plasma ambient conditions (see e.g. Jian et al., 2016), and therefore in the reliability of the forecasting for the arrival times of solar disturbances (Riley et al., 2018). Thus, a model capable of reproducing the finer details of the longitudinal structuring of the Parker spiral could contribute to understand the details of the heliospheric propagation of solar perturbations. As discussed in sections 2.2 and Biondo et al. (2021a), RIMAP could be that model.

## 3.2 Tracing plasma in the interplanetary medium

We used RIMAP to test the interaction of an artificial ICME with a longitudinally structured interplanetary medium reconstructed from in situ data measured by the Wind probe on March 3-29, 2009, discussed in section 2.3. In particular, the goal is to quantify the mixing of the propagating cloud with the ambient solar wind plasma, so to estimate to what extent the plasma composition measured at 1 AU can be expected to be traced back to the coronal one. The idea is to mark the initial ICME with a tracer, and to track the propagation of this tracer as compared with the proper MHD evolution.

We study the propagation of the ICME from 21.5 up to 236.5 solar radii ( $\approx 0.1$ -1.1 AU) in the radial direction. The computational domain is 2.5D, and it extends over  $360^\circ$  in longitude. For computational convenience we consider also a minimum latitude interval of 2 degrees centred around the solar equator at  $\pi/2$ , but we have no evolution along this direction. The time-dependent MHD equations (1.20) are then solved in a 3D spherical coordinate system corotating with the solar equator. The grid used has 256 cells in the radial direction, 6 cells have the same length up to 24.5 solar radii, the other 250 cells (up to 236.5 solar radii) have stretched length, with stretching ratio  $\xi$  computed as

$$\xi \frac{1 - \xi^{250}}{1 - \xi} = \frac{r_{\text{end}} - r_{\text{u}}}{\Delta r_{\text{u}}} = \frac{212}{3.25} = 65.2308 \quad (3.1)$$

according to equation (2.22). This allows us to resolve most of the ICME propagation in cells with a regular aspect ratio. In the latitudinal and longitudinal direction we have 8 and 768 equispaced cells, respectively. The grid features are summarized in Table 3.1..

Table 3.1: Computational grid for the ICME simulation

Direction	Interval	Number of cells	Style
$r$	$21.5 R_{\odot} - 236.5 R_{\odot}$	256	u + s
$\theta$	$89^\circ - 91^\circ$	8	u
$\varphi$	$-180^\circ - 180^\circ$	768	u

As a first step, the in situ data are back-mapped to the inner radial boundary and used to solve the MHD equations with the PLUTO code, as discussed in chapter 2 and section 2.2. The time frame of March 3-29, 2009, was chosen due to its relatively calm solar wind condition, being around the minimum of solar cycle 23. Nevertheless,

the RIMAP-reconstructed equatorial Parker spiral is highly structured in longitude (as can be seen in the first panel of figure 3.2), thus offering diverse condition to the ICME propagation. The longitude of the cloud central axis is chosen to be  $\varphi_0=112.5^\circ$  (arrow in fig. 3.2 and 3.3), corresponding to a relatively high-density streamline. Thus, we are addressing the impact of an ICME on a dense, slow stream that may result in the interplanetary formation of geo-effective disturbances.

A conservative approach was used to maximize the condition of coronal plasma mixing with the interplanetary medium in the equatorial plane. Accordingly, the interplanetary CME is described as an ejected plasma bubble without internal flux-rope that has constant angular width and velocity in the early phases of its propagation, i.e. an ice-cream cone-model (described in section 1.5).

### 3.2.1 Ice-cream Cone Modelled ICME

The kinematic parameters of a cone-modeled ICME are determined by its angular width  $\omega$  and its radial speed  $v_{\text{ICME}}$ . A nearly circular cross section is assumed, such that, before entering the computational domain at 0.1 AU, the ICME can be thought of as a spheroid pushed at constant speed through a plane. The cone-modelled perturbation is thus a time-dependent boundary condition, as in the cases of Odstrčil and Pizzo (1999a) and Pomoell and Poedts (2018). If  $r_b$  denotes the spherical radius of the inner boundary and  $t_0$  is the onset time of insertion into the computational domain, then

$$\alpha(t) = \frac{\omega}{2} \sin \left( \frac{\pi}{2} (t - t_0) \frac{v_{\text{ICME}}}{r_b} \tan^{-1} \frac{\omega}{2} \right) \quad (3.2)$$

is the angle subtended by a spheroid with the inner boundary surface during its passage.  $\alpha(t)$  is operationally used to determine whether a cell on the longitudinal axis of the inner radial boundary belongs to the ICME or not. The longitude of the ICME center is chosen to be a certain  $\varphi_0$ : hence, if

$$(\varphi - \varphi_0)^2 \leq \alpha^2(t) \quad (3.3)$$

holds true, the background solar wind parameters are replaced with those of the modelled perturbation. From equation (3.2) one can determine the ICME radius, defined as

$$r_{\text{ICME}} = r_b \tan \left( \frac{\omega}{2} \right) \quad (3.4)$$

and the half time  $t_{\text{half}}$ , i.e. the time taken by the perturbation to traverse halfway through the boundary:

$$t_{\text{half}} = \frac{r_{\text{ICME}}}{v_{\text{ICME}}}. \quad (3.5)$$

At  $t = t_0 + 2t_{1/2}$  the perturbation has completed the crossing of the boundary, and the condition ((3.3)) on the cells is no longer applied. Figure 3.1 shows a cartoon of an ice-cream cone model entering the RIMAP computational domain.

As discussed in the previous section, cone models reasonably assume that in the early phases of their evolution, the ICME plasma clouds propagate radially homogeneously. Therefore, the velocity  $\mathbf{v}_{\text{ICME}}$  at each grid point on the inner radial boundary during the passage of the perturbation will be parallel to the purely radial one found at  $(\theta, \varphi) = (\theta_0, \varphi_0)$ , and will have non-zero latitudinal and longitudinal components, dependent on  $\theta$  and  $\varphi$ , according to:

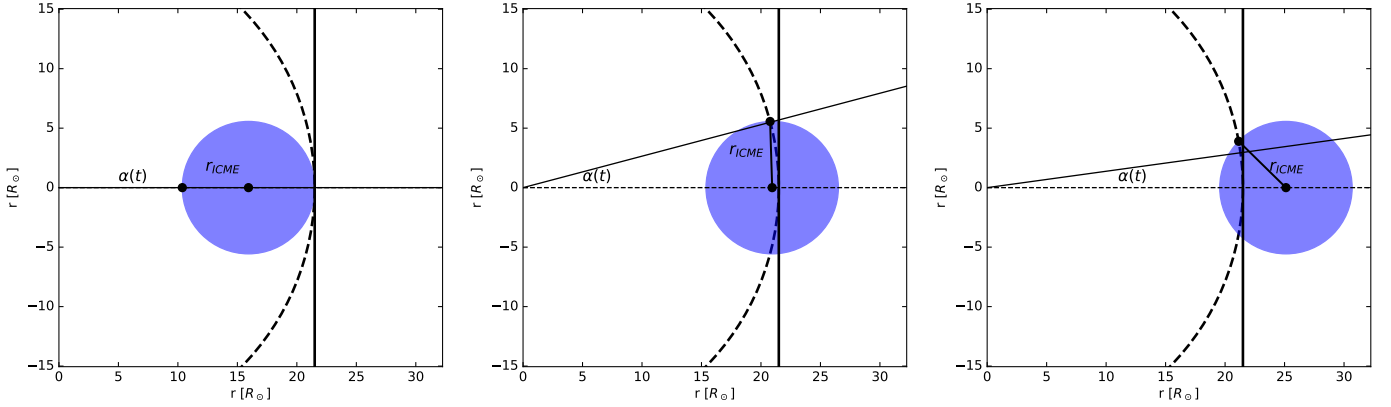


Figure 3.1: Three frames showing the passage of the perturbation through the internal boundary. The cone-modelled ICME (blue circle) can be thought of as a spheroid pushed at constant speed through a plane (black solid line).  $\alpha(t)$ , the angle subtended by the modelled plasma bubble and this plane, and defined in (3.2), depends only on the ICME angular width  $\omega$ , and its bulk speed  $v_{\text{ICME}}$ . The dashed black line here is the simulation internal boundary at  $21.5 R_{\odot}$ .

$$\begin{bmatrix} v_r \\ v_{\theta} \\ v_{\varphi} \end{bmatrix} = v_{\text{ICME}} \begin{bmatrix} \sin \theta \cos \varphi & \sin \theta \sin \varphi & \cos \theta \\ \cos \theta \cos \varphi & \cos \theta \sin \varphi & -\sin \theta \\ -\sin \varphi & \cos \varphi & 0 \end{bmatrix} \begin{bmatrix} \sin \theta_0 \cos \varphi_0 \\ \sin \theta_0 \sin \varphi_0 \\ \cos \theta_0 \end{bmatrix} \quad (3.6)$$

We simulated a relatively small and slow ICME, with angular width of  $15^{\circ}$  and bulk speed of 800 km/s, thus its radius is approximately 2.83 solar radii and it would entirely cross the internal boundary in nearly 1 hour and 21 minutes. Number density  $n_{\text{ICME}}$  and plasma temperature  $T_{\text{ICME}}$  inside the cone model are chosen to be homogeneous for all the grid point satisfying condition ((3.3)), with values close to the average event ones during solar cycle 23 and 24 (see e.g. figure 3 of Gopalswamy et al., 2014). This simulated ICME, relatively small and slow with no proper internal magnetic field, may resembles a stealth CME (Howard and Harrison, 2013), described in section 1.2.3. The parameters chosen to initialize the perturbation at the inner radial boundary are summarized in Table 3.2.

Parameters of ICME cone model		
Angular width	$\omega$	$15^{\circ}$
Radius	$r_{\text{ICME}}$	$2.83 R_{\odot}$
Bulk speed	$v_{\text{ICME}}$	800 km/s
Number density	$n_{\text{ICME}}$	$600 \text{ cm}^{-3}$
Temperature	$T_{\text{ICME}}$	$8 \cdot 10^5 \text{ K}$
Tracer	$\mathcal{T}_{\mathcal{R}}$	1.0

Table 3.2: Input parameters for the cone-modelled ICME at 0.1 AU, before entering the computational domain and being subject to the interaction with the ambient plasma. This would be a fairly modest and relatively common event (Gopalswamy et al., 2014), or possibly even a stealth CME (Ruffenach et al., 2015), usually not capable of inflicting severe geomagnetic storms on Earth’s magnetosphere.

Finally, an artificial scalar  $\mathcal{T}_{\mathcal{R}}$  is added to the the ICME model, and used as a tracer of its plasma flow. This passive scalar is simply advected, and interacts in no

way with the physical quantity of the model. Before the insertion time, when  $t < t_0$ , this tracer is null across the entire computational domain. When  $t_0 \leq t \leq t_0 + 2t_{\text{half}}$ , in the boundary cells for which the condition (3.3) holds true this quantity has a value of 1. Therefore, during the MHD evolution, the tracer can flow in and out of each grid cell of the simulation domain, thus attaining a mixing with the background solar wind plasma at the grid length scale. To measure the mixing between perturbation and ambient plasma, the mass percentage of the tracer,  $\mathcal{T}_{Rg}$ , is calculated as:

$$\mathcal{T}_{Rg}(r, \varphi) = \frac{\int d\theta r \mathcal{T}_{Rg}(r, \theta, \varphi) \rho(r, \theta, \varphi)}{\int d\theta r \rho(r, \theta, \varphi)} \times 100 \quad (3.7)$$

where  $\rho$  is the plasma density and the integrals are done on the entire latitudinal domain.

### 3.2.2 Results

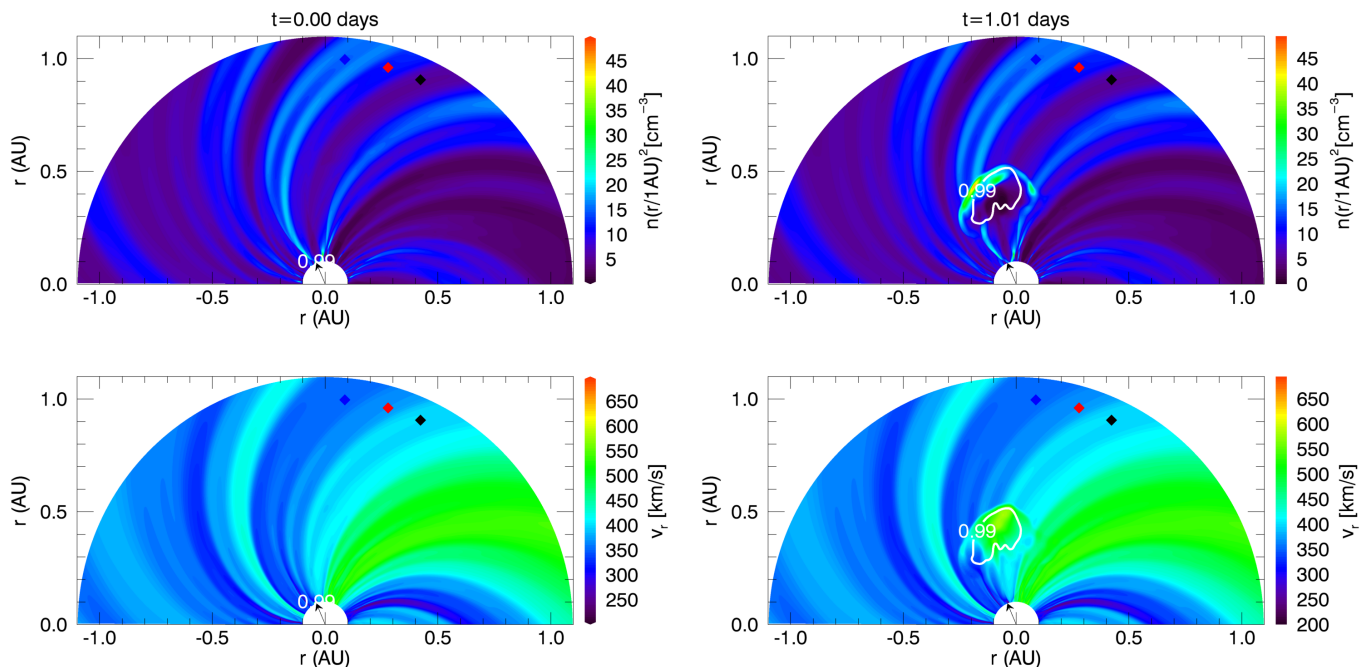


Figure 3.2: Interplanetary propagation of the cone-modelled ICME across the Parker spiral reconstructed via RIMAP from in situ measurements. Plasma density and velocity in the equatorial plane are shown, respectively, in the top and bottom half of each panel. The white contour line contains 99% of the ICME tracer mass. The colored diamonds at  $\varphi=85^\circ$ ,  $73.8^\circ$ , and  $65^\circ$  are the positions of three virtual spacecraft, which would detect the time profiles in Figure 3.4. The black arrow is the entry point of the ICME into the inner boundary of the simulation.

We now describe the propagation of the cloud after it enters the inner boundary of our Parker spiral. At variance from previous modeling, here we consider a proper evolution over a steady-state condition, instead of letting the system relax to the steady-state condition.

At the initial time  $t = 0$ , the simulated ICME enters the computational domain at the inner radial boundary and  $\varphi = 112.5^\circ$ . In Figures 3.2 and 3.3 the equatorial maps of plasma density and radial speed are shown at progressing times of the ICME propagation.

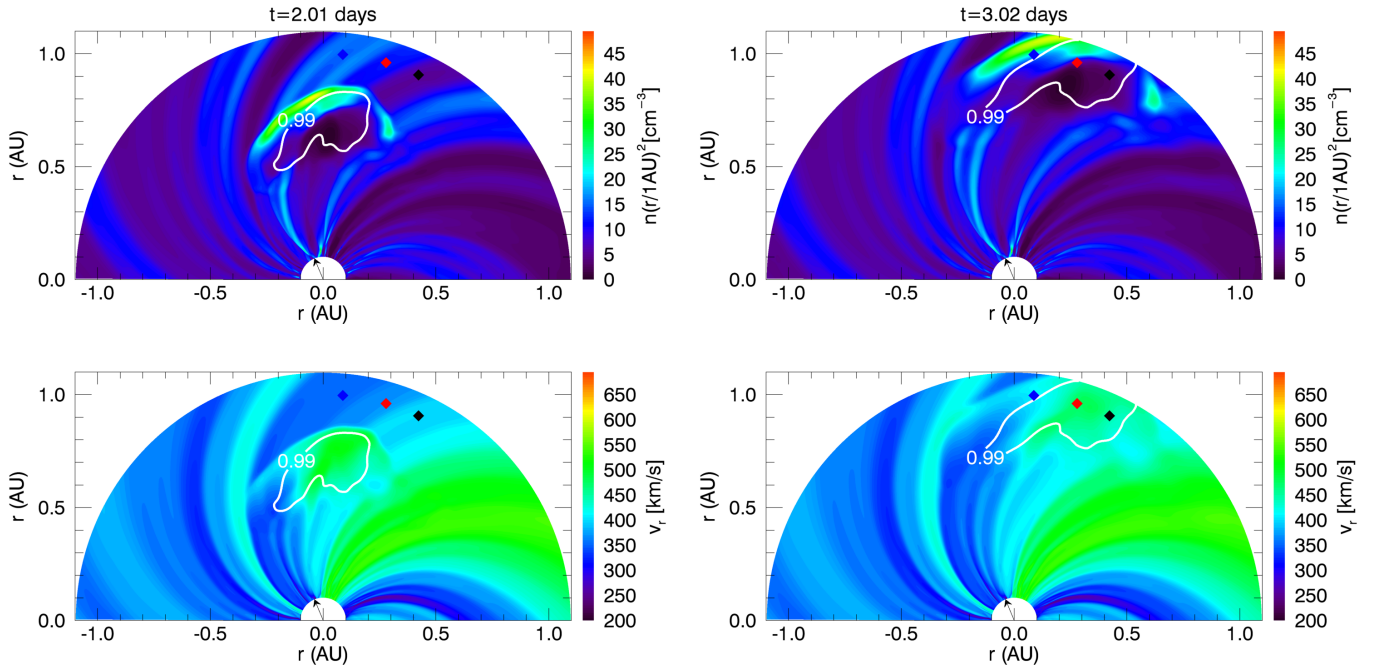


Figure 3.3: Interplanetary propagation of the cone-modelled ICME across the Parker spiral reconstructed via RIMAP from in situ measurements. See the caption of Figure 3.2 for a more detailed description.

As soon as the previously homogeneous, spheroidal plasma cloud appears in the computational domain, it is soon stretched (especially in the non-radial directions) and slowed down by the interaction with the interplanetary medium. The speed of the perturbation drops below 500 km/s at 1 AU, and its trajectory is significantly deflected from the purely radial one. This deceleration to the ambient speed of the solar wind is a common feature in observed ICME events (Gopalswamy et al., 2000; Kilpua et al., 2017; Lindsay et al., 1999) and in simulated ones (see e.g. Manchester et al., 2014).

In the early stages of the propagation, a compression front forms ahead of the plasma cloud, and it develops an internal structure due to the inhomogeneity of the background solar wind in density and (a little less) in speed. In particular from approximately day 1 onward, being torn by two adjacent streams of wind at different regimes, the right edge of the front begins to detach from the rest, and at  $t = 2.5$  days it has formed a separate blob. At the same time, behind the front, the cloud is expanding, its density decreasing and a void forms where plasma density is one tenth of the surrounding medium at 1 AU.

In figures 3.2 and 3.3 the contours of the passive tracer mass  $\mathcal{T}_R$  are also shown. Each white contour bounds the area where 99% of the tracer mass is contained, and it is interesting to notice that, in spite of the interaction with the different arms of the Parker spiral, the original material of the ICME remains compact behind the front as a single coherent structure, and it is more co-spatial with the velocity field (as a clearly distinguishable green ‘island’). This result may bring important implications regarding the chemical composition of ICME plasma measured with in situ data.

Three locations at 1 AU are marked in the equatorial maps of figures 3.2 and 3.3, which are along the perturbation path and also in solar wind with different properties. In order to study how the passage of an ICME affects in situ measurements at 1

AU, we analyse the evolution of the plasma parameters and magnetic field at these locations as a function of time. This mimics the configuration in which multiple

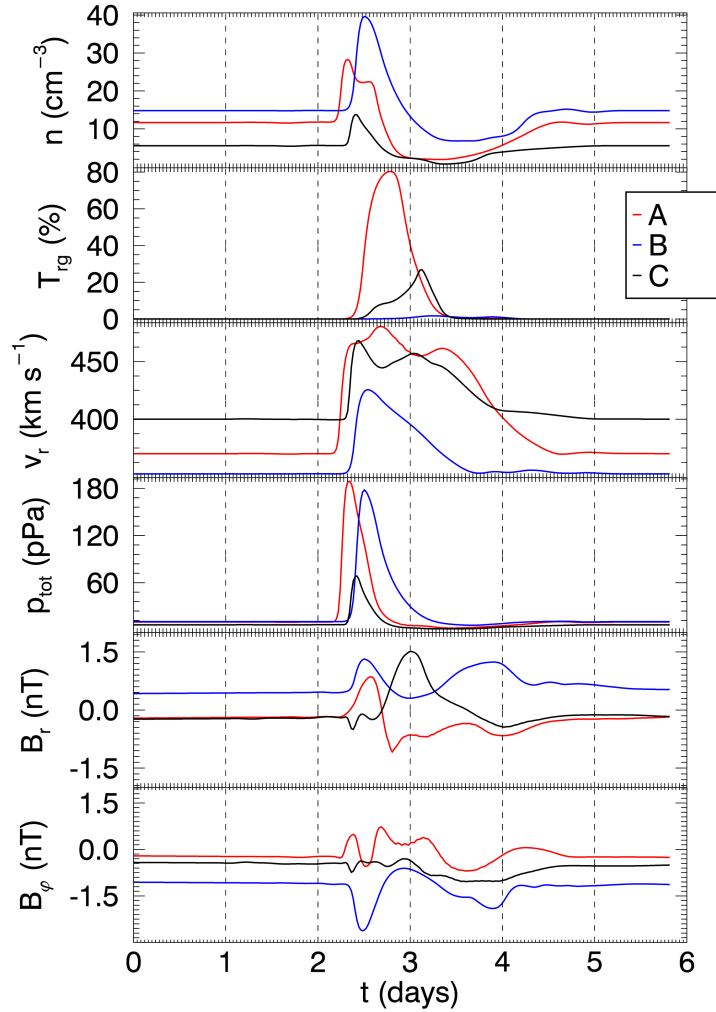


Figure 3.4: From top to bottom, time profiles of plasma number density, percentage of tracer, radial speed, pressure, and the radial and longitudinal components of magnetic field, as measured at 1 AU by three virtual spacecraft that encounter different regions of the perturbation. The color code for A (red line), B (blue line), and C (black line) is the same used in figure 3.2. Here, the simulated ICME enters the internal boundary at  $t=0$ .

spacecraft detect the interplanetary plasma at different locations along Earth’s orbit and/or along the passage of solar transients. The red diamond (hereafter, position A) is positioned where the tracer has its maximum on the domain, that is, where the percentage of original ICME plasma is the largest at the time when the perturbation reached 1 AU. The blue diamond (position B) is taken at an intermediate distance between the center and the boundaries of the ICME at 1 AU. Finally, the black diamond (position C) is almost outside the outer ICME contour line of the tracer and it is hit only marginally by the perturbation front. Hence, the encounters of the virtual spacecraft closely resemble all the three cases of groups that categorize magnetic clouds events (Jian et al., 2006), as discussed in section 1.5.

Figure 3.4 shows, from top to bottom, the time profiles of plasma density, tracer mass percentage, radial speed, total pressure, and magnetic field components that

would be measured at position A (red profile), B (blue), and C (black). All quantities are averaged over the narrow latitudinal domain.

Approximately 2.5 days after the insertion time, a rapid increase in density, pressure, speed and magnetic field magnitude is detected at 1 AU in A, B, and C, marking the beginning of the event. Plasma density reaches a higher peak value ( $\sim 40 \text{ cm}^{-3}$ ) at position B, somewhat later than at positions A and C. This happens because, as can be seen in figure 3.3, the perturbation front which hits position B is more compressed against a high density stream, while at position A the front has travelled through more tenuous streams and thus accumulated less plasma. Instead, position C is just outside of the cloud boundaries and on the trajectory of the region where the front has split into two; there we see only a small and short-lasting bump of a few  $\text{cm}^{-3}$ , all before the third day, followed by a longer-lasting slight decrease back to the unperturbed ambient value after the fifth day. The density bump lasts much less than one day at all positions. The total pressure shows similar and simultaneous bumps. After the bump, we still see a density perturbation in the form of a broad dip, which brings the density down to about 0 at position B and C, and lasting about 1 day or more.

Interestingly, the tracer evolution shows a significantly delayed bump at positions A and even more at C, almost no change at position B. The tracer peak at position A tells us that there about 80% of the plasma consists of the original ICME plasma. On the other hand, this peak occurs later than the peak of total density, when the density is already steeply decreasing, that is in the tail of the perturbation. At position C the fraction of original ICME plasma has a much lower peak ( $\sim 30\%$ ), and this occurs even later, close to the density dip. Overall, while position A is close to the cloud core, rich of original ICME material, and C is intermediate, position B is still significantly perturbed but empty of tracer. Contrary to common sense, we clearly see that the original ejected plasma is well detached from the compression front moving ahead of it, visible in the density and pressure plots, and permeates instead the void behind it.

The radial speed profiles show a much longer-lasting bump, quite similar at the three positions. In both positions A and C the plasma speed jumps by  $\sim 150 - 200 \text{ km/s}$ , from their pre-event values up to  $\sim 450 - 500 \text{ km/s}$ , and remains at these speeds during most of the two days of the perturbation. As the equatorial maps show, the perturbation is quite homogeneous in velocity even at 1 AU, and despite being just outside of the bulk of the ICME, position C still shows a velocity jump similar to positions A and B. On the other hand, at position B the perturbation hits a higher density wind streams and decelerates more rapidly to the pre-event value, in about 1 day.

As mentioned before, the total pressure shows sharp peaks similar to the density ones, up to about 180 pPa, lasting less than one day, while in position C the bump is much smaller, up to only about 60 pPa. This is consistent with the fact that positions A and B are directly hit by the full perturbation front while in position C the front is attenuated by the interaction with the denser wind stream.

Despite having no magnetic structure of its own, the cone-modelled ICME still perturbs the magnetic configuration at 1 AU, as shown by the profiles of radial and transverse components of the magnetic field. Both show significant fluctuations which are significantly out of phase and significantly different at the 3 positions. This is evidence of strong distortion and compression of the magnetic field lines, a signature often detected on in situ measurements, where it is associated with the

passage of ICME sheath regions (Kilpua et al., 2013, 2017).

### 3.3 Conclusions

In this part of the work we modelled an ICME propagation in a structured Parker spiral with the specific aim to track the original ICME plasma in the heliosphere. This is interesting to correctly interpret the chemical composition of the plasma detected at 1 AU, and to understand how stellar material mixes with interstellar medium.

In section 1.5, we presented a brief overview of methods and approaches to model the propagation of solar transients, with particular focus on interplanetary coronal mass ejections. We discussed how no model is currently capable of capturing all aspects of this phenomenon, and how despite the development of advanced models of magnetic clouds (both in the form of flux rope loops and toroidal or spheroidal configurations), unmagnetized cone-models still play an important role in research due to their versatility and ease of use. In this chapter, we reported on the propagation of an ice-cream cone-modelled ICME inside a realistic ambient solar wind reliably reconstructed from in situ measurements around the lagrangian point L1 of the Sun-Earth system at the minimum of solar cycle 23 (Biondo et al., 2021b), with the RIMAP model (see chapter 2 and Biondo et al., 2021a).

The original perturbation plasma is tracked by using an artificial tracer, and its arrival at 1 AU is sampled in situ by virtual spacecraft located at three different longitudes. We show that, although the complex interaction with multiple fast and slow wind streams leads to ICME non-uniform deceleration and deformation, the original ICME bubble remains compact and is not eroded, thus preserving its chemical composition. This is not entirely surprising, since the absence of internal flux rope makes our ICME less prone to erosion via magnetic reconnection with the IMF, a feature that in situ measurements suggest may be the reason why magnetic clouds often occupy only a small portion of the more extended ICME structure (Kilpua et al., 2017). This gradual peeling of magnetic flux has been estimated near 1 AU as much as 40% of the original ejecta flux (Ruffenach et al., 2015). Recently, Pal et al. (2022) used measurements of a slow CME acquired by Parker Solar Probe and observation from BepiColombo and Wind to estimate an erosion of 18% of the original magnetic flux, that began around 0.35 AU. On the other hand, the perturbation front is almost entirely composed of interplanetary plasma compressed during its propagation against the pre-ICME background. These results have potential impact on the interpretation of multi-spacecraft observations of solar eruptive phenomena, both at 1 AU and/or closer to the Sun.

This work sheds some light on how coronal mass ejections observed near the Sun evolve becoming ICMEs detected in the interplanetary space. In the past, after some first attempts by using test-particles (e.g. Odstrčil and Pizzo, 1999a; Riley et al., 1997), a real particle tracking method was applied to a MHD simulation of an ICME for instance by Riley et al. (2008). In that work, it was shown that in the interplanetary evolution the counterpart of the CME front is buried within the sheath material of the ICME, formed by upstream solar wind plasma swept-up by the CME. However, by using a tracer for which we describe the advection in the MHD code, instead of sampling particles, we can provide a more quantitative analysis of this effect. We find that only a very small fraction of the original CME plasma is present in the compression front but that this fraction can rise up to about 80% at

other locations and times during the event. Our modeling confirms then that strong variations of chemical composition measured at 1 AU can trace back, at least in part, directly to the original CME composition. More recently, Brooks and Yardley (2021) have identified the source region of the energetic particles during an eruption, by linking the chemical composition detected remotely on an active region with in situ measurements acquired near 1 AU, thus localizing the solar sources of a transient event. Again, our model corroborates and explains those findings, as it shows that an interplanetary coronal mass ejection, even with very weak internal magnetic fields, could maintain a distinguished chemical composition during its motion in the interplanetary space with a limited mixing of the plasma.

# Chapter 4

## Connecting PSP in situ measurements and Metis remote sensing observations with the RIMAP model

### 4.1 Context

The Sun, the solar atmosphere, and the heliosphere are large and massive environments, the vastness of which makes it extremely difficult, if not impossible, to fully understand their phenomena through a single observation point. For instance, ICMEs at Earth's orbit have on average radial diameters about 0.4 AU, and they can span several tens of degrees in latitude (Jian et al., 2006; Kilpua et al., 2011).

Establishing a connection between solar plasma observed in the corona and its signature measured in situ in the interplanetary space, and finding events where multiple spacecraft observe the same phenomenon at different locations have been for long time goals in space weather research (Möstl et al., 2022). To this end, the number of spacecraft dedicated to the study of the heliosphere has significantly increased in the last years, shedding light on open questions related to the emergence of the solar magnetic field, the generation of the solar wind and the acceleration of energy particles.

Observations of the same solar wind plasma parcel at different points of measurement were first attempted by Schwartz and Marsch (1983) from studying a rare alignment between the twin Helios probes (one at 0.51 and the other at 0.72 AU), showing the radial evolution of solar wind temperatures during its expansion and founding evidences of ion perpendicular heating. Successive alignments in the inner heliosphere between Wind and MESSENGER (Bruno and Trenchi, 2014; Bruno et al., 2014; Telloni et al., 2015), and in the outer heliosphere between Wind and the Ulysses mission (Bruno and Trenchi, 2014) or ACE and Ulysses (D'Amicis et al., 2010) were exploited to study the evolution of solar wind turbulence and interplanetary coronal mass ejections (Telloni et al., 2020). In particular, Telloni et al. (2021b) recently investigated the first PSP-Solo of such alignments, showing the radial evolution of plasma turbulence from a highly Alfvénic state near the Sun, to fully developed turbulence at 1 AU.

Understanding the connection between remote sensing observations and in situ measurements is essential to exploit the strengths and overcome the disadvantages of both approaches (Telloni et al., 2021a; Velli et al., 2020). The former ones are critical to appreciate the global magnetic configurations of the solar corona, but are

affected by integrations along the line of sight (Dolei et al., 2018) (being the corona an optical thin plasma) and by the low cadence measurements of coronagraphs. The latter ones give direct access to the physical parameters of solar wind and coronal plasma and magnetic field, but they alone yield only a series of snapshots at single positions in space, and cannot provide information about the topology and the general three-dimensional view of the phenomena surrounding the probe, unless multiple in situ observations from a fleet of nearby spacecraft are combined. Finding this connection would provide the opportunity to track the solar wind and its related transients from their sources on the Sun to the inner interplanetary space and beyond. Among the possible configurations between two spacecraft which make this possible, quadratures are of particular interest. They happen when the angular separation of two probes is  $90^\circ$  with the Sun as point of reference, and they were first attempted with SOHO and Ulysses (Poletto et al., 2002; Suess and Poletto, 2001; Suess et al., 2000). Plasma observed by the UltraViolet Coronagraph Spectrometer (UVCS; Kohl et al., 1995) on board SOHO was later measured in situ when it left its coronal source in direction of Ulysses by its Solar Wind Ion Composition Spectrometer (SWICS; Gloeckler et al., 1992). SOHO and Ulysses offered this configuration twice a year until June 2009, when Ulysses ended mission operation. During this era, much was given to the study of solar wind parameters such as density, speed and temperature and their evolution across the heliosphere. Other quantities such as chemical composition, ionization state, and first ionization potential (FIP), which remain almost untouched by solar wind expansion due to them being froze-in, have been used to compare plasma properties from different solar wind streams and conclusively connect plasma measured in situ with its coronal source (Bemporad et al., 2003). These quadratures also allowed the scientific community to follow for the first time plasma observed during and after solar eruptions with remote sensing and in situ data (Bemporad et al., 2006; Owens, 2008; Poletto et al., 2004; Suess et al., 2004). Later on, with the launch of the STEREO probes in 2006, combinations of remote sensing and in situ data analysis focused on transient events (Innes et al., 2010; Kilpua et al., 2011, 2009; Möstl et al., 2009b). There were also attempts to identify the slow solar wind sources on the Sun, using abundance measurements carried out with the Extreme-ultraviolet Imaging Spectrometer (EIS; Korendyke et al., 2007) on board Hinode (Brooks et al., 2015; Brooks and Warren, 2011).

All the previous works made various assumptions to reconstruct the path followed by the solar plasma propagating from the inner corona towards the interplanetary medium. Here we illustrate a model that accurately reconstructs the Parker spiral and connects the coronal features observed remotely by the Metis coronagraph on board SolO with those detected in situ by PSP, at the time of the first SolO-Sun-PSP quadrature which occurred on January 2021 (Telloni et al., 2021a), by using RIMAP (Biondo et al., 2022).

In this application, RIMAP uses as internal boundary conditions the measurements collected by PSP between 0.1 and 0.2 AU, remapping them to 5 solar radii. The plasma and the magnetic field structures are then reconstructed according to the MHD equations solved with the PLUTO code up to 60 solar radii (as described in Biondo et al. (ibid.)). Our reconstruction connects density and wind speed measurements derived by Metis observations to those acquired by PSP along a single streamline.

## 4.2 Spacecraft data

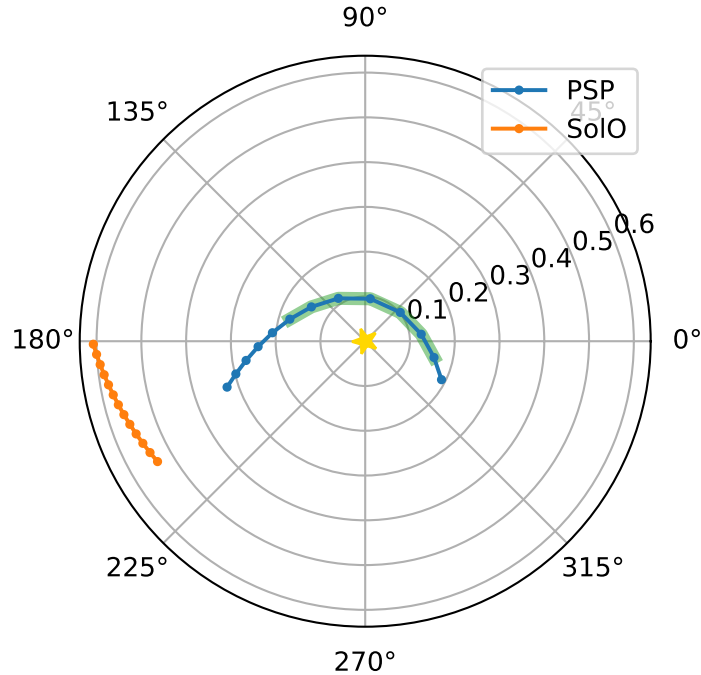


Figure 4.1: Positions of PSP and SolO in the Heliocentric Inertial (HCI) frame, from January 14th to January 25th 2021, during their first quadrature. Here thirteen data points for spacecraft are plotted, one for each day starting from January 14th, when PSP was at 0.19 AU from the Sun and  $\varphi=-25.74^\circ$ , while SolO was at 0.6 AU and  $\varphi=180.63^\circ$ . In green, the subset of PSP positions from January 15-21, when PSP was faster than the equatorial solar rotation, is highlighted.

Plotted using the Sunpy suite (The SunPy Community et al., 2020).

The measurements of Parker Solar Probe were collected from January 14th to 25th 2021, during its seventh solar encounter. In this configuration, its orbit placed PSP on the same side of the Sun as Earth, such that Earth-based observatories could observe our star and the solar wind coming from the visible solar disk from the same perspective as PSP. During encounter #7, PSP reached perihelion on January 17th, at 17:439:21 UT, at a heliocentric distance equal to 0.09 AU ( $20.3 R_\odot$ ), with an angle between Earth and PSP of  $30^\circ$ . The magnetic field data come from the fluxgate magnetometer of the FIELDS suite, while the plasma measurements were taken with the electrostatic analyzer SPAN-Ai of the SWEAP suite (see section 1.6.3 for a description of PSP instruments). Both were averaged at one minute resolution. Figure 4.2 shows the PSP’s positions and measurements during the time interval mentioned.

We further selected a subset of these measurements to be inserted as input for RIMAP, using as a criterion the longitudinal velocity of the spacecraft. Since from January 15th to 21th PSP was faster than the solar equatorial rotation, each solar wind stream during this period was sampled only once. Thus, using only measurements from this subset, there is no need to choose from different measurements of a single stream, and the raw data can be used.

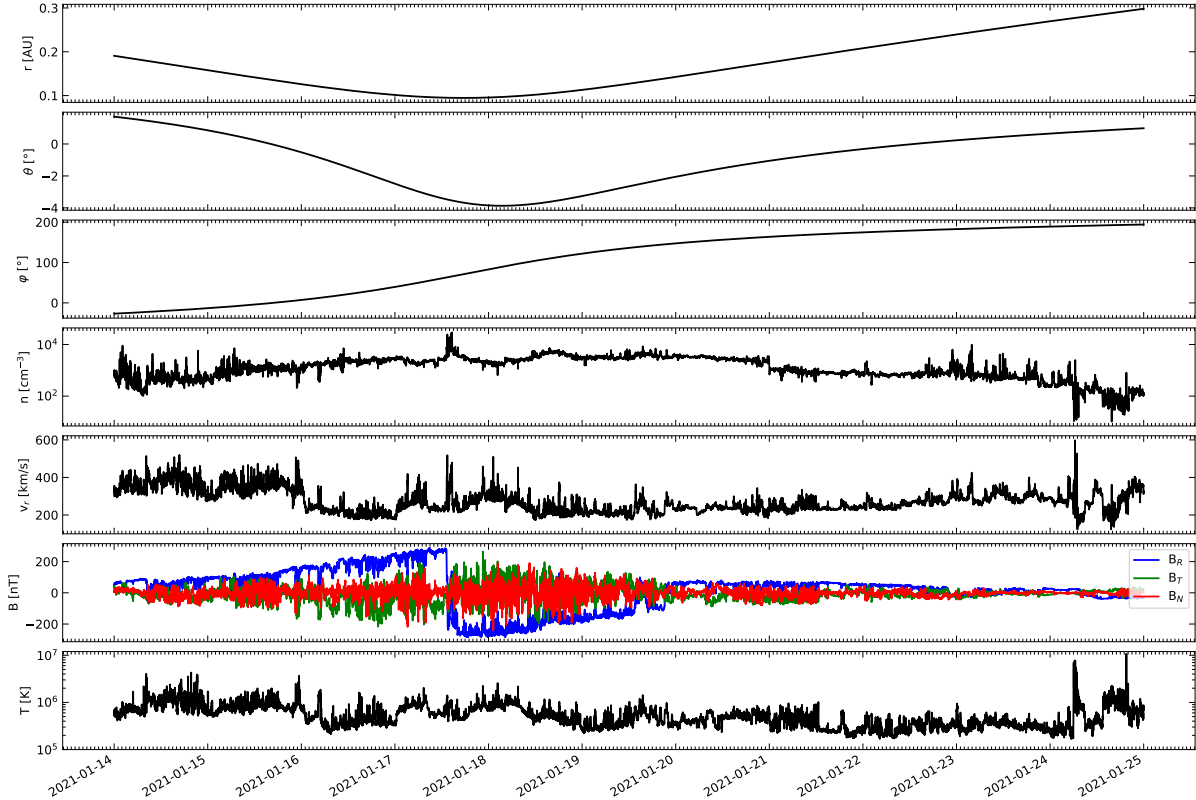


Figure 4.2: Positions and measurements collected by PSP from January 14 to January 25, 2021. From top to bottom: radial distance, latitude and longitude in the HCI frame, plasma density, radial speed, the components of magnetic field in the radial-tangential-normal (RTN) frame, and proton temperature. On January 17 at 13:30 UT and on January 19 at 21:00 UT, PSP crossed the heliospheric current sheet, as can be seen by the sudden change in polarity of magnetic field and by the associated density and speed increases.

When PSP reached perihelion, on January 17th, Solar Orbiter was at heliocentric distance equal to 0.583 AU. When the spacecraft was at  $188.9^\circ$  longitude from the Sun-Earth line and  $91.2^\circ$  colatitude (anti-clockwise from the north pole), the Metis coronagraph (see section 1.6.4) obtained simultaneous images in the visible light (VL) channel between 580 and 640 nm, and in the ultraviolet (UV) channel around the resonantly scattered HI Ly- $\alpha$  line at 121.6 nm (Antonucci et al., 2020). One polarized-brightness sequence of four polarimetric images and two UV images with detector integration times of 30 and 60 seconds respectively, were acquired in the time interval from 16:30 to 17:00 UT. Figure 4.3 shows the VL polarized brightness and the UV HI Ly- $\alpha$  coronal images of the solar corona in an annular field of view between 3.5 and 6.3 solar radii. In particular, its plane of the sky was at  $99^\circ$  longitude in the HCI frame.

The reduction of the Metis data follows the steps given in Romoli et al. (2021). As anticipated in Antonucci et al. (2020), the final radiometric calibration was verified and updated using calibration stars. The additional UV channel correction steps such as the correction of the spatial response disuniformity, were performed according to Andretta et al. (2021).

From the Metis data, the electron density and solar wind radial velocity on the plane-of-the-sky in the wind acceleration region were inferred, as discussed in Telloni

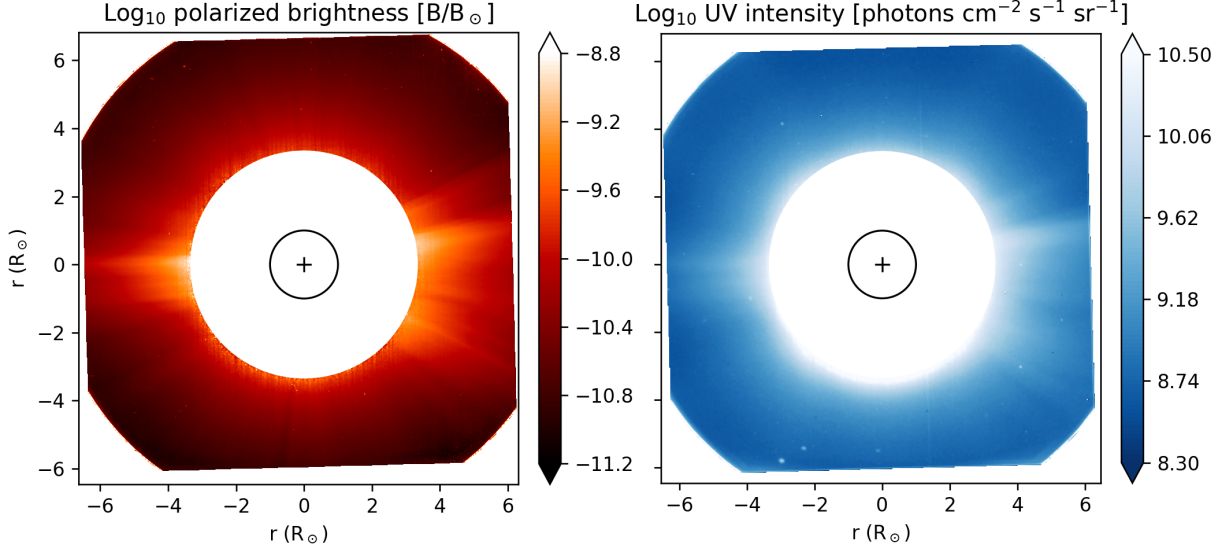


Figure 4.3: Metis coronal images of VL polarized brightness (left) and UV HI Ly-alpha (right) in the solar corona acquired on January 17, 2021, from 16:30 to 17:00 UT within the  $3.5\text{-}6.3 R_{\odot}$  field of view.

et al. (2022a) and Telloni et al. (2021a). Electron density is derived by inverting the polarized brightness data (fitted with a polynomial function) according to the technique developed by van de Hulst (1950). On the other hand, the coronal outflow velocity is inferred from the intensity of the hydrogen atoms, which to a very first approximation is a function of density and velocity. Therefore, relying on the electron density derived as above, and making plausible assumptions about the hydrogen temperature ( $T_p=1.6\cdot 10^6$  K; Antonucci et al., 2005), helium abundance (of 2.5%; Moses et al., 2020), and temperature anisotropy ( $T_{\perp}/T_{\parallel}=1.72$ ; as constrained by PSP observations), the intensity on the Lyman- $\alpha$  line was synthesized as a function of only the expansion velocity of the hydrogen atoms (Dolei et al., 2016, 2018). From the comparison with the intensity observed by Metis, the speed of the outflowing plasma was then estimated. Figure 4.6 shows the density and outflow velocity profiles estimates as black squares, for a single solar wind stream.

### 4.3 Magnetic connection between super and sub-Alfvénic Corona

We used RIMAP to connect the coronagraphic observation from Metis/Solo of the inner solar corona, just a few solar radii above the surface of the Sun, to in situ measurements collected by PSP just above the Alfvén radius, in the very inner heliosphere. The goal is to accurately reconstruct the connection between the two regimes, in order to provide a method to obtain detailed test benches for subsequent studies and modeling of the propagation of transient phenomena and MHD fluctuations such as turbulence and switchbacks.

The computational grid used here extends from 5 to 60 solar radii ( $\approx 0.02\text{-}0.27$  AU) in the radial direction, from  $89.0^{\circ}$  to  $91.0^{\circ}$  in the latitudinal direction, and from  $-28.65^{\circ}$  to  $171.89^{\circ}$  in the longitudinal one, in the HCI coordinate frame. The

longitudinal range is chosen to be a little narrower than the back-mapped PSP’s longitudes corresponding to the time interval in which the spacecraft was faster than the angular velocity of the solar equator  $\Omega_{\odot}$ . This is done in order to avoid the situation where the probe is slower than the rotation of the Parker spiral, and samples the same wind stream multiple times. The time-dependent MHD equation (1.20) are solved in a 3D spherical coordinate system corotating with the solar equator. The limited extension in latitude makes our description effectively 2D. The grid used has 256 cells in the radial direction, 8 in the latitudinal direction, and 1024 in the longitudinal one, all with uniform lengths. Hence, the cell aspect is maintained regular since the longitudinal extension is more than  $\pi$  times larger than the radial one. Although the Metis field of view is not entirely within the computational domain, it is far enough from the solar surface to exclude complex chromospheric and coronal structures which would affect the reconstruction of a steady Parker spiral. The domain largely includes the considered PSP orbit, which extends to about 30 solar radii at most in our longitudinal range. Table 4.1 summarises the computational grid parameters.

Direction	Interval	Number of cells	Style	Boundary conditions
$r$	$5.0 R_{\odot} - 60.0 R_{\odot}$	256	u	userdef-outflow
$\theta$	$89^{\circ} - 91^{\circ}$	8	u	reflective-reflective
$\varphi$	$-28.65^{\circ} - 171.89^{\circ}$	1024	u	outflow-outflow

Table 4.1: Computational grid used for the numerical simulation in this section.

As for the previous RIMAP applications, one uses the Parker spiral equation (1.32) to map in situ data to the inner boundary along their corresponding solar wind streamlines. At the inner boundary, the only non-zero speed component is the radial component, since the longitudinal one is null in the steady regime. Plasma temperature is rescaled as

$$T(5 R_{\odot}) = T(r_{\text{PSP}}) \left( \frac{r_{\text{PSP}}}{5 R_{\odot}} \right)^{0.5} \quad (4.1)$$

in order to obtain the best agreement between input and output profiles at the PSP orbit. As described in chapter 2, the temperature trend is a free-parameter in RIMAP.

The radial and longitudinal magnetic field components are rescaled according to Weber and Davis (1967), as discussed in section 2.2, while the latitudinal component is instead set equal to zero.

These scaled plasma and magnetic field parameters are used as inner steady boundary conditions to solve the time-dependent MHD equation with the PLUTO code. These conditions progressively build outwards a coherent Parker spiral, until a steady condition is reached throughout the computational domain.

### 4.3.1 Refinements of the RIMAP technique

As discussed in Section 2.2, the Parker spiral equation (1.32) is used to connect each PSP data point at  $r_{\text{PSP}}$  to a location in the RIMAP boundary at  $5 R_{\odot}$  through a streamline. When streamlines cross one another due to difference in speed, one is removed, such that each grid point at the inner radial boundary is connected to a unique PSP data point on its orbit, and the gaps in the plasma parameters

are filled by interpolating between the surviving remapped data. In chapter 2 and chapter 3 (and the corresponding works Biondo et al., 2021a,b) this preliminary phase was performed on in situ measurements from spacecraft with small-eccentricity heliocentric orbits (such as Wind and ACE), which were assumed to be circular. Now, instead, RIMAP can ingest input data from spacecraft with pronounced-eccentricity orbits (i.e. non constant heliocentric distances and irregular  $d\varphi$ ) such as PSP, SolO and BepiColombo.

Furthermore, improvements have been made in the construction of the internal boundary. In the previous iterations of RIMAP, the ballistic back-mapping was done between distances where the solar wind acceleration was negligible. This is no longer the case, since the focus of this chapter is the connection between the region of the solar atmosphere where most of that acceleration happens, and the region when it is starting to decline. A way to proceed would be to numerically integrate equation (1.31), assuming for each  $i$ -streamline radial speed  $v_{r\varphi_i}(r)$  varying with radial distance according to a Parker-like trend (the class II solutions depicted in figure 1.16), and assuming constant temperature  $T_i(r) = T_{\varphi_i}$ . However, so close to the solar corona, this assumption on temperature could be too simplistic. On the other hand, using more realistic radial trends for temperature (such as polytropic curves) could lead to unwanted complications in the back-mapping, which currently is the computationally lightest component of the RIMAP method. Instead, we used an empirical approach: one preliminary run of RIMAP based on the PSP in situ measurements was computed, assuming constant speed as in the previous iterations. Then, we computed the longitudinal average of the radial acceleration experienced by the wind in the this setup (similarly to what can be seen in figure 2.10), which was found to be approximately around 12.5%. Finally, in the final run, plasma and magnetic field parameters are mapped using the unaltered, measured speed, which is then appropriately reduced in the inner radial boundary, to compensate for the simulated acceleration along the streamlines outwards in the less dense medium.

### 4.3.2 Results

Figure 4.4 shows the Parker spiral reconstructed with RIMAP: from top to bottom, the maps of plasma density and velocity, and radial magnetic field are shown from 5 to 30 solar radii, with an inset in the lower left of each panel showing a close-up around the field of view (FOV) of Metis. The dashed arrowed black line is the PSP equatorial trajectory from which the data were extracted, the black segment is the Metis' FOV (3.5 to 6.3  $R_{\odot}$ , at the longitude of its plane of the sky (POS),  $99^\circ$ ), and the solid red line is the field line passing through the intersection between the PSP trajectory and Metis POS longitude.

The RIMAP technique allows one to reproduce the fine structures of the Parker spiral down to a size of  $0.2 R_{\odot}$ , which is sufficient as each of the streamlines extracted from the PSP data is individually discernible. Most of the reconstructed Parker spiral has low density ( $n(r/1 \text{ AU})^2 \leq 50 \text{ cm}^{-3}$ ). One portion of the domain, the one with  $\varphi < 90^\circ$ , is even less dense than the other one; exceptions include the streamline around  $15^\circ$ , the two close streamlines between  $45^\circ$  and  $60^\circ$ , and the ones around  $90^\circ$  that almost reach a density of  $150 \text{ cm}^{-3}$ .

As expected, the solar wind speed is overall anti-correlated with the plasma density according to the continuity Equation ((1.24a)), with values close to the average speed of 400 km/s. The lowest speed is found in a streamline between  $90^\circ$

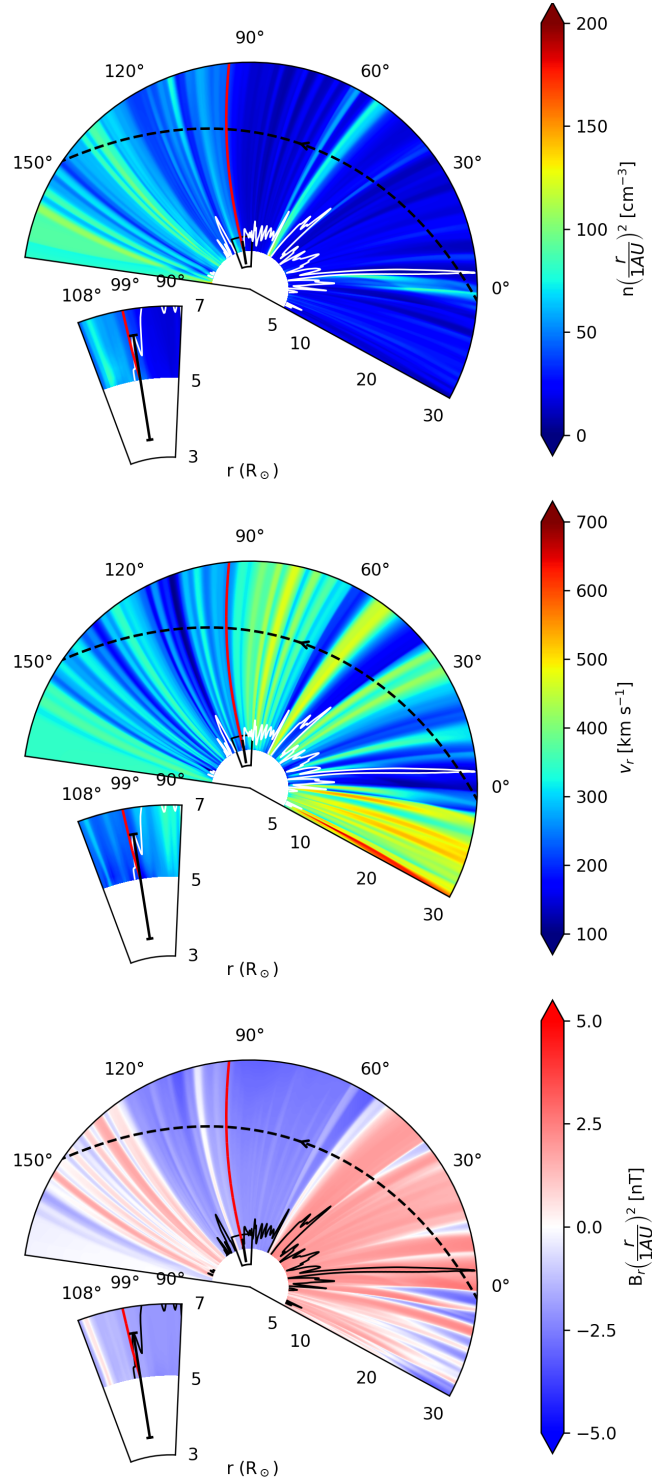


Figure 4.4: Equatorial maps of plasma density, radial speed and magnetic field as simulated by RIMAP, starting from the PSP data collected from January 15 to 21, 2021. The dashed black line is the PSP trajectory (projected on the equatorial plane), and the black segment from 3.5 to 6.3  $R_{\odot}$  is drawn at the Metis' plane-of-the-sky latitude on January 17. The solid red line is the field line connecting PSP measurements and Metis observations. The white line (black in the third panel) represents the Alfvén point for each streamline.

and 110° and is approximately 100 km/s, while the highest one (slightly less than 700 km/s) is found the the streamlines close to the initial longitudinal boundary of the

model, between  $-30^\circ$  and  $-15^\circ$ .

The radial component of the magnetic field shows three polarity inversions as the most striking feature: the first one at  $50^\circ$ , going from 2.5 to  $-2.5 (r/1 \text{ AU})^2$  nT, the second one one after  $120^\circ$ , where it goes from  $-2.5$  to less than  $1.25 (r/1 \text{ AU})^2$  nT, and a third one after  $150^\circ$ , where  $B_r$  returns negative. These inversions were in fact measured by PSP as it crossed the heliospheric current sheet (HCI).

Relying on the plasma and magnetic field estimates modelled by RIMAP, for each streamline it is possible to assess the Alfvén critical point, that is, the location where the solar wind speed equals that of the Alfvén waves and the Alfvén Mach number defined in Equation (1.44) is equal to one. This is displayed in Figure 4.4 as a function of the longitude (white line in the maps of density and speed, black in the  $B_r$  one), and provides a very interesting piece of information, marking where the wind becomes super-Alfvénic: this can be considered the outermost boundary of the solar corona (DeForest et al., 2014; Zhao and Hoeksema, 2010). For most of the reconstructed Parker spiral, the super-Alfvénic regime begins around  $10 R_\odot$ , with a significant outlier around 10 degrees, where the Alfvén point is  $30 R_\odot$  due to the presence of slow and dense solar wind in correspondence to a more intense magnetic field. During this orbit, PSP was thus traveling in a super-Alfvénic wind, and had not yet entered the solar corona.

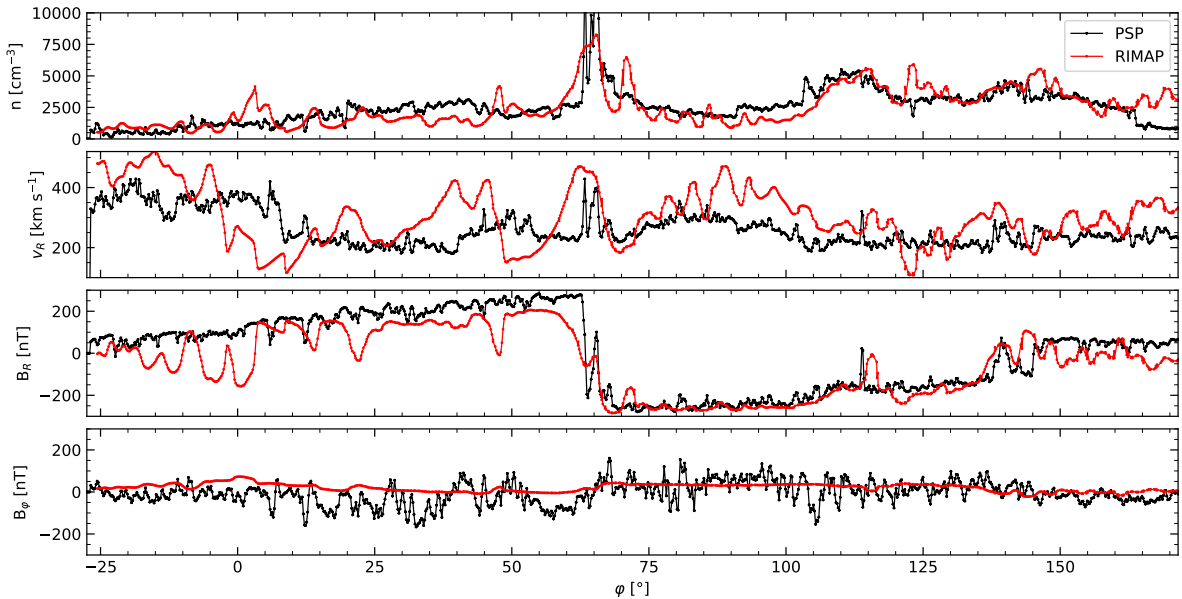


Figure 4.5: Comparison between PSP-measured (black) and RIMAP-modelled (red) solar wind parameters from January 15<sup>th</sup>-21<sup>st</sup>, 2021. From top to bottom, the panels display the proton number density, the solar wind speed, the radial, and the tangential components of the interplanetary magnetic field (RTN).

In figure 4.5 we scan the computational domain reproducing the trajectory of PSP in this perihelion transit. We then compare relevant solar wind measurements by PSP on this scan (black line) to the RIMAP results (red one). From top to bottom, the proton number density, the solar wind bulk speed, and the radial and longitudinal magnetic field components in the RTN coordinate system, taken along the PSP trajectory, are shown.

Remarkably, RIMAP reproduces the large-scale trends and the main features of the solar wind plasma sampled by PSP, especially the crossing of the heliospheric current sheet. The HCS-associated reversal of the background magnetic field, the null magnetic field intensity, and the enhancements of the bulk speed and plasma density are all satisfactorily modelled by RIMAP.

The major disagreements between PSP and RIMAP profiles in the density and magnetic field happen where the agreement between input and output speed is worst, in particular in correspondence with the longitude intervals of  $[-5^\circ; 15^\circ]$ ,  $[30^\circ; 55^\circ]$ , and  $[85^\circ; 110^\circ]$ , where the speed is over-estimated. As discussed in Section 2.2 (and Biondo et al. (2021a)), with RIMAP the slower solar wind streams followed by high bulk speed gradients are not well reproduced, since many of them are removed during the back reconstruction in order to assure physical consistency of the model by eliminating the crossings. Nevertheless, the proton density and the radial magnetic field show a good degree of accuracy in the reproduction of the main features encountered by PSP during the selected time interval, in particular during the HCS crossings at  $65^\circ$ ,  $115^\circ$ , and  $140^\circ$ .

It is worth noting that an equally good agreement between model and observations cannot be obtained for the transverse components of the magnetic field, since its full three dimensional treatment is still beyond the scope of RIMAP, in which the reconstruction of  $\mathbf{B}$  is based on the classical two dimensional description of Weber and Davis (1967) and Barker and Marlborough (1982). At the same time, PSP measurements show a transverse component of the magnetic field that is generally significantly smaller than the radial component and fluctuates around  $B_\varphi = 0$ . The global Parker spiral reconstruction made by RIMAP shows the same trend and thus it remains accurate even if it cannot reproduce the small-scale transients of the transverse magnetic field.

In order to test the likelihood of the Parker spiral reconstructed by RIMAP from PSP data in the very inner heliosphere, the model results extrapolated to the extended corona (i.e. for distances larger than  $5 R_\odot$ ) were compared with outflow velocity and plasma density estimates inferred from Metis observations (acquired on January 17 at 16:30-17:00 UT, when SolO was in quadrature with PSP at the east limb), as discussed in the previous section.

Figure 4.6 shows the observed and modelled outflow velocity and proton number density (a helium abundance of 2.5% is assumed to relate electron and proton density; Moses et al., 2020) along the same streamline, in the top and bottom panel, respectively. Metis observation are represented by black squares, PSP measurements by red ones, while the RIMAP reconstruction is the solid red line. Observed and modelled quantities are in striking agreements with each other, indicating that the RIMAP reconstruction of the Parker spiral is very reliable. On the other hand, the consistency of the model profiles with the observations corroborates the calibration and the reliability of Metis data processing.

After the steep radial trend close to the solar surface (similar to the profiles found for coronal streamers by Gibson et al., 1999), proton density begins to decline with a slope akin to those of Cranmer et al. (1999) and Guhathakurta et al. (1999), reaching approximately  $3 \cdot 10^3 \text{ cm}^{-3}$  at  $21.4 R_\odot$ , above the the corresponding measurement of PSP.

Solar wind across the selected streamline starts with the sharp Parker-like acceleration close to the Sun, before attaining an almost constant speed of nearly 250 km/s, very close to the one measured by PSP at 21.4 solar radii.

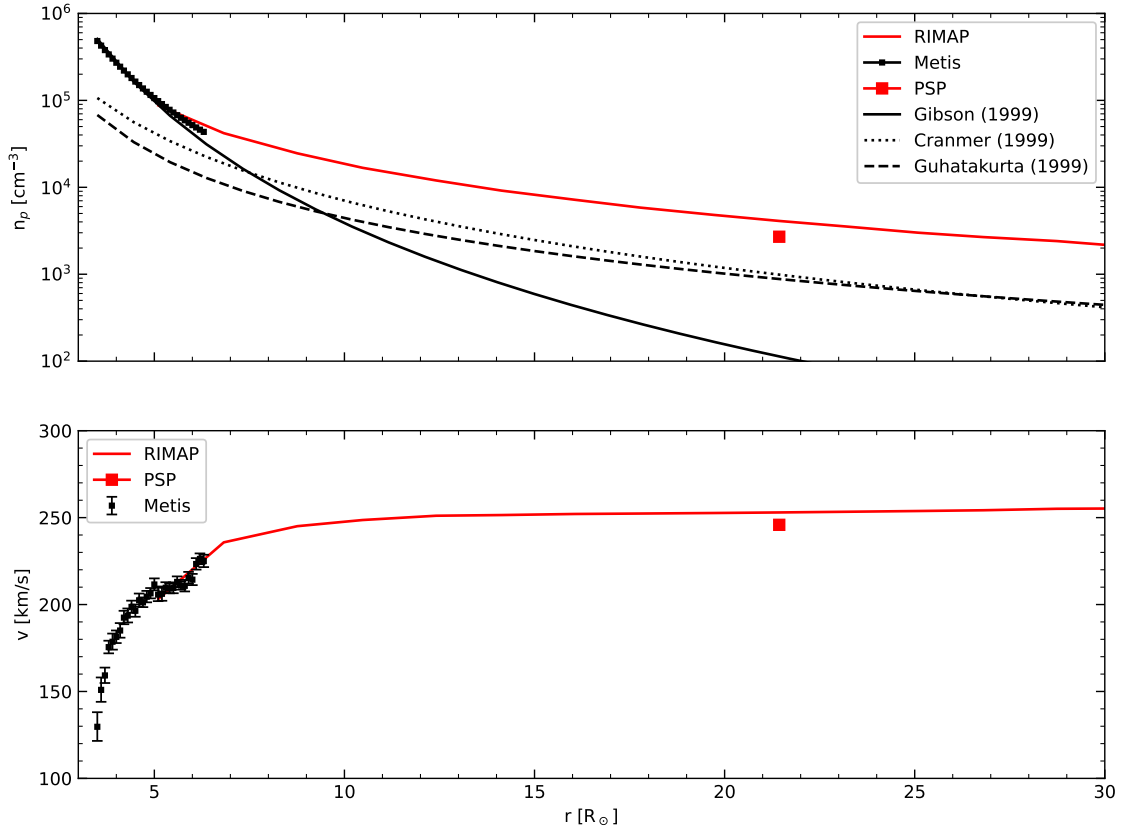


Figure 4.6: Comparison between observed (squares) and RIMAP-modelled (red line) proton number density (top panel) and outflow velocity (bottom panel) along the streamline highlighted in figure 4.4, from 3 to 25  $R_{\odot}$ . Black and red squares refer to Metis and PSP estimates, respectively.

## 4.4 Conclusions

Multi-spacecraft observations constitute a fundamental tool for the full understanding of solar phenomena and their dynamic evolution, as well as the full distribution of the solar wind from a purely observational point of view (Hadid et al., 2021; Velli et al., 2020). Among the possible configurations that can be assumed by two or more spacecraft, the quadratures offer the opportunity to remotely observing from a spacecraft the plasma parcel that would later be detected in situ by another one. This gives the possibility to reconstruct the magnetic connectivity of plasma observed in the interplanetary space with its source near the Sun.

The inner heliospheric missions of Parker Solar Probe and Solar Orbiter are devoted to the understanding the mechanisms at the heart of the solar wind physics. By design, cooperation between the two spacecraft is encouraged by their complementarity, and further enhanced by the presence of other assets along the Sun-Earth line. (Velli et al., 2020).

Using observations from the first PSP-Sun-SolO quadrature of January 2021, Telloni et al. (2021a) followed, for the first time, the same plasma parcel of solar wind from the sub-Alfvénic solar corona (observed with the Metis coronagraph on board SolO), to just above the Alfvén surface, where PSP measured its in situ properties. Their work studied the magnetic connection between the two regions relying on an empirical function to extrapolate the radial coronal magnetic field, and then estimate the values of Alfvén speed, Alfvén radius, and bulk kinetic density of the solar wind

in the acceleration region.

A first theoretical modeling of the joint PSP-Metis/Solo observation during their first quadrature was presented in Adhikari et al. (2022), using the Near Incompressible MHD theory (NI MHD; Zank et al., 2017) to model the heating of the turbulent slow solar wind flowing from the extended corona to the very inner heliosphere. Their modelled profiles of density, speed, and pressure are very similar to PSP measurements.

In this part of the work, instead, we used the hybrid analytical-numerical MHD model RIMAP (see chapter 2 and Biondo et al., 2021a) to obtain a detailed reconstruction of the Parker spiral, binding it to PSP in situ data collected between January 15 and 21, 2021.

This required improving the model over its previous iterations. As discussed in section 4.3.1 and in Biondo et al. (2022), RIMAP can now ingest as inputs also data from spacecraft with pronounced eccentricity orbits and thus non-constant heliocentric distances and irregular  $d\varphi$ . In addition, we made improvements in the ballistic construction of the internal boundary, which now takes into account the acceleration experienced by the solar wind during the expansion of the streamlines, conveniently reducing the speed in the back-mapping phase.

We accurately modelled the super-Alfvénic wind in which PSP traveled, several crossings of the heliospheric current sheet, and the structured shape of the Alfvén surface, finding results in overall agreement with the measurements of PSP and the estimates of Telloni et al. (2021a) and Verscharen et al. (2021).

Then, we extracted the streamline passing through the intersection of the longitude of the Metis plane of the sky on January 17, with the PSP trajectory. In this way, a detailed data-driven MHD simulation magnetically connect the plasma properties detected in the outer solar corona by PSP to those observed immediately above the solar surface by Metis/Solo (Biondo et al., 2022).

The satisfactory agreement between the remote-sensing observation of Metis and the in situ measurements of PSP confirms the validity of RIMAP reconstructions of the Parker spiral even at heliocentric distances very close to the Sun. Moreover, it offers a glimpse on the possibilities offered by multi-spacecraft observations to investigate heliospheric physics and the connection between the through the refinement of MHD simulations at unprecedented level of detail. In particular, close-to-the-Sun simultaneous observations of the same solar wind plasma are a big step forward in the estimation of coronal magnetic fields (Telloni et al., 2022a; Telloni et al., 2021a), since these are not directly measurable. The accuracy offered by MHD simulations will likely improve vastly as PSP and Solo approach distances closer to the Sun, especially when the former enters the solar corona, and even more when the latter will reach higher solar latitudes.

Further application of RIMAP will include the PSP-Sun-Solo quadrature occurred on June 2022, during which PSP was just  $0.4 R_{\odot}$  of the Metis field of view and, very likely, in the sub-Alfvénic regime. RIMAP could then be used to reconstruct remote-sensing and in situ measurements of the coronal plasma and magnetic field. Furthermore, accurate reconstructions of the very inner Parker spiral bound to in situ data could provide a more than adequate test bench for the study and model of the early propagation of transient phenomena and MHD fluctuations such as turbulence and solar wind switchback (Bale et al., 2019, more in section 5.1).

# Chapter 5

## Future prospects and conclusions

The studies described in this thesis open the way to interesting future developments of the RIMAP model. We discuss some of them in the following.

### 5.1 Switchback simulations

One of the first dramatic observations (Velli et al., 2020) made by the Parker Solar Probe during its first orbit around the Sun was that of extremely large, intermittent amplitude oscillations in the radial magnetic field. They are associated with jets of plasma and enhanced Poynting flux, interspersed in a smoother and less turbulent flow with near-radial magnetic field, with a duration going from seconds to tens of minutes (e.g. Bale et al., 2019; de Wit et al., 2020; Kasper et al., 2019; Rouillard et al., 2020; Schwadron and McComas, 2021). These reversals of  $B_r$  (some of them depicted in figure 5.2) did not correspond to crossings of the heliospheric current sheet, as demonstrated by the permanence of the electron pitch angle (Bale et al., 2019; Velli et al., 2020), but instead they are rapid S-shaped folds in the magnetic field, as depicted in figure 5.1. They are called switchbacks.

By looking to the in situ profiles, it is noticeable how the fluctuations in radial velocity  $\delta v_R$  are correlated to those of  $\delta B_R$ , corresponding to outwards-propagating Alfvén waves. Moreover, the magnitude of total magnetic field is almost constant, meaning that the compressibility of the fluctuations is very small (Velli et al., 2020). Therefore, the vectors of  $\mathbf{B}$  and  $\mathbf{v}$  rotate on a sphere: switchbacks are spherical-arc, polarized, large-amplitude Alfvén waves (Matteini et al., 2019). Such waves have one interesting property: in correspondence of a magnetic field with an S-shaped fold, the radial component of the velocity must always present a positive enhancement, that is, a radial jet (Matteini et al., 2019; Velli et al., 2020).

Before the PSP observations, magnetic switchback have been studied at 1 AU in fast solar wind from coronal holes (e.g. Kahler et al., 1996), beyond 1 AU with *Ulysses* (e.g. Balogh et al., 1999; Neugebauer and Goldstein, 2013), and inside 1 AU with the *Helios* probes (Borovsky, 2016; Horbury et al., 2018). However, extensive measurements by PSP suggest that the presence of switchbacks increases drastically near the Sun (Bale et al., 2019; Kasper et al., 2019). These strong deviations from the Parker-spiral-like magnetic field are observed in correspondence to increases in radial solar wind speed (Michel, 1967) and are associated with pulsed or one-sided Alfvénic fluctuations (Gosling et al., 2009, 2011). In PSP measurements, this one-sided feature is especially clear: if the magnetic field rotates more than  $60^\circ$ , then its tangential component  $B_T$  is always positive and the tangential proton velocity

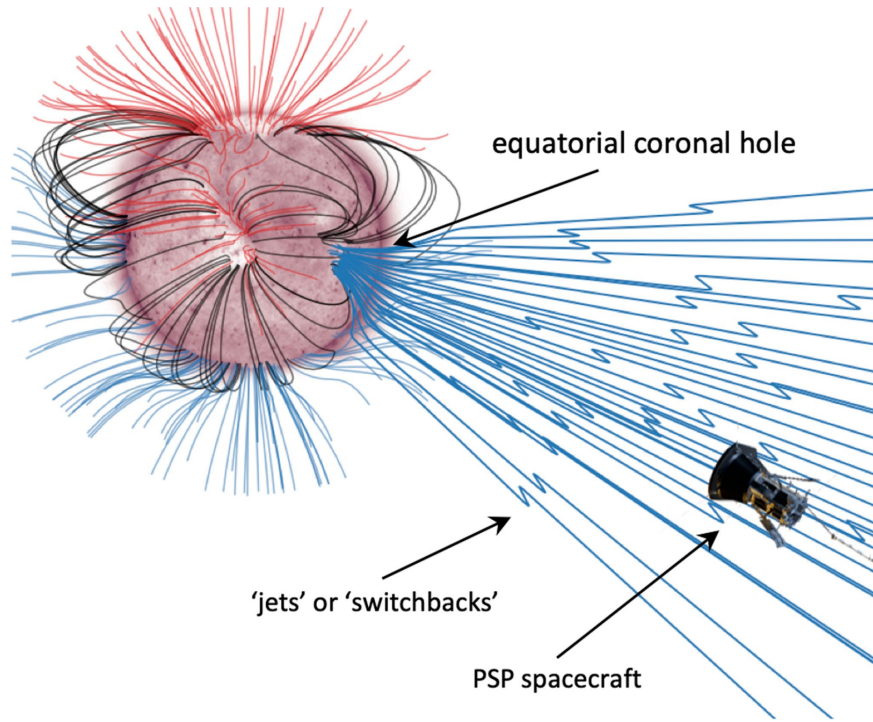


Figure 5.1: Schematics of the magnetic field crossed by PSP during its first solar encounter, when the switchback observations happened. The solar surface is shown coloured by the EUV emission in the 211 Å line as measured by SDO, with coronal holes appearing as lighter shades. The magnetic field line depicted come from a PFSS extrapolation of the solar magnetic field at the time of the first PSP perihelion. Black lines represents closed loops, blue and red lines are open field lines with negative and positive polarities, respectively. The switchback are illustrated as S-shaped kinks in the open field lines emerging from the coronal hole.

Reproduced from Bale et al. (2019), © Springer Nature.

$v_T$  always exceeds 33 km/s (Kasper et al., 2019). These large transverse flows far exceed those considered by the axisymmetric Weber and Davis (1967) model, in which  $v_T(r_A) < 0.1\Omega_\odot r_A$  (Kasper et al., 2019; Schwadron and McComas, 2021): for  $r_A = 15 R_\odot$ , it should be  $v_T(r_A) < 3$  km/s according to Weber and Davis (1967). One-sided transverse flows are key observable from PSP that any theoretical formulation of switchbacks must explain (Schwadron and McComas, 2021).

The mechanisms responsible of generating the switchbacks are under debate (Telloni et al., 2022b). It is not clear if they are self-consistently generated in the solar wind (Shoda et al., 2021; Squire et al., 2020) or driven by lower solar atmosphere processes (Magyar et al., 2021). Their average occurrence features observed by PSP suggest a possible source in the coronal transition region rather than in situ (Bale et al., 2021; Fargette et al., 2021; Mozer et al., 2021), nevertheless different models have been proposed. Switchbacks could be a signature of magnetic reconnection events in the solar corona (e.g. Fisk and Kasper, 2020; Zank et al., 2020) or they could be geometrical effects associated with the motion of coronal magnetic field footpoints from slow to fast solar wind sectors (Schwadron and McComas, 2021). They could be Alfvénic structures originating in the low corona and propagating outwards into interplanetary space (as suggested by MHD simulations, see e.g. Jakob and Brandenburg, 2021; Matteini et al., 2015) or be related to dynamics driven by velocity-shear instabilities (Landi et al., 2006; Ruffolo et al., 2020).

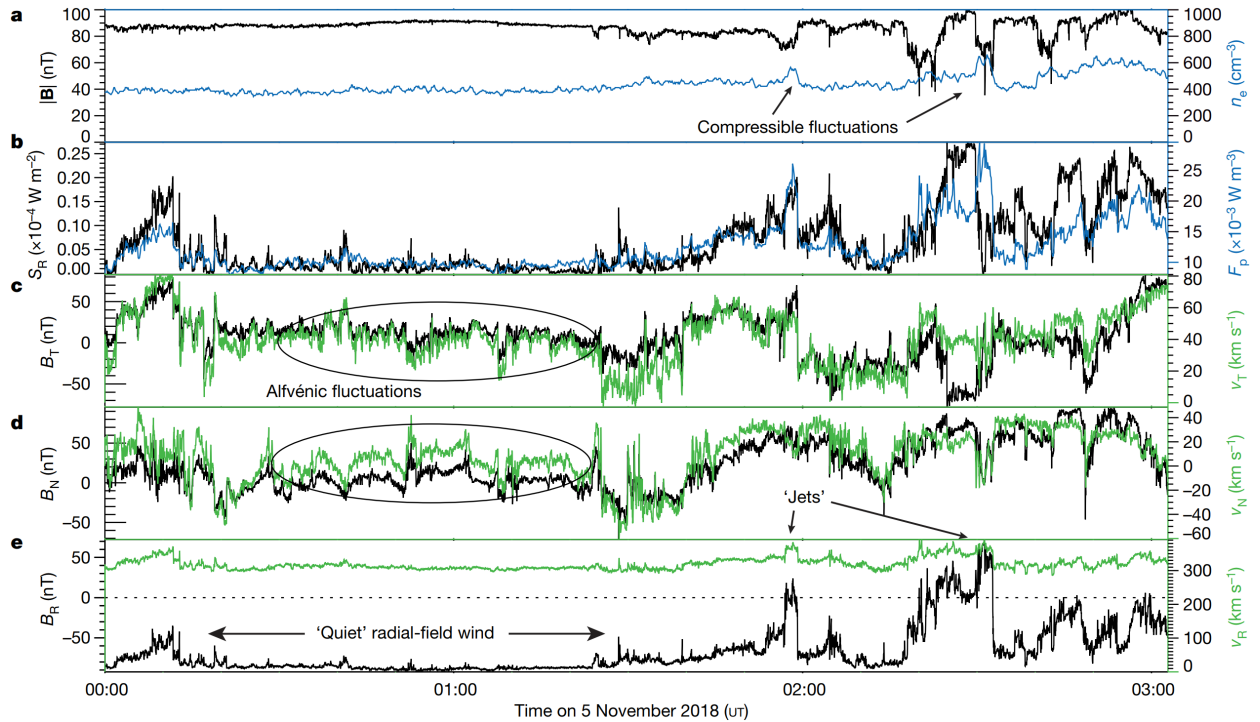


Figure 5.2: Time profiles of PSP taken on 5 November 2018 UT at about  $36.6 R_{\odot}$ , showing switchbacks as radial magnetic field reversals and plasma jets carrying a Poynting flux. Panel a shows magnetic field magnitude ( $|\mathbf{B}|$ , black line) and electron density ( $n_e$ , blue line). Panel b show the radial Poynting flux ( $S_R$ , black line) and ion kinetic energy ( $F_p$ , blue line). The last three panels shows the components of  $\mathbf{B}$  (black lines) and plasma velocity ( $\mathbf{v}$ , green lines) in the RTN system: the non radial components show Alfvénic fluctuations, while the radial ones shows a large enhancement of radial field in correspondence to jets of plasma. Reproduced from Bale et al. (2019), © Springer Nature.

Using the MHD PLUTO code, we performed a first, simple test simulation of a switchback within the RIMAP framework. We explore the possibility that they are produced by the propagation of disturbances expelled from the low corona. The goal of the preliminary simulation is to reproduce the in situ signatures associated with switchbacks, mainly the reversals of  $B_r$  and enhancements of  $v_r$  measured by spacecraft such as PSP.

We used a computational domain spanning from  $5$  to  $30 R_{\odot}$ ,  $89^{\circ}$  to  $91^{\circ}$ , and  $0$  to  $30^{\circ}$  in the radial, latitudinal, and longitudinal direction respectively. The number of grids points is 256, 8, and 256. Table 5.1 summarizes the grid parameters used for the test simulation.

Direction	Interval	Number of cells	Style	Boundary conditions
$r$	$5.0 R_{\odot} - 30.0 R_{\odot}$	256	u	userdef-outflow
$\theta$	$89^{\circ} - 91^{\circ}$	8	u	reflective-reflective
$\varphi$	$0.0^{\circ} - 30^{\circ}$	256	u	periodic-periodic

Table 5.1: Computational grid used for the test simulation of switchbacks.

At the initial background condition, the computational domain is filled with the spherically symmetric profiles taken from Perrone et al. (2019) and described

in section 2.2.1. The inner radial boundary at 5 solar radii is latitudinally and longitudinally uniform, with values of density, radial speed, and radial, latitudinal, and longitudinal magnetic field being, respectively, equal to  $10^4 \text{ cm}^{-3}$ , 250 km/s,  $10^4$  nT, 0 nT, and -10 nT. Solving the MHD equations in the solar corotating frame as in Eq. (2.30), plasma and magnetic field flowing from the inner radial boundary fill the computational domain until a steady state is reached approximately in  $500 t_0$ , around 10 days of code time.

Then, at  $t = 0$ , a bounded perturbation consisting of a time-limited fast plasma stream is injected as a time-dependent boundary condition: at the computational cells corresponding to the longitudes between  $17.5^\circ$  and  $18^\circ$  at  $5 R_\odot$ , the former values of density and radial speed are replaced by  $2.5 \cdot 10^3 \text{ cm}^{-3}$  and 1000 km/s for a time interval of 1.2 hours. The magnetic field of the perturbation is the same of the unperturbed medium.

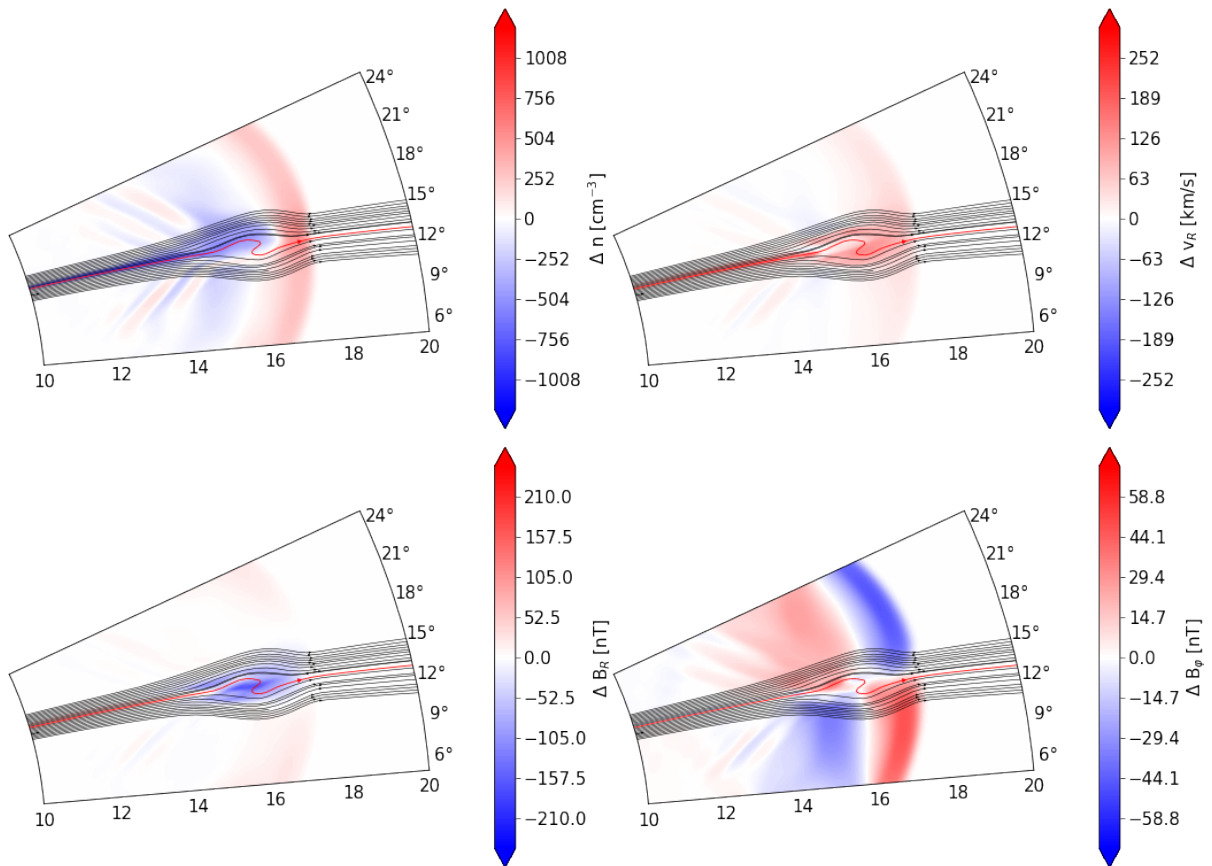


Figure 5.3: Close-ups of the propagation of a faster jet of plasma in a uniform medium. In the four panels, the difference between the particle density (top left), radial velocity (top right), radial magnetic field (bottom left), and longitudinal magnetic field (bottom right) at  $t = 0$ , before the perturbation enters the domain, and their values at  $t = 220 t_0 \approx 4.43$  days. Plotted as black and red arrowed lines, the magnetic field lines on the equatorial plane. A reversal of magnetic field that resembles a switchback (marked by the red field line) can be seen just behind the perturbation front.

Figure 5.3 shows a snapshot of the simulation, as equatorial maps of the difference between the pre-perturbation values of number density, radial speed, radial and longitudinal field at  $t = 0$ , and those at  $t = 220 t_0$ , when the tip of plasma stream

has reached  $15 R_{\odot}$ . As the fast thin wind stream propagates in the denser, slower medium, it is slowed down until it starts to dissipate; it forms a front of enhanced density ahead of itself followed by a depression; and it causes ripples in the adjacent background streams. The radial component of magnetic field, which is enhanced with respect to the ambient value along the fast stream and in the extremities of the perturbation front, presents instead a reduction of  $\sim 200$  nT behind the front. The longitudinal component is divided in four quadrants: two of enhancement ( $+50$  nT) with respect to the ambient  $B_{\varphi}$  and two of decrease ( $-50$  nT). Therefore, magnetic field lines in correspondence of the fast thin stream are bent in an S-shape, very reminiscent of the feature we are trying to simulate.

The resulted orientation of the simulated switchback is consistent with the findings of Fargette et al. (2022), which observed a systematic bias in these deflections towards lower values of  $\varphi$  (that is, in the clockwise direction) regardless of the main magnetic field polarity. The authors also found a slight latitudinal bias, also independent of magnetic polarity, which cause the majority of switchbacks to lean towards the equator. Future three-dimensional simulations of this phenomenon should be able to capture this behaviour.

Since an important signature of switchbacks is the increase in the Poynting flux, the next natural step is to introduce also a perturbation of magnetic field in the fast thin stream. Moreover, in the future we plan to introduce a perturbation of this kind in a RIMAP-reconstructed Parker spiral built from PSP in situ measurements, in order to reproduce them and thus investigating some of the possible mechanisms of switchback's formation.

## 5.2 Magnetized ICMEs

As discussed in section 1.2.3 and 1.5, while only one third of ICME events show clear signatures of magnetic clouds, it is commonly accepted that this fraction is significantly larger (see e.g. Kilpua et al., 2017, and reference therein). Due to their simplicity of use, heliospheric MHD models such as ENLIL still use cone models for their routine space-weather applications. However, in recent years a transition is happening towards more sophisticated models (e.g. Verbeke, C. et al., 2019).

Magnetic clouds can be modelled as magnetic flux ropes in force-free (when plasma effects can be neglected, e.g. Vandas and Romashets, 2003) or non-force-free (e.g. Hidalgo, 2016) configurations. Great interest also revolves on flux ropes because their instabilities can trigger and drive coronal eruptions (Titov et al., 2014). There is convincing observational evidence that magnetic clouds are part of curved flux rope loops (Kilpua et al., 2017), and local curvature of its axis can be taken into account using toroidal geometry (e.g. Hidalgo, 2016; Titov and Démoulin, 1999; Titov et al., 2014).

A natural progression of the work described in chapter 3 is the insertion of a magnetized perturbation in order to simulate the propagation of a magnetic cloud. As discussed in the conclusion of that chapter, we found that the cone-modelled ICME did not undergo significant erosion, since the absence of magnetic field implies no reconnection with the interplanetary magnetic field. Choosing the global morphology of the modelled magnetic field is not a trivial task, since it can have drastic effects on the results and their interpretation (Kilpua et al., 2017; Scolini et al., 2019). Figure 5.4 shows four different possible geometry choices for a magnetic cloud model: a torus model similar to that of Titov and Démoulin (1999); a cylindrical model,

similar to that of Low and Berger (2003); a curved flux rope loop with the flanks still attached to the Sun; a spheroidal model, similar to the spheromaks of Shiota and Kataoka (2016).

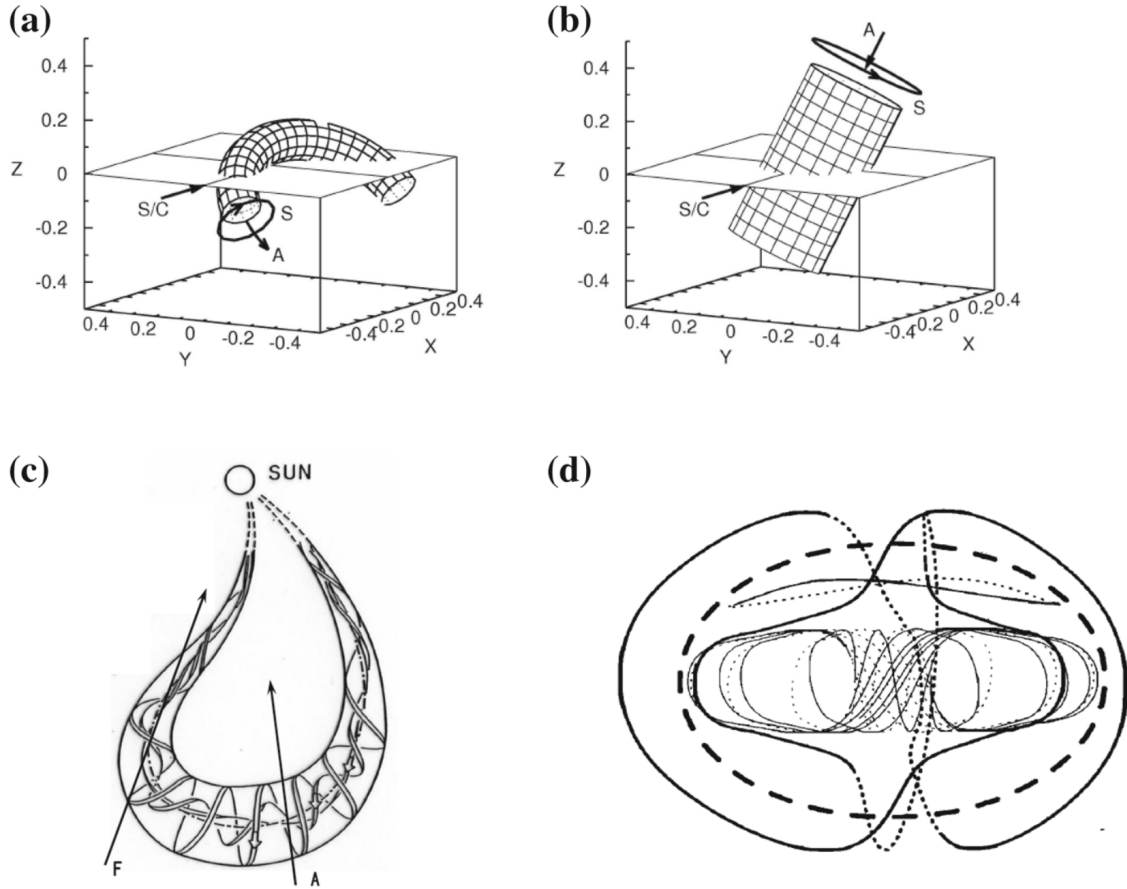


Figure 5.4: Four different global topologies for magnetic clouds models. Top row shows a toroidal configuration on the left, with S being the the magnetic field on the torus surface, A the axial field, and S/C the spacecraft trajectory; on the right top row a cylindrical flux rope model, with S, A, and S/C having the same meaning of panel (a); the bottom row shows on the left a curved flux rope loop, with arrows A and F indicating two different kinds of spacecraft encounter; on the right bottom row, a spheroidal oblate flux rope, with solid lines depicting the field lines above the plane of the figure, and the dashed lines depictig those below it.

Panels a-b-c reproduced from Marubashi and Lepping (2007), © to the authors; Panel d is reproduced from Vandas et al. (1993), © American Geophysical Union.

While the curved force-free flux ropes can describe very precisely the magnetic field data within the clouds (Marubashi and Lepping, 2007), their pre-release phase requires coupling with full-MHD coronal models such as MAS or PFSS and SCS extrapolations, that is, three-dimensional models with considerable latitudinal apertures. Nevertheless, the reconstructions of RIMAP are obtained from in situ data acquired on orbital planes very close to the ecliptic, thus we mostly deal with quasi-two dimensional configurations (until an extension to the third dimension is developed, as discussed in section 5.4). Therefore, adapting a cylindrical model is the most straightforward step.

We plan to combine the full ice-cream cone model described in chapter 3 with the Gold and Hoyle (1960) solution (1.51) of the force-free equation (1.49). The

cone-model assumes that, before entering the computational domain, the ICME bubble keeps constant angular widths and velocity  $\mathbf{v}_{\text{ICME}}$  (as depicted in figure 3.1). Therefore, we write the magnetic field expression (1.51) in the frame of reference moving with the plasma bubble, which in cartesian coordinates with  $z$ -axis chosen to be parallel to the solar one, is written as

$$\begin{aligned} B_x(t) &= k \left( y - \mathbf{v}_{\text{ICME}} \cdot \hat{\mathbf{j}}t \right) B_z \\ B_y(t) &= k \left( x - \mathbf{v}_{\text{ICME}} \cdot \hat{\mathbf{i}}t \right) B_z \\ B_z(t) &= \frac{B_0}{1 + k^2 \left( \left( x - \mathbf{v}_{\text{ICME}} \cdot \hat{\mathbf{i}}t \right)^2 + \left( y - \mathbf{v}_{\text{ICME}} \cdot \hat{\mathbf{j}}t \right)^2 \right)} \end{aligned} \quad (5.1)$$

where  $\hat{\mathbf{i}}$  and  $\hat{\mathbf{j}}$  are the versors in the  $x$  and  $y$  direction, respectively. This combination of cylindrical flux-rope and cone model will be inserted into the computational domain of a RIMAP-reconstructed Parker spiral as a time-dependent internal boundary. We will study the propagation of the magnetized ICME and compare the results to the unmagnetized case.

### 5.3 Two-fluid treatment

A further step in increasing the realism of RIMAP reconstructions and simulations would be the extension from the the Parker (1958) and Weber and Davis (1967) treatment of the solar wind to a two-fluid model. In fact, in solar wind the interaction between protons and electrons is too weak to equalise their temperatures (Priest, 2014). Therefore, it is natural to picture protons and electrons as separate fluids that possess the same number density  $n = n_p = n_e$  (due to charge neutrality), the same velocity  $v$  (since the Sun is electrically neutral) but different temperatures  $T_p$ ,  $T_e$  and heat fluxes  $Q_p$ ,  $Q_e$  (Hartle and Sturrock, 1968).

Since proton and electron masses differ by a factor of  $m_p/m_e \approx 1837$ , electrons have a larger thermal speed by a factor  $(m_p/m_e)^{1/2} \approx 43$ . Because of this, protons feel the solar gravity, much more than electrons; in order to preserve quasi-neutrality, an electric field must be in place between protons and electrons; protons carry heat much more slowly than the electrons; since they are weakly collisional, proton and electron temperatures differ; their energy exchange-rate is a factor  $m_p/m_e$  slower than their momentum exchange.

Thus, assuming that for electrons inertia and gravity can be neglected (since  $m_p \gg m_e$ ), the equation of mass continuity and for the conservation of proton and electron momentum are (Priest, 2014):

$$4\pi r^2 n v = \text{constant} \quad (5.2a)$$

$$n m_p v \frac{dv}{dr} = -\frac{d}{dr} (n k_B T_p) + n e E - \frac{G M_\odot n m_p}{r^2} \quad (5.2b)$$

$$0 = -\frac{d}{dr} (n k_B T_e) - n e E \quad (5.2c)$$

If the collisional energy-transfer between particles is negligible, the energy equations apply separately for protons and electrons, and the proton heat flux is much

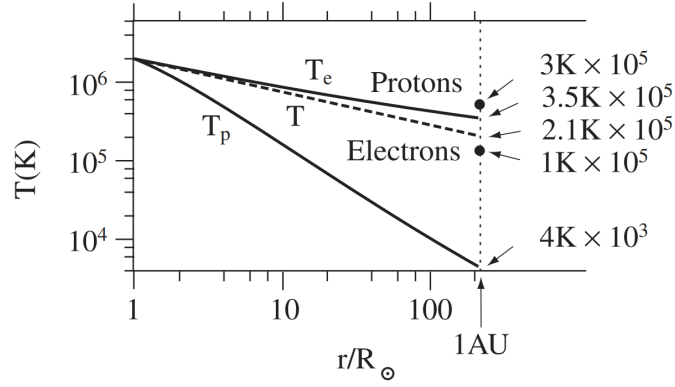


Figure 5.5: Proton and electron temperatures as functions of distance (solid lines), for the classical two-fluid solar wind model of Hartle and Sturrock (1968). The single-fluid profile is shown in dashed lines. Observed values for fast solar wind streams are shown by dots.

Reproduced from Priest (2014), © Cambridge University Press.

smaller than the electron one (Hartle and Sturrock, 1968; Priest, 2014):

$$\frac{d}{dr} \left( \frac{n}{T_p^{3/2}} \right) = 0 \quad (5.3a)$$

$$\frac{k_B T_e^{5/2}}{n} \frac{d}{dr} \left( \frac{n}{T_e^{3/2}} \right) = \frac{d}{dr} \left( \frac{Q_e}{nv} \right). \quad (5.3b)$$

The first equation implies that the fluid composed by protons is adiabatic, with  $T_p \propto n^{2/3}$  and thus for  $r \rightarrow \infty$   $v \sim \text{constant}$ ,  $n \propto r^2$  and  $T_p \propto r^{-4/3}$ . The second equation instead implies that, when the heat flux  $Q_e$  drops more rapidly than  $nv$ , the electron temperature will fall off less rapidly than the proton temperature. These equations can also be generalized to include the proton heat-flux and the collisional energy exchange term  $\propto \nu(T_e - T_p)$ , where  $\nu$  is the frequency of collisions, which is important close to the Sun. Numerical integration gives the temperature profiles shown in figure 5.5.

In a single fluid model, such as the one currently implemented in RIMAP, the 1 AU temperature is typical around  $2 \cdot 10^5$  K. The two-fluid model of Hartle and Sturrock (1968) instead gives for electrons a 1 AU temperature higher ( $T_e \approx 3.5 \cdot 10^5$  K) than for protons ( $T_p \approx 0.04 \cdot 10^5$  K). Protons cool adiabatically, while the electrons, no longer forced to share their energy with protons, remain hot. These values do not agree well with fast solar-wind observations, since  $T_e$  is too high,  $T_p$  is too low, and  $v$  is also too low. Much more sophisticated models exist however, that include, for instance, extra energy sources for the protons above the Alfvén critical point in order to enhance their temperatures and flow speed (e.g. van der Holst et al., 2010), the separate treatment of flows parallel and perpendicular to the magnetic field, and anisotropic temperatures (e.g. Hu et al., 2000), and the inclusion of heavier ions (e.g. Lie-Svendsen and Esser, 2005).

Currently, temperature is a free parameter in RIMAP, that we tune in order to obtain the best overall agreement between input and output information. The validity of this assumption is limited by having to use a single-fluid picture of the solar wind. Implementing one of the above mentioned models into RIMAP could be beneficial to the quality of reconstructions and validity of MHD simulations, since it

will allow to impose more realistic constraints, and to compare the simulated and in situ measured values of  $T_p$  and  $T_e$  at 1 AU, separately.

## 5.4 3D internal boundary from coronagraphic observations

A limitation of the RIMAP model is its confinement in the orbital plane of the spacecraft that acquired its input from in situ measurements. Therefore, increasing its latitudinal aperture would be a big step forward, allowing RIMAP simulations to become fully three-dimensional. However, as discussed in chapter 1, the availability of out-of-ecliptic in situ measurements will remain scarce until Solar Orbiter reaches its mission extended phase, and even then there will be no continuous sampling of the conditions of the heliospheric plasma at higher latitudes.

That is why we are planning to use remote sensing observations of the solar wind plasma from space-based coronagraphs as starting point to build a  $\theta$ -varying internal radial boundary for RIMAP simulations. Several diagnostic techniques exist to infer plasma density, velocity, and temperature on the plane of the sky from coronagraphic images. In section 4.2 we briefly mentioned those of van de Hulst (1950) for electron density and the so-called full inversion method of Dolei et al. (2016, 2018) for outflow velocity (see figure 5.6). Recently, Bemporad et al. (2021b) showed the advantages of a technique called the quick inversion method to obtain two-dimensional maps of velocity from the combination of white-light and UV images. In addition to the obvious advantage of being able to perform purely

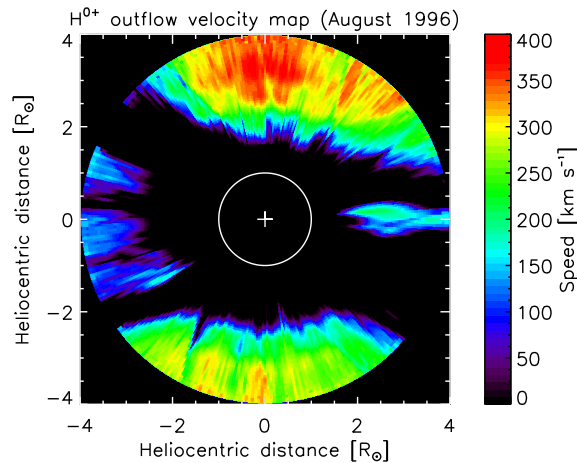


Figure 5.6: A two-dimensional map of the outflow velocity for the neutral hydrogen in the solar corona out to  $4 R_{\odot}$ , inferred from the observations obtained with UVCS/SOHO on June 14, 1997.

Reproduced from Dolei et al. (2018), © European Southern Observatory.

three-dimensional reconstructions of the Parker spiral, the use of these parameters as input for RIMAP would allow to have part of the boundary independent of the back-reconstruction and its crossings-removal procedure, and it would allow to reduce the stationarity assumption to an interval of an half solar rotation. This interval could be reduced even more by employing coronagraphic observations from multiple points of view.

## 5.5 Summary and conclusions

The essential role of the Sun in life on Earth has been known long before modern civilization. However, with the development of modern science, the public and the scientific community have progressively realized how its influence goes well beyond the light and heat it generates. Today we know that not only a large part of the motions in the solar system is governed by its overwhelming mass, but also that interplanetary space is constantly subject to a continuous flow of materials blown away at hundreds of km/s by the outer layers of the Sun, that these materials can have outstanding effects on our skies, like the auroras, and on our technologies and lives, and that the solar activity is regulated by a 11-year cycle, marked by the number of sunspots on the solar surface. While huge progress has been made, the full understanding of the solar and heliospheric phenomena is still far from being achieved.

In this work, we have described the solar atmosphere and its outer layer, the solar corona, which is the source of solar wind. We described how the solar wind is constituted by two regimes with different properties and sources on the Sun, the fast and slow winds, and how in addition to the ambient wind the heliosphere is home to a plethora of transients phenomena. Among these transients, coronal mass ejections were highlighted as the major sources of disturbances in the heliospheric plasma, due to their massive extension and momentum, and the main drivers of magnetic storms on Earth.

A derivation of the set of equations describing the collective behaviour of system of charged particle was provided. Under certain assumptions, a system of such particles can be described as a conductive fluid, which is called a plasma. The magnetohydrodynamics equations were also discussed in the limit of infinite conductivity of the plasma, a condition that when true open some interesting possibilities, one of the main ones being the fact that total magnetic field flux is conserved. Thus, in ideal MHD, magnetic field is frozen into the plasma, and when the thermal pressure dominates the magnetic pressure, the field has to move with the fluid. We described the classical theoretical models of solar wind, the isothermal Parker (1958) one, and the magnetized Weber and Davis (1967) one. While simple, these models capture some of the main features of solar wind. Among these features, the fact that solar rotation causes the magnetic field lines to be bent in a spiraling shape, called the interplanetary Parker spiral. We gave an overview of the techniques employed in the modelling of interplanetary coronal mass ejections, and briefly described the instruments of the spacecraft which were used to obtain in situ and remote sensing measurements of the solar wind plasma, Wind, STEREO, Parker Solar Probe, and Solar Orbiter.

In heliospheric physics, having a good grasp on the conditions of the solar wind plasma and magnetic field of Parker spiral is fundamental, since these conditions determine the propagation of solar transients. This work makes extensive use of the Reverse In situ and MHD Approach (Biondo et al., 2021a). This technique is the first to couple the two main approaches followed in the reconstructions of ambient conditions of the heliosphere: the analytical ballistic one, which trace solar wind quantities from in situ information acquired in heliosphere back to its solar sources, and the numerical one, which starts from remote-sensing observation of the photospheric magnetic field to reconstruct the entire corona and the inner heliosphere with different methods. What RIMAP does is to assume a certain

stationarity in the plasma condition to perform a ballistic back-propagation of in situ data acquired by spacecraft with heliocentric orbits in order to reconstruct the plasma and magnetic field parameters at distances closer to the Sun, and then use these parameters as boundary conditions for a MHD numerical simulation carried with the PLUTO code (Mignone et al., 2007, 2012). Thus, RIMAP obtains the ecliptic or equatorial distributions of plasma and magnetic field with the accuracy of the analytical models (especially in the longitudinal variations of the profiles) and the physical-insights possibilities offered by MHD simulations. Two test-cases, corresponding to measurements acquired by the Wind spacecraft during two solar minima, are shown to highlights limits and strengths of the model.

In view of space weather, we focussed our attention on ICME events, and for the first time we used RIMAP to study a time-dependent event. Measurements at 1 AU typically include the abundance of ion species, and therefore it is very interesting to understand whether and how the chemical composition can change as an ICME travels from the Sun to Earth and therefore trace back the original one when the cloud is expelled from the Sun. It is interesting to have information about material directly coming from the Sun. We simulated the propagation of a typical ICME event in the Parker spiral reconstructed with the Wind data collected during March 2009 (Biondo et al., 2021b). The ICME was described by an ice-cream cone model as an unmagnetized plasma bubble, in which we added a passive tracer to follow the mixing of its plasma with the realistic ambient solar wind streams reconstructed with RIMAP. The tracer shows us that even if it warps and stretches, the cloud does not fragment and up to 80% of the plasma detected at 1 AU can be traced back to its coronal source, although this fraction can drop significantly depending on which part of the ICME the encounter with a spacecraft happens.

A complementary step has been to improve on the degree of realism and to check the possibility to bridge between measurements from different missions with a single MHD model. In particular we establish a connection between coronal features observed by the Metis coronagraph on board Solar Orbiter and in situ measurements acquired by the Parker Solar Probe during their first quadrature of January 2021. We carried out a data-driven reconstruction with RIMAP based on the data of the latter spacecraft (Biondo et al., 2022). The in situ measurements are reproduced with good accuracy, especially the multiple crossings of the heliospheric current sheet experienced by PSP. This is an important milestone of RIMAP, since the reproduction of plasma so close to the Alfvénic surface (the outer limit of the corona) may have tested the limits of the classic models used in its back-propagation phase. Nevertheless, some refinement of RIMAP was required, mostly regarding the inclusion of a simple reduction in speed in order to taking into better account the subsequent acceleration experienced by the wind during its propagation. Then, we extracted the field line passing through the intersection between PSP trajectory and Metis plane-of-the sky longitude at the time of Solo perihelion, which happened on January 17. In this way we magnetically connected density and velocity values inferred from Metis observation very close to the solar surface to the corresponding super-Alfvénic solar wind values via an MHD simulation, finding a remarkable agreement on several medium scale features, although missing the finest structure.

Finally, we list some of the works currently in progress and possible future developments of our work. The increasingly expanding number of missions devoted to the investigation of solar phenomena make the current period a sort of golden age for heliospheric exploration, in which MHD models such as the one presented here could

offer a significant contribution in shedding some light on some unanswered questions. The RIMAP model could offer not only contributions in fundamental heliospheric physics, but also in space weather forecasting applications. Low-resolution versions of the model could operate in quasi-real time, providing daily reconstruction based on in situ measurements from space-based assets. This is currently done on the portal of the Space Weather project in Turin Observatory (SWELTO; Bemporad et al., [2021a](#)), and could be done for the European Space Weather Service Network (SWESNET) project of ESA.

# Chapter 6

## Bibliography

- Abbo, L., L. Ofman, S. K. Antiochos, V. H. Hansteen, L. Harra, et al. (Nov. 2016). “Slow Solar Wind: Observations and Modeling”. In: *Space Sci. Rev.* 201.1-4, pp. 55–108. DOI: [10.1007/s11214-016-0264-1](https://doi.org/10.1007/s11214-016-0264-1) (cit. on p. 9).
- Adhikari, L., G. P. Zank, D. Telloni, and L. -L. Zhao (Oct. 2022). “Modeling of Joint Parker Solar Probe-Metis/Solar Orbiter Observations”. In: *Astrophys. J. Lett.* 937.2, L29, p. L29. DOI: [10.3847/2041-8213/ac91c6](https://doi.org/10.3847/2041-8213/ac91c6) (cit. on p. 99).
- Alfvén, Hannes (1977). “Electric currents in cosmic plasmas”. In: *Reviews of Geophysics* 15.3, pp. 271–284. DOI: <https://doi.org/10.1029/RG015i003p00271> (cit. on p. 36).
- Altschuler, M. D. and G. Newkirk (Sept. 1969). “Magnetic Fields and the Structure of the Solar Corona. I: Methods of Calculating Coronal Fields”. In: *Solar Physics* 9.1, pp. 131–149. DOI: [10.1007/BF00145734](https://doi.org/10.1007/BF00145734) (cit. on p. 47).
- Andretta, V., A. Bemporad, Y. De Leo, G. Jerse, F. Landini, et al. (Dec. 2021). “The first coronal mass ejection observed in both visible-light and UV H I Ly-alpha channels of the Metis coronagraph on board Solar Orbiter”. In: *Astron. Astrophys.* 656, L14, p. L14. DOI: [10.1051/0004-6361/202142407](https://doi.org/10.1051/0004-6361/202142407) (cit. on p. 91).
- Antiochos, S. K., Z. Mikić, V. S. Titov, R. Lionello, and J. A. Linker (Apr. 2011). “A Model for the Sources of the Slow Solar Wind”. In: *Astrophys. J.* 731.2, 112, p. 112. DOI: [10.1088/0004-637X/731/2/112](https://doi.org/10.1088/0004-637X/731/2/112) (cit. on p. 9).
- Antonucci, E., L. Abbo, and M. A. Doderò (May 2005). “Slow wind and magnetic topology in the solar minimum corona in 1996-1997”. In: *Astron. Astrophys.* 435.2, pp. 699–711. DOI: [10.1051/0004-6361:20047126](https://doi.org/10.1051/0004-6361:20047126) (cit. on p. 92).
- Antonucci, E., S. Giordano, and M. A. Doderò (Jan. 2000). “Hydrogen and Oxygen Temperatures in Coronal Holes”. In: *Advances in Space Research* 25.9, pp. 1923–1926. DOI: [10.1016/S0273-1177\(99\)00604-3](https://doi.org/10.1016/S0273-1177(99)00604-3) (cit. on p. 9).
- Antonucci, E., M. Romoli, V. Andretta, Fineschi, Silvano, Heinzl, Petr, et al. (2020). “Metis: the Solar Orbiter visible light and ultraviolet coronal imager”. In: *A&A* 642, A10. DOI: [10.1051/0004-6361/201935338](https://doi.org/10.1051/0004-6361/201935338) (cit. on pp. 44, 91).
- Anzer, U. and G. W. Pneuman (July 1982). “Magnetic reconnection and coronal transients”. In: *Solar Physics* 79.1, pp. 129–147. ISSN: 1573-093X. DOI: [10.1007/BF00146978](https://doi.org/10.1007/BF00146978) (cit. on p. 16).
- Arge, C. N., J. G. Luhmann, D. Odstrcil, C. J. Schrijver, and Y. Li (Oct. 2004). “Stream structure and coronal sources of the solar wind during the May 12th, 1997 CME”. In: *Journal of Atmospheric and Solar-Terrestrial Physics* 66.15-16, pp. 1295–1309. DOI: [10.1016/j.jastp.2004.03.018](https://doi.org/10.1016/j.jastp.2004.03.018) (cit. on pp. 48, 49).

- Arge, C. N. and V. J. Pizzo (May 2000). “Improvement in the prediction of solar wind conditions using near-real time solar magnetic field updates”. In: *J. Geophys. Res.* 105.A5, pp. 10465–10480. DOI: [10.1029/1999JA000262](https://doi.org/10.1029/1999JA000262) (cit. on p. 48).
- Arge, C. Nick, Carl J. Henney, Irene Gonzalez Hernandez, W. Alex Toussaint, Josef Koller, et al. (June 2013). “Modeling the corona and solar wind using ADAPT maps that include far-side observations”. In: *Solar Wind 13*. Ed. by Gary P. Zank, Joe Borovsky, Roberto Bruno, Jonathan Cirtain, Steve Cranmer, et al. Vol. 1539. American Institute of Physics Conference Series, pp. 11–14. DOI: [10.1063/1.4810977](https://doi.org/10.1063/1.4810977) (cit. on p. 50).
- Arge, C. Nick, Carl J. Henney, Josef Koller, C. Rich Compeau, Shawn Young, et al. (Mar. 2010). “Air Force Data Assimilative Photospheric Flux Transport (ADAPT) Model”. In: *Twelfth International Solar Wind Conference*. Ed. by M. Maksimovic, K. Issautier, N. Meyer-Vernet, M. Moncuquet, and F. Pantellini. Vol. 1216. American Institute of Physics Conference Series, pp. 343–346. DOI: [10.1063/1.3395870](https://doi.org/10.1063/1.3395870) (cit. on p. 50).
- Arge, Charles N., Dusan Odstrcil, Victor J. Pizzo, and Leslie R. Mayer (Sept. 2003). “Improved Method for Specifying Solar Wind Speed Near the Sun”. In: *Solar Wind Ten*. Ed. by Marco Velli, Roberto Bruno, Francesco Malara, and B. Bucci. Vol. 679. American Institute of Physics Conference Series, pp. 190–193. DOI: [10.1063/1.1618574](https://doi.org/10.1063/1.1618574) (cit. on p. 48).
- Aschwanden, Markus J. (June 2016). “The Vertical-current Approximation Nonlinear Force-free Field Code—Description, Performance Tests, and Measurements of Magnetic Energies Dissipated in Solar Flares”. In: *Astrophys. J. Suppl. Ser.* 224.2, 25, p. 25. DOI: [10.3847/0067-0049/224/2/25](https://doi.org/10.3847/0067-0049/224/2/25) (cit. on p. 48).
- Asvestari, E., S. G. Heinemann, M. Temmer, J. Pomoell, E. Kilpua, et al. (Nov. 2019). “Reconstructing Coronal Hole Areas With EUHFORIA and Adapted WSA Model: Optimizing the Model Parameters”. In: *Journal of Geophysical Research (Space Physics)* 124.11, pp. 8280–8297. DOI: [10.1029/2019JA027173](https://doi.org/10.1029/2019JA027173) (cit. on p. 47).
- Badruddin and Y. P. Singh (Mar. 2009). “Geoeffectiveness of magnetic cloud, shock/sheath, interaction region, high-speed stream and their combined occurrence”. In: *Planet. Space Sci.* 57.3, pp. 318–331. DOI: [10.1016/j.pss.2008.12.009](https://doi.org/10.1016/j.pss.2008.12.009) (cit. on p. 72).
- Baker, Daniel N (2005). “Introduction to space weather”. In: *Space Weather*. Springer, pp. 3–20 (cit. on p. 18).
- Bale, S. D., S. T. Badman, J. W. Bonnell, T. A. Bowen, D. Burgess, et al. (Dec. 2019). “Highly structured slow solar wind emerging from an equatorial coronal hole”. In: *Nature* 576.7786, pp. 237–242. ISSN: 1476-4687. DOI: [10.1038/s41586-019-1818-7](https://doi.org/10.1038/s41586-019-1818-7) (cit. on pp. 9, 99–102).
- Bale, S. D., K. Goetz, P. R. Harvey, Turin, P., Bonnell, J. W., et al. (Dec. 2016). “The FIELDS Instrument Suite for Solar Probe Plus”. In: *Space Sci. Rev.* 204 (1), pp. 49–82. DOI: [10.1007/s11214-016-0244-5](https://doi.org/10.1007/s11214-016-0244-5) (cit. on pp. 9, 42).
- Bale, S. D., T. S. Horbury, M. Velli, M. I. Desai, J. S. Halekas, et al. (Dec. 2021). “A Solar Source of Alfvénic Magnetic Field Switchbacks: In Situ Remnants of Magnetic Funnel on Supergranulation Scales”. In: *The Astrophysical Journal* 923.2, p. 174. DOI: [10.3847/1538-4357/ac2d8c](https://doi.org/10.3847/1538-4357/ac2d8c) (cit. on p. 101).
- Balogh, A., R. J. Forsyth, E. A. Lucek, T. S. Horbury, and E. J. Smith (1999). “Heliospheric magnetic field polarity inversions at high heliographic latitudes”.

- In: *Geophysical Research Letters* 26.6, pp. 631–634. DOI: <https://doi.org/10.1029/1999GL900061> (cit. on p. 100).
- Balsara, Dinshaw S and Daniel S Spicer (1999). “A Staggered Mesh Algorithm Using High Order Godunov Fluxes to Ensure Solenoidal Magnetic Fields in Magnetohydrodynamic Simulations”. In: *Journal of Computational Physics* 149.2, pp. 270–292. ISSN: 0021-9991. DOI: <https://doi.org/10.1006/jcph.1998.6153> (cit. on p. 57).
- Barker, P. K. and J. M. Marlborough (Mar. 1982). “Weber and Davis revisited - Mass losing rotating magnetic winds”. In: *Astrophys. J.* 254, pp. 297–300. DOI: [10.1086/159733](https://doi.org/10.1086/159733) (cit. on p. 97).
- Bartels, J (1949). “The standardized Index Ks, and the Planetary index Kp, IATME Bull., 12 (b), 97; IUGG Publ”. In: *Office, Paris* (cit. on p. 18).
- Bartels, J., N. H. Heck, and H. F. Johnston (1939). “The three-hour-range index measuring geomagnetic activity”. In: *Terrestrial Magnetism and Atmospheric Electricity* 44.4, pp. 411–454. DOI: <https://doi.org/10.1029/TE044i004p00411> (cit. on p. 18).
- Behannon, K. W. (Feb. 1978). “Heliocentric distance dependence of the interplanetary magnetic field.” In: *Reviews of Geophysics and Space Physics* 16, pp. 125–145. DOI: [10.1029/RG016i001p00125](https://doi.org/10.1029/RG016i001p00125) (cit. on p. 45).
- Bělák, M., E. Marková, and M. Vandas (May 2007). “Source Surface Radius and its Development During Solar Cycle”. In: *Solar and Stellar Physics Through Eclipses*. Ed. by O. Demircan, S. O. Selam, and B. Albayrak. Vol. 370. Astronomical Society of the Pacific Conference Series, p. 255 (cit. on p. 47).
- Bemporad, A., L. Abbo, D. Barghini, C. Benna, R. Biondo, et al. (Jan. 2021a). “SWELTO – Space WEather Laboratory in Turin Observatory”. In: *arXiv e-prints*, arXiv:2101.07037, arXiv:2101.07037 (cit. on p. 111).
- Bemporad, A., S. Giordano, L. Zangrilli, and F. Frassati (Oct. 2021b). “Combining white light and UV Lyman- $\alpha$  coronagraphic images to determine the solar wind speed. The quick inversion method”. In: *Astron. Astrophys.* 654, A58, A58. DOI: [10.1051/0004-6361/202141276](https://doi.org/10.1051/0004-6361/202141276) (cit. on p. 108).
- Bemporad, A., G. Poletto, S. T. Suess, Y. -K. Ko, N. A. Schwadron, et al. (Feb. 2006). “Current Sheet Evolution in the Aftermath of a CME Event”. In: *Astrophys. J.* 638.2, pp. 1110–1128. DOI: [10.1086/497529](https://doi.org/10.1086/497529) (cit. on p. 89).
- Bemporad, A., G. Poletto, S. T. Suess, Y. K. Ko, S. Parenti, et al. (Aug. 2003). “Temporal Evolution of a Streamer Complex: Coronal and in Situ Plasma Parameters”. In: *Astrophys. J.* 593.2, pp. 1146–1163. DOI: [10.1086/376605](https://doi.org/10.1086/376605) (cit. on p. 89).
- Benkhoff, J., G. Murakami, W. Baumjohann, S. Besse, E. Bunce, et al. (Dec. 2021). “BepiColombo - Mission Overview and Science Goals”. In: *Space Science Reviews* 217.8, p. 90. ISSN: 1572-9672. DOI: [10.1007/s11214-021-00861-4](https://doi.org/10.1007/s11214-021-00861-4) (cit. on pp. 39, 76).
- Biermann, L. (Jan. 1951). “Kometenschweife und solare Korpuskularstrahlung”. In: *Zeitschrift für Astrophysik* 29, p. 274 (cit. on p. 26).
- Biondo, R., A. Bemporad, A. Mignone, and F. Reale (2021a). “Reconstruction of the Parker spiral with the Reverse In situ data and MHD Approach - RIMAP”. In: *J. Space Weather Space Clim.* 11, p. 7. DOI: [10.1051/swsc/2020072](https://doi.org/10.1051/swsc/2020072) (cit. on pp. 51, 79, 86, 94, 97, 99, 109).
- Biondo, R., A. Bemporad, P. Pagano, D. Telloni, F. Reale, et al. (2022). “Connecting Solar Orbiter remote-sensing observations and Parker Solar Probe in-situ mea-

- surements with a numerical MHD reconstruction of the Parker spiral”. In: *A&A*. DOI: [10.1051/0004-6361/202244535](https://doi.org/10.1051/0004-6361/202244535) (cit. on pp. 51, 89, 99, 110).
- Biondo, R., P. Pagano, F. Reale, and A. Bemporad (2021b). “Tracing the ICME plasma with a MHD simulation”. In: *A&A* 654, p. L3. DOI: [10.1051/0004-6361/202141892](https://doi.org/10.1051/0004-6361/202141892) (cit. on pp. 51, 86, 94, 110).
- Borovsky, Joseph E. (2016). “The plasma structure of coronal hole solar wind: Origins and evolution”. In: *Journal of Geophysical Research: Space Physics* 121.6, pp. 5055–5087. DOI: <https://doi.org/10.1002/2016JA022686> (cit. on p. 100).
- Brodrick, David, Steven Tingay, and Mark Wieringa (2005). “X-ray magnitude of the 4 November 2003 solar flare inferred from the ionospheric attenuation of the galactic radio background”. In: *Journal of Geophysical Research: Space Physics* 110.A9. DOI: <https://doi.org/10.1029/2004JA010960> (cit. on p. 13).
- Brooks, David H., Ignacio Ugarte-Urra, and Harry P. Warren (Jan. 2015). “Full-Sun observations for identifying the source of the slow solar wind”. In: *Nature Communications* 6, 5947, p. 5947. DOI: [10.1038/ncomms6947](https://doi.org/10.1038/ncomms6947) (cit. on p. 89).
- Brooks, David H. and Harry P. Warren (Jan. 2011). “Establishing a Connection Between Active Region Outflows and the Solar Wind: Abundance Measurements with EIS/Hinode”. In: *Astrophys. J. Lett.* 727.1, L13, p. L13. DOI: [10.1088/2041-8205/727/1/L13](https://doi.org/10.1088/2041-8205/727/1/L13) (cit. on p. 89).
- Brooks, David H. and Stephanie L. Yardley (Mar. 2021). “The source of the major solar energetic particle events from super active region 11944”. In: *Science Advances* 7.10, eabf0068. DOI: [10.1126/sciadv.abf0068](https://doi.org/10.1126/sciadv.abf0068) (cit. on pp. 78, 87).
- Brueckner, G. E., R. A. Howard, M. J. Koomen, C. M. Korendyke, D. J. Michels, et al. (Dec. 1995). “The Large Angle Spectroscopic Coronagraph (LASCO)”. In: *Sol. Phys.* 162.1-2, pp. 357–402. DOI: [10.1007/BF00733434](https://doi.org/10.1007/BF00733434) (cit. on p. 7).
- Bruno, R. and L. Trenchi (June 2014). “Radial Dependence of the Frequency Break between Fluid and Kinetic Scales in the Solar Wind Fluctuations”. In: *Astrophys. J. Lett.* 787.2, L24, p. L24. DOI: [10.1088/2041-8205/787/2/L24](https://doi.org/10.1088/2041-8205/787/2/L24) (cit. on p. 88).
- Bruno, R., L. Trenchi, and D. Telloni (Sept. 2014). “SPECTRAL SLOPE VARIATION AT PROTON SCALES FROM FAST TO SLOW SOLAR WIND”. In: *The Astrophysical Journal* 793.1, p. L15. DOI: [10.1088/2041-8205/793/1/L15](https://doi.org/10.1088/2041-8205/793/1/L15) (cit. on p. 88).
- Burlaga, L. F. (1974). “Interplanetary stream interfaces”. In: *Journal of Geophysical Research (1896-1977)* 79.25, pp. 3717–3725. DOI: <https://doi.org/10.1029/JA079i025p03717> (cit. on p. 46).
- (July 1988). “Magnetic clouds and force-free fields with constant alpha”. In: *J. Geophys. Res.* 93.A7, pp. 7217–7224. DOI: [10.1029/JA093iA07p07217](https://doi.org/10.1029/JA093iA07p07217) (cit. on p. 37).
- Burt, Joe and Bob Smith (2012). “Deep Space Climate Observatory: The DSCOVR mission”. In: *2012 IEEE Aerospace Conference*, pp. 1–13. DOI: [10.1109/AERO.2012.6187025](https://doi.org/10.1109/AERO.2012.6187025) (cit. on p. 63).
- Cane, H. V. and I. G. Richardson (2003). “Interplanetary coronal mass ejections in the near-Earth solar wind during 1996–2002”. In: *Journal of Geophysical Research: Space Physics* 108.A4. DOI: <https://doi.org/10.1029/2002JA009817> (cit. on pp. 18, 36).
- Cane, H. V., I. G. Richardson, and G. Wibberenz (1997). “Helios 1 and 2 observations of particle decreases, ejecta, and magnetic clouds”. In: *Journal of Geophysical Research: Space Physics* 102.A4, pp. 7075–7086. DOI: <https://doi.org/10.1029/97JA00149> (cit. on p. 36).

- Carrington, R. C. (Nov. 1859). “Description of a Singular Appearance seen in the Sun on September 1, 1859”. In: *Mon. Not. R. Astron. Soc.* 20, pp. 13–15. DOI: [10.1093/mnras/20.1.13](https://doi.org/10.1093/mnras/20.1.13) (cit. on pp. 13, 18).
- Chané, E., B. Jacobs C. and Van der Holst, S. Poedts, and D. Kimpe (2005). “On the effect of the initial magnetic polarity and of the background wind on the evolution of CME shocks”. In: *A&A* 432.1, pp. 331–339. DOI: [10.1051/0004-6361:20042005](https://doi.org/10.1051/0004-6361:20042005) (cit. on pp. 18, 78).
- Chapman, S. (Mar. 1929). “Solar Streams of Corpuscles: Their Geometry, Absorption of Light, and Penetration”. In: *Monthly Notices of the Royal Astronomical Society* 89.5, pp. 456–470. ISSN: 0035-8711. DOI: [10.1093/mnras/89.5.456](https://doi.org/10.1093/mnras/89.5.456) (cit. on p. 26).
- Chapman, Sydney and Harold Zirin (Jan. 1957). “Notes on the Solar Corona and the Terrestrial Ionosphere”. In: *Smithsonian Contributions to Astrophysics* 2, p. 1 (cit. on p. 26).
- Chen, P. F. (Apr. 2011). “Coronal Mass Ejections: Models and Their Observational Basis”. In: *Living Reviews in Solar Physics* 8.1, p. 1. ISSN: 1614-4961. DOI: [10.12942/lrsp-2011-1](https://doi.org/10.12942/lrsp-2011-1) (cit. on pp. 14, 16).
- Chen, Y., X. Li, H. Q. Song, Q. Q. Shi, S. W. Feng, et al. (Feb. 2009). “Intrinsic Instability of Coronal Streamers”. In: *Astrophys. J.* 691.2, pp. 1936–1942. DOI: [10.1088/0004-637X/691/2/1936](https://doi.org/10.1088/0004-637X/691/2/1936) (cit. on p. 10).
- Chiuderi, C. and M. Velli (2012). *Fisica del Plasma: Fondamenti e applicazioni Astrofisiche*. UNITEXT. Springer Milan. ISBN: 9788847018488 (cit. on p. 24).
- Clinger, E.W. (Dec. 2006). “The 1859 space weather event: Then and now”. In: *Advances in Space Research* 38, pp. 119–129. DOI: [10.1016/j.asr.2005.07.077](https://doi.org/10.1016/j.asr.2005.07.077) (cit. on p. 13).
- Clinger, Edward W. and William F. Dietrich (Oct. 2013). “The 1859 space weather event revisited: limits of extreme activity”. In: *Journal of Space Weather and Space Climate* 3, A31, A31. DOI: [10.1051/swsc/2013053](https://doi.org/10.1051/swsc/2013053) (cit. on p. 13).
- Courant, R., K. Friedrichs, and H. Lewy (Dec. 1928). “Über die partiellen Differenzgleichungen der mathematischen Physik”. In: *Mathematische Annalen* 100.1, pp. 32–74. ISSN: 1432-1807. DOI: [10.1007/BF01448839](https://doi.org/10.1007/BF01448839) (cit. on p. 57).
- Cowen, Ron (Sept. 2013). “Voyager 1 has reached interstellar space”. In: *Nature*. ISSN: 1476-4687. DOI: [10.1038/nature.2013.13735](https://doi.org/10.1038/nature.2013.13735) (cit. on p. 4).
- Cranmer, S. R., J. L. Kohl, G. Noci, E. Antonucci, G. Tondello, et al. (Jan. 1999). “An Empirical Model of a Polar Coronal Hole at Solar Minimum”. In: *The Astrophysical Journal* 511.1, pp. 481–501. DOI: [10.1086/306675](https://doi.org/10.1086/306675) (cit. on p. 97).
- Cranmer, Steven R. (Aug. 2002). “Coronal Holes and the High-Speed Solar Wind”. In: *Space Science Reviews* 101 (3), pp. 229–294. DOI: [10.1023/A:1020840004535](https://doi.org/10.1023/A:1020840004535) (cit. on pp. 9, 76).
- (Sept. 2009). “Coronal Holes”. In: *Living Reviews in Solar Physics* 6.1, 3, p. 3. DOI: [10.12942/lrsp-2009-3](https://doi.org/10.12942/lrsp-2009-3) (cit. on p. 9).
- Cranmer, Steven R., Sarah E. Gibson, and Pete Riley (Nov. 2017). “Origins of the Ambient Solar Wind: Implications for Space Weather”. In: *Space Sci. Rev.* 212.3-4, pp. 1345–1384. DOI: [10.1007/s11214-017-0416-y](https://doi.org/10.1007/s11214-017-0416-y) (cit. on p. 13).
- Cranmer, Steven R. and Amy R. Winebarger (Aug. 2019). “The Properties of the Solar Corona and Its Connection to the Solar Wind”. In: *Annu. Rev. Astron. Astrophys.* 57, pp. 157–187. DOI: [10.1146/annurev-astro-091918-104416](https://doi.org/10.1146/annurev-astro-091918-104416) (cit. on p. 13).

- D'Amicis, R., R. Bruno, G. Pallocchia, B. Bavassano, D. Telloni, et al. (June 2010). "RADIAL EVOLUTION OF SOLAR WIND TURBULENCE DURING EARTH AND ULYSSES ALIGNMENT OF 2007 AUGUST". In: *The Astrophysical Journal* 717.1, pp. 474–480. DOI: [10.1088/0004-637x/717/1/474](https://doi.org/10.1088/0004-637x/717/1/474) (cit. on p. 88).
- D'Huys, E., D. B. Seaton, S. Poedts, and D. Berghmans (Oct. 2014). "OBSERVATIONAL CHARACTERISTICS OF CORONAL MASS EJECTIONS WITHOUT LOW-CORONAL SIGNATURES". In: *The Astrophysical Journal* 795.1, p. 49. DOI: [10.1088/0004-637x/795/1/49](https://doi.org/10.1088/0004-637x/795/1/49) (cit. on p. 14).
- Darnel, Jonathan M., Daniel B. Seaton, Christian Bethge, Laurel Rachmeler, Alison Jarvis, et al. (2022). "The GOES-R Solar UltraViolet Imager". In: *Space Weather* 20.4. e2022SW003044 2022SW003044, e2022SW003044. DOI: <https://doi.org/10.1029/2022SW003044> (cit. on p. 13).
- Davis, L. (Jan. 1965). "Mariner II observations relevant to solar fields". In: *Stellar and Solar Magnetic Fields*. Ed. by R. Lust. Vol. 22, p. 202 (cit. on p. 31).
- De Pontieu, B., A. M. Title, J. R. Lemen, G. D. Kushner, D. J. Akin, et al. (July 2014). "The Interface Region Imaging Spectrograph (IRIS)". In: *Sol. Phys.* 289.7, pp. 2733–2779. DOI: [10.1007/s11207-014-0485-y](https://doi.org/10.1007/s11207-014-0485-y) (cit. on p. 39).
- De Rosa, Marc L., Carolus J. Schrijver, Graham Barnes, K. D. Leka, Bruce W. Lites, et al. (May 2009). "A Critical Assessment of Nonlinear Force-Free Field Modeling of the Solar Corona for Active Region 10953". In: *Astrophys. J.* 696.2, pp. 1780–1791. DOI: [10.1088/0004-637x/696/2/1780](https://doi.org/10.1088/0004-637x/696/2/1780) (cit. on p. 48).
- de Wit, Thierry Dudok, Vladimir V. Krasnoselskikh, Stuart D. Bale, John W. Bonnell, Trevor A. Bowen, et al. (Feb. 2020). "Switchbacks in the Near-Sun Magnetic Field: Long Memory and Impact on the Turbulence Cascade". In: *The Astrophysical Journal Supplement Series* 246.2, p. 39. DOI: [10.3847/1538-4365/ab5853](https://doi.org/10.3847/1538-4365/ab5853) (cit. on p. 100).
- Dedner, A., F. Kemm, D. Kröner, C. -D. Munz, T. Schnitzer, et al. (Jan. 2002). "Hyperbolic Divergence Cleaning for the MHD Equations". In: *Journal of Computational Physics* 175.2, pp. 645–673. DOI: [10.1006/jcph.2001.6961](https://doi.org/10.1006/jcph.2001.6961) (cit. on p. 58).
- DeForest, C. E., T. A. Howard, and D. J. McComas (May 2014). "INBOUND WAVES IN THE SOLAR CORONA: A DIRECT INDICATOR OF ALFVÉN SURFACE LOCATION". In: *The Astrophysical Journal* 787.2, p. 124. DOI: [10.1088/0004-637x/787/2/124](https://doi.org/10.1088/0004-637x/787/2/124) (cit. on p. 96).
- Detman, Thomas, Zdenka Smith, Murray Dryer, Craig D. Fry, C. Nick Arge, et al. (2006). "A hybrid heliospheric modeling system: Background solar wind". In: *Journal of Geophysical Research: Space Physics* 111.A7. DOI: <https://doi.org/10.1029/2005JA011430> (cit. on p. 50).
- Dolei, S., D. Spadaro, and R. Ventura (Aug. 2016). "Mapping the coronal hydrogen temperature in view of the forthcoming coronagraph observations by Solar Orbiter". In: *Astron. Astrophys.* 592, A137, A137. DOI: [10.1051/0004-6361/201628753](https://doi.org/10.1051/0004-6361/201628753) (cit. on pp. 92, 108).
- Dolei, S., R. Susino, C. Sasso, A. Bemporad, V. Andretta, et al. (May 2018). "Mapping the solar wind HI outflow velocity in the inner heliosphere by coronagraphic ultraviolet and visible-light observations". In: *Astron. Astrophys.* 612, A84, A84. DOI: [10.1051/0004-6361/201732118](https://doi.org/10.1051/0004-6361/201732118) (cit. on pp. 89, 92, 108).
- Domingo, V., B. Fleck, and A. I. Poland (Dec. 1995). "The SOHO Mission: an Overview". In: *Sol. Phys.* 162.1-2, pp. 1–37. DOI: [10.1007/BF00733425](https://doi.org/10.1007/BF00733425) (cit. on p. 7).

- Doschek, G. A. and H. P. Warren (Oct. 2019). “The Variability of Solar Coronal Abundances in Active Regions and the Quiet Sun”. In: *The Astrophysical Journal* 884.2, p. 158. DOI: [10.3847/1538-4357/ab426e](https://doi.org/10.3847/1538-4357/ab426e) (cit. on p. 78).
- Dryer, Murray (Feb. 1974). “Interplanetary shock waves generated by solar flares”. In: *Space Science Reviews* 15.4, pp. 403–468. ISSN: 1572-9672. DOI: [10.1007/BF00178215](https://doi.org/10.1007/BF00178215) (cit. on p. 46).
- Eastwood, J. P., E. Biffis, M. A. Hapgood, L. Green, M. M. Bisi, et al. (2017). “The Economic Impact of Space Weather: Where Do We Stand?” In: *Risk Analysis* 37.2, pp. 206–218. DOI: <https://doi.org/10.1111/risa.12765> (cit. on p. 18).
- Edlén, Bengt (Jan. 1943). “Die Deutung der Emissionslinien im Spektrum der Sonnenkorona. Mit 6 Abbildungen.” In: *Zeitschrift für Astrophysik* 22, p. 30 (cit. on p. 5).
- Einaudi, Giorgio, Paolo Boncinelli, Russell B. Dahlburg, and Judith T. Karpen (Jan. 1999). “Formation of the slow solar wind in a coronal streamer”. In: *J. Geophys. Res.* 104.A1, pp. 521–534. DOI: [10.1029/98JA02394](https://doi.org/10.1029/98JA02394) (cit. on p. 9).
- Fargette, Naïs, Benoit Lavraud, Alexis P. Rouillard, Victor Réville, Thierry Dudok De Wit, et al. (Sept. 2021). “Characteristic Scales of Magnetic Switchback Patches Near the Sun and Their Possible Association With Solar Supergranulation and Granulation”. In: *The Astrophysical Journal* 919.2, p. 96. DOI: [10.3847/1538-4357/ac1112](https://doi.org/10.3847/1538-4357/ac1112) (cit. on p. 101).
- Fargette, Naïs, Benoit Lavraud, Alexis P. Rouillard, Victor Réville, Stuart D. Bale, et al. (July 2022). “The preferential orientation of magnetic switchbacks and its implications for solar magnetic flux transport”. In: *Astron. Astrophys.* 663, A109, A109. DOI: [10.1051/0004-6361/202243537](https://doi.org/10.1051/0004-6361/202243537) (cit. on p. 104).
- Feldman, U. (Sept. 1992). “Elemental abundances in the upper solar atmosphere.” In: *Phys. Scr.* 46.3, pp. 202–220. DOI: [10.1088/0031-8949/46/3/002](https://doi.org/10.1088/0031-8949/46/3/002) (cit. on p. 78).
- Feng, Xueshang, Xiaopeng Ma, and Changqing Xiang (Dec. 2015). “Data-driven modeling of the solar wind from 1  $R_s$  to 1 AU”. In: *Journal of Geophysical Research (Space Physics)* 120.12, pp. 10, 159–10, 174. DOI: [10.1002/2015JA021911](https://doi.org/10.1002/2015JA021911) (cit. on p. 47).
- Fisk, L. A. and J. C. Kasper (Apr. 2020). “Global Circulation of the Open Magnetic Flux of the Sun”. In: *The Astrophysical Journal Letters* 894.1, p. L4. DOI: [10.3847/2041-8213/ab8acd](https://doi.org/10.3847/2041-8213/ab8acd) (cit. on p. 101).
- Fisk, L. A. and N. A. Schwadron (Oct. 2001). “The Behavior of the Open Magnetic Field of the Sun”. In: *Astrophys. J.* 560.1, pp. 425–438. DOI: [10.1086/322503](https://doi.org/10.1086/322503) (cit. on p. 9).
- Fletcher, L., B. R. Dennis, H. S. Hudson, S. Krucker, K. Phillips, et al. (Sept. 2011). “An Observational Overview of Solar Flares”. In: *Space Sci. Rev.* 159.1-4, pp. 19–106. DOI: [10.1007/s11214-010-9701-8](https://doi.org/10.1007/s11214-010-9701-8) (cit. on p. 12).
- Florens, M. S. L., Iver H. Cairns, S. A. Knock, and P. A. Robinson (2007). “Data-driven solar wind model and prediction of type II bursts”. In: *Geophysical Research Letters* 34.4. DOI: <https://doi.org/10.1029/2006GL028522> (cit. on p. 46).
- Forbes, T. G. (1990). “Numerical simulation of a catastrophe model for coronal mass ejections”. In: *Journal of Geophysical Research: Space Physics* 95.A8, pp. 11919–11931. DOI: <https://doi.org/10.1029/JA095iA08p11919> (cit. on p. 16).
- (2000). “A review on the genesis of coronal mass ejections”. In: *Journal of Geophysical Research: Space Physics* 105.A10, pp. 23153–23165. DOI: <https://doi.org/10.1029/2000JA000005> (cit. on p. 45).

- Forbush, Scott E. (Nov. 1946). “Three Unusual Cosmic-Ray Increases Possibly Due to Charged Particles from the Sun”. In: *Physical Review* 70.9-10, pp. 771–772. DOI: [10.1103/PhysRev.70.771](https://doi.org/10.1103/PhysRev.70.771) (cit. on p. 13).
- Fox, N. J., M. C. Velli, S. D. Bale, R. Decker, A. Driesman, et al. (2016). “The Solar Probe Plus Mission: Humanity’s First Visit to Our Star”. In: *Space Sci. Rev.* 204.1-4, pp. 7–48. DOI: [10.1007/s11214-015-0211-6](https://doi.org/10.1007/s11214-015-0211-6) (cit. on p. 41).
- Galvin, A. B., L. M. Kistler, M. A. Popecki, C. J. Farrugia, K. D. C. Simunac, et al. (Apr. 2008). “The Plasma and Suprathermal Ion Composition (PLASTIC) Investigation on the STEREO Observatories”. In: *Space Science Reviews* 136.1, pp. 437–486. ISSN: 1572-9672. DOI: [10.1007/s11214-007-9296-x](https://doi.org/10.1007/s11214-007-9296-x) (cit. on p. 40).
- Gardiner, Thomas A. and James M. Stone (2005). “An unsplit Godunov method for ideal MHD via constrained transport”. In: *Journal of Computational Physics* 205.2, pp. 509–539. ISSN: 0021-9991. DOI: <https://doi.org/10.1016/j.jcp.2004.11.016> (cit. on p. 57).
- Gary, G. Allen (Oct. 2001). “Plasma Beta above a Solar Active Region: Rethinking the Paradigm”. In: *Sol. Phys.* 203.1, pp. 71–86. DOI: [10.1023/A:1012722021820](https://doi.org/10.1023/A:1012722021820) (cit. on p. 22, 23).
- Gerontidou, M., H. Mavromichalaki, and T. Daglis (Sept. 2018). “High-Speed Solar Wind Streams and Geomagnetic Storms During Solar Cycle 24”. In: *Sol. Phys.* 293.9, 131, p. 131. DOI: [10.1007/s11207-018-1348-8](https://doi.org/10.1007/s11207-018-1348-8) (cit. on p. 72).
- Gibson, S. E., A. Fludra, F. Bagenal, D. Biesecker, G. del Zanna, et al. (May 1999). “Solar minimum streamer densities and temperatures using Whole Sun Month coordinated data sets”. In: *J. Geophys. Res.* 104.A5, pp. 9691–9700. DOI: [10.1029/98JA02681](https://doi.org/10.1029/98JA02681) (cit. on p. 97).
- Gibson, S. E. and B. C. Low (Jan. 1998). “A Time-Dependent Three-Dimensional Magnetohydrodynamic Model of the Coronal Mass Ejection”. In: *Astrophys. J.* 493.1, pp. 460–473. DOI: [10.1086/305107](https://doi.org/10.1086/305107) (cit. on p. 38).
- Gloeckler, G., J. Geiss, H. Balsiger, P. Bedini, J. C. Cain, et al. (Jan. 1992). “The Solar Wind Ion Composition Spectrometer”. In: *Astron. Astrophys. Suppl.* 92.2, pp. 267–289 (cit. on p. 89).
- Godunov, Sergei K. and I. Bohachevsky (1959). “Finite difference method for numerical computation of discontinuous solutions of the equations of fluid dynamics”. In: *Matematičeskij sbornik* 47(89).3, pp. 271–306 (cit. on p. 56).
- Gold, T. and F. Hoyle (Feb. 1960). “On the Origin of Solar Flares”. In: *Monthly Notices of the Royal Astronomical Society* 120.2, pp. 89–105. ISSN: 0035-8711. DOI: [10.1093/mnras/120.2.89](https://doi.org/10.1093/mnras/120.2.89) (cit. on pp. 37, 105).
- Golub, L. and J.M. Pasachoff (1997). *The Solar Corona*. The Solar Corona. Cambridge University Press. ISBN: 9780521485357 (cit. on p. 37).
- Gonzalez, W. D., J. A. Joselyn, Y. Kamide, H. W. Kroehl, G. Rostoker, et al. (Apr. 1994). “What is a geomagnetic storm?” In: *J. Geophys. Res.* 99.A4, pp. 5771–5792. DOI: [10.1029/93JA02867](https://doi.org/10.1029/93JA02867) (cit. on p. 17).
- González Hernández, I., F. Hill, and C. Lindsey (Nov. 2007). “Calibration of Seismic Signatures of Active Regions on the Far Side of the Sun”. In: *Astrophys. J.* 669.2, pp. 1382–1389. DOI: [10.1086/521592](https://doi.org/10.1086/521592) (cit. on p. 50).
- Gopalswamy, N., A. Dal Lago, S. Yashiro, and S. Akiyama (Jan. 2009). “The Expansion and Radial Speeds of Coronal Mass Ejections”. In: *Central European Astrophysical Bulletin* 33, pp. 115–124 (cit. on p. 38).
- Gopalswamy, N., A. Lara, R. P. Lepping, M. L. Kaiser, D. Berdichevsky, et al. (2000). “Interplanetary acceleration of coronal mass ejections”. In: *Geophysical Research*

- Letters* 27.2, pp. 145–148. DOI: <https://doi.org/10.1029/1999GL003639> (cit. on p. 83).
- Gopalswamy, N., R. Mewaldt, and J. Torsti (Oct. 2006). “Solar Eruptions and Energetic Particles: An Introduction”. In: *Geophysical Monograph Series* 165, p. 1. DOI: [10.1029/165GM02](https://doi.org/10.1029/165GM02) (cit. on p. 17).
- Gopalswamy, Nat, Sachiko Akiyama, Seiji Yashiro, Hong Xie, Pertti Mäkelä, et al. (2014). “Anomalous expansion of coronal mass ejections during solar cycle 24 and its space weather implications”. In: *Geophysical Research Letters* 41.8, pp. 2673–2680. DOI: <https://doi.org/10.1002/2014GL059858> (cit. on pp. 16, 81).
- Gopalswamy, Nat, Alejandro Lara, Seiji Yashiro, Steven Nunes, and Russell A. Howard (Sept. 2003). “Coronal mass ejection activity during solar cycle 23”. In: *Solar Variability as an Input to the Earth’s Environment*. Ed. by Andrew Wilson. Vol. 535. ESA Special Publication, pp. 403–414 (cit. on p. 15).
- Gosling, J. T. (1990). “Coronal Mass Ejections and Magnetic Flux Ropes in Interplanetary Space”. In: *Physics of Magnetic Flux Ropes*. American Geophysical Union (AGU), pp. 343–364. ISBN: 9781118663868. DOI: <https://doi.org/10.1029/GM058p0343> (cit. on p. 36).
- (1997). “Coronal Mass Ejections: An Overview”. In: *Coronal Mass Ejections*. American Geophysical Union (AGU), pp. 9–16. ISBN: 9781118664377. DOI: <https://doi.org/10.1029/GM099p0009> (cit. on pp. 16, 77).
- Gosling, J. T., D. N. Baker, S. J. Bame, W. C. Feldman, R. D. Zwickl, et al. (1987). “Bidirectional solar wind electron heat flux events”. In: *Journal of Geophysical Research: Space Physics* 92.A8, pp. 8519–8535. DOI: <https://doi.org/10.1029/JA092iA08p08519> (cit. on p. 77).
- Gosling, J. T., D. J. McComas, D. A. Roberts, and R. M. Skoug (Apr. 2009). “A One-Sided Aspect of Alfvénic Fluctuations in the Solar Wind”. In: *Astrophys. J. Lett.* 695.2, pp. L213–L216. DOI: [10.1088/0004-637X/695/2/L213](https://doi.org/10.1088/0004-637X/695/2/L213) (cit. on p. 100).
- Gosling, J. T., H. Tian, and T. D. Phan (Aug. 2011). “PULSED ALFVÉN WAVES IN THE SOLAR WIND”. In: *The Astrophysical Journal Letters* 737.2, p. L35. DOI: [10.1088/2041-8205/737/2/L35](https://doi.org/10.1088/2041-8205/737/2/L35) (cit. on p. 100).
- Green, Lucie and Deb Baker (2015). “Coronal mass ejections: a driver of severe space weather”. In: *Weather* 70.1, pp. 31–35. DOI: <https://doi.org/10.1002/wea.2437> (cit. on pp. 16, 77).
- Gressl, C., A. M. Veronig, M. Temmer, D. Odstrčil, J. A. Linker, et al. (May 2014). “Comparative Study of MHD Modeling of the Background Solar Wind”. In: *Sol. Phys.* 289.5, pp. 1783–1801. DOI: [10.1007/s11207-013-0421-6](https://doi.org/10.1007/s11207-013-0421-6) (cit. on p. 47).
- Grotian, W. (Mar. 1939). “Zur Frage der Deutung der Linien im Spektrum der Sonnenkorona”. In: *Naturwissenschaften* 27.13, pp. 214–214. DOI: [10.1007/BF01488890](https://doi.org/10.1007/BF01488890) (cit. on p. 5).
- Gruesbeck, J. R., S. T. Lepri, T. H. Zurbuchen, and S. K. Antiochos (Apr. 2011). “Constraints on Coronal Mass Ejection Evolution from in Situ Observations of Ionic Charge States”. In: *Astrophys. J.* 730.2, 103, p. 103. DOI: [10.1088/0004-637X/730/2/103](https://doi.org/10.1088/0004-637X/730/2/103) (cit. on p. 78).
- Guhathakurta, M., A. Fludra, S. E. Gibson, D. Biesecker, and R. Fisher (1999). “Physical properties of a coronal hole from a coronal diagnostic spectrometer, Mauna Loa Coronagraph, and LASCO observations during the Whole Sun Month”. In: *Journal of Geophysical Research: Space Physics* 104.A5, pp. 9801–9808. DOI: <https://doi.org/10.1029/1998JA900082> (cit. on p. 97).

- Hadid, L. Z., V. Génot, S. Aizawa, A. Milillo, J. Zender, et al. (2021). “BepiColombo’s Cruise Phase: Unique Opportunity for Synergistic Observations”. In: *Frontiers in Astronomy and Space Sciences* 8. ISSN: 2296-987X. DOI: [10.3389/fspas.2021.718024](https://doi.org/10.3389/fspas.2021.718024) (cit. on p. 98).
- Hansen, R. T., C. J. Garcia, R. J. -M. Grogard, and K. V. Sheridan (July 1971). “A coronal disturbance observed simultaneously with a white-light corona-meter and the 80 MHz Culgoora radioheliograph”. In: *Publ. Astron. Soc. Aust.* 2, p. 57. DOI: [10.1017/S1323358000012856](https://doi.org/10.1017/S1323358000012856) (cit. on p. 13).
- Hapgood, M.A. (2011). “Towards a scientific understanding of the risk from extreme space weather”. In: *Advances in Space Research* 47.12. Recent Advances in Space Weather Monitoring, Modelling, and Forecasting - 2, pp. 2059–2072. ISSN: 0273-1177. DOI: <https://doi.org/10.1016/j.asr.2010.02.007> (cit. on pp. 16, 77).
- Harten, Amiram, Peter D. Lax, and Bram van Leer (1983). “On Upstream Differencing and Godunov-Type Schemes for Hyperbolic Conservation Laws”. In: *SIAM Review* 25.1, pp. 35–61. DOI: [10.1137/1025002](https://doi.org/10.1137/1025002) (cit. on pp. 57, 62).
- Harten, Ronald and Kenn Clark (Feb. 1995). “The Design Features of the GGS Wind and Polar Spacecraft”. In: *Space Sci. Rev.* 71.1-4, pp. 23–40. DOI: [10.1007/BF00751324](https://doi.org/10.1007/BF00751324) (cit. on p. 39).
- Hartle, R. E. and P. A. Sturrock (Mar. 1968). “Two-Fluid Model of the Solar Wind”. In: *Astrophys. J.* 151, p. 1155. DOI: [10.1086/149513](https://doi.org/10.1086/149513) (cit. on pp. 106, 107).
- Harvey, J. W., F. Hill, R. P. Hubbard, J. R. Kennedy, J. W. Leibacher, et al. (May 1996). “The Global Oscillation Network Group (GONG) Project”. In: *Science* 272.5266, pp. 1284–1286. DOI: [10.1126/science.272.5266.1284](https://doi.org/10.1126/science.272.5266.1284) (cit. on p. 50).
- He, H. -Q., G. Qin, and M. Zhang (June 2011). “Propagation of Solar Energetic Particles in Three-dimensional Interplanetary Magnetic Fields: In View of Characteristics of Sources”. In: *Astrophys. J.* 734.2, 74, p. 74. DOI: [10.1088/0004-637X/734/2/74](https://doi.org/10.1088/0004-637X/734/2/74) (cit. on pp. 18, 52, 78).
- Hellinger, P., L. Matteini, Š. Štverák, P. M. Trávníček, and E. Marsch (2011). “Heating and cooling of protons in the fast solar wind between 0.3 and 1 AU: Helios revisited”. In: *Journal of Geophysical Research: Space Physics* 116.A9. DOI: [10.1029/2011JA016674](https://doi.org/10.1029/2011JA016674) (cit. on p. 76).
- Hellinger, P., P. Trávníček, J. C. Kasper, and A. J. Lazarus (May 2006). “Solar wind proton temperature anisotropy: Linear theory and WIND/SWE observations”. In: *Geophys. Res. Lett.* 33.9, L09101, p. L09101. DOI: [10.1029/2006GL025925](https://doi.org/10.1029/2006GL025925) (cit. on p. 30).
- Hidalgo, M. A. (May 2016). “A global magnetic topology model for magnetic clouds. IV.” In: *The Astrophysical Journal* 823.1, p. 3. DOI: [10.3847/0004-637x/823/1/3](https://doi.org/10.3847/0004-637x/823/1/3) (cit. on pp. 37, 104).
- Hinterreiter, Jürgen, Jasmina Magdalenic, Manuela Temmer, Christine Verbeke, Immanuel Christopher Jebaraj, et al. (Dec. 2019). “Assessing the Performance of EUHFORIA Modeling the Background Solar Wind”. In: *Sol. Phys.* 294.12, 170, p. 170. DOI: [10.1007/s11207-019-1558-8](https://doi.org/10.1007/s11207-019-1558-8) (cit. on p. 75).
- Hodgson, R. (Nov. 1859). “On a curious Appearance seen in the Sun”. In: *Mon. Not. R. Astron. Soc.* 20, pp. 15–16. DOI: [10.1093/mnras/20.1.15](https://doi.org/10.1093/mnras/20.1.15) (cit. on p. 13).
- Hoeksema, J. T. (Sept. 1984). “Structure and Evolution of the Large Scale Solar and Heliospheric Magnetic Fields.” PhD thesis. Stanford University, California (cit. on p. 47).

- Hoeksema, J. T., J. M. Wilcox, and P. H. Scherrer (Dec. 1983). “The structure of the heliospheric current sheet: 1978-1982”. In: *J. Geophys. Res.* 88.A12, pp. 9910–9918. DOI: [10.1029/JA088iA12p09910](https://doi.org/10.1029/JA088iA12p09910) (cit. on pp. 31, 47).
- Horbury, T S, L Matteini, and D Stansby (Apr. 2018). “Short, large-amplitude speed enhancements in the near-Sunfast solar wind”. In: *Monthly Notices of the Royal Astronomical Society* 478.2, pp. 1980–1986. ISSN: 0035-8711. DOI: [10.1093/mnras/sty953](https://doi.org/10.1093/mnras/sty953) (cit. on p. 100).
- Horbury, T. S., H. O’Brien, I. Carrasco Blazquez, M. Bendyk, P. Brown, et al. (Oct. 2020). “The Solar Orbiter magnetometer”. In: *Astron. Astrophys.* 642, A9, A9. DOI: [10.1051/0004-6361/201937257](https://doi.org/10.1051/0004-6361/201937257) (cit. on p. 43).
- Hosteaux, S., E. Chané, B. Decraemer, D. -C. Talpeanu, and S. Poedts (Nov. 2018). “Ultrahigh-resolution model of a breakout CME embedded in the solar wind”. In: *Astron. Astrophys.* 620, A57, A57. DOI: [10.1051/0004-6361/201832976](https://doi.org/10.1051/0004-6361/201832976) (cit. on p. 76).
- Howard, R. A., D. J. Michels, Jr. Sheeley N. R., and M. J. Koomen (Dec. 1982). “The observation of a coronal transient directed at Earth.” In: *Astrophys. J. Lett.* 263, pp. L101–L104. DOI: [10.1086/183932](https://doi.org/10.1086/183932) (cit. on p. 38).
- Howard, R. A., A. Vourlidas, R. C. Colaninno, C. M. Korendyke, S. P. Plunkett, et al. (Oct. 2020). “The Solar Orbiter Heliospheric Imager (SoloHI)”. In: *Astron. Astrophys.* 642, A13, A13. DOI: [10.1051/0004-6361/201935202](https://doi.org/10.1051/0004-6361/201935202) (cit. on p. 44).
- Howard, Timothy A. and Richard A. Harrison (July 2013). “Stealth Coronal Mass Ejections: A Perspective”. In: *Sol. Phys.* 285.1-2, pp. 269–280. DOI: [10.1007/s11207-012-0217-0](https://doi.org/10.1007/s11207-012-0217-0) (cit. on pp. 14, 81).
- Howard, Timothy A. and S. James Tappin (Oct. 2009). “Interplanetary Coronal Mass Ejections Observed in the Heliosphere: 1. Review of Theory”. In: *Space Science Reviews* 147.1, pp. 31–54. ISSN: 1572-9672. DOI: [10.1007/s11214-009-9542-5](https://doi.org/10.1007/s11214-009-9542-5) (cit. on p. 45).
- Hu, You Qiu, Ruth Esser, and Shadia R. Habbal (2000). “A four-fluid turbulence-driven solar wind model for preferential acceleration and heating of heavy ions”. In: *Journal of Geophysical Research: Space Physics* 105.A3, pp. 5093–5111. DOI: <https://doi.org/10.1029/1999JA900430> (cit. on p. 107).
- Hudson, Hugh S. (Jan. 2011). “Global Properties of Solar Flares”. In: *Space Science Reviews* 158.1, pp. 5–41. ISSN: 1572-9672. DOI: [10.1007/s11214-010-9721-4](https://doi.org/10.1007/s11214-010-9721-4) (cit. on p. 12).
- (Oct. 2020). “Solar Flare Build-Up and Release”. In: *Solar Physics* 295.10, p. 132. ISSN: 1573-093X. DOI: [10.1007/s11207-020-01698-w](https://doi.org/10.1007/s11207-020-01698-w) (cit. on p. 13).
- Hundhausen, A. J. (Jan. 1977). “An interplanetary view of coronal holes.” In: *Coronal Holes and High Speed Wind Streams*. Ed. by J. B. Zirker, pp. 225–329 (cit. on p. 11).
- (1995). “The Solar Wind”. In: *Introduction to Space Plasma Physics*. Ed. by M. G. Kivelson and C. T. Russell. U. Chap. 4 (cit. on p. 37).
- Hundhausen, A. J., C. B. Sawyer, L. House, R. M. E. Illing, and W. J. Wagner (1984). “Coronal mass ejections observed during the Solar Maximum Mission: Latitude distribution and rate of occurrence”. In: *Journal of Geophysical Research: Space Physics* 89.A5, pp. 2639–2646. DOI: <https://doi.org/10.1029/JA089iA05p02639> (cit. on p. 13).
- Hundhausen, A.J. (1972). *Coronal Expansion and Solar Wind*. Lecture Notes in Economic and Mathematical Systems. Springer-Verlag. ISBN: 9780387058757 (cit. on p. 28).

- Hunter, A. (Dec. 1942). “ORIGIN OF THE CORONIUM LINES”. In: *Nature* 150.3817, pp. 756–759. ISSN: 1476-4687. DOI: [10.1038/150756a0](https://doi.org/10.1038/150756a0) (cit. on p. 5).
- Innes, D. E., S. W. McIntosh, and A. Pietarila (2010). “STEREO quadrature observations of coronal dimming at the onset of mini-CMEs\*”. In: *A&A* 517, p. L7. DOI: [10.1051/0004-6361/201014366](https://doi.org/10.1051/0004-6361/201014366) (cit. on p. 89).
- Intriligator, Devrie S. (1980). “Transient Phenomena Originating at the Sun — An Interplanetary View”. In: *Solar and Interplanetary Dynamics*. Ed. by M. Dryer and E. Tandberg-Hanssen. Dordrecht: Springer Netherlands, pp. 357–374. ISBN: 978-94-009-9100-2. DOI: [10.1007/978-94-009-9100-2\\_57](https://doi.org/10.1007/978-94-009-9100-2_57) (cit. on pp. 12, 77).
- Jakab, P. and A. Brandenburg (2021). “The effect of a dynamo-generated field on the Parker wind”. In: *A&A* 647, A18. DOI: [10.1051/0004-6361/202038564](https://doi.org/10.1051/0004-6361/202038564) (cit. on p. 101).
- Jian, L., C. T. Russell, J. G. Luhmann, and R. M. Skoug (Dec. 2006). “Properties of Interplanetary Coronal Mass Ejections at One AU During 1995 – 2004”. In: *Solar Physics* 239.1, pp. 393–436. ISSN: 1573-093X. DOI: [10.1007/s11207-006-0133-2](https://doi.org/10.1007/s11207-006-0133-2) (cit. on pp. 36, 84, 88).
- Jian, L. K., J. G. Luhmann, C. T. Russell, and A. B. Galvin (Mar. 2019). “Solar Terrestrial Relations Observatory (STEREO) Observations of Stream Interaction Regions in 2007 - 2016: Relationship with Heliospheric Current Sheets, Solar Cycle Variations, and Dual Observations”. In: *Sol. Phys.* 294.3, 31, p. 31. DOI: [10.1007/s11207-019-1416-8](https://doi.org/10.1007/s11207-019-1416-8) (cit. on pp. 68–70, 73).
- Jian, L. K., P. J. MacNeice, M. L. Mays, A. Taktakishvili, D. Odstrcil, et al. (Aug. 2016). “Validation for global solar wind prediction using Ulysses comparison: Multiple coronal and heliospheric models installed at the Community Coordinated Modeling Center”. In: *Space Weather* 14.8, pp. 592–611. DOI: [10.1002/2016SW001435](https://doi.org/10.1002/2016SW001435) (cit. on pp. 51, 79).
- Jian, L. K., C. T. Russell, J. G. Luhmann, and A. B. Galvin (Mar. 2018). “STEREO Observations of Interplanetary Coronal Mass Ejections in 2007–2016”. In: *The Astrophysical Journal* 855.2, p. 114. DOI: [10.3847/1538-4357/aab189](https://doi.org/10.3847/1538-4357/aab189) (cit. on p. 40).
- Kahler, S. W., N. U. Crooker, and J. T. Gosling (Nov. 1996). “The topology of intrasector reversals of the interplanetary magnetic field”. In: *J. Geophys. Res.* 101.A11, pp. 24373–24382. DOI: [10.1029/96JA02232](https://doi.org/10.1029/96JA02232) (cit. on p. 100).
- Kamide, Y., W. Baumjohann, I. A. Daglis, W. D. Gonzalez, M. Grande, et al. (1998). “Current understanding of magnetic storms: Storm-substorm relationships”. In: *Journal of Geophysical Research: Space Physics* 103.A8, pp. 17705–17728. DOI: <https://doi.org/10.1029/98JA01426> (cit. on p. 31).
- Kamide, Y. and Y.P. Maltsev (2007). “Geomagnetic Storms”. In: *Handbook of the Solar-Terrestrial Environment*. Ed. by Y. Kamide and A. Chian. Berlin, Heidelberg: Springer Berlin Heidelberg, pp. 355–374. ISBN: 978-3-540-46315-3. DOI: [10.1007/978-3-540-46315-3\\_14](https://doi.org/10.1007/978-3-540-46315-3_14) (cit. on pp. 9, 17, 72, 77).
- Kamide, Yohsuke and Abraham C. -L. Chian (2007). *Handbook of the Solar-Terrestrial Environment*. Springer-Verlag (cit. on p. 18).
- Kasper, J. C., S. D. Bale, J. W. Belcher, M. Berthomier, A. W. Case, et al. (Dec. 2019). “Alfvénic velocity spikes and rotational flows in the near-Sun solar wind”. In: *Nature* 576.7786, pp. 228–231. DOI: [10.1038/s41586-019-1813-z](https://doi.org/10.1038/s41586-019-1813-z) (cit. on pp. 100, 101).

- Kasper, J. C., K. G. Klein, E. Lichko, Jia Huang, C. H. K. Chen, et al. (Dec. 2021). “Parker Solar Probe Enters the Magnetically Dominated Solar Corona”. In: *Phys. Rev. Lett.* 127.25, 255101, p. 255101. DOI: [10.1103/PhysRevLett.127.255101](https://doi.org/10.1103/PhysRevLett.127.255101) (cit. on p. 41).
- Kasper, J. C., A. J. Lazarus, J. T. Steinberg, K. W. Ogilvie, and A. Szabo (Mar. 2006). “Physics-based tests to identify the accuracy of solar wind ion measurements: A case study with the Wind Faraday Cups”. In: *Journal of Geophysical Research (Space Physics)* 111.A3, A03105, A03105. DOI: [10.1029/2005JA011442](https://doi.org/10.1029/2005JA011442) (cit. on p. 30).
- Kasper, Justin C., Robert Abiad, Austin, Gerry, Balat-Pichelin, Marianne, Bale, Stuart D., et al. (2016). “Solar Wind Electrons Alphas and Protons (SWEAP) Investigation: Design of the Solar Wind and Coronal Plasma Instrument Suite for Solar Probe Plus”. In: *Space Sci. Rev.* 204 (1), pp. 131–186. DOI: [10.1007/s11214-015-0206-3](https://doi.org/10.1007/s11214-015-0206-3) (cit. on p. 41).
- Kataoka, R., T. Ebisuzaki, K. Kusano, D. Shiota, S. Inoue, et al. (2009). “Three-dimensional MHD modeling of the solar wind structures associated with 13 December 2006 coronal mass ejection”. In: *Journal of Geophysical Research: Space Physics* 114.A10. DOI: <https://doi.org/10.1029/2009JA014167> (cit. on p. 38).
- Kellogg, Paul J. (Jan. 2022). “A Fundamental Instability for the Solar Wind”. In: *The Astrophysical Journal* 925.2, p. 106. DOI: [10.3847/1538-4357/ac32e0](https://doi.org/10.3847/1538-4357/ac32e0) (cit. on p. 30).
- Kilpua, E. K. J., A. Isavnin, A. Vourlidas, H. E. J. Koskinen, and L. Rodriguez (2013). “On the relationship between interplanetary coronal mass ejections and magnetic clouds”. In: *Annales Geophysicae* 31.7, pp. 1251–1265. DOI: [10.5194/angeo-31-1251-2013](https://doi.org/10.5194/angeo-31-1251-2013) (cit. on pp. 16, 77, 86).
- Kilpua, E. K. J., L.K. Jian, Y. Li, J.G. Luhmann, and C.T. Russell (2011). “Multipoint ICME encounters: Pre-STEREO and STEREO observations”. In: *Journal of Atmospheric and Solar-Terrestrial Physics* 73.10. Three dimensional aspects of CMEs, their source regions and interplanetary manifestations, pp. 1228–1241. ISSN: 1364-6826. DOI: <https://doi.org/10.1016/j.jastp.2010.10.012> (cit. on pp. 36, 88, 89).
- Kilpua, E. K. J., H. E. J. Koskinen, and T. I. Pulkkinen (2017). “Coronal mass ejections and their sheath regions in interplanetary space”. In: *Living Reviews in Solar Physics* 14.1. DOI: [10.1007/s41116-017-0009-6](https://doi.org/10.1007/s41116-017-0009-6) (cit. on pp. 13, 15–18, 36–38, 77, 83, 86, 104).
- Kilpua, E. K. J., M. Mierla, A. N. Zhukov, L. Rodriguez, A. Vourlidas, et al. (Oct. 2014). “Solar Sources of Interplanetary Coronal Mass Ejections During the Solar Cycle 23/24 Minimum”. In: *Sol. Phys.* 289.10, pp. 3773–3797. DOI: [10.1007/s11207-014-0552-4](https://doi.org/10.1007/s11207-014-0552-4) (cit. on p. 14).
- Kilpua, E. K. J., J. Pomoell, A. Vourlidas, R. Vainio, J. Luhmann, et al. (Dec. 2009). “STEREO observations of interplanetary coronal mass ejections and prominence deflection during solar minimum period”. In: *Annales Geophysicae* 27.12, pp. 4491–4503. DOI: [10.5194/angeo-27-4491-2009](https://doi.org/10.5194/angeo-27-4491-2009) (cit. on p. 89).
- Klein, L. W. and L. F. Burlaga (1982). “Interplanetary magnetic clouds At 1 AU”. In: *Journal of Geophysical Research: Space Physics* 87.A2, pp. 613–624. DOI: <https://doi.org/10.1029/JA087iA02p00613> (cit. on p. 46).
- Kohl, J. (Jan. 2006). “Ultraviolet spectroscopy of the extended solar corona”. In: *36th COSPAR Scientific Assembly*. Vol. 36, p. 3317 (cit. on p. 10).

- Kohl, J. L., R. Esser, L. D. Gardner, S. Habbal, P. S. Daigneau, et al. (Dec. 1995). “The Ultraviolet Coronagraph Spectrometer for the Solar and Heliospheric Observatory”. In: *Sol. Phys.* 162.1-2, pp. 313–356. DOI: [10.1007/BF00733433](https://doi.org/10.1007/BF00733433) (cit. on p. 89).
- Korendyke, C., Charles Brown, Roger Thomas, Christian Keyser, Joseph Davila, et al. (Jan. 2007). “Optics and mechanisms for the Extreme-Ultraviolet Imaging Spectrometer on the Solar-B satellite”. In: *Applied optics* 45, pp. 8674–88. DOI: [10.1364/AO.45.008674](https://doi.org/10.1364/AO.45.008674) (cit. on p. 89).
- Kosugi, T., K. Matsuzaki, T. Sakao, T. Shimizu, Y. Sone, et al. (June 2007). “The Hinode (Solar-B) Mission: An Overview”. In: *Solar Physics* 243.1, pp. 3–17. ISSN: 1573-093X. DOI: [10.1007/s11207-007-9014-6](https://doi.org/10.1007/s11207-007-9014-6) (cit. on p. 39).
- Krucker, Säm, G. J. Hurford, O. Grimm, S. Kögl, H. -P. Gröbelbauer, et al. (Oct. 2020). “The Spectrometer/Telescope for Imaging X-rays (STIX)”. In: *Astron. Astrophys.* 642, A15, A15. DOI: [10.1051/0004-6361/201937362](https://doi.org/10.1051/0004-6361/201937362) (cit. on p. 44).
- Kruse, M., V. Heidrich-Meisner, and R. F. Wimmer-Schweingruber (Jan. 2021). “Evaluation of a potential field source surface model with elliptical source surfaces via ballistic back mapping of in situ spacecraft data”. In: *Astron. Astrophys.* 645, A83, A83. DOI: [10.1051/0004-6361/202039120](https://doi.org/10.1051/0004-6361/202039120) (cit. on p. 48).
- Landi, E. and P. Testa (Feb. 2015). “Neon and Oxygen Abundances and Abundance Ratio in the Solar Corona”. In: *Astrophys. J.* 800.2, 110, p. 110. DOI: [10.1088/0004-637X/800/2/110](https://doi.org/10.1088/0004-637X/800/2/110) (cit. on p. 78).
- Landi, Simone, Petr Hellinger, and Marco Velli (2006). “Heliospheric magnetic field polarity inversions driven by radial velocity field structures”. In: *Geophysical Research Letters* 33.14. DOI: <https://doi.org/10.1029/2006GL026308> (cit. on p. 101).
- Lanzerotti, Louis J. (2001). “Space Weather Effects on Technologies”. In: *Space Weather*. American Geophysical Union (AGU), pp. 11–22. ISBN: 9781118668351. DOI: <https://doi.org/10.1029/GM125p0011> (cit. on p. 18).
- Lapenta, Giovanni and D. A. Knoll (May 2005). “Effect of a Converging Flow at the Streamer Cusp on the Genesis of the Slow Solar Wind”. In: *Astrophys. J.* 624.2, pp. 1049–1056. DOI: [10.1086/429262](https://doi.org/10.1086/429262) (cit. on p. 9).
- Lee, C. O., J. G. Luhmann, J. T. Hoeksema, X. Sun, C. N. Arge, et al. (Apr. 2011). “Coronal Field Opens at Lower Height During the Solar Cycles 22 and 23 Minimum Periods: IMF Comparison Suggests the Source Surface Should Be Lowered”. In: *Sol. Phys.* 269.2, pp. 367–388. DOI: [10.1007/s11207-010-9699-9](https://doi.org/10.1007/s11207-010-9699-9) (cit. on p. 47).
- Lee, C. O., J. G. Luhmann, D. Odstreil, P. J. MacNeice, I. de Pater, et al. (Jan. 2009). “The Solar Wind at 1 AU During the Declining Phase of Solar Cycle 23: Comparison of 3D Numerical Model Results with Observations”. In: *Sol. Phys.* 254.1, pp. 155–183. DOI: [10.1007/s11207-008-9280-y](https://doi.org/10.1007/s11207-008-9280-y) (cit. on p. 47).
- Lee, Jin-Yi and John C. Raymond (Oct. 2012). “Low Ionization State Plasma in Coronal Mass Ejections”. In: *Astrophys. J.* 758.2, 116, p. 116. DOI: [10.1088/0004-637X/758/2/116](https://doi.org/10.1088/0004-637X/758/2/116) (cit. on p. 78).
- Lemen, James R., Alan M. Title, David J. Akin, Paul F. Boerner, Catherine Chou, et al. (Jan. 2012). “The Atmospheric Imaging Assembly (AIA) on the Solar Dynamics Observatory (SDO)”. In: *Sol. Phys.* 275.1-2, pp. 17–40. DOI: [10.1007/s11207-011-9776-8](https://doi.org/10.1007/s11207-011-9776-8) (cit. on p. 4).
- Lepping, R. P., M. H. Acuña, L. F. Burlaga, W. M. Farrell, J. A. Slavin, et al. (Feb. 1995). “The Wind Magnetic Field Investigation”. In: *Space Sci. Rev.* 71.1-4, pp. 207–229. DOI: [10.1007/BF00751330](https://doi.org/10.1007/BF00751330) (cit. on p. 40).

- Lepri, Susan T. and Yeimy J. Rivera (May 2021). “Elemental Abundances of Prominence Material inside ICMEs”. In: *Astrophys. J.* 912.1, 51, p. 51. DOI: [10.3847/1538-4357/abea9f](https://doi.org/10.3847/1538-4357/abea9f) (cit. on p. 78).
- LeVeque, R.J., O. Steiner, A. Gautschy, D. Mihalas, E.A. Dorfi, et al. (1998). *Computational Methods for Astrophysical Fluid Flow: Saas-Fee Advanced Course 27. Lecture Notes 1997 Swiss Society for Astrophysics and Astronomy*. Saas-Fee Advanced Course. Springer Berlin Heidelberg. ISBN: 9783540644484 (cit. on p. 56).
- Levine, R. H., M. D. Altschuler, J. W. Harvey, and B. V. Jackson (July 1977). “Open magnetic structures on the sun.” In: *Astrophys. J.* 215, pp. 636–651. DOI: [10.1086/155398](https://doi.org/10.1086/155398) (cit. on pp. 31, 47, 48).
- Lie-Svendsen, Øystein and Ruth Esser (Jan. 2005). “Modeling the Energy Budget of Solar Wind Minor Ions: Implications for Temperatures and Abundances”. In: *The Astrophysical Journal* 618.2, p. 1057. DOI: [10.1086/426073](https://doi.org/10.1086/426073) (cit. on p. 107).
- Lindsay, G. M., J. G. Luhmann, C. T. Russell, and J. T. Gosling (1999). “Relationships between coronal mass ejection speeds from coronagraph images and interplanetary characteristics of associated interplanetary coronal mass ejections”. In: *Journal of Geophysical Research: Space Physics* 104.A6, pp. 12515–12523. DOI: <https://doi.org/10.1029/1999JA900051> (cit. on p. 83).
- Lionello, Roberto, Jon A. Linker, and Zoran Mikić (Sept. 2003). “Three-Dimensional Magnetohydrodynamics of the Solar Corona and of the Solar Wind with Improved Energy Transport”. In: *Solar Wind Ten*. Ed. by Marco Velli, Roberto Bruno, Francesco Malara, and B. Bucci. Vol. 679. American Institute of Physics Conference Series, pp. 222–225. DOI: [10.1063/1.1618582](https://doi.org/10.1063/1.1618582) (cit. on p. 49).
- Livingston, W., L. Wallace, O. R. White, and M. S. Giampapa (Mar. 2007). “Sun-as-a-Star Spectrum Variations 1974-2006”. In: *The Astrophysical Journal* 657.2, p. 1137. DOI: [10.1086/511127](https://doi.org/10.1086/511127) (cit. on p. 78).
- Low, B. C. (Feb. 1977). “Evolving force-free magnetic fields. I. The development of the preflare stage.” In: *Astrophys. J.* 212, pp. 234–242. DOI: [10.1086/155042](https://doi.org/10.1086/155042) (cit. on p. 37).
- Low, B. C. and M. A. Berger (May 2003). “A Morphological Study of Helical Coronal Magnetic Structures”. In: *Astrophys. J.* 589.1, pp. 644–657. DOI: [10.1086/374614](https://doi.org/10.1086/374614) (cit. on pp. 37, 105).
- Luhmann, J.G., D.W. Curtis, R.P. Lin, D. Larson, P. Schroeder, et al. (2005). “IMPACT: Science goals and firsts with STEREO”. In: *Advances in Space Research* 36.8. Solar Encounter, Solar-B and STEREO, pp. 1534–1543. ISSN: 0273-1177. DOI: <https://doi.org/10.1016/j.asr.2005.03.033> (cit. on p. 41).
- Luhmann, J.G., N. Gopalswamy, L. K. Jian, and N. Lugaz (2020). “ICME Evolution in the Inner Heliosphere”. In: *Solar Physics* 295.4. DOI: [10.1007/s11207-020-01624-0](https://doi.org/10.1007/s11207-020-01624-0) (cit. on pp. 13, 18, 77).
- Lundquist, S. (1950). “Magnetohydrostatic fields”. In: *Ark. Fys.* 2, pp. 361–365 (cit. on p. 37).
- Lynch, B. J., A. A. Reinard, T. Mulligan, K. K. Reeves, C. E. Rakowski, et al. (Oct. 2011). “Ionic Composition Structure of Coronal Mass Ejections in Axisymmetric Magnetohydrodynamic Models”. In: *Astrophys. J.* 740.2, 112, p. 112. DOI: [10.1088/0004-637X/740/2/112](https://doi.org/10.1088/0004-637X/740/2/112) (cit. on p. 78).
- Lyot, Bernard (June 1939). “The study of the solar corona and prominences without eclipses (George Darwin Lecture, 1939)”. In: *Mon. Not. R. Astron. Soc.* 99, p. 580. DOI: [10.1093/mnras/99.8.580](https://doi.org/10.1093/mnras/99.8.580) (cit. on p. 7).

- Mackay, Duncan H. and Anthony R. Yeates (Nov. 2012). “The Sun’s Global Photospheric and Coronal Magnetic Fields: Observations and Models”. In: *Living Reviews in Solar Physics* 9.1, p. 6. ISSN: 1614-4961. DOI: [10.12942/lrsp-2012-6](https://doi.org/10.12942/lrsp-2012-6) (cit. on pp. 31, 47).
- MacNeice, P., L. K. Jian, S. K. Antiochos, C. N. Arge, C. D. Bussy-Virat, et al. (2018). “Assessing the Quality of Models of the Ambient Solar Wind”. In: *Space Weather* 16.11, pp. 1644–1667. DOI: <https://doi.org/10.1029/2018SW002040> (cit. on pp. 49–52, 75).
- Magyar, Norbert, Dominik Utz, Robertus Erdélyi, and Valery M. Nakariakov (Apr. 2021). “Could Switchbacks Originate in the Lower Solar Atmosphere? I. Formation Mechanisms of Switchbacks”. In: *The Astrophysical Journal* 911.2, p. 75. DOI: [10.3847/1538-4357/abec49](https://doi.org/10.3847/1538-4357/abec49) (cit. on p. 101).
- Maksimovic, M., S. D. Bale, T. Chust, Y. Khotyaintsev, V. Krasnoselskikh, et al. (Oct. 2020). “The Solar Orbiter Radio and Plasma Waves (RPW) instrument”. In: *Astron. Astrophys.* 642, A12, A12. DOI: [10.1051/0004-6361/201936214](https://doi.org/10.1051/0004-6361/201936214) (cit. on p. 43).
- Maloney, Shane A. and Peter T. Gallagher (Dec. 2010). “Solar Wind Drag and the Kinematics of Interplanetary Coronal Mass Ejections”. In: *Astrophys. J. Lett.* 724.2, pp. L127–L132. DOI: [10.1088/2041-8205/724/2/L127](https://doi.org/10.1088/2041-8205/724/2/L127) (cit. on p. 78).
- Manchester, W. B., Tamas I. Gombosi, Ilia Roussev, Darren L. De Zeeuw, I. V. Sokolov, et al. (2004). “Three-dimensional MHD simulation of a flux rope driven CME”. In: *Journal of Geophysical Research: Space Physics* 109.A1. DOI: <https://doi.org/10.1029/2002JA009672> (cit. on p. 38).
- Manchester, W. B., J. U. Kozyra, S. T. Lepri, and B. Lavraud (2014). “Simulation of magnetic cloud erosion during propagation”. In: *Journal of Geophysical Research: Space Physics* 119.7, pp. 5449–5464. DOI: <https://doi.org/10.1002/2014JA019882> (cit. on pp. 38, 83).
- Mandrini, C. H., F. A. Nuevo, A. M. Vásquez, P. Démoulin, L. van Driel-Gesztelyi, et al. (Nov. 2014). “How Can Active Region Plasma Escape into the Solar Wind from Below a Closed Helmet Streamer?” In: *Sol. Phys.* 289.11, pp. 4151–4171. DOI: [10.1007/s11207-014-0582-y](https://doi.org/10.1007/s11207-014-0582-y) (cit. on p. 48).
- Marubashi, K. and R. P. Lepping (2007). “Long-duration magnetic clouds: a comparison of analyses using torus- and cylinder-shaped flux rope models”. In: *Annales Geophysicae* 25.11, pp. 2453–2477. DOI: [10.5194/angeo-25-2453-2007](https://doi.org/10.5194/angeo-25-2453-2007) (cit. on p. 105).
- Matteini, L., T. S. Horbury, F. Pantellini, M. Velli, and S. J. Schwartz (Mar. 2015). “Ion Kinetic Energy Conservation and Magnetic Field Strength Constancy in Multi-fluid Solar Wind Alfvénic Turbulence”. In: *Astrophys. J.* 802.1, 11, p. 11. DOI: [10.1088/0004-637X/802/1/11](https://doi.org/10.1088/0004-637X/802/1/11) (cit. on p. 101).
- Matteini, L., D. Stansby, T. S. Horbury, and C. H. K. Chen (Jan. 2019). “The rotation angle distribution underlying magnetic field fluctuations in the 1/f range of solar wind turbulent spectra”. In: *Nuovo Cimento C Geophysics Space Physics C* 42.1, 16, p. 16. DOI: [10.1393/ncc/i2019-19016-y](https://doi.org/10.1393/ncc/i2019-19016-y) (cit. on p. 100).
- Matzka, J., C. Stolle, Y. Yamazaki, O. Bronkalla, and A. Morschhauser (2021). “The Geomagnetic Kp Index and Derived Indices of Geomagnetic Activity”. In: *Space Weather* 19.5. e2020SW002641 2020SW002641, e2020SW002641. DOI: <https://doi.org/10.1029/2020SW002641> (cit. on pp. 17, 18).
- McComas, D. J., N. Alexander, N. Angold, S. Bale, C. Beebe, et al. (Dec. 2016). “Integrated Science Investigation of the Sun (ISIS): Design of the Energetic Particle

- Investigation”. In: *Space Science Reviews* 204.1, pp. 187–256. ISSN: 1572-9672. DOI: [10.1007/s11214-014-0059-1](https://doi.org/10.1007/s11214-014-0059-1) (cit. on p. 41).
- McComas, D. J., H. A. Elliott, N. A. Schwadron, J. T. Gosling, R. M. Skoug, et al. (2003). “The three-dimensional solar wind around solar maximum”. In: *Geophysical Research Letters* 30.10. DOI: <https://doi.org/10.1029/2003GL017136> (cit. on pp. 10, 11).
- Merkin, V. G., J. G. Lyon, S. L. McGregor, and D. M. Pahud (July 2011). “Disruption of a heliospheric current sheet fold”. In: *Geophys. Res. Lett.* 38.14, L14107, p. L14107. DOI: [10.1029/2011GL047822](https://doi.org/10.1029/2011GL047822) (cit. on p. 50).
- Michel, F. C. (1967). “Model of solar wind structure”. In: *Journal of Geophysical Research (1896-1977)* 72.7, pp. 1917–1932. DOI: <https://doi.org/10.1029/JZ072i007p01917> (cit. on p. 100).
- Mignone, A., G. Bodo, S. Massaglia, T. Matsakos, O. Tesileanu, et al. (May 2007). “PLUTO: A Numerical Code for Computational Astrophysics”. In: *Astrophys. J. Suppl. Ser.* 170.1, pp. 228–242. DOI: [10.1086/513316](https://doi.org/10.1086/513316) (cit. on pp. 52, 56, 110).
- Mignone, A., C. Zanni, P. Tzeferacos, B. van Straalen, P. Colella, et al. (Jan. 2012). “The PLUTO Code for Adaptive Mesh Computations in Astrophysical Fluid Dynamics”. In: *Astrophys. J. Suppl. Ser.* 198.1, 7, p. 7. DOI: [10.1088/0067-0049/198/1/7](https://doi.org/10.1088/0067-0049/198/1/7) (cit. on pp. 52, 56, 110).
- Mignone, Andrea, Petros Tzeferacos, and Gianluigi Bodo (2010). “High-order conservative finite difference GLM–MHD schemes for cell-centered MHD”. In: *Journal of Computational Physics* 229.17, pp. 5896–5920. ISSN: 0021-9991. DOI: <https://doi.org/10.1016/j.jcp.2010.04.013> (cit. on p. 58).
- Mikić, Zoran, Cooper Downs, Jon A. Linker, Ronald M. Caplan, et al. (Aug. 2018). “Predicting the corona for the 21 August 2017 total solar eclipse”. In: *Nature Astronomy* 2, pp. 913–921. DOI: [10.1038/s41550-018-0562-5](https://doi.org/10.1038/s41550-018-0562-5) (cit. on p. 49).
- Mikić, Z. and M. A. Lee (Mar. 2006). “An Introduction to Theory and Models of CMEs, Shocks, and Solar Energetic Particles”. In: *Space Science Reviews* 123.1, pp. 57–80. ISSN: 1572-9672. DOI: [10.1007/s11214-006-9012-2](https://doi.org/10.1007/s11214-006-9012-2) (cit. on pp. 36, 37).
- Mikić, Zoran, Jon A. Linker, Dalton D. Schnack, Roberto Lionello, and Alfonso Tarditi (May 1999). “Magnetohydrodynamic modeling of the global solar corona”. In: *Physics of Plasmas* 6.5, pp. 2217–2224. DOI: [10.1063/1.873474](https://doi.org/10.1063/1.873474) (cit. on pp. 47, 49).
- Mishra, Wageesh, Urmi Doshi, and Nandita Srivastava (2021). “Radial Sizes and Expansion Behavior of ICMEs in Solar Cycles 23 and 24”. In: *Frontiers in Astronomy and Space Sciences* 8. ISSN: 2296-987X. DOI: [10.3389/fspas.2021.713999](https://doi.org/10.3389/fspas.2021.713999) (cit. on pp. 18, 77).
- Moses, John D., Ester Antonucci, Jeffrey Newmark, Auchère, Frédéric, Fineschi, Silvano, et al. (2020). “Global helium abundance measurements in the solar corona”. In: *Nature Astronomy* 4 (12), pp. 1134–1139. DOI: [10.1038/s41550-020-1156-6](https://doi.org/10.1038/s41550-020-1156-6) (cit. on pp. 92, 97).
- Möstl, C., C. J. Farrugia, C. Miklenic, M. Temmer, A. B. Galvin, et al. (2009a). “Multispacecraft recovery of a magnetic cloud and its origin from magnetic reconnection on the Sun”. In: *Journal of Geophysical Research: Space Physics* 114.A4. DOI: <https://doi.org/10.1029/2008JA013657> (cit. on p. 37).
- Möstl, C., C. J. Farrugia, M. Temmer, C. Miklenic, A. M. Veronig, et al. (Nov. 2009b). “Linking Remote Imagery of a Coronal Mass Ejection to Its In Situ Signatures

- at 1 AU”. In: *Astrophys. J. Lett.* 705.2, pp. L180–L185. DOI: [10.1088/0004-637X/705/2/L180](https://doi.org/10.1088/0004-637X/705/2/L180) (cit. on p. 89).
- Möstl, Christian, Andreas J. Weiss, Martin A. Reiss, Tanja Amerstorfer, Rachel L. Bailey, et al. (Jan. 2022). “Multipoint Interplanetary Coronal Mass Ejections Observed with Solar Orbiter, BepiColombo, Parker Solar Probe, Wind, and STEREO-A”. In: *The Astrophysical Journal Letters* 924.1, p. L6. DOI: [10.3847/2041-8213/ac42d0](https://doi.org/10.3847/2041-8213/ac42d0) (cit. on p. 88).
- Moussas, X., J. M. Polygiannakis, A. Hillaris, P. Preka-Papadema, and E. Andrikopoulou (Oct. 2002). “CME velocities, accelerations, widths and positions in the ascending phase of the solar cycle 23 (1996-2001)”. In: *SOLMAG 2002. Proceedings of the Magnetic Coupling of the Solar Atmosphere Euroconference*. Ed. by Huguette Sawaya-Lacoste. Vol. 505. ESA Special Publication, pp. 513–516 (cit. on p. 15).
- Mozer, F. S., S. D. Bale, J. W. Bonnell, J. F. Drake, E. L. M. Hanson, et al. (Sept. 2021). “On the Origin of Switchbacks Observed in the Solar Wind”. In: *The Astrophysical Journal* 919.1, p. 60. DOI: [10.3847/1538-4357/ac110d](https://doi.org/10.3847/1538-4357/ac110d) (cit. on p. 101).
- Müller, D., R. G. Marsden, O. C. St. Cyr, H. R. Gilbert, and The Solar Orbiter Team (July 2013). “Solar Orbiter”. In: *Solar Physics* 285.1, pp. 25–70. ISSN: 1573-093X. DOI: [10.1007/s11207-012-0085-7](https://doi.org/10.1007/s11207-012-0085-7) (cit. on p. 42).
- Müller, D., St. Cyr, O. C., Zouganelis, I., Gilbert, H. R., Marsden, R., et al. (2020). “The Solar Orbiter mission - Science overview”. In: *A&A* 642, A1. DOI: [10.1051/0004-6361/202038467](https://doi.org/10.1051/0004-6361/202038467) (cit. on pp. 42–44).
- Musa, Omer, Guoping Huang, Zonghan Yu, and Qian Li (2020). “An improved Roe solver for high order reconstruction schemes”. In: *Computers & Fluids* 207, p. 104591. ISSN: 0045-7930. DOI: <https://doi.org/10.1016/j.compfluid.2020.104591> (cit. on p. 57).
- Na, Hyeonock, Y. J. Moon, and Harim Lee (Apr. 2017). “Development of a Full Ice-cream Cone Model for Halo Coronal Mass Ejections”. English. In: *Astrophysical Journal* 839.2. ISSN: 0004-637X. DOI: [10.3847/1538-4357/aa697c](https://doi.org/10.3847/1538-4357/aa697c) (cit. on pp. 38, 39).
- National Research Council (2003). *New Frontiers in the Solar System: An Integrated Exploration Strategy*. Washington, DC: The National Academies Press. DOI: [10.17226/10432](https://doi.org/10.17226/10432) (cit. on p. 78).
- (2008). *Severe Space Weather Events: Understanding Societal and Economic Impacts: A Workshop Report*. Washington, DC: The National Academies Press. ISBN: 978-0-309-12769-1. DOI: [10.17226/12507](https://doi.org/10.17226/12507) (cit. on pp. 18, 78).
- Ness, Norman F. and John M. Wilcox (Oct. 1964). “Solar Origin of the Interplanetary Magnetic Field”. In: *Phys. Rev. Lett.* 13 (15), pp. 461–464. DOI: [10.1103/PhysRevLett.13.461](https://doi.org/10.1103/PhysRevLett.13.461) (cit. on pp. 8, 26).
- Neugebauer, M., R. J. Forsyth, A. B. Galvin, K. L. Harvey, J. T. Hoeksema, et al. (July 1998). “Spatial structure of the solar wind and comparisons with solar data and models”. In: *J. Geophys. Res.* 103.A7, pp. 14587–14600. DOI: [10.1029/98JA00798](https://doi.org/10.1029/98JA00798) (cit. on pp. 45, 47).
- Neugebauer, M., P. C. Liewer, E. J. Smith, R. M. Skoug, and T. H. Zurbuchen (2002). “Sources of the solar wind at solar activity maximum”. In: *Journal of Geophysical Research: Space Physics* 107.A12, SSH 13-1-SSH 13–15. DOI: <https://doi.org/10.1029/2001JA000306> (cit. on p. 45).

- Neugebauer, Marcia and Bruce E. Goldstein (June 2013). “Double-proton beams and magnetic switchbacks in the solar wind”. In: *Solar Wind 13*. Ed. by Gary P. Zank, Joe Borovsky, Roberto Bruno, Jonathan Cirtain, Steve Cranmer, et al. Vol. 1539. American Institute of Physics Conference Series, pp. 46–49. DOI: [10.1063/1.4810986](https://doi.org/10.1063/1.4810986) (cit. on p. 100).
- Neugebauer, Marcia and Conway W. Snyder (Dec. 1962). “Solar Plasma Experiment”. In: *Science* 138.3545, pp. 1095–1097. DOI: [10.1126/science.138.3545.1095-a](https://doi.org/10.1126/science.138.3545.1095-a) (cit. on pp. 8, 26).
- Nitta, Nariaki V., Donald V. Reames, Marc L. De Rosa, Yang Liu, Seiji Yashiro, et al. (Oct. 2006). “Solar Sources of Impulsive Solar Energetic Particle Events and Their Magnetic Field Connection to the Earth”. In: *Astrophys. J.* 650.1, pp. 438–450. DOI: [10.1086/507442](https://doi.org/10.1086/507442) (cit. on p. 48).
- Nitti, Simona, Tatiana Podladchikova, Stefan J Hofmeister, Astrid M Veronig, Giuliana Verbanac, et al. (Jan. 2023). “Geomagnetic storm forecasting from solar coronal holes”. In: *Monthly Notices of the Royal Astronomical Society* 519.2, pp. 3182–3193. ISSN: 0035-8711. DOI: [10.1093/mnras/stac3533](https://doi.org/10.1093/mnras/stac3533) (cit. on p. 17).
- Nolte, J. T., A. S. Krieger, E. C. Roelof, and R. E. Gold (Mar. 1977). “High coronal structure of high velocity solar wind stream sources.” In: *Sol. Phys.* 51.2, pp. 459–471. DOI: [10.1007/BF00216379](https://doi.org/10.1007/BF00216379) (cit. on p. 46).
- Nolte, J. T. and E. C. Roelof (Nov. 1973). “Large-Scale Structure of the Interplanetary Medium, I: High Coronal Source Longitude of the Quiet-Time Solar Wind”. In: *Sol. Phys.* 33.1, pp. 241–257. DOI: [10.1007/BF00152395](https://doi.org/10.1007/BF00152395) (cit. on p. 45).
- O’Kane, Jennifer, Cecilia Mac Cormack, Cristina H. Mandrini, Pascal Démoulin, Lucie M. Green, et al. (Feb. 2021). “The Magnetic Environment of a Stealth Coronal Mass Ejection”. In: *The Astrophysical Journal* 908.1, p. 89. DOI: [10.3847/1538-4357/abd2bf](https://doi.org/10.3847/1538-4357/abd2bf) (cit. on p. 14).
- Odstřil, D. (2003). “Modeling 3-D solar wind structure”. In: *Advances in Space Research* 32.4. Heliosphere at Solar Maximum, pp. 497–506. ISSN: 0273-1177. DOI: [https://doi.org/10.1016/S0273-1177\(03\)00332-6](https://doi.org/10.1016/S0273-1177(03)00332-6) (cit. on p. 50).
- Odstřil, D., P. Riley, and X. P. Zhao (2004). “Numerical simulation of the 12 May 1997 interplanetary CME event”. In: *Journal of Geophysical Research: Space Physics* 109.A2. DOI: <https://doi.org/10.1029/2003JA010135> (cit. on pp. 38, 50).
- Odstřil, D. and V. J. Pizzo (1999a). “Three-dimensional propagation of coronal mass ejections (CMEs) in a structured solar wind flow: 1. CME launched within the streamer belt”. In: *Journal of Geophysical Research: Space Physics* 104.A1, pp. 483–492. DOI: <https://doi.org/10.1029/1998JA900019> (cit. on pp. 38, 50, 80, 86).
- (1999b). “Three-dimensional propagation of coronal mass ejections (CMEs) in a structured solar wind flow: 2. CME launched adjacent to the streamer belt”. In: *Journal of Geophysical Research: Space Physics* 104.A1, pp. 493–503. DOI: <https://doi.org/10.1029/1998JA900038> (cit. on p. 50).
- Odstřil, D., Z. Smith, and M. Dryer (1996). “Distortion of the heliospheric plasma sheet by interplanetary shocks”. In: *Geophysical Research Letters* 23.18, pp. 2521–2524. DOI: <https://doi.org/10.1029/96GL00159> (cit. on p. 50).
- Ogilvie, K. W., D. J. Chornay, R. J. Fritzenreiter, F. Hunsaker, J. Keller, et al. (Feb. 1995). “SWE, A Comprehensive Plasma Instrument for the Wind Spacecraft”. In: *Space Sci. Rev.* 71.1-4, pp. 55–77. DOI: [10.1007/BF00751326](https://doi.org/10.1007/BF00751326) (cit. on p. 39).

- Owen, C. J., R. Bruno, S. Livi, P. Louarn, K. Al Janabi, et al. (Oct. 2020). “The Solar Orbiter Solar Wind Analyser (SWA) suite”. In: *Astron. Astrophys.* 642, A16, A16. DOI: [10.1051/0004-6361/201937259](https://doi.org/10.1051/0004-6361/201937259) (cit. on p. 43).
- Owens, M. J. (Dec. 2008). “Combining remote and in situ observations of coronal mass ejections to better constrain magnetic cloud reconstruction”. In: *Journal of Geophysical Research (Space Physics)* 113.A12, A12102, A12102. DOI: [10.1029/2008JA013589](https://doi.org/10.1029/2008JA013589) (cit. on p. 89).
- Owens, M. J., N. U. Crooker, and T. S. Horbury (Oct. 2009). “The expected imprint of flux rope geometry on suprathermal electrons in magnetic clouds”. In: *Annales Geophysicae* 27.10, pp. 4057–4067. DOI: [10.5194/angeo-27-4057-2009](https://doi.org/10.5194/angeo-27-4057-2009) (cit. on p. 16).
- Owens, M. J., H. E. Spence, S. McGregor, W. J. Hughes, J. M. Quinn, et al. (2008). “Metrics for solar wind prediction models: Comparison of empirical, hybrid, and physics-based schemes with 8 years of L1 observations”. In: *Space Weather* 6.8. DOI: <https://doi.org/10.1029/2007SW000380> (cit. on p. 76).
- Owens, Mathew J. (Nov. 2018). “Time-Window Approaches to Space-Weather Forecast Metrics: A Solar Wind Case Study”. In: *Space Weather* 16.11, pp. 1847–1861. DOI: [10.1029/2018SW002059](https://doi.org/10.1029/2018SW002059) (cit. on p. 76).
- Pal, Sanchita, Benjamin J. Lynch, Simon W. Good, Erika Palmerio, Eleanna Asvestari, et al. (May 2022). “Eruption and Interplanetary Evolution of a Stealthy Streamer-Blowout CME Observed by PSP at  $\sim 0.5$  AU”. In: *Frontiers in Astronomy and Space Sciences* 9, 903676, p. 903676. DOI: [10.3389/fspas.2022.903676](https://doi.org/10.3389/fspas.2022.903676) (cit. on pp. 14, 86).
- Panasenco, Olga, Marco Velli, Raffaella D’Amicis, Chen Shi, Victor Réville, et al. (Feb. 2020). “Exploring Solar Wind Origins and Connecting Plasma Flows from the Parker Solar Probe to 1 au: Nonspherical Source Surface and Alfvénic Fluctuations”. In: *The Astrophysical Journal Supplement Series* 246.2, p. 54. DOI: [10.3847/1538-4365/ab61f4](https://doi.org/10.3847/1538-4365/ab61f4) (cit. on p. 48).
- Parker, E. N. (Nov. 1958). “Dynamics of the Interplanetary Gas and Magnetic Fields.” In: *Astrophys. J.* 128, p. 664. DOI: [10.1086/146579](https://doi.org/10.1086/146579) (cit. on pp. 26, 27, 32, 34, 52, 53, 75, 106, 109).
- Pei, C., J. R. Jokipii, and J. Giacalone (Apr. 2006). “Effect of a Random Magnetic Field on the Onset Times of Solar Particle Events”. In: *Astrophys. J.* 641.2, pp. 1222–1226. DOI: [10.1086/427161](https://doi.org/10.1086/427161) (cit. on p. 76).
- Perrone, Denise, D. Stansby, T. S. Horbury, and L. Matteini (Mar. 2019). “Radial evolution of the solar wind in pure high-speed streams: HELIOS revised observations”. In: *Mon. Not. R. Astron. Soc.* 483.3, pp. 3730–3737. DOI: [10.1093/mnras/sty3348](https://doi.org/10.1093/mnras/sty3348) (cit. on pp. 64, 67, 76, 102).
- Pesnell, W. Dean, B. J. Thompson, and P. C. Chamberlin (Jan. 2012). “The Solar Dynamics Observatory (SDO)”. In: *Sol. Phys.* 275.1-2, pp. 3–15. DOI: [10.1007/s11207-011-9841-3](https://doi.org/10.1007/s11207-011-9841-3) (cit. on p. 4).
- Pinto, Rui F. and Alexis P. Rouillard (2017). “A Multiple Flux-tube Solar Wind Model”. In: *The Astrophysical Journal* 838.2, p. 89. DOI: [10.3847/1538-4357/aa6398](https://doi.org/10.3847/1538-4357/aa6398) (cit. on p. 47).
- Pizzo, Vic, George Millward, Annette Parsons, Douglas Biesecker, Steve Hill, et al. (Mar. 2011). “Wang-Sheeley-Arge-Enlil Cone Model Transitions to Operations”. In: *Space Weather* 9.3, 03004, p. 03004. DOI: [10.1029/2011SW000663](https://doi.org/10.1029/2011SW000663) (cit. on p. 50).

- Pizzo, Victor J. (1981). “On the application of numerical models to the inverse mapping of solar wind flow structures”. In: *Journal of Geophysical Research: Space Physics* 86.A8, pp. 6685–6690. DOI: <https://doi.org/10.1029/JA086iA08p06685> (cit. on pp. 45, 46).
- Plunkett, S. P., G. E. Brueckner, K. P. Dere, R. A. Howard, M. J. Koomen, et al. (Oct. 1997). “The Relationship of Green-Line Transients to White-Light Coronal Mass Ejections”. In: *Solar Physics* 175.2, pp. 699–718. ISSN: 1573-093X. DOI: [10.1023/A:1004981125702](https://doi.org/10.1023/A:1004981125702) (cit. on p. 38).
- Pogorelov, N. V., S. N. Borovikov, V. Florinski, J. Heerikhuisen, I. A. Kryukov, et al. (Apr. 2009). “Multi-scale Fluid-Kinetic Simulation Suite: A Tool for Efficient Modeling of Space Plasma Flows”. In: *Numerical Modeling of Space Plasma Flows: ASTRONUM-2008*. Ed. by N. V. Pogorelov, E. Audit, P. Colella, and G. P. Zank. Vol. 406. Astronomical Society of the Pacific Conference Series, p. 149 (cit. on p. 50).
- Poletto, G., S. T. Suess, D. A. Biesecker, R. Esser, G. Gloeckler, et al. (2002). “Low-latitude solar wind during the Fall 1998 SOHO-Ulysses quadrature”. In: *Journal of Geophysical Research: Space Physics* 107.A10, SSH 9-1-SSH 9–16. DOI: <https://doi.org/10.1029/2001JA000275> (cit. on p. 89).
- Poletto, G., Steven T. Suess, Alessandro Bemporad, Nathan A. Schwadron, Heather A. Elliott, et al. (Oct. 2004). “Evidence for the Same Hot Plasma after Coronal Mass Ejection Events, in Both Remote and In Situ Observations”. In: *Astrophys. J. Lett.* 613.2, pp. L173–L176. DOI: [10.1086/425136](https://doi.org/10.1086/425136) (cit. on p. 89).
- Pomoell, Jens and S. Poedts (June 2018). “EUHFORIA: European heliospheric forecasting information asset”. In: *Journal of Space Weather and Space Climate* 8, A35, A35. DOI: [10.1051/swsc/2018020](https://doi.org/10.1051/swsc/2018020) (cit. on pp. 18, 38, 50, 77, 80).
- Porsche, H. (Jan. 1977). “Overview of the HELIOS 1 and HELIOS 2 Missions and Their Participation in STIP Intervals I and II”. In: *Study of Travelling Interplanetary Phenomena*. Ed. by M. A. Shea, D. F. Smart, and S. T. Wu. Vol. 71. Astrophysics and Space Science Library, p. 421. DOI: [10.1007/978-90-277-0860-1\\_20](https://doi.org/10.1007/978-90-277-0860-1_20) (cit. on p. 8).
- (June 1981). “Solar probes Helios 1 and 2”. In: *DFVLR* 33, p. 33 (cit. on p. 8).
- Powell, Kenneth G. (1997). “An Approximate Riemann Solver for Magnetohydrodynamics”. In: *Upwind and High-Resolution Schemes*. Ed. by M. Yousuff Hussaini, Bram van Leer, and John Van Rosendale. Berlin, Heidelberg: Springer Berlin Heidelberg, pp. 570–583. ISBN: 978-3-642-60543-7. DOI: [10.1007/978-3-642-60543-7\\_23](https://doi.org/10.1007/978-3-642-60543-7_23) (cit. on p. 57).
- Powell, Kenneth G., Philip L. Roe, Timur J. Linde, Tamas I. Gombosi, and Darren L. De Zeeuw (1999). “A Solution-Adaptive Upwind Scheme for Ideal Magnetohydrodynamics”. In: *Journal of Computational Physics* 154.2, pp. 284–309. ISSN: 0021-9991. DOI: <https://doi.org/10.1006/jcph.1999.6299> (cit. on p. 57).
- Priest, E. (2014). *Magnetohydrodynamics of the Sun*. Cambridge University Press. ISBN: 9780521854719 (cit. on pp. 3–7, 9–11, 14, 15, 24, 25, 29, 33, 34, 77, 106, 107).
- Reames, Donald V. (Oct. 1999). “Particle acceleration at the Sun and in the heliosphere”. In: *Space Sci. Rev.* 90, pp. 413–491. DOI: [10.1023/A:1005105831781](https://doi.org/10.1023/A:1005105831781) (cit. on p. 13).
- (June 2013). “The Two Sources of Solar Energetic Particles”. In: *Space Science Reviews* 175.1, pp. 53–92. ISSN: 1572-9672. DOI: [10.1007/s11214-013-9958-9](https://doi.org/10.1007/s11214-013-9958-9) (cit. on p. 13).

- Reames, Donald V. (Feb. 2020). “Four Distinct Pathways to the Element Abundances in Solar Energetic Particles”. In: *Space Science Reviews* 216.2, p. 20. ISSN: 1572-9672. DOI: [10.1007/s11214-020-0643-5](https://doi.org/10.1007/s11214-020-0643-5) (cit. on pp. 13, 15).
- Reginald, Nelson L., Joseph M. Davila, O. C. St. Cyr, Douglas M. Rabin, Madhulika Guhathakurta, et al. (May 2011). “Electron Temperatures and Flow Speeds of the Low Solar Corona: MACS Results from the Total Solar Eclipse of 29 March 2006 in Libya”. In: *Sol. Phys.* 270.1, 235, p. 235. DOI: [10.1007/s11207-011-9736-3](https://doi.org/10.1007/s11207-011-9736-3) (cit. on p. 33).
- Reinard, Alysha A., Benjamin J. Lynch, and Tamitha Mulligan (Dec. 2012). “Composition structure of Interplanetary Coronal Mass Ejections from multispacecraft observations, modeling, and comparison with numerical simulations”. In: *The Astrophysical Journal* 761.2, p. 175. DOI: [10.1088/0004-637x/761/2/175](https://doi.org/10.1088/0004-637x/761/2/175) (cit. on p. 78).
- Réville, Victor and Allan Sacha Brun (Nov. 2017). “Global Solar Magnetic Field Organization in the Outer Corona: Influence on the Solar Wind Speed and Mass Flux Over the Cycle”. In: *The Astrophysical Journal* 850.1, p. 45. DOI: [10.3847/1538-4357/aa9218](https://doi.org/10.3847/1538-4357/aa9218) (cit. on p. 47).
- Richardson, I. G. and H. V. Cane (2010). “Near-Earth Interplanetary Coronal Mass Ejections During Solar Cycle 23 (1996-2009): Catalog and Summary of Properties”. In: *Solar Physics* 264 (1), pp. 189–237. DOI: [10.1007/s11207-010-9568-6](https://doi.org/10.1007/s11207-010-9568-6) (cit. on pp. 18, 77).
- Richardson, I. G., E. W. Cliver, and H. V. Cane (2001). “Sources of geomagnetic storms for solar minimum and maximum conditions during 1972–2000”. In: *Geophysical Research Letters* 28.13, pp. 2569–2572. DOI: <https://doi.org/10.1029/2001GL013052> (cit. on p. 16).
- Richardson, Ian G. (Jan. 2018). “Solar wind stream interaction regions throughout the heliosphere”. In: *Living Reviews in Solar Physics* 15.1, p. 1. ISSN: 1614-4961. DOI: [10.1007/s41116-017-0011-z](https://doi.org/10.1007/s41116-017-0011-z) (cit. on p. 13).
- Riley, P., R. Lionello, J. A. Linker, Z. Mikić, J. Luhmann, et al. (Dec. 2011). “Global MHD Modeling of the Solar Corona and Inner Heliosphere for the Whole Heliosphere Interval”. In: *Sol. Phys.* 274.1-2, pp. 361–377. DOI: [10.1007/s11207-010-9698-x](https://doi.org/10.1007/s11207-010-9698-x) (cit. on pp. 49, 62).
- Riley, Pete, J. T. Gosling, D. J. McComas, V. J. Pizzo, J. G. Luhmann, et al. (May 1999). “Relationship between Ulysses plasma observations and solar observations during the Whole Sun Month campaign”. In: *J. Geophys. Res.* 104.A5, pp. 9871–9880. DOI: [10.1029/1998JA900078](https://doi.org/10.1029/1998JA900078) (cit. on p. 46).
- Riley, Pete, J. T. Gosling, and V. J. Pizzo (July 1997). “A two-dimensional simulation of the radial and latitudinal evolution of a solar wind disturbance driven by a fast, high-pressure coronal mass ejection”. In: *J. Geophys. Res.* 102.A7, pp. 14677–14686. DOI: [10.1029/97JA01131](https://doi.org/10.1029/97JA01131) (cit. on p. 86).
- Riley, Pete, J. A. Linker, Z. Mikić, R. Lionello, S. A. Ledvina, et al. (Dec. 2006). “A Comparison between Global Solar Magnetohydrodynamic and Potential Field Source Surface Model Results”. In: *Astrophys. J.* 653.2, pp. 1510–1516. DOI: [10.1086/508565](https://doi.org/10.1086/508565) (cit. on p. 47).
- Riley, Pete, Roberto Lionello, Zoran Mikić, and Jon Linker (Jan. 2008). “Using Global Simulations to Relate the Three-Part Structure of Coronal Mass Ejections to In Situ Signatures”. In: *Astrophys. J.* 672.2, pp. 1221–1227. DOI: [10.1086/523893](https://doi.org/10.1086/523893) (cit. on p. 86).

- Riley, Pete, M. Leila Mays, Jesse Andries, Tanja Amerstorfer, Douglas Biesecker, et al. (Sept. 2018). “Forecasting the Arrival Time of Coronal Mass Ejections: Analysis of the CCMC CME Scoreboard”. In: *Space Weather* 16.9, pp. 1245–1260. DOI: [10.1029/2018SW001962](https://doi.org/10.1029/2018SW001962) (cit. on pp. 51, 79).
- Robbrecht, E., D. Berghmans, and R. A. M. Van der Linden (Feb. 2009). “Automated LASCO CME Catalog for Solar Cycle 23: Are CMEs Scale Invariant?” In: *Astrophys. J.* 691.2, pp. 1222–1234. DOI: [10.1088/0004-637X/691/2/1222](https://doi.org/10.1088/0004-637X/691/2/1222) (cit. on pp. 14, 15).
- Rochus, P., F. Auchère, D. Berghmans, L. Harra, W. Schmutz, et al. (Oct. 2020). “The Solar Orbiter EUI instrument: The Extreme Ultraviolet Imager”. In: *Astron. Astrophys.* 642, A8, A8. DOI: [10.1051/0004-6361/201936663](https://doi.org/10.1051/0004-6361/201936663) (cit. on p. 44).
- Rodriguez, L., J. J. Masías-Meza, S. Dasso, P. Démoulin, A. N. Zhukov, et al. (2016). “Typical Profiles and Distributions of Plasma and Magnetic Field Parameters in Magnetic Clouds at 1 AU”. In: *Solar Physics* 291 (7), pp. 2145–2163. DOI: [10.1007/s11207-016-0955-5](https://doi.org/10.1007/s11207-016-0955-5) (cit. on pp. 77, 78).
- Rodriguez Hidalgo, I., M. Collados, and M. Vazquez (Mar. 1994). “Variations of properties of the quiet photosphere along the equator and the central meridian: Spectroscopic results”. In: *Astron. Astrophys.* 283.1, pp. 263–274 (cit. on p. 78).
- Rodriguez-Pacheco, J., R. F. Wimmer-Schweingruber, G. M. Mason, G. C. Ho, S. Sánchez-Prieto, et al. (Oct. 2020). “The Energetic Particle Detector. Energetic particle instrument suite for the Solar Orbiter mission”. In: *Astron. Astrophys.* 642, A7, A7. DOI: [10.1051/0004-6361/201935287](https://doi.org/10.1051/0004-6361/201935287) (cit. on p. 43).
- Roe, P L (1986). “Characteristic-Based Schemes for the Euler Equations”. In: *Annual Review of Fluid Mechanics* 18.1, pp. 337–365. DOI: [10.1146/annurev.fl.18.010186.002005](https://doi.org/10.1146/annurev.fl.18.010186.002005) (cit. on pp. 56, 62).
- Romoli, M., E. Antonucci, V. Andretta, Capuano, G. E., Da Deppo, V., et al. (2021). “First light observations of the solar wind in the outer corona with the Metis coronagraph”. In: *A&A* 656, A32. DOI: [10.1051/0004-6361/202140980](https://doi.org/10.1051/0004-6361/202140980) (cit. on p. 91).
- Rouillard, Alexis P., Athanasios Kouloumvakos, Angelos Vourlidas, Justin Kasper, Stuart Bale, et al. (Feb. 2020). “Relating Streamer Flows to Density and Magnetic Structures at the Parker Solar Probe”. In: *The Astrophysical Journal Supplement Series* 246.2, p. 37. DOI: [10.3847/1538-4365/ab579a](https://doi.org/10.3847/1538-4365/ab579a) (cit. on p. 100).
- Ruffenach, A., B. Lavraud, C. J. Farrugia, P. Démoulin, S. Dasso, et al. (2015). “Statistical study of magnetic cloud erosion by magnetic reconnection”. In: *Journal of Geophysical Research: Space Physics* 120.1, pp. 43–60. DOI: <https://doi.org/10.1002/2014JA020628> (cit. on pp. 81, 86).
- Ruffolo, D., W. H. Matthaeus, R. Chhiber, A. V. Usmanov, Y. Yang, et al. (Oct. 2020). “Shear-driven Transition to Isotropically Turbulent Solar Wind Outside the Alfvén Critical Zone”. In: *The Astrophysical Journal* 902.2, p. 94. DOI: [10.3847/1538-4357/abb594](https://doi.org/10.3847/1538-4357/abb594) (cit. on p. 101).
- Ruffolo, D., W. H. Matthaeus, and P. Chuychai (Nov. 2003). “Trapping of Solar Energetic Particles by the Small-Scale Topology of Solar Wind Turbulence”. In: *Astrophys. J. Lett.* 597.2, pp. L169–L172. DOI: [10.1086/379847](https://doi.org/10.1086/379847) (cit. on p. 76).
- Samara, E., B. Laperre, R. Kieokaew, M. Temmer, C. Verbeke, et al. (Mar. 2022). “Dynamic Time Warping as a Means of Assessing Solar Wind Time Series”. In: *The Astrophysical Journal* 927.2, p. 187. DOI: [10.3847/1538-4357/ac4af6](https://doi.org/10.3847/1538-4357/ac4af6) (cit. on p. 76).

- Samara, E., R. F. Pinto, Magdalenić, J., Wijsen, N., Jerić, V., et al. (2021). “Implementing the MULTI-VP coronal model in EUHFORIA: Test case results and comparisons with the WSA coronal model”. In: *A&A* 648, A35. DOI: [10.1051/0004-6361/202039325](https://doi.org/10.1051/0004-6361/202039325) (cit. on p. 51).
- Schatten, K. H. (Jan. 1971). “Current sheet magnetic model for the solar corona.” In: *Cosmic Electrodynamics* 2, pp. 232–245 (cit. on pp. 31, 48).
- Schatten, Kenneth H., Norman F. Ness, and John M. Wilcox (Oct. 1968). “Influence of a Solar Active Region on the Interplanetary Magnetic Field”. In: *Sol. Phys.* 5.2, pp. 240–256. DOI: [10.1007/BF00147968](https://doi.org/10.1007/BF00147968) (cit. on p. 45).
- Schatten, Kenneth H., John M. Wilcox, and Norman F. Ness (Mar. 1969). “A model of interplanetary and coronal magnetic fields”. In: *Sol. Phys.* 6.3, pp. 442–455. DOI: [10.1007/BF00146478](https://doi.org/10.1007/BF00146478) (cit. on pp. 31, 32, 47, 48).
- Schrijver, Carolus J., Kirsti Kauristie, Alan D. Aylward, Clezio M. Denardini, Sarah E. Gibson, et al. (2015). “Understanding space weather to shield society: A global road map for 2015–2025 commissioned by COSPAR and ILWS”. In: *Advances in Space Research* 55.12, pp. 2745–2807. ISSN: 0273-1177. DOI: <https://doi.org/10.1016/j.asr.2015.03.023> (cit. on pp. 16, 77).
- Schulte in den Bäumen, Hagen, Iver H. Cairns, and P. A. Robinson (2011). “Modeling 1 AU solar wind observations to estimate azimuthal magnetic fields at the solar source surface”. In: *Geophysical Research Letters* 38.24. DOI: <https://doi.org/10.1029/2011GL049578> (cit. on p. 46).
- (2012). “Nonzero azimuthal magnetic fields at the solar source surface: Extraction, model, and implications”. In: *Journal of Geophysical Research: Space Physics* 117.A10. DOI: <https://doi.org/10.1029/2012JA017705> (cit. on p. 46).
- Schwadron, N. A. and D. J. McComas (Mar. 2021). “Switchbacks Explained: Super-Parker Fields—The Other Side of the Sub-Parker Spiral”. In: *The Astrophysical Journal* 909.1, p. 95. DOI: [10.3847/1538-4357/abd4e6](https://doi.org/10.3847/1538-4357/abd4e6) (cit. on pp. 100, 101).
- Schwartz, S. J. and I. W. Roxburgh (1980). “Instabilities in the Solar Wind”. In: *Philosophical Transactions of the Royal Society of London. Series A, Mathematical and Physical Sciences* 297.1433, pp. 555–563. ISSN: 00804614 (cit. on p. 30).
- Schwartz, Steven J. and Eckart Marsch (1983). “The radial evolution of a single solar wind plasma parcel”. In: *Journal of Geophysical Research: Space Physics* 88.A12, pp. 9919–9932. DOI: <https://doi.org/10.1029/JA088iA12p09919> (cit. on p. 88).
- Schwenn, Rainer (Aug. 2006). “Space Weather: The Solar Perspective”. In: *Living Reviews in Solar Physics* 3.1, 2, p. 2. DOI: [10.12942/lrsp-2006-2](https://doi.org/10.12942/lrsp-2006-2) (cit. on pp. 13, 16, 18, 36).
- Scolini, C., L. Rodriguez, M. Mierla, J. Pomoell, and S. Poedts (2019). “Observation-based modelling of magnetised coronal mass ejections with EUHFORIA”. In: *A&A* 626, A122. DOI: [10.1051/0004-6361/201935053](https://doi.org/10.1051/0004-6361/201935053) (cit. on pp. 38, 51, 104).
- Scolini, C., C. Verbeke, S. Poedts, E. Chané, J. Pomoell, et al. (2018). “Effect of the Initial Shape of Coronal Mass Ejections on 3-D MHD Simulations and Geoeffectiveness Predictions”. In: *Space Weather* 16.6, pp. 754–771. DOI: <https://doi.org/10.1029/2018SW001806> (cit. on pp. 38, 51).
- Sheeley N. R., Jr. and Y. -M. Wang (Jan. 1991). “Magnetic Field Configurations Associated with Fast Solar Wind”. In: *Sol. Phys.* 131.1, pp. 165–186. DOI: [10.1007/BF00151752](https://doi.org/10.1007/BF00151752) (cit. on p. 48).

- Sheeley, N. R., Y.-M. Wang, S. H. Hawley, G. E. Brueckner, K. P. Dere, et al. (July 1997). “Measurements of Flow Speeds in the Corona Between 2 and 30  $R_{\odot}$ ”. In: *The Astrophysical Journal* 484.1, p. 472. DOI: [10.1086/304338](https://doi.org/10.1086/304338) (cit. on p. 10).
- Sheeley Jr., N. R. (2017). “Origin of the Wang–Sheeley–Arge solar wind model”. In: *History of Geo- and Space Sciences* 8.1, pp. 21–28. DOI: [10.5194/hgss-8-21-2017](https://doi.org/10.5194/hgss-8-21-2017) (cit. on pp. 48, 50).
- Shibata, Kazunari and Tetsuya Magara (Dec. 2011). “Solar Flares: Magnetohydrodynamic Processes”. In: *Living Reviews in Solar Physics* 8.1, 6, p. 6. DOI: [10.12942/lrsp-2011-6](https://doi.org/10.12942/lrsp-2011-6) (cit. on p. 12).
- Shiota, D. and R. Kataoka (2016). “Magnetohydrodynamic simulation of interplanetary propagation of multiple coronal mass ejections with internal magnetic flux rope (SUSANOO-CME)”. In: *Space Weather* 14.2, pp. 56–75. DOI: <https://doi.org/10.1002/2015SW001308> (cit. on pp. 38, 105).
- Shiota, D., R. Kataoka, Y. Miyoshi, T. Hara, C. Tao, et al. (2014). “Inner heliosphere MHD modeling system applicable to space weather forecasting for the other planets”. In: *Space Weather* 12.4, pp. 187–204. DOI: <https://doi.org/10.1002/2013SW000989> (cit. on p. 50).
- Shoda, Munehito, Benjamin D. G. Chandran, and Steven R. Cranmer (June 2021). “Turbulent Generation of Magnetic Switchbacks in the Alfvénic Solar Wind”. In: *The Astrophysical Journal* 915.1, p. 52. DOI: [10.3847/1538-4357/abfdbc](https://doi.org/10.3847/1538-4357/abfdbc) (cit. on p. 101).
- Snodgrass, Herschel B. and Roger K. Ulrich (Mar. 1990). “Rotation of Doppler Features in the Solar Photosphere”. In: *Astrophys. J.* 351, p. 309. DOI: [10.1086/168467](https://doi.org/10.1086/168467) (cit. on p. 63).
- Solanki, S. K., J. C. del Toro Iniesta, J. Woch, A. Gandorfer, J. Hirzberger, et al. (Oct. 2020). “The Polarimetric and Helioseismic Imager on Solar Orbiter”. In: *Astron. Astrophys.* 642, A11, A11. DOI: [10.1051/0004-6361/201935325](https://doi.org/10.1051/0004-6361/201935325) (cit. on pp. 44, 49).
- Sonett, C. P., D. S. Colburn, L. Davis, E. J. Smith, and P. J. Coleman (Aug. 1964). “Evidence for a Collision-Free Magnetohydrodynamic Shock in Interplanetary Space”. In: *Phys. Rev. Lett.* 13.5, pp. 153–156. DOI: [10.1103/PhysRevLett.13.153](https://doi.org/10.1103/PhysRevLett.13.153) (cit. on p. 13).
- Song, HongQiang and Shuo Yao (Nov. 2020). “Characteristics and applications of interplanetary coronal mass ejection composition”. In: *Science in China E: Technological Sciences* 63.11, pp. 2171–2187. DOI: [10.1007/s11431-020-1680-y](https://doi.org/10.1007/s11431-020-1680-y) (cit. on p. 78).
- SPICE Consortium, M. Anderson, T. Appourchaux, F. Auchère, R. Aznar Cuadrado, et al. (Oct. 2020). “The Solar Orbiter SPICE instrument. An extreme UV imaging spectrometer”. In: *Astron. Astrophys.* 642, A14, A14. DOI: [10.1051/0004-6361/201935574](https://doi.org/10.1051/0004-6361/201935574) (cit. on p. 44).
- Squire, J., B. D. G. Chandran, and R. Meyrand (Feb. 2020). “In-situ Switchback Formation in the Expanding Solar Wind”. In: *The Astrophysical Journal Letters* 891.1, p. L2. DOI: [10.3847/2041-8213/ab74e1](https://doi.org/10.3847/2041-8213/ab74e1) (cit. on p. 101).
- St. Cyr, O. C., R. A. Howard, N. R. Sheeley Jr., S. P. Plunkett, D. J. Michels, et al. (2000). “Properties of coronal mass ejections: SOHO LASCO observations from January 1996 to June 1998”. In: *Journal of Geophysical Research: Space Physics* 105.A8, pp. 18169–18185. DOI: <https://doi.org/10.1029/1999JA000381> (cit. on p. 16).

- Stephenson, F. R. (Apr. 1990). “Historical Evidence concerning the Sun: Interpretation of Sunspot Records during the Telescopic and Pretelescopic Eras”. In: *Philosophical Transactions of the Royal Society of London Series A* 330.1615, pp. 499–512. DOI: [10.1098/rsta.1990.0031](https://doi.org/10.1098/rsta.1990.0031) (cit. on p. 35).
- Stone, E. C., A. M. Frandsen, R. A. Mewaldt, E. R. Christian, D. Margolies, et al. (July 1998). “The Advanced Composition Explorer”. In: *Space Sci. Rev.* 86, pp. 1–22. DOI: [10.1023/A:1005082526237](https://doi.org/10.1023/A:1005082526237) (cit. on p. 16).
- Suess, S. and G. Poletto (May 2001). “The Fall 2000 and Fall 2001 SOHO-Ulysses Quadratures”. In: *Space Science Reviews* 97.1, pp. 59–62. ISSN: 1572-9672. DOI: [10.1023/A:1011865825442](https://doi.org/10.1023/A:1011865825442) (cit. on p. 89).
- Suess, S. T., A. Bemporad, and G. Poletto (Mar. 2004). “A slow streamer blowout at the Sun and Ulysses”. In: *Geophys. Res. Lett.* 31.5, L05801, p. L05801. DOI: [10.1029/2003GL018895](https://doi.org/10.1029/2003GL018895) (cit. on p. 89).
- Suess, S. T., G. Poletto, M. Romoli, M. Neugebauer, B. E. Goldstein, et al. (2000). “The May 1997 SOHO-Ulysses quadrature”. In: *Journal of Geophysical Research: Space Physics* 105.A11, pp. 25033–25051. DOI: <https://doi.org/10.1029/2000JA000044> (cit. on p. 89).
- Sylwester, J., J. R. Lemen, R. D. Bentley, A. Fludra, and M. -C. Zolcinski (July 1998). “Detailed Evidence for Flare-to-Flare Variations of the Coronal Calcium Abundance”. In: *Astrophys. J.* 501.1, pp. 397–407. DOI: [10.1086/305785](https://doi.org/10.1086/305785) (cit. on p. 78).
- Tasnim, S. and Iver H. Cairns (2016). “An equatorial solar wind model with angular momentum conservation and nonradial magnetic fields and flow velocities at an inner boundary”. In: *Journal of Geophysical Research: Space Physics* 121.6, pp. 4966–4984. DOI: <https://doi.org/10.1002/2016JA022725> (cit. on p. 46).
- Tasnim, S., Iver H. Cairns, and M. S. Wheatland (2018). “A Generalized Equatorial Model for the Accelerating Solar Wind”. In: *Journal of Geophysical Research: Space Physics* 123.2, pp. 1061–1085. DOI: <https://doi.org/10.1002/2017JA024532> (cit. on p. 46).
- Taylor, J. B. (July 1986). “Relaxation and magnetic reconnection in plasmas”. In: *Rev. Mod. Phys.* 58 (3), pp. 741–763. DOI: [10.1103/RevModPhys.58.741](https://doi.org/10.1103/RevModPhys.58.741) (cit. on p. 37).
- Telloni, D., R. Bruno, and L. Trenchi (May 2015). “Radial Evolution of Spectral Characteristics of Magnetic Field Fluctuations at Proton Scales”. In: *Astrophys. J.* 805.1, 46, p. 46. DOI: [10.1088/0004-637X/805/1/46](https://doi.org/10.1088/0004-637X/805/1/46) (cit. on p. 88).
- Telloni, D., G. P. Zank, L. Sorriso-Valvo, and al. (2022a). “Linking Small-Scale Solar Wind Properties with Large-Scale Coronal Source Regions through Joint Parker Solar Probe - Metis/Solar Orbiter Observations”. In: *Astrophys. J.* (cit. on pp. 91, 99).
- Telloni, Daniele, Vincenzo Andretta, Ester Antonucci, Alessandro Bemporad, Giuseppe E. Capuano, et al. (Oct. 2021a). “Exploring the Solar Wind from Its Source on the Corona into the Inner Heliosphere during the First Solar Orbiter–Parker Solar Probe Quadrature”. In: *The Astrophysical Journal Letters* 920.1, p. L14. ISSN: 2041-8213. DOI: [10.3847/2041-8213/ac282f](https://doi.org/10.3847/2041-8213/ac282f) (cit. on pp. 88, 89, 91, 92, 98, 99).
- Telloni, Daniele, Luca Sorriso-Valvo, Lloyd D. Woodham, Olga Panasenco, Marco Velli, et al. (May 2021b). “Evolution of Solar Wind Turbulence from 0.1 to 1 au during the First Parker Solar Probe–Solar Orbiter Radial Alignment”. In: *The Astrophysical Journal Letters* 912.2, p. L21. DOI: [10.3847/2041-8213/abf7d1](https://doi.org/10.3847/2041-8213/abf7d1) (cit. on pp. 30, 88).

- Telloni, Daniele, Gary P. Zank, Marco Stangalini, Cooper Downs, Haoming Liang, et al. (Sept. 2022b). “Observation of a Magnetic Switchback in the Solar Corona”. In: *Astrophys. J. Lett.* 936.2, L25, p. L25. DOI: [10.3847/2041-8213/ac8104](https://doi.org/10.3847/2041-8213/ac8104) (cit. on p. 101).
- Telloni, Daniele, Lingling Zhao, Gary P. Zank, Haoming Liang, Masaru Nakanotani, et al. (Dec. 2020). “Magnetohydrodynamic Turbulent Evolution of a Magnetic Cloud in the Outer Heliosphere”. In: *The Astrophysical Journal* 905.1, p. L12. DOI: [10.3847/2041-8213/abcb03](https://doi.org/10.3847/2041-8213/abcb03) (cit. on p. 88).
- Temmer, M. and N. V. Nitta (Mar. 2015). “Interplanetary Propagation Behavior of the Fast Coronal Mass Ejection on 23 July 2012”. In: *Sol. Phys.* 290.3, pp. 919–932. DOI: [10.1007/s11207-014-0642-3](https://doi.org/10.1007/s11207-014-0642-3) (cit. on pp. 18, 52, 78).
- The SunPy Community, Will T. Barnes, Monica G. Bobra, Steven D. Christe, Nabil Freij, et al. (2020). “The SunPy Project: Open Source Development and Status of the Version 1.0 Core Package”. In: *The Astrophysical Journal* 890 (1), pp. 68–. DOI: [10.3847/1538-4357/ab4f7a](https://doi.org/10.3847/1538-4357/ab4f7a) (cit. on p. 90).
- Titov, V. S. and P. Démoulin (Nov. 1999). “Basic topology of twisted magnetic configurations in solar flares”. In: *Astron. Astrophys.* 351, pp. 707–720 (cit. on p. 104).
- Titov, V. S., T. Török, Z. Mikic, and J. A. Linker (July 2014). “A METHOD FOR EMBEDDING CIRCULAR FORCE-FREE FLUX ROPES IN POTENTIAL MAGNETIC FIELDS”. In: *The Astrophysical Journal* 790.2, p. 163. DOI: [10.1088/0004-637X/790/2/163](https://doi.org/10.1088/0004-637X/790/2/163) (cit. on p. 104).
- Toro, E.F. (2009). *Riemann Solvers and Numerical Methods for Fluid Dynamics: A Practical Introduction*. Springer Berlin Heidelberg. ISBN: 9783540498346 (cit. on pp. 56, 57).
- Tousey, R. (Jan. 1973). “The solar corona.” In: *Space Research Conference*. Vol. 2, pp. 713–730 (cit. on p. 13).
- Usmanov, A. V. (Aug. 1993). “A Global Numerical Three-Dimensional Magnetohydrodynamic Model of the Solar Wind”. In: *Sol. Phys.* 146.2, pp. 377–396. DOI: [10.1007/BF00662021](https://doi.org/10.1007/BF00662021) (cit. on p. 50).
- van de Hulst, H. C. (Feb. 1950). “The electron density of the solar corona”. In: *Bulletin of the Astronomical Institutes of the Netherlands* 11, p. 135 (cit. on pp. 92, 108).
- van der Holst, B., C. Jacobs, and S. Poedts (Dec. 2007). “Simulation of a Breakout Coronal Mass Ejection in the Solar Wind”. In: *Astrophys. J. Lett.* 671.1, pp. L77–L80. DOI: [10.1086/524732](https://doi.org/10.1086/524732) (cit. on p. 78).
- van der Holst, B., IV Manchester W. B., R. A. Frazin, A. M. Vásquez, G. Tóth, et al. (Dec. 2010). “A Data-driven, Two-temperature Solar Wind Model with Alfvén Waves”. In: *Astrophys. J.* 725.1, pp. 1373–1383. DOI: [10.1088/0004-637X/725/1/1373](https://doi.org/10.1088/0004-637X/725/1/1373) (cit. on p. 107).
- van der Holst, B., I. V. Sokolov, X. Meng, M. Jin, IV Manchester W. B., et al. (Feb. 2014). “Alfvén Wave Solar Model (AWSoM): Coronal Heating”. In: *Astrophys. J.* 782.2, 81, p. 81. DOI: [10.1088/0004-637X/782/2/81](https://doi.org/10.1088/0004-637X/782/2/81) (cit. on p. 47).
- Vandas, M., S. Fischer, M. Dryer, Z. Smith, and T. Detman (1998). “Propagation of a spheromak: 2. Three-dimensional structure of a spheromak”. In: *Journal of Geophysical Research: Space Physics* 103.A10, pp. 23717–23725. DOI: <https://doi.org/10.1029/98JA01902> (cit. on p. 38).
- Vandas, M., S. Fischer, P. Pelant, M. Dryer, Z. Smith, et al. (1997). “Propagation of a spheromak: 1. Some comparisons of cylindrical and spherical magnetic clouds”.

- In: *Journal of Geophysical Research: Space Physics* 102.A11, pp. 24183–24193. DOI: <https://doi.org/10.1029/97JA02257> (cit. on p. 38).
- Vandas, M., S. Fischer, P. Pelant, and A. Geranios (1993). “Spheroidal models of magnetic clouds and their comparison with spacecraft measurements”. In: *Journal of Geophysical Research: Space Physics* 98.A7, pp. 11467–11475. DOI: <https://doi.org/10.1029/93JA00055> (cit. on p. 105).
- Vandas, M. and E. P. Romashets (2003). “A force-free field with constant alpha in an oblate cylinder: A generalization of the Lundquist solution”. In: *A&A* 398.3, pp. 801–807. DOI: [10.1051/0004-6361:20021691](https://doi.org/10.1051/0004-6361:20021691) (cit. on pp. 37, 104).
- Velli, M., Harra, L. K., Vourlidas, A., Schwadron, N., Panasenco, O., et al. (2020). “Understanding the origins of the heliosphere: integrating observations and measurements from Parker Solar Probe, Solar Orbiter, and other space- and ground-based observatories”. In: *A&A* 642, A4. DOI: [10.1051/0004-6361/202038245](https://doi.org/10.1051/0004-6361/202038245) (cit. on pp. 76, 88, 98, 100).
- Verbeke, C., Pomoell, J., and Poedts, S. (2019). “The evolution of coronal mass ejections in the inner heliosphere: Implementing the spheromak model with EUHFORIA”. In: *A&A* 627, A111. DOI: [10.1051/0004-6361/201834702](https://doi.org/10.1051/0004-6361/201834702) (cit. on pp. 38, 51, 104).
- Vernazza, J. E., E. H. Avrett, and R. Loeser (Apr. 1981). “Structure of the solar chromosphere. III. Models of the EUV brightness components of the quiet sun.” In: *Astrophys. J. Suppl. Ser.* 45, pp. 635–725. DOI: [10.1086/190731](https://doi.org/10.1086/190731) (cit. on pp. 4, 5).
- Verscharen, Daniel, Stuart D Bale, and Marco Velli (July 2021). “Flux conservation, radial scalings, Mach numbers, and critical distances in the solar wind: magneto-hydrodynamics and Ulysses observations”. In: *Mon. Not. R. Astron. Soc.* 506.4, pp. 4993–5004. ISSN: 0035-8711. DOI: [10.1093/mnras/stab2051](https://doi.org/10.1093/mnras/stab2051) (cit. on p. 99).
- Vourlidas, A., R. A. Howard, S. P. Plunkett, C. M. Korendyke, A. F. R. Thernisien, et al. (Dec. 2016). “The Wide-Field Imager for Solar Probe Plus (WISPR)”. In: *Space Sci. Rev.* 204.1-4, pp. 83–130. DOI: [10.1007/s11214-014-0114-y](https://doi.org/10.1007/s11214-014-0114-y) (cit. on p. 41).
- Vourlidas, A., B. J. Lynch, R. A. Howard, and Y. Li (May 2013). “How Many CMEs Have Flux Ropes? Deciphering the Signatures of Shocks, Flux Ropes, and Prominences in Coronagraph Observations of CMEs”. In: *Solar Physics* 284.1, pp. 179–201. ISSN: 1573-093X. DOI: [10.1007/s11207-012-0084-8](https://doi.org/10.1007/s11207-012-0084-8) (cit. on pp. 14, 16, 36).
- Vourlidas, Angelos and David F. Webb (July 2018). “Streamer-blowout Coronal Mass Ejections: Their Properties and Relation to the Coronal Magnetic Field Structure”. In: *Astrophys. J.* 861.2, 103, p. 103. DOI: [10.3847/1538-4357/aaca3e10](https://doi.org/10.3847/1538-4357/aaca3e10). [arXiv.1806.00644](https://arxiv.org/abs/1806.00644) (cit. on p. 14).
- Vršnak, B., T. Žic, D. Vrbanec, M. Temmer, T. Rollett, et al. (July 2013). “Propagation of Interplanetary Coronal Mass Ejections: The Drag-Based Model”. In: *Sol. Phys.* 285.1-2, pp. 295–315. DOI: [10.1007/s11207-012-0035-4](https://doi.org/10.1007/s11207-012-0035-4) (cit. on pp. 52, 78).
- Wang, Y. -M. and Jr. Sheeley N. R. (June 1990). “Solar Wind Speed and Coronal Flux-Tube Expansion”. In: *Astrophys. J.* 355, p. 726. DOI: [10.1086/168805](https://doi.org/10.1086/168805) (cit. on p. 48).
- (June 1992). “On Potential Field Models of the Solar Corona”. In: *Astrophys. J.* 392, p. 310. DOI: [10.1086/171430](https://doi.org/10.1086/171430) (cit. on pp. 9, 47, 48).

- Webb, D. F., J. Burkepile, T. G. Forbes, and P. Riley (2003). “Observational evidence of new current sheets trailing coronal mass ejections”. In: *Journal of Geophysical Research: Space Physics* 108.A12. DOI: <https://doi.org/10.1029/2003JA009923> (cit. on p. 16).
- Webb, D. F., S. W. Kahler, P. S. McIntosh, and J. A. Klimchuck (1997). “Large-scale structures and multiple neutral lines associated with coronal mass ejections”. In: *Journal of Geophysical Research: Space Physics* 102.A11, pp. 24161–24174. DOI: <https://doi.org/10.1029/97JA01867> (cit. on p. 38).
- Webb, David F. and Timothy A. Howard (June 2012). “Coronal Mass Ejections: Observations”. In: *Living Reviews in Solar Physics* 9.1, p. 3. ISSN: 1614-4961. DOI: [10.12942/lrsp-2012-3](https://doi.org/10.12942/lrsp-2012-3) (cit. on pp. 13, 14).
- Weber, E. J. and L. Jr. Davis (Apr. 1967). “The Angular Momentum of the Solar Wind”. In: *Astrophys. J.* 148, pp. 217–227. DOI: [10.1086/149138](https://doi.org/10.1086/149138) (cit. on pp. 31, 32, 34, 52–54, 70, 75, 93, 97, 101, 106, 109).
- Wenzel, K. P., R. G. Marsden, D. E. Page, and E. J. Smith (Jan. 1992). “The ULYSSES Mission”. In: *Astron. Astrophys. Suppl.* 92, p. 207 (cit. on p. 9).
- Wiegelmann, Thomas, Gordon J. D. Petrie, and Pete Riley (Sept. 2017). “Coronal Magnetic Field Models”. In: *Space Sci. Rev.* 210.1-4, pp. 249–274. DOI: [10.1007/s11214-015-0178-3](https://doi.org/10.1007/s11214-015-0178-3) (cit. on p. 49).
- Wiengarten, T., J. Kleimann, H. Fichtner, R. Cameron, J. Jiang, et al. (Jan. 2013). “MHD simulation of the inner-heliospheric magnetic field”. In: *Journal of Geophysical Research (Space Physics)* 118.1, pp. 29–44. DOI: [10.1029/2012JA018089](https://doi.org/10.1029/2012JA018089) (cit. on p. 50).
- Wilcox, John M. (Apr. 1968). “The Interplanetary Magnetic Field. Solar Origin and Terrestrial Effects”. In: *Space Sci. Rev.* 8.2, pp. 258–328. DOI: [10.1007/BF00227565](https://doi.org/10.1007/BF00227565) (cit. on pp. 9, 45).
- Wilcox, John M. and Norman F. Ness (1965). “Quasi-stationary corotating structure in the interplanetary medium”. In: *Journal of Geophysical Research (1896-1977)* 70.23, pp. 5793–5805. DOI: <https://doi.org/10.1029/JZ070i023p05793> (cit. on pp. 11, 13).
- Wöhl, H., R. Brajša, A. Hanslmeier, and S. F. Gissot (Sept. 2010). “A precise measurement of the solar differential rotation by tracing small bright coronal structures in SOHO-EIT images. Results and comparisons for the period 1998-2006”. In: *Astron. Astrophys.* 520, A29, A29. DOI: [10.1051/0004-6361/200913081](https://doi.org/10.1051/0004-6361/200913081) (cit. on p. 63).
- Woltjer, L. (1958). “A THEOREM ON FORCE-FREE MAGNETIC FIELDS”. In: *Proceedings of the National Academy of Sciences* 44.6, pp. 489–491. DOI: [10.1073/pnas.44.6.489](https://doi.org/10.1073/pnas.44.6.489) (cit. on p. 37).
- Worden, John and John Harvey (Aug. 2000). “An Evolving Synoptic Magnetic Flux map and Implications for the Distribution of Photospheric Magnetic Flux”. In: *Sol. Phys.* 195.2, pp. 247–268. DOI: [10.1023/A:1005272502885](https://doi.org/10.1023/A:1005272502885) (cit. on p. 50).
- Wu, C. and R. P. Lepping (Mar. 2011). “Statistical Comparison of Magnetic Clouds with Interplanetary Coronal Mass Ejections for Solar Cycle 23”. In: *Solar Physics* 269.1, pp. 141–153. ISSN: 1573-093X. DOI: [10.1007/s11207-010-9684-3](https://doi.org/10.1007/s11207-010-9684-3) (cit. on p. 36).
- Wuelser, Jean-Pierre, James R. Lemen, Theodore D. Tarbell, C. J. Wolfson, Joseph C. Cannon, et al. (Feb. 2004). “EUVI: the STEREO-SECCHI extreme ultraviolet imager”. In: *Telescopes and Instrumentation for Solar Astrophysics*. Ed. by Silvano Fineschi and Mark A. Gummin. Vol. 5171. Society of Photo-Optical Instrumenta-

- tion Engineers (SPIE) Conference Series, pp. 111–122. DOI: [10.1117/12.506877](https://doi.org/10.1117/12.506877) (cit. on p. 40).
- Xie, Hong, Leon Ofman, and Gareth Lawrence (2004). “Cone model for halo CMEs: Application to space weather forecasting”. In: *Journal of Geophysical Research: Space Physics* 109.A3. DOI: <https://doi.org/10.1029/2003JA010226> (cit. on p. 38).
- Xu Zhen-tao (1980). “The hexagram “Feng” in “the book of changes” as the earliest written record of sunspot”. In: *Chinese Astronomy* 4.4, p. 406. ISSN: 0146-6364. DOI: [https://doi.org/10.1016/0146-6364\(80\)90034-1](https://doi.org/10.1016/0146-6364(80)90034-1) (cit. on p. 35).
- Xue, X. H., C. B. Wang, and X. K. Dou (2005). “An ice-cream cone model for coronal mass ejections”. In: *Journal of Geophysical Research: Space Physics* 110.A8. DOI: <https://doi.org/10.1029/2004JA010698> (cit. on p. 38).
- Yang, L. P., X. S. Feng, C. Q. Xiang, Yang Liu, Xuepu Zhao, et al. (Aug. 2012). “Time-dependent MHD modeling of the global solar corona for year 2007: Driven by daily-updated magnetic field synoptic data”. In: *Journal of Geophysical Research (Space Physics)* 117.A8, A08110, A08110. DOI: [10.1029/2011JA017494](https://doi.org/10.1029/2011JA017494) (cit. on p. 47).
- Zank, G. P., L. Adhikari, P. Hunana, D. Shiota, R. Bruno, et al. (Jan. 2017). “Theory and Transport of Nearly Incompressible Magnetohydrodynamic Turbulence”. In: *The Astrophysical Journal* 835.2, p. 147. DOI: [10.3847/1538-4357/835/2/147](https://doi.org/10.3847/1538-4357/835/2/147) (cit. on p. 99).
- Zank, G. P., M. Nakanotani, L.-L. Zhao, L. Adhikari, and J. Kasper (Oct. 2020). “The Origin of Switchbacks in the Solar Corona: Linear Theory”. In: *The Astrophysical Journal* 903.1, p. 1. DOI: [10.3847/1538-4357/abb828](https://doi.org/10.3847/1538-4357/abb828) (cit. on p. 101).
- Zhang, J. and K. P. Dere (Oct. 2006). “A Statistical Study of Main and Residual Accelerations of Coronal Mass Ejections”. In: *Astrophys. J.* 649.2, pp. 1100–1109. DOI: [10.1086/506903](https://doi.org/10.1086/506903) (cit. on p. 15).
- Zhang, Jie, Manuela Temmer, Nat Gopalswamy, Olga Malandraki, Nariaki V. Nitta, et al. (Oct. 2021). “Earth-affecting solar transients: a review of progresses in solar cycle 24”. In: *Progress in Earth and Planetary Science* 8.1, p. 56. ISSN: 2197-4284. DOI: [10.1186/s40645-021-00426-7](https://doi.org/10.1186/s40645-021-00426-7) (cit. on pp. 12, 13, 15, 16, 18, 77).
- Zhang, Q. M. (2021). “A revised cone model and its application to non-radial prominence eruptions”. In: *A&A* 653, p. L2. DOI: [10.1051/0004-6361/202141982](https://doi.org/10.1051/0004-6361/202141982) (cit. on p. 38).
- Zhao, L., T. H. Zurbuchen, and L. A. Fisk (2009). “Global distribution of the solar wind during solar cycle 23: ACE observations”. In: *Geophysical Research Letters* 36.14. DOI: <https://doi.org/10.1029/2009GL039181> (cit. on p. 78).
- Zhao, X. P. and J. T. Hoeksema (Oct. 2010). “The Magnetic Field at the Inner Boundary of the Heliosphere Around Solar Minimum”. In: *Sol. Phys.* 266.2, pp. 379–390. DOI: [10.1007/s11207-010-9618-0](https://doi.org/10.1007/s11207-010-9618-0) (cit. on p. 96).
- Zhao, X. P., S. P. Plunkett, and W. Liu (2002). “Determination of geometrical and kinematical properties of halo coronal mass ejections using the cone model”. In: *Journal of Geophysical Research: Space Physics* 107.A8, SSH 13-1-SSH 13–9. DOI: <https://doi.org/10.1029/2001JA009143> (cit. on pp. 38, 50).
- Zhou, G., H.-Q. He, and W. Wan (Aug. 2020). “Effects of Solar Activity on Taylor Scale and Correlation Scale in Solar Wind Magnetic Fluctuations”. In: *The Astrophysical Journal Letters* 899.2, p. L32. DOI: [10.3847/2041-8213/abaaa9](https://doi.org/10.3847/2041-8213/abaaa9) (cit. on p. 9).

Zwickl, R. D., J. R. Asbridge, S. J. Bame, W. C. Feldman, J. T. Gosling, et al. (Nov. 1983). "Plasma properties of driver gas following interplanetary shocks observed by ISEE-3." In: *NASA Conference Publication*. Vol. 228. NASA Conference Publication, p. 0.711 (cit. on p. 77).

# List of Figures

1.1	Schematics of the average variation with height of temperature and density in the solar atmosphere, according to the theoretical 1D model of Vernazza et al. (1981). In practice, the solar atmosphere is an highly inhomogeneous, dynamic, and time-varying environment, hence this schematics is an oversimplification of the actual conditions. Source: Priest (2014), © Cambridge University Press. . . . .	5
1.2	Images of different layers of the Sun obtained by the Solar Dynamics Observatory on November 1, 2022 with the instruments HMI and AIA at different wavelengths. The left top panel shows the photospheric magnetic field on the line of sight, with positive polarity in white and negative in black (6173 Å); in the right top panel, the photosphere and a layer of the chromosphere at its temperature minimum are depicted (1700 Å); the left bottom panel shows the chromosphere and the transition region (304 Å); in the right bottom panel we find the solar corona (193 Å). . . . .	6
1.3	The corona in white light during a total solar eclipse, as seen during a solar minimum (on the left, November 1994), and during a solar maximum (on the right, February 1980). Credits: National Center for Atmospheric Research's High Altitude Observatory and Rhodes College.	7
1.4	The solar corona observed on October 27, 2022 in the 193 Å spectral line by SDO. The dark regions that draw the "smiley face" are coronal holes. Coronal loops and bright points are also visible. . . . .	8
1.5	The outer solar corona observed on November 2, 2022 in white light with two of the coronagraphs that compose LASCO, called C2 (on the left, imaging from 2.5 to 6 $R_{\odot}$ ) and C3 (on the right, 3.7-30 $R_{\odot}$ ). Multiple coronal streamers are visible, which begin to be distributed on higher latitudes as the Sun approaches the maximum of the current activity cycle (estimated to be in 2025). . . . .	8
1.6	Polar plots of solar wind speed as a function of solar latitude for the first two orbits of the Ulysses mission. Both are plotted over composite solar images characteristic of solar minimum (1996, on the left) and maximum (2000, on the right). Outward-directed magnetic field is colored in red, the inward-directed one in blue. Notice how the solar wind speed distribution is much more isotropic in the right panel. Reproduced from McComas et al. (2003), © American Geophysical Union. . . . .	10

1.7	On the left panel, a sketch taken from Hundhausen (1977) of the warped heliospheric current sheet (bounded by the black solid line), with the magnetic field lines represented as arrowed lines. On the right, taken from Wilcox and Ness (1965), a sketch of the sector boundaries encountered at 1 AU as the Sun rotates. The plus symbols indicate outward magnetic field, while the minus symbols stand for inward magnetic field. © American Geophysical Union. . . . .	11
1.8	In situ measurements of the solar wind and interplanetary magnetic field acquired at 0.99 AU over the year 2007 by the spacecraft Wind, taken from the OMNI database. From top to bottom: the profiles of particle density, bulk speed, proton temperature, and radial magnetic field. . . . .	12
1.9	Observation of the same transient emerging in the eastern limb of the Sun, as seen in May 1, 2013 by SDO in the chromosphere (left panel), by LASCO-C2 in the inner corona (center panel), and by LASCO-C3 in the outer corona (right panel). An erupting solar prominence emerges from the chromosphere into the upper layers of the solar atmosphere, until it is explosively ejected into outer space by yet not fully understood mechanisms of magnetic nature. . . . .	14
1.10	Coronal mass ejections observed in white light with LASCO C2, on July 16 (left) and December 12, 2002 (right). In the first case, the CME was directed towards Earth, so it appeared to expand in all direction from the Sun: this kind of event is called Halo CME. In the second case, the CME moved from one limb of the Sun, and its 3-part, lightbulb-like structure is visible: a bright core, a dark cavity, and an arcade feature. . . . .	15
1.11	On the left, a cartoon depiction of the structure of an ICME. The ICME has a magnetic flux rope, still connected at both end to the corona, a feature not always detected in situ. The ICME drives an interplanetary shock, behind which the ambient solar wind is compressed in the turbulent sheat. On the right, in situ measurements of magnetic field magnitude, longitudinal and latitudinal inclination of the magnetic field, and solar wind speed acquired by the ACE spacecraft. The blue dashed line marks the shock, while the actual ICME is bounded by red lines. Reproduced from Kilpua et al. (2017), © Springer Nature. . . . .	17
1.12	Artist’s depiction of the interaction between solar wind and Earth’s magnetosphere. When the former impacts on the magnetopause most of the solar materials are deflected away, while some of them are directly channeled into the polar cusps towards Earth’s atmosphere. Source: NASA, from wikimedia. . . . .	19
1.13	Plasma beta above an active region, depending on the height. The convective motion of plasma still dominates the dynamic of the innermost layers of the solar atmosphere, so that $\beta \gtrsim 1$ in al the photosphere. It rapidly decreases in the chromosphere and in the transition region, reaching a minimum in the corona, where the magnetic field lead plasma motion. Adapted from Gary (2001), © Springer Nature. . . .	23

1.14	On the left (panel a), ripples of magnetic field caused by a transverse wave propagating along the magnetic field lines in direction $\mathbf{k}$ . On the right (panel b), the compression and rarefaction of magnetic field lines due to a compressional wave propagating across the field in direction $\mathbf{k}$ . Source: Priest (2014), © Cambridge University Press. . . . .	24
1.15	The conservation of total magnetic flux through a surface. If the curve $C_1$ is distorted into $C_2$ by plasma motion, the flux through $C_1$ at $t_1$ equals the flux through $C_2$ at $t_2$ . Source: Priest (2014), © Cambridge University Press. . . . .	25
1.16	The four classes of solutions of equation (1.28) for an isothermal and spherical coronal expansion. Only class 2 satisfies the requirements of supersonic flow ( $u_c \equiv c_s$ ) at $r/r_c \gg 1$ and small speed very close to the Sun. Source: Hundhausen (1972), © Springer-Verlag. . . . .	28
1.17	A spiral field line attached to the Sun in the equatorial plane. The wind moves radially with speed $v$ inclined to the field at angle $\psi$ . Source: Priest (2014), © Cambridge University Press. . . . .	29
1.18	Schematic of the formation of corotating interaction regions (CIRs), from Kamide et al. (1998). The interaction between a high-speed stream (B) and a slow-speed stream (A) are shown together with the CIR (shaded) The forward shock (FS), interface surface (IF), and reverse shock (RS) are also indicated. . . . .	31
1.19	Schematic representation of the purely radial IMF spiraling out due to solar rotation from the source surface (dashed circle), which is placed above the solar surface (solid circle, enclosing 1). In the region (2) between those two surfaces, closed magnetic field exist. Reproduced from Schatten et al. (1969), © Springer Nature. . . . .	32
1.20	Schematic showing of solutions to equation (1.48). Consistently with the Parker treatment, the only physical solution is the one with low speed for $r \rightarrow 0$ and low pressure for $r \rightarrow \infty$ , in this case class I. The solution passes through the three critical points where the flow attains the speed of slow, alfvénic and fast-mode waves. The latter two are very close. Source: Priest (2014), © Cambridge University Press. . . . .	34
1.21	The "ballerina skirt" model of the three-dimensional heliosphere, according to Alfvén (1977). Reproduced from Schwenn (2006), © Springer Nature. . . . .	36
1.22	Geometry for determining cone shape parameters. Here, $\alpha$ is the angular width of a CME, $a$ its half linear width, $a'$ the distance from the center of the linear width to the CME front, $c$ the curvature radius of the CME front and $r$ a distance from the center of the Sun to the CME front. If $c/r \rightarrow \infty$ , $a'/a \rightarrow 0$ and the CME is described by a flat cone. A shallow ice-cream is obtained when $c/r = 1$ , so that $a'/a = \text{constant}$ under the assumption of self-similar expansion. If $a'/a = 1$ , the CME is a full ice-cream, and in this case $c/r$ is constant under the assumption of self-similar expansion. Source: Na et al. (2017), © The American Astronomical Society. . . . .	39
1.23	Renderings of the Wind spacecraft (left) and STEREO (right). . . . .	40
1.24	Rendering of the Parker Solar Probe ram-facing view. The positions of the four instrument suites ISIS, WISPR, SWEAP and FIELDS are labelled. Source: NASA/JPL. . . . .	41

1.25	The speed (orange line) and distance from the Sun (blue line, in $10^{11}$ cm) of PSP, from launch until 2026. The red circles mark the perihelii at each solar encounter, the green ones mark the flyby with Venus. Source: NASA / JPL, <a href="#">from wikimedia</a> . . . . .	42
1.26	ESA poster depicting the rear view of the Solar Orbiter spacecraft. Labeled in red the positions of the four in situ instrument suites, in yellow those of the six remote sensing ones. . . . .	43
1.27	The speed (orange line) and distance from the Sun (blue line, in $10^{11}$ cm) of Solar Orbiter, from launch until 2031. The red and black triangles mark the Venus and Earth flybys. Data source: NASA/JPL, <a href="#">from wikimedia</a> . . . . .	43
1.28	Solar Orbiter heliocentric latitude plotted as a function of time. The blue vertical lines mark the Venus and Earth flybys. Reproduced from Müller et al. (2020), © European Southern Observatory. . . . .	44
2.1	An example of ballistic reconstructions provided with the accelerating-wind model of Tasnim et al. (2018) (on the columns a, e, i, m, and c, g, k, o) compared with the constant-speed model of Schulte in den Bäumen et al. (2012) (on the remaining columns) from data acquired by the Wind spacecraft for the period 1-27 August 2010. From top to bottom, ecliptic maps of solar wind bulk speed, ion number density, ion temperature, and longitudinal magnetic field. Reproduced from Tasnim et al. (2018), © American Geophysical Union. . . . .	46
2.2	(a) A drawing of the real solar corona as seen in an eclipse, (b) the standard Potential Field Source Surface model of Schatten et al. (1969), and (c) the standard Current-Sheet model of Schatten (1971). . . . .	48
2.3	A synoptic map is used to build the photospheric field polarity map (dark and light grey as negative and positive polarity), used in turn as input by a PFSS+SCS combination to infer the coronal hole distribution (colored dots) at $5 R_{\odot}$ . Then, an empirical function give the speed (color) of the solar wind outflowing from these coronal holes. Reproduced from Arge et al. (2004), © Elsevier. . . . .	49
2.4	Cells of the outer ring are mapped into cells of the inner ring according to equation (2.2). It may be necessary to interpolate between the mapped $\varphi'_i$ and the equidistant $\varphi_j^{\text{ib}}$ of the computational grid to have cell-centred values. Then, the quantities $q'_i$ at the inner cells are scaled according to the theoretical models. . . . .	54
2.5	Having two different values of speed that do not satisfy condition given by eq. (2.8), the streamlines of cells $i$ and $j$ cross at $(R_X; \varphi_X)$ before being mapped in $i'$ and $j'$ . One of them must be discarded, then the azimuthal profiles are refilled by interpolating the adjacent non-crossing streams. . . . .	55
2.6	Representation of cell-centered collocation of physical variables inside a 2D grid. Filled symbols represents domain values part of the solution, empty symbols stands for the boundary values. Source: Mignone et al. (2018), PLUTO User's Guide, <a href="http://plutocode.ph.unito.it">http://plutocode.ph.unito.it</a> . . . . .	58

2.7	Two-dimensional grid with $NX1=NX2=4$ and 1 ghost zone. The $i$ and $j$ indices span internal zones (solid boxes) from I,JBEG to I,JEND, while the ghost cells are filled with the boundary conditions. Source: Mignone et al. (2018), PLUTO User’s Guide, <a href="http://plutocode.ph.unito.it">http://plutocode.ph.unito.it</a> . . . . .	61
2.8	A schematic of the steps involved in RIMAP for the reconstruction of heliospheric plasma conditions starting from in situ measurements. . .	65
2.9	Ecliptic maps of the plasma number density (top panel), radial speed (middle panel), and radial magnetic field (bottom panel) obtained with RIMAP from the in situ observations acquired by the Wind spacecraft at 0.99 AU during March 2009. . . . .	66
2.10	The mean trend for the radial speed, as derived by averaging at each altitude over all longitudes; a slight acceleration is still present, mainly due to the thermal pressure gradient. . . . .	67
2.11	In solid red, the mean radial behaviour for the plasma temperature, as derived by averaging at each altitude over all longitudes. Overplotted in dashed black is the reference trend (2.35) of Perrone et al. (2019). .	67
2.12	For the March 2009 Wind data set: 1 AU longitudinal comparisons between the input (black line) and the output (red line) profiles of (from top to bottom) plasma density, radial speed, radial and longitudinal components of the magnetic field. Superimposed as vertical grey bars, longitude intervals corresponding to SIRs/CIRs identified with STEREO (Jian et al., 2019). In this plots, the time direction runs from right to left. . . . .	69
2.13	Longitudinal comparisons between the profiles of plasma density and radial speed measured by STEREO-A (orange line), STEREO-B (blue), and Wind (black line) on March 3-29, 2009. Superimposed as vertical grey bars, longitude intervals corresponding to SIRs/CIRs identified with STEREO (Jian et al., 2019). Time runs from right to left. . . . .	70
2.14	Ecliptic maps of the plasma number density (left panel) and radial speed (on the right) obtained with RIMAP from the in situ observations acquired by the Wind spacecraft at 0.99 AU during January 2018. . . . .	72
2.15	For the January 2018 Wind data set: 1 AU longitudinal comparisons between the input (black line) and the output (red line) profiles of (from top to bottom) plasma density, radial speed, radial and longitudinal components of the magnetic field. Delimited by vertical dashed lines, longitude intervals corresponding to SIRs/CIRs identified with STEREO (Jian et al., 2019). In this plots, the time direction runs from right to left. . . . .	73
2.16	Comparison between the longitudinal profiles of number density (top) and radial speed (bottom) as measured at 1 AU by GGS Wind (black line) and simulated by WSA-ENLIL (blue) and RIMAP (red). The RMSE between ENLIL forecasts and Wind measurements are $\Delta n \simeq 6 \text{ cm}^{-3}$ and $\Delta v \simeq 110 \text{ km s}^{-1}$ . . . . .	73

2.17	Visual comparison between the ENLIL forecast of the plasma conditions on the ecliptic plane of January 16, 2018 (on the left) and the simulation made with RIMAP starting from data acquired at 1 AU (on the right). Notice that the ENLIL domain extends nearly up to 2.0 AU, while the RIMAP one extends to 1.1 AU ( $\simeq 236.5 R_{\odot}$ ). . . .	74
3.1	Three frames showing the passage of the perturbation through the internal boundary. The cone-modelled ICME (blue circle) can be thought of as a spheroid pushed at constant speed through a plane (black solid line). $\alpha(t)$ , the angle subtended by the modelled plasma bubble and this plane, and defined in (3.2), depends only on the ICME angular width $\omega$ , and its bulk speed $v_{\text{ICME}}$ . The dashed black line here is the simulation internal boundary at $21.5 R_{\odot}$ . . . . .	81
3.2	Interplanetary propagation of the cone-modelled ICME across the Parker spiral reconstructed via RIMAP from in situ measurements. Plasma density and velocity in the equatorial plane are shown, respectively, in the top and bottom half of each panel. The white contour line contains 99% of the ICME tracer mass. The colored diamonds at $\varphi=85^{\circ}$ , $73.8^{\circ}$ , and $65^{\circ}$ are the positions of three virtual spacecraft, which would detect the time profiles in Figure 3.4. The black arrow is the entry point of the ICME into the inner boundary of the simulation.	82
3.3	Interplanetary propagation of the cone-modelled ICME across the Parker spiral reconstructed via RIMAP from in situ measurements. See the caption of Figure 3.2 for a more detailed description. . . . .	83
3.4	From top to bottom, time profiles of plasma number density, percentage of tracer, radial speed, pressure, and the radial and longitudinal components of magnetic field, as measured at 1 AU by three virtual spacecraft that encounter different regions of the perturbation. The color code for A (red line), B (blue line), and C (black line) is the same used in figure 3.2. Here, the simulated ICME enters the internal boundary at $t=0$ . . . . .	84
4.1	Positions of PSP and SolO in the HelioCentric Inertial (HCI) frame, from January 14th to January 25th 2021, during their first quadrature. Here thirteen data points for spacecraft are plotted, one for each day starting from January 14th, when PSP was at 0.19 AU from the Sun and $\varphi=-25.74^{\circ}$ , while SolO was at 0.6 AU and $\varphi=180.63^{\circ}$ . In green, the subset of PSP positions from January 15-21, when PSP was faster than the equatorial solar rotation, is highlighted. Plotted using the Sunpy suite (The SunPy Community et al., 2020). . . . .	90
4.2	Positions and measurements collected by PSP from January 14 to January 25, 2021. From top to bottom: radial distance, latitude and longitude in the HCI frame, plasma density, radial speed, the components of magnetic field in the radial-tangential-normal (RTN) frame, and proton temperature. On January 17 at 13:30 UT and on January 19 at 21:00 UT, PSP crossed the heliospheric current sheet, as can be seen by the sudden change in polarity of magnetic field and by the associated density and speed increases. . . . .	91

4.3	Metis coronal images of VL polarized brightness (left) and UV HI Ly-alpha (right) in the solar corona acquired on January 17, 2021, from 16:30 to 17:00 UT within the 3.5-6.3 $R_{\odot}$ field of view. . . . .	92
4.4	Equatorial maps of plasma density, radial speed and magnetic field as simulated by RIMAP, starting from the PSP data collected from January 15 to 21, 2021. The dashed black line is the PSP trajectory (projected on the equatorial plane), and the black segment from 3.5 to 6.3 $R_{\odot}$ is drawn at the Metis' plane-of-the-sky latitude on January 17. The solid red line is the field line connecting PSP measurements and Metis observations. The white line (black in the third panel) represents the Alfvén point for each streamline. . . . .	95
4.5	Comparison between PSP-measured (black) and RIMAP-modelled (red) solar wind parameters from January 15 <sup>th</sup> -21 <sup>st</sup> , 2021. From top to bottom, the panels display the proton number density, the solar wind speed, the radial, and the tangential components of the interplanetary magnetic field (RTN). . . . .	96
4.6	Comparison between observed (squares) and RIMAP-modelled (red line) proton number density (top panel) and outflow velocity (bottom panel) along the streamline highlighted in figure 4.4, from 3 to 25 $R_{\odot}$ . Black and red squares refer to Metis and PSP estimates, respectively. . . . .	98
5.1	Schematics of the magnetic field crossed by PSP during its first solar encounter, when the switchback observations happened. The solar surface is shown coloured by the EUV emission in the 211 Å line as measured by SDO, with coronal holes appearing as lighter shades. The magnetic field line depicted come from a PFSS extrapolation of the solar magnetic field at the time of the first PSP perihelion. Black lines represents closed loops, blue and red lines are open field lines with negative and positive polarities, respectively. The switchback are illustrated as S-shaped kinks in the open field lines emerging from the coronal hole. Reproduced from Bale et al. (2019), © Springer Nature.	101
5.2	Time profiles of PSP taken on 5 November 2018 UT at about 36.6 $R_{\odot}$ , showing switchbacks as radial magnetic field reversals and plasma jets carrying a Poynting flux. Panel a shows magnetic field magnitude ( $ \mathbf{B} $ , black line) and electron density ( $n_e$ , blue line). Panel b show the radial Poynting flux ( $S_R$ , black line) and ion kinetic energy ( $F_p$ , blue line). The last three panels shows the components of $\mathbf{B}$ (black lines) and plasma velocity ( $\mathbf{v}$ , green lines) in the RTN system: the non radial components show Alfvénic fluctuations, while the radial ones shows a large enhancement of radial field in correspondence to jets of plasma. Reproduced from Bale et al. (2019), © Springer Nature.	102
5.3	Close-ups of the propagation of a faster jet of plasma in a uniform medium. In the four panels, the difference between the particle density (top left), radial velocity (top right), radial magnetic field (bottom left), and longitudinal magnetic field (bottom right) at $t = 0$ , before the perturbation enters the domain, and their values at $t = 220 t_0 \approx 4.43$ days. Plotted as black and red arrowed lines, the magnetic field lines on the equatorial plane. A reversal of magnetic field that resembles a switchback (marked by the red field line) can be seen just behind the perturbation front. . . . .	103

5.4	Four different global topologies for magnetic clouds models. Top row shows a toroidal configuration on the left, with S being the the magnetic field on the torus surface, A the axial field, and S/C the spacecraft trajectory; on the right top row a cylindrical flux rope model, with S, A, and S/C having the same meaning of panel (a); the bottom row shows on the left a curved flux rope loop, with arrows A and F indicating two different kinds of spacecraft encounter; on the right bottom row, a spheroidal oblate flux rope, with solid lines depicting the field lines above the plane of the figure, and the dashed lines depictig those below it. Panels a-b-c reproduced from Marubashi and Lepping (2007), © to the authors; Panel d is reproduced from Vandas et al. (1993), © American Geophysical Union. . . . .	105
5.5	Proton and electron temperatures as functions of distance (solid lines), for the classical two-fluid solar wind model of Hartle and Sturrock (1968). The single-fluid profile is shown in dashed lines. Observed values for fast solar wind streams are shown by dots. Reproduced from Priest (2014), © Cambdridge University Press. . . . .	107
5.6	A two-dimensional map of the outflow velocity for the neutral hydrogen in the solar corona out to $4 R_{\odot}$ , inferred from the observations obtained with UVCS/SOHO on June 14, 1997. Reproduced from Dolei et al. (2018), © European Southern Observatory. . . . .	108

# List of Tables

1.1	Properties of the ambient solar wind at 1 AU, from Zhou et al. (2020) and Priest (2014). . . . .	9
1.2	The fast and slow solar wind show different typical properties at 1 AU. . . . .	10
2.1	Computational grid used for the numerical simulations in this section. . . . .	64
3.1	Computational grid for the ICME simulation . . . . .	79
3.2	Input parameters for the cone-modelled ICME at 0.1 AU, before entering the computational domain and being subject to the interaction with the ambient plasma. This would be a fairly modest and relatively common event (Gopalswamy et al., 2014), or possibly even a stealth CME (Ruffenach et al., 2015), usually not capable of inflicting severe geomagnetic storms on Earth’s magnetosphere. . . . .	81
4.1	Computational grid used for the numerical simulation in this section. . . . .	93
5.1	Computational grid used for the test simulation of switchbacks. . . . .	102

# Acknowledgments

At last, I would like to thank those who helped me along the way to achieve the goals of this work.

Dr. Fabio Reale, who guides me with his experience and mentorship through scientific and scientific-related issues, helping me to consider multiple points of view in approaching a problem.

Dr. Alessandro Bemporad, who first instilled in me the interest for the fields of solar physics and space weather, and continues to teach me what it means to do good science.

Dr. Paolo Pagano, who patiently devoted his time to help me in the design and implementation of many of the numerical models described here, and offers key insights to overcome many obstacles.

I would also like to mention the precious help Dr. Antonino Petralia gave me in many technical issues regarding multi-core parallel computing, programming, and how to visualize the results. I also acknowledge the fundamental contributions given by Dr. Andrea Mignone and Dr. Daniele Telloni for the works presented in chapter 2 and 4, respectively.

Finally, I am grateful to my family, my friends, and Olga, who with their support and love push me to offer the best I can. This work is dedicated to them.

This work acknowledges support by ASI-INAF contract nbr. 2018-30-HH.0 “Scientific support to the development of the instruments Metis, SWA DPU and STIX Phases D/E”.